Brno University of Technology
Faculty of Mechanical Engineering
New Technologies for Mechanical Engineering Centre

VŠB - Technical University of Ostrava
Faculty of Metallurgy and Materials Engineering
Regional Materials Science and Technology Centre

Numerical Models of Solidification and their Application in Metal and Ceramic Technology

František Kavička, Jana Dobrovská, Josef Štětina, Karel Stránský, Jaroslav Katolický, Bohumil Sekanina, Jaromír Heger, Hana Francová

The research leading to these results has received **funding from the Ministry of Education, Youth and Sports under the National Sustainability Programme I (Projects LO1202 and LO1203).**

Brno and Ostrava, 2016

MINISTRY OF EDUCATION,
YOUTH AND SPORTS

This book was elaborated with support of NETME Centre, regional research and development centre, built with the financial support from the OP RDI within the project NETME Centre (New Technologies for Mechanical Engineering), Reg. No. CZ.1.05/2.1.00/01.0002 and in the follow-up sustainability stage, financially supported through NETME CENTRE PLUS (LO1202) by the Ministry of Education, Youth and Sports of the Czech Republic under the „National Sustainability Programme I“.

This book was elaborated also with support of the Regional Materials Science and Technology Centre (RMSTC), Reg. No. CZ.1.05/2.1.00/01.0040 and in the follow-up sustainability stage, in the frame of the Regional Materials Science and Technology Centre – Sustainability Program (LO1203), funded by the Ministry of Education, Youth and Sports of the Czech Republic.

Autors:

prof. Ing. František Kavička, CSc.; prof. Ing. Jana Dobrovská, CSc.
prof. Ing. Josef Štětina, Ph.D.; prof. Ing. Karel Stránský, DrSc.
doc. Ing. Jaroslav Katolický, Ph.D.; Ing. Bohumil Sekanina, CSc.
doc. Ing. Jaromír Heger, CSc., Ing. Hana Francová, Ph.D.

Scientific reviewer:

prof. Ing. Margita Longauerová, CSc.

ISBN 978-80-214-5377-7

ISBN 978-80-248-3966-0

Content page

1 Introduction

Solidification (crystallization) phenomena play a major role in such diverse operations as casting, crystal growth, and welding. Solidification proceeds at various rates, which are sometimes far from equilibrium. Thus, the micro-structure obtained is generally not homogeneous and gives rise to variations in composition with position at both small and large scales, which is known as segregation. Solute segregation is important because it leads to non-equilibrium phases, cracks, and other problems, which lower the mechanical properties of the final product. Segregation is classified, according to its scale, as macro-segregation or micro-segregation. Macro-segregation occurs on the scale of the grains or the entire casting and it can be observed with naked eye. It arises from large-scale fluid flow, caused by forced, natural, and solutal convection. It requires the transport of solute-rich or solute-poor liquid and solid phases during solidification over distances much larger than the dendrite arm spacing. One unavoidable cause is the inter-dendritic flow of liquid due to solidification shrinkage and changes in the liquid density. These density changes can be caused by temperature changes or by changes in the liquid composition [L1-1 to 1-3]. Macro-segregation is also affected by nozzles, which direct the liquid; electromagnetic forces, which enhance mixing [L1-4 to 1-6] and by thermal or mechanical bulging or deformation of the casting during solidification [L1-7].

Clearly, macro-segregation prediction is very complex. Among many other things, it depends on an accurate prediction of micro-segregation. Micro-segregation refers to a composition variation within the columnar or equiaxed dendritic solidification structure, which has a length scale of the order of only few micrometers. It is usual to characterize the extent of micro-segregation using a ranking scheme of randomly sampled electron micro-analysis data. Thermodynamic quantities are often calculated from measurements of the as-cast segregation profile, in particular, the partition coefficient. These thermodynamic quantities are used for alloy development programs [L1-8] and in casting process models [L1-9 and 1-10] both as input properties and for validation. A well-founded technique is thus imperative for evaluating compositional data from X-ray microanalysis [L1-11 to 1-14]. No such complex investigation has yet been done for samples taken from continuously cast steel slab. Micro-segregation is caused by the redistribution of solute during solidification, as solute is generally rejected into the liquid. Its fundamental cause is the difference between the thermodynamic equilibrium solubility of alloy elements in the different phases that coexist in the mushy region during solidification. This is combined with the inability of solid state diffusion to fully return the composition to its equilibrium constant level after solidification is complete, owing to the short times and small diffusion coefficients involved. Quantitative prediction of these phenomena is complicated by several difficulties:

(1) Quantifying the equilibrium solubility of each phase as a function of temperature. This is traditionally done using partition coefficients, which are reasonable for low concentrations, but which require the full multi-component phase diagram for complex systems or for higher alloy contents [L1-15].

(2) Solving for diffusion transport within the solid phases, which requires knowledge of (a) the diffusion coefficients for each element, (b) the length scale, which depends on the solidifying micro-structure and varies from the secondary to the primary dendrite arm spacing to the grain size, and (c) the cooling conditions, which depend on macroscopic heat conduction in the casting.

(3) Linking of the micro-segregation phenomena with the fluid flow and associated macro-segregation. This is complicated, because flow occurs on at least three size scales, including flow within the inter-dendritic spaces, flow between grains, and flow in the bulk liquid [L1-16]. A micro-structure prediction is a very difficult task, which requires computationally intensive modelling methods, such as of the phase field [L1-17 to 1-19] and cellular automata [L1-20 and 1-21]. Many simple micro-segregation models [L1-22] have been proposed, which assume a fixed dendrite arm spacing, constant physical properties in the solid phase, thermodynamic equilibrium at the solid-liquid interface, and straight liquidus or/and solidus lines in the equilibrium phase diagram.

Won and Thomas [L1-23] introduced a new "simple micro-segregation model" for the solidification of multi-component steel alloys. The solubility levels are based on liquidus temperatures and partition coefficients taken from available measurements for multi-component steel alloys, as are the diffusion coefficients. To obtain the micro-structural-length scales, an empirical equation is developed to quantify the secondary dendrite arm spacing as a function of carbon content and cooling rate, based on experimental measurements of the final micro-structures. The cooling history needed by the model is simply input to match experiments or treated as a parameter. Linking of the model with the flow is ignored. To validate this simple micro-segregation model, experimental measurements are needed.

Commercially available softwares are not able to predict the chemical heterogeneity of continuously cast material components of multi-component alloys. It is possible to present as an example the world-renowned software ProCast (ESI Group), which offers a comprehensive solution for the simulation of continuous and semi-continuous foundry processes. However, this software either is not able to solve (to simulate) the final chemical heterogeneity of the continuously cast blank, which is significantly influenced by macro-segregation and micro-segregation processes at crystallization, solidification and cooling of the material. This software offers so far only a simple simulation of macro-segregation of individual elements in 2D, and only for horizontal or vertical technology of continuous casting. This software is so far unable to solve casting of radial continuous casting machine (CCM), or the resulting overall chemical heterogeneity, which is influenced by macro-segregation and micro-segregation of all the additive elements.

1.1 Substance of 3D numerical models of the transient temperature and heterogeneity field

Crystallization and chemical heterogeneity resp. dendritic segregation of constitutive elements and admixtures in solidifying (crystallising) and cooling gravitationally cast casting (shortly casting) or continuously cast casting (shortly concasting) is directly dependent on character of formation of its temperature field, rate and duration of the running crystallisation at any place of the casting or concasting, so called local solidification time.

Solidification and cooling down of a casting as well as the simultaneous heating of a metal or non-metal mould is a rather complex problem of transient heat and mass transfer. This process in a system casting (riser)-mould (chills)-ambient can be described by the Fourier's equation (eq. 1-1) of 3D transient conduction of heat.

$$\rho \cdot c \frac{\partial T}{\partial \tau} = \frac{\partial}{\partial x}\left(k \frac{\partial T}{\partial x}\right) + \frac{\partial}{\partial y}\left(k \frac{\partial T}{\partial y}\right) + \frac{\partial y}{\partial z}\left(k \frac{\partial T}{\partial z}\right) + \dot{Q}_{source} \qquad \text{(eq. 1-1)}$$

In eq. 1-1 are T temperature (K), τ time (s), k heat conductivity ($W \cdot m^{-1} \cdot K^{-1}$), ρ density ($kg \cdot m^{-3}$), c specific heat capacity ($J \cdot kg^{-1} \cdot K^{-1}$), $\dot{Q}_{source}$ latent heat of the phase or structural change ($W \cdot m^{-3}$), x, y, z axes in given main directions [m]

Implementation of concasting, which considerably increased rate of melt cooling between temperatures of liquidus and solidus brought about time necessary for crystallic structure homogenisation. 3D transient temperature field of the system of concasting-mould (crystallizer) or concasting-ambient (in so called a concasting machine-CCM, shortly a caster) is described by Fourier-Kirchoff's equation (eq. 1-2).

$$\rho \cdot c \frac{\partial T}{\partial \tau} = \frac{\partial}{\partial x}\left(k \frac{\partial T}{\partial x}\right) + \frac{\partial}{\partial y}\left(k \frac{\partial T}{\partial y}\right) + \frac{\partial y}{\partial z}\left(k \frac{\partial T}{\partial z}\right) + \varrho \cdot c \left(w_x \frac{\partial T}{\partial x} + w_y \frac{\partial T}{\partial y} + w_z \frac{\partial T}{\partial z}\right) + \dot{Q}_{source} \qquad \text{(eq. 1-2)}$$

In equation (eq. 1-2) w_x, w_y, w_z are velocity in given main directions ($m \cdot s^{-1}$)

These equations are solvable only by means of modern numerical methods. The numerical model for the simulation of the temperature field of a system casting- mould-ambient was created by ANSYS (see Chapters 2 to 4). The original numerical model for the simulation of the temperature field of a caster was developed (see Chapters 3 to 10).

Both models (**models A**) of the temperature field of a casting and concasting are based on the 1st and 2nd Fourier's laws on transient heat conduction, and the 1st and the 2nd law of thermodynamics. They are based on the numerical method of finite differences with explicit formula for the unknown temperature of the mesh node in the next time step, which is a function of temperatures of the same node and all adjacent nodes of a calculation net in the previous time step. Models take into account non-linearity of the task, it means dependence of thermo-physical properties of all materials of the systems on temperature and dependence of heat transfer coefficients on temperature of all external surfaces. Models are equipped with and interactive graphical environment for automatic generation of a mesh, and for evaluation of results, it means by so called pre-processing and post-processing.

Off-line version of the models A has been designed for general analysis of influence of various initial and marginal conditions (for so called parametric studies) in order to achieve optimal distribution of temperatures in a casting or concasting for enhancement of its quality; therefore in the simulation of gravitationally cast casting or continuously cast casting. On-line version of the model follows development of temperature field only of a caster in real time and confronts the results with continuously measured parameters.

Another **model B** is model of chemical heterogeneity of chemical elements, enables description and measurement of dendritic segregation of constitutive elements and admixtures in solidifying (crystallising) and cooling casting (gravitationally cast casting) or concasting (continuously cast casting) too. This model is based on the 1st and 2nd Fick's laws of diffusion and it comprises implicitly also the law of conservation of mass. The solution itself is based on the Nernst distribution law, which quantifies at crystallisation distribution of chemical elements between liquid and solid phases of currently crystallising melt (metallic or ceramic) in the so called mushy zone (i.e. in the zone lying between the temperature of liquidus and solidus). Majority of parameters necessary for application of the model A is known, but parameters necessary for use of the model B had to be determined by measurements on the work itself, i.e. on suitably chosen samples from the crystallised casting or concasting.

At solution of the research projects experimental measurements of chemical heterogeneity were performed on many casting and concasting systems [L1-24 to 1-42]. Large number of the measured and archived concentration data of chemical elements were therefore available and which were efficiently used, since both the above mentioned models A and B may be by their use conjugated, i.e. mutually unified into the model (AB) in its off-line version (see Chapters 2 to 8). In the near future this conjugated model will make it possible first in its off-line version to determine unsteady 3D concentration field of elements of a designed system without any further experiments.

1.2 Abstracts of the chapters 2 to 10

Chapter 2

A three-dimensional (3D) model of solidification (ANSYS) is used to describe the process of solidification and cooling of massive $500 \times 1\,000 \times 500$ mm cast-iron castings. The following dependences are later determined according to the experimental and calculated data: the average size of the graphite spheroids R_g, graphite cells R_c and the average distances among the particles of graphite L_g – always as a function of the local solidification time $\theta\ (x_i, y_i, z_i)$. Furthermore, it has been found out that the given basic characteristics of the structure of the cast iron are directly proportional to the logarithm of the local solidification time. The original spatial model of solidification can therefore be used in its first approximation for the assessment of the pouring structure of massive cast-iron castings. The main economic goal observed is the saving of liquid material, moulding and insulation materials, the saving of energy and the already mentioned optimization of pouring and the properties of the cast product.

Chapter 3

The quality of the working rollers used for rolling rails of different profiles is determined by the chemical and structural composition of the material of the rollers and the production technology. The diameter of the actual roller is 1 180 mm and height 2 100 mm. It is therefore necessary to find and ensure optimal relationships between the matrix structure and the resultant values of the mechanical

properties of the rollers in order to maximize the length of life. The requirements introduced here cannot be ensured without perfect knowledge of the course of solidification, cooling and heat treatment of the cast rollers as well as the kinetics of the temperature field of the casting and mould (ANSYS). The kinetics of the solidification has a measurable and non-negligible influence on the chemical and structural heterogeneity of the investigated type of cast-iron. Tying on to the results of the model of the temperature field of the cast rollers, an original methodology was developed for the measurement of chemical microheterogeneity.

Chapter 4

Corundo-baddeleyit material EUCOR is a heat- and wear-resistant material even at extreme temperatures. This chapter introduces a numerical model (ANSYS) of solidification and cooling of this material in a non-metallic mold. The model is capable of determining the total solidification time of the casting and also the place of the casting which solidifies last. Furthermore, it is possible to calculate the temperature gradient at any point and time, and also determine the local solidification time and the solidification interval of any point. The local solidification time is one of the input parameters for the cooperating model of chemical heterogeneity. This second model and its application on EUCOR samples prove that the applied method of measuring the chemical heterogeneity provides the detailed quantitative information on the material structure and makes it possible to analyze the solidification process. The analysis of this process entails statistical processing of the measurement results of the heterogeneity of the EUCOR components and performs the correlation of individual components during solidification. The verification of both numerical models was conducted on a real cast 350 × 200 × 400 mm block.

Chapter 5

This chapter introduces a 3D original numerical model of the temperature field of the slab caster (CCM - concasting machine) and billet caster in the form of in-house software. The model includes the main thermodynamic transfer phenomena during the solidification of concasting. The temperature model is used for monitoring and for parametric studies of the changes in chemical composition, the casting speed, the superheating temperature and the dimensions of the concast slab and billet.

The application of the numerical model requires systematic experimentation and measurement of operational parameters on a real caster as well as in the laboratory (heat transfer coefficients). The measurement results, especially temperatures, serve not only for the verification of the exactness of the model, but mainly for optimization of the process procedure: real process → input data → numerical analysis → optimization → correction of real process. The most important part of the investigation is the measurement of the temperatures in the walls of the mould and the surface of the slab and billet in the zones of secondary and tertiary cooling.

The on-line version of the 3D dynamic model of the temperature field of a caster is based on its off-line version. It enables the simulation of the temperature field of the caster in real time. It receives the data from the first and second level of control of the caster via an interface program, evaluates the measured data and carries out a calculation of the temperature field and other aggregated quantities that are sent back to the information system of the steelworks/plant. It aims to enhance the quality and accuracy of the input data, the mutual connections between them and the qualitative parameters, including the establishing of their limit values. This creates a system that not only quickly but also very accurately displays the temperature field of the blank during the course of the actual process, including all necessary technological data from the caster.

Chapter 6

Subchapters 6.1 and 6.2 presents the result of an application of the numerical model of solidification and the model of chemical heterogeneity to the estimation and description of the solidification and heterogeneity parameters of a continuously cast slab (dimensions 1 530 × 250 mm) of non-alloyed low carbon steel (the connection of the two models *AB)*. The nine experimental samples were taken from one half of the slab cross section. The chemical heterogeneity of elements (Al, Si, P, S, Ti, Cr, Mn and

Fe) was measured by means of electron microprobe in 101 points of sample structures. The following heterogeneity parameters of elements were established: microheterogeneity indexes, effective partition coefficients and pair correlation coefficients among the elements i and j of the slab. Besides these parameters, the dimensionless Brody-Flemings parameters $\alpha_i = D_i \cdot \theta / L^2$ were calculated for each element and each sample and compared with literature data. For each sample, the local times of solidification θ and the dendrite arm spacing L were calculated by means of an original numerical method. Then the diffusion coefficient of each element was calculated by relation of $D_i = \alpha_i \cdot L^2/\theta$. The calculated values of diffusion coefficients were compared with those in literature.

Parameter of back diffusion (the mass Fourier number) occurs in majority of the used micro-segregation models. It characterises diffusion of elements in solid phase in respect to the secondary dendrite arms spacing and to the local time of solidification. The subchapter 6.3 presents calculates parameters of back diffusion of determined elements (C, Si, Mn, P and S) in selected areas of cross-section of continuously cast steel billet. Calculations were made with use of our own experimental data, tabulated data and also outputs from heat model simulating temperature field of billet at solidification and cooling. On the basis of these results it is possible to formulate a hypothesis about influence of cooling rate on back diffusion of investigated elements at solidification of steel billet.

Chapter 7

Two original numerical models have been developed and used in the investigation of a contcast steel slab. The model of the temperature field of a concasting is capable of simulating the temperature field of a caster. Experimental research and data acquisition have to be conducted simultaneously with the numerical computation—not only to confront it with the actual numerical model, but also to make it more accurate throughout the process. The second numerical model of dendritic segregation of elements assesses critical points of slabs from the viewpoint of their increased susceptibility to crack and fissure. In order to apply this model, it is necessary to analyze the heterogeneity of samples of the constituent elements and impurities in characteristic places of the solidifying slab. The combination of both models enables the prediction of cracks and fissures in critical points of the continuously cast carbon-steel slab. Both models had been applied in the industrial investigation of a cast steel slab (subchapter 7.2-3).

Subchapter 7.4 tries to verify the hypothesis on the initiation and propagation of the cross crack by means of behaviour in tensile tests with the con-cast slab of the same basic chemical composition in the range of temperature moving from 25 °C to 1 450 °C. The tensile tests were made on 18 test bars at suitably chosen temperature differences and gradually led to the tension ruptures of the bars under exactly defined conditions. Simultaneously, the roughness of the resultant rupture surface depending upon the temperature was studied in detail. Thus relations between the roughness of the rupture surface, tension force, work to rupture and contraction with the test bars at the given range of temperature were determined. On the basis of the comparison of the rupture surfaces of cross cracks found in the study and the rupture surfaces obtained at the given interval of test temperatures in the course of this study, properties of material of the slab affected by the cross crack and its most probable behaviour during solidification and cooling were then evaluated by analogy. In this way it was possible to specify and verify the mechanism of cross crack initiation and propagation and to assess the temperature interval, within which the initiation was the most probable.

Chapter 8

Subchapter 8.1 Original numerical model was applied for simulation of the transient temperature field of continuously cast steel slab of two different chemical compositions. When both melts follow closely after each other, the critical state of the so called breakout occurs at a certain point of the secondary cooling zone of a caster. It is obviously caused by a combination of surface defects. However, different chemical composition of two steels and their mixing is apparently decisive. Therefore the temperature model has simulated the temperature history of every point of the cross-section of the slab during its movement through the whole caster from the level of the melt in the mould to the cutting torch for both melts and for their mixture (with average chemical composition). Calculation of the temperature field of a slab has focused mainly on the part of the slab before the

breakout and its surroundings. Calculation results were compared graphically by means of a graph of temperatures in characteristic points of the cross section, a graph of isotherms in the critical cross-section passing through the breakout, including iso-liquidus and iso-solidus, a graph of isotherms in longitudinal sections and a graph of increase in thickness of solidified shell. Definition of the boundary conditions in primary and tertiary cooling zone of the caster is identical for all three variants of calculation, in secondary cooling zone depends on the cooling curves. The results of the temperature field can establish a model of the chemical heterogeneity of steel supported by material expertise on the samples taken from the breakout.

Subchapter 8.2 Changes of the chemical composition of the steel during continuous casting of of the slab 250 × 1 530 mm are particularly dangerous. In the event that two melts are cast one right after another, i.e. if the melt of steel with chemical composition A ends and it is immediately followed by the steel B, it may automatically stop the caster and an atypical breakout may take place. It happened during continuous casting in the area of straightening, 20 minutes after flying change of tundish. With use of dimensional analysis altogether 8 criteria of similarity were derived according to the π-theorem. Table of 12 technological, geometrical and thermo-physical dimensional quantities was compiled for these criteria, which characterise both steel grades A and B and process of their continuous casting. Thermo-physical properties of both steels for the table were determined with use of commercial software IDS. Important data in temperature field of the slab, such as maximum and minimum length of iso-liquidus and iso-solidus, range of the so called mushy zone and zone of melt at the place of breakout, temperature of the slab surface, etc. were calculated by the original model. Five of these criteria are at the same time functions of thermo-physical parameters, but also of technological and geometrical parameters. Numerical values of eight criteria were determined for the steels A and B and then standard operations were made with the criteria, such as evaluation of partial shares of pairs of the same criteria for both steels. This application of the theory of physical similarity clearly proved markedly increased tendency of the steel B to breakouts in comparison with the steel A. In order to prevent repetition of this accident of the caster for another pair of steels cast immediately one after another, it is necessary to assess the derived individual criteria of similarity for both steels and other operations with these criteria. The way to reduce the risk of breakouts may be found mainly in the change of thermo-physical properties of both steels, consisting primarily of reduction of differences of chemical composition of both melts, so that partial shares of similarity criteria were close to the value of one.

Subchapter 8.3 Altogether 11 samples were taken from the part of a solidified slab. The samples were taken both from the breakout areas and from the areas not affected by the breakout. First the concentration of selected elements was measured in individual samples by spectrometry. Concentrations of selected elements (Al, Si, P, S, Cr, Mn, Ni and Mo) were measured in these samples using scanning electron microscope and energy dispersive spectroscopy. Concentration data were measured in each sample at 101 points along the selected line of 1 000 μm. Concentration data from the individual samples were then subjected to basic statistical analysis. Using the original mathematical models the basic micro-segregation characteristics were further determined for each analysed element. The parameter of macro-heterogeneity was also determined for individual elements from the measured concentration data. Furthermore a quantitative measurement of inclusions ("micro-cleanness") in the samples was performed using a metallographic microscope. Then method of differential thermal analysis was used for the measurements of temperatures of phase transformations, namely the liquidus and solidus temperatures. The following main results were found: – magnitude of micro-segregation of the analysed elements in the measured sections of 1 000 μm is approximately the same in all the analysed samples, – chemical macro-heterogeneity is very high across the analysed slab section, elements with different concentration in the melts of the steels A and B are along the longitudinal axis distributed very unevenly, – very uneven mixing of melts of both steels was probably one of the main causes of formation of the breakout.

Chapter 9

Electromagnetic stirring (EMS) suppresses the growth of columnar crystals of billets and reduces the tendency to cracking during casting and at low temperatures. A caster was used for the testing of two induction stirrers – one on the actual mould and the other beneath the mould – to determine the effect of EMS on the formation of the structure of non-alloy steel. As part of these tests, certain parts of the

billets had been cast without the use of stirrers and other parts underwent alternate switching on and off of the stirrers for as many as nine combinations of modes. Samples were taken from the sections of these billets, fine-ground and etched in order to make the dendritic structure visible. The mode with the highest efficiency was when both stirrers ran simultaneously. The growth of the columnar crystals, which pointed inward, was limited to 1/4-to-1/3 of the length of the case when there was no stirring. Experimental research was also confronted with results acquired from the application of the models of the temperature field and chemical heterogeneity and the physical-similarity theory. Statistical monitoring of the quality of concast billets has proven that stirring significantly reduces the occurrence of defects – in this case cracks.

Chapter 10

The chapter deals with the method of quantitative wave dispersive X-ray spectral micro-analysis used for measurement of the mass concentration of carbon in the continuously cast steel billet. The main conditions for preparation of metallographic sections from the samples taken from continuously cast billets are described, if the samples are designated for determination of the carbon concentration by the above mentioned method. These conditions must be unconditionally adhered to in order to ensure a reproducibility of the measurements of the mass concentrations of carbon. A limit of detectability of carbon and of errors of the measurement of carbon at the measurement on the limit of detectability at the measurement of its mass concentration on the spectral line C Kα with use of the standard Fe_3C is given. The proposed method of measurement of the carbon concentration was applied for simultaneous determination of the distribution of mass concentration of carbon, manganese, silicon and phosphorus in nine samples taken from the continuously cast billets made of unalloyed steel. Concentrations of these four elements were in individual samples measured in the segment with the length of approx. 1 mm at 100 points with the use of an analytical complex JEOL JXA-8600/KEVEX DELTA V-Sesame and wave dispersion analysis (VDA). Mathematical-statistical processing of the results of measurement showed that the carbon concentration can be determined in a reproducible manner and that it is possible at the same time to explain its relationship with the distribution of simultaneously analysed elements - manganese, silicon and phosphorus in the structure of the continuously cast steel billet.

1.3 Literature

[L1-1] Flemings M.C. and Nereo G.E.: *Trans. TMS-AIME*, 239 (1967), 1449–61.
[L1-2] Mehrabian R., Keane M. and Flemings M.C.: *Metall. Trans.*, 1 (1970), 1209–20.
[L1-3] Fuji T., Poirier D.R. and Flemings M.C.: *Metall. Trans. B*, 10B (1979), 331–39.
[L1-4] Mizukami H., Komatsu M., Kitagawa T. and Kawakami K.: *Trans. Iron Steel Inst. Jpn.,* 24 (1984), 940–49.
[L1-5] Oh K.S., Lee I.R., Shin Y.K., Koo Y.S., Lee I.J. and Lee D.Y.: *Proc. 6th Int. Iron Steel Congr.*, ISIJ, Nagoya, 1990, pp. 256–63.
[L1-6] Ayata K., Koyama S., Nakata H., Kawasaki S., Ebina K., and Hata T.: *Proc. 6th Int. Iron Steel Congr.*, ISIJ, Nagoya, 1990, pp. 279–84.
[L1-7] El-Bealy M.: *Scand. J. Metall.*, 24 (1995), 63–80.
[L1-8] Zhao J.-C. and Henry M.F.: *Adv. Eng. Mater.,* 4 (2002), 501–08.
[L1-9] Wang W., Lee P.D. and McLean M.: *Acta Mater.,* 51 (2003), 2971–87.
[L1-10] Wang W., Kermanpur A., Lee P.D. and M. McLean: *J. Mater. Sci.,* 38 (2003), 4385-91.
[L1-11] Howe, A., Lacaze J. and Benigni P.: *Adv. Eng. Mater.,* 5 (2003), 37–46.
[L1-12] Xie F., Yan X., Ding L., Zhang F., Chen S., Chu M.G. and Chang Y.A.: *Mater. Sci. Eng. A,* 355A (2003), 144–53.
[L1-13] Tin S. and Pollock T.M.: *Mater. Sci. Eng. A,* 348A (2003), 111–21.
[L1-14] Ganesan M., Dye D. and Lee P.D.: *Met. Mat. Trans A*, 36A (2005), 2191–2204.
[L1-15] Miettinen J.: *Metall. Trans. A*, 23A (1992), 1155–70.
[L1-16] Wang C.Y. and Beckermann C.: *Mater. Sci. Eng.*, 171 (1993), 199–211.
[L1-17] Lee J.S., Kim S.G., Kim W.T. and Suzuki T.: *Iron Steel Inst. Jpn. Int.*, 39 (1999), 730–36.
[L1-18] Nestler B. and Wheeler A.A.: *Physica D*, 138 (2000), 114–33.
[L1-19] Rappaz J. and Scheid J.F.: *Math. Methods Appl. Sci.*, 23 (2000), 491–513.

[L1-20] Kim K., Yeo T., Oh K.H. and Lee D.N.: *Iron Steel Inst. Jpn. Int.*, 36 (1996), 284–89.
[L1-21] Won Y.M., Kim K.H, Yeo T. and Oh K.H.: *Iron Steel Inst. Jpn. Int.*, 38 (1998), 1093–99.
[L1-22] Clyne T.W. and Kurz W.: *Metall. Trans. A*, 12A (1981), 965–71.
[L1-23] Won Y.M. and Thomas B. G.: *Met. Mat. Trans A*, 32A (2001), 1755–1761.
[L1-24] Kavička F., et al.: Thermokinetics of technological processes. *Final research report of the project GAČR GA106/93/0440*, Brno, Czech Republic, 1995.
[L1-25] Kavička, F., et al.: Thermokinetics of Technology. *Final research report of the project No. 93006 of U.S.- Czechoslovak Science and Technology Program*, Brno, Czech Republic, 1998.
[L1-26] Kavička F., et al.: Optimization of slab continuous casting with use of numerical model. *Final research report of the project GAČR GA106/98/0296*, Brno, Czech Republic, 2001
[L1-27] Kavička, F., et al.: Optimization of Quality of Continiuously Cast Billets Required for Subsequent Technological Processing. *Final research report of the project of the project EUREKA No. 1867 CONMOD, Brno*, Czech Republic, 2002.
[L1-28] Kavička F., et al.: The optimization of utility properties of corundo-baddeleyit materials (EUCOR) and the technology of its casting. *Final research report of the project GAČR GA106/99/0728*, Brno, Czech Republic, 2002.
[L1-29] Kavička F., et al.: Numerical simulation of physical phenomena of concasting. *Final research report of the project COST OC P3.20*, Brno, Czech Republic, 2002.
[L1-30] Dobrovská J., et al.: Heterogeneity and dendritic segregation of the constitutive elements and impurities in steel – their evaluation, measurement and control. *Final research report of the project GAČR GA106/00/0083*, Ostrava, Czech Republic, 2002.
[L1-31] Kavička F., et al.: Optimization of properties and production technology of heavy ductile-cast iron castings. *Final research report of the project GAČR GA106/01/1164*, Brno, Czech Republic, 2003.
[L1-32] Kavička F., et al.: Complete optimization of technology for concasting of steels, including special steels. *Final research report of the project GAČR GA106/01/1464*, Brno, Czech Republic, 2004.
[L1-33] Kavička F., et al.: Optimization of technology of material EUCOR. *Final research report of the project MŠMT KONTAKT No. 23/2003*, Brno, Czech Republic, 2004.
[L1-34] Kavička, F., et al.: Optimization of Casting of Corundobaddeleyit Material EUCOR. *Final research report of the project COST OC 526.10 APOMAT*, Brno, Czech Republic, 2005.
[L1-35] Dobrovská J., et al.: The chemical heterogeneity and dendritic segregation of elements in polycomponenet metallic systems -alloyed steels, Ni-alloys and ductile cast iron. *Final research report of the project GAČR GA106/03/0271*, Ostrava, Czech Republic, 2005.
[L1-36] Kavička F., et al.: Creation of Set of Models For Prediction of Technological Parameters And Thermal Processes For Enhancement of TQM System. *Final research report of the project EUREKA 2716 COOP*, Brno, Czech Republic, 2006.
[L1-37] Kavička F., et al.: Research, development and field application of a dynamic model for the control of technology of continuous billet caster. *Final research report of the project MPO FI-IM/021*, Brno, Czech Republic, 2006.
[L1-38] Kavička F., et al.: Optimization of technological parameters of the gravity-cast rolls for rolling rails. *Final research report of the project MŠMT KONTAKT No. 14/2005*, Brno, Czech Republic, 2006.
[L1-39] Molínek J., et al.: Optimization of technological parameters of the gravity-cast rolls for rolling. *Final research report of the project GAČR GA106/04/1334*, Ostrava, Czech Republic, 2007.
[L1-40] Kavička F., et al.: Modelling of heat and mass transfer in large systems of massive metal materials during solidification. *Final research report of the project GAČR GA106/08/0606*, Brno, Czech Republic, 2011.
[L1-41] Štětina J., et al: Mathematical & stochastic modelling of the concasting of rectangular profile steels blanks. *Final research report of the project GAČR GA106/09/0940*, Brno, Czech Republic, 2012.
[L1-42] Kavička F., et al.: Analysis of influence of metallurgical-material and technological parameters of concast steel blanks on their quality and proces stability. *Final research report of the project GAČR GAP107/11/1566*, Brno, Czech Republic, 2014.

2 Numerical optimization of the method of cooling of a massive casting of ductile cast-iron

2.1 Introduction

The quality of a massive casting of cast iron with spheroidal graphite is determined by all the parameters and factors that affect the metallographic process and also others. This means the factors from sorting, melting in, modification and inoculation, casting, solidification and cooling inside the mould and heat treatment. The centre of focus were not only the purely practical questions relating to metallurgy and foundry technology, but mainly the verification of the possibility of applying two original models – the 3D model of transient solidification and the cooling of a massive cast-iron casting and the model of chemical and structural heterogeneity. Both models have only been applied to describing the temperature field, the control of crystallisation and the cooling of continually cast steel slabs, to the descriptions of their chemical heterogeneity and to determining the basic characteristics of their microstructure [L1-31].

In this combination of two models, it is possible to optimise the technology of pouring cast-iron castings and successive cooling in order to achieve the most convenient structure. This includes a structure created of spheroids of graphite, preferably with as high a density as possible and spread throughout the casting as evenly as possible, with a minimal ratio of particles of graphite marked as degenerated shapes.

The used 3D model of the temperature field of the system is based on the numerical finite-element method. The simulation of the release of the latent heats of phase or structural changes is carried out by introducing the thermodynamic enthalpy function. It enables the evaluation of the temperature field within the actual casting, chills and mould at any point in time within the process of solidification and cooling using contour lines (i.e. so-called iso-lines and iso-zones) or temperature-time curves for any nodal point of the system. The model establishes a system via which it is possible to pre-simulate the method of eutectic crystallisation of the melt of ductile cast-iron. With the liquidus and solidus known, it is also possible – in selected parts of the casting (that would be suitably discretized) – to determine the time the temperature of the relevant part of the metal remains between the liquidus and solidus. This region is characterised by the coexistence of solid and liquid states – the so-called 'mushy zone'. In describing the crystallisation of the steel, the time for which the metal remains at a temperature between the liquidus and solidus is called the local solidification time, and the volume of metal corresponding to this time is determined by the sizes of the dendrites [L2-1 and 2-2]. This paper deals with the simulation of solidification and cooling of a massive casting, with various ways of accelerated cooling using steel chills in order to reduce the heterogeneity of the pouring temperature field and to increase the rate of cooling of the casting. The results of the simulation are compared with experimentally measured temperatures. Having one's own numerical model available makes it possible to integrate one's own idea of the optimal course of solidification and cooling of the object under investigation in accordance with the latest findings and experiences of a specific operation. This is the main part of the role of the technological worker, irreplaceable by any computer technology whatsoever. Computer technology, despite its perfection, is only a tool enabling real-time prediction of his/her technical thinking and decisions.

2.2 Assignment and proposal of the calculation of the 3D temperature field of a massive casting (a block)

A real 500 × 1 000 × 500 mm ductile cast-iron block had been used for the numerical calculation and the experiment [L1-31]. The density of investigated experimental castings is approximately $2 \cdot 10^3$ kg. The average chemical composition of the cast-iron before casting is given in **Tab. 2-1.** The calculation of the temperature of the liquidus T_L and solidus T_S for a melt was performed using special software with the values: $T_L = 1\,130$ °C and $T_S = 1\,110$ °C. The interval of the solidification is therefore $\Delta T = 20$ °C.

Tab. 2-1 Chemical composition of ductile cast-iron

Element	C	Mn	Si	P	S	Ti	Al	Cr	Ni	Mg
(wt.%)	3.75	0.12	2.15	0.039	0.004	0.01	0.013	0.07	0.03	0.045

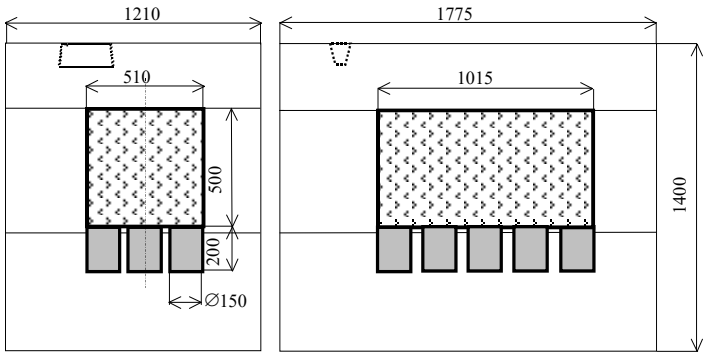

Fig. 2-1 The moulding of the block with chills on one side

The block was cast into sand moulds with various arrangements of steel chills of cylindrical shape. The dimensions of the block, the mould, the chills and their arrangements are illustrated in **Fig. 2-1** (chills on one side) and in **Fig. 2-2** (chills on three sides). An example of the moulding of the block with chills on one side and its pouring is in **Fig. 2-3**.

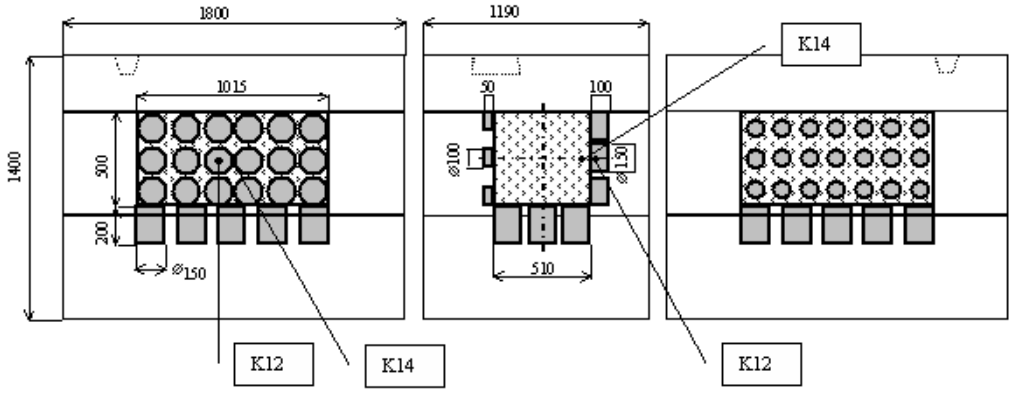

Fig. 2-2 The moulding of the block with chills on three sides

Fig. 2-3 The moulding of the block with chills on one side and its pouring

The numerical model of the temperature field observes two main goals: directed solidification as the basic condition for the healthiness of a casting and the optimization of the technology of pouring while optimizing the utility properties of the product. The main goal observed – in terms of the economics – is the saving of liquid metal, moulding materials, the saving of energy and the already mentioned optimization of pouring and also the improvement of the properties of the cast product.

The solidification and cooling of a classically cast (i.e. gravitationally poured) casting and the simultaneous heating of the mould and chills is, from the viewpoint of themokinetcs, a case of 3D transient heat and mass transfer. In systems comprising the casting, the mould, chills and ambient, all three kinds of heat transfer take place. Since these problems cannot be solved analytically, even with the second-order partial differential Fourier equation (where mass transfer is neglected and conduction is considered as the most important of the three kinds of heat transfer), it is necessary to engage numerical methods.

$$\rho \cdot c \frac{\partial T}{\partial \tau} = \frac{\partial}{\partial x}\left(k \frac{\partial T}{\partial x}\right) + \frac{\partial}{\partial y}\left(k \frac{\partial T}{\partial y}\right) + \frac{\partial y}{\partial z}\left(k \frac{\partial T}{\partial z}\right) + \dot{Q}_{source} \qquad \text{(eq. 2-1)}$$

The Fourier equation (**eq. 2-1**) for a casting must be adapted so as to describe the temperature field of a casting in all its three phases: in the melt, in the mushy zone and in the solid phase. Here it is necessary to introduce the specific volume enthalpy $H_v = c \cdot \rho \cdot T$, which is dependent on temperature. The thermodynamic enthalpy function includes latent heat of phase or structural changes. The equation (**eq. 2-1**) then takes on the form:

$$\frac{\partial H_v}{\partial \tau} = \frac{\partial}{\partial x}\left(k \frac{\partial T}{\partial x}\right) + \frac{\partial}{\partial y}\left(k \frac{\partial T}{\partial y}\right) + \frac{\partial y}{\partial z}\left(k \frac{\partial T}{\partial z}\right) + w_z \frac{\partial H_v}{\partial z} \qquad \text{(eq. 2-2)}$$

The specific heat capacity c, density ρ and heat conductivity k are also functions of temperature. The temperature of the general nodal point of the casting is obtained from the enthalpy-temperature dependence, which must be known for the relevant ductile cast-iron. The software pack ANSYS had been chosen for this investigation because it enables the application of the most convenient method of numerical simulation of the release of latent heat of phase and structural changes using the thermodynamic enthalpy function.

The software also considers the non-linearity of the task, i.e.:

- The dependence of the thermophysical properties (of all materials entering the system) on the temperature, and
- The dependence of the heat-transfer coefficients (on all boundaries of the system) on the temperature of the surface – of the casting and mould.

ANSYS has an integrated mesh generator (i.e. pre-processing) as well as graphical output (i.e. post-processing) of the results and the user can change the pouring parameters, the dimensions of the casting-mould system and the dimensions of the elementary mesh volume before the actual calculation. The density of the mesh makes it possible to approximate the linear distribution of temperatures between individual points of the 3D mesh, and even within time intervals.

The exactness of the numerical solution depends not only on the spatial and temporal discretization, but also on the precision with which the thermophysical properties of all materials entering the system are determined, and also on how precisely the boundary conditions are derived.

Fig. 2-4 shows the proposal of computational mesh for the block with chills on one side and for the mould.

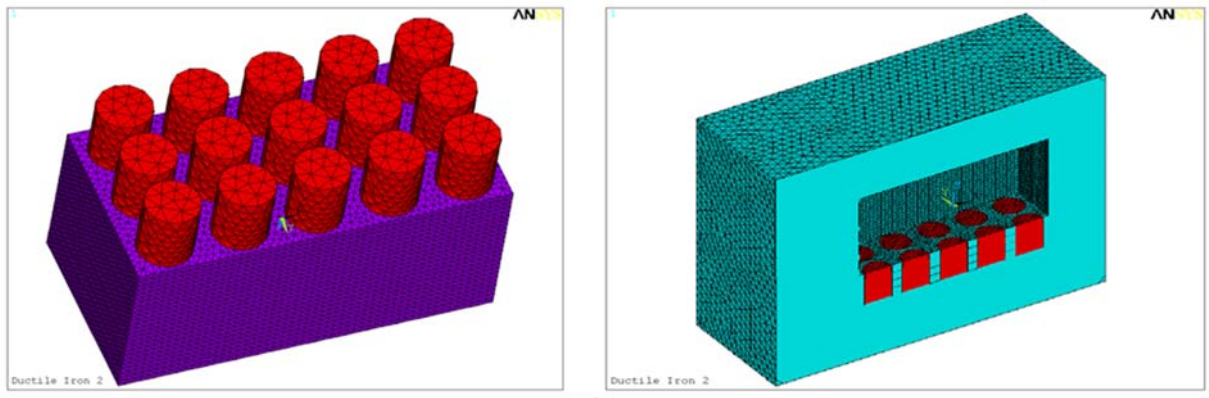

Fig. 2-4 The proposal of computational mesh for the block with chills on one side and for the mould

2.3 Temperature measurement

The application of the 3D numerical model on a transient temperature field requires systematic experimentation, including the relevant measurement of the operational parameters directly in the foundry. The results of the measurement (which is focused on measuring temperatures) serve not only to verify the exactness of the model, but also to maintain continuity of the procedure: real process (risering, melting, pouring, solidification, etc.) → input data → numerical analysis → optimization → correction of real process (risering, melting, pouring, solidification, etc.).

Temperature measurement (using thermocouples) and its successive confrontation with the calculation proved that it is possible to apply the numerical model on basic calculations of solidification and cooling of the casting. It is also possible to determine the temperature gradients, the rate of solidification and the local solidification times (i.e. the time for which the given point of the casting finds itself between the liquidus and solidus temperatures). The local solidification time θ significantly influences the forming of the pouring structure of the given material.

The temperature was measured using K- and B-type thermocouples and special thermocouple probes of type PtRh6 – PtRh30. The recording was carried out by the GRANT 1250 data-acquisition device. The measuring ends of the thermocouples were placed in holes of 2 mm in diameter. The initial temperature of the mould and chills was approximately 20 °C, the mould was filled through the top inlet gate with a melt of 1 300 °C. The courses of the temperatures were measured on block with chills on one side for 19 hours 11 min and 19 after pouring. The positions of the probes and a view of the actual installation in mould are illustrated in **Fig. 2-5**.

2.4 The calculation and experimental results

The points in the block (**Fig. 2-1**) and the chill were selected for comparison (**Fig. 2-5**). The computation and experimental curves are in **Figs. 2-6 and 2-7**. It is obvious that in the compared points of the mould and chills the results from the numerical model correspond to those measured, which applies to most other places where both the mould and chills were measured. In the centres of the block it was not possible to carry out the comparison due to a failure in the thermocouple probes.

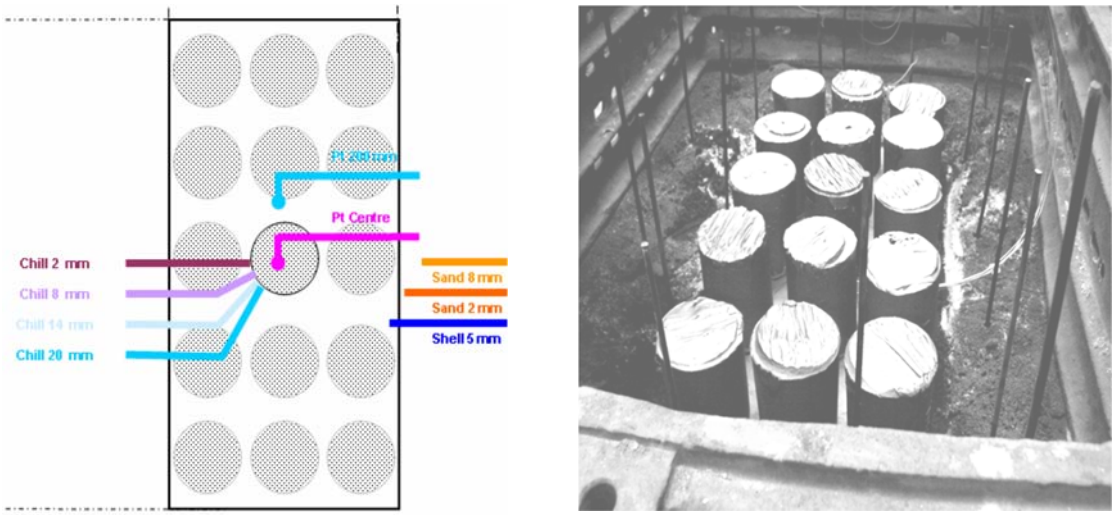

Fig. 2-5 The measured positions and the installation of thermocouples while moulding the block with chills on one side

The iso-zones, calculated in the block and in the chills in various parts after pouring, are illustrated in **Fig. 2-8** (chills on one side) **and 2-9** (chills on three sides). The comparison of the iso-zones, including the mushy zone in castings shows that this time is, relatively, not very much influenced by the increase in the number of chills or by the increase in the number of walls on which the chills are mounted. The total solidification time of the block with chills on one side is 5:08:10 hours and with chills in three sides 4:33:35 hours. Even the various arrangements of chills do not significantly influence the difference in the total solidification time.

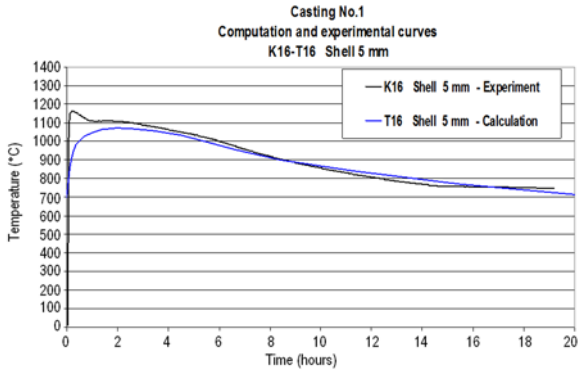

Fig. 2-6 The measured and calculated temperature history in the block 5 mm beneath its surface (chills on one side)

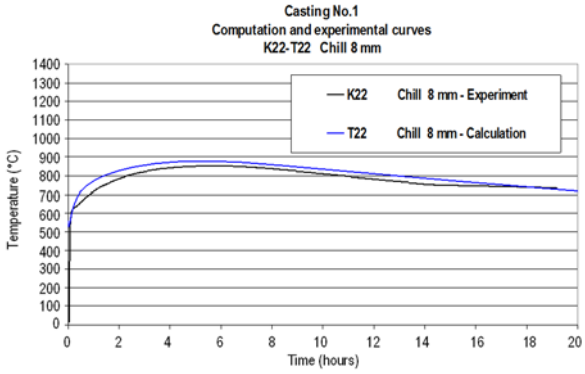

Fig. 2-7 The measured and calculated temperature history in the chill for the block (chills on one side)

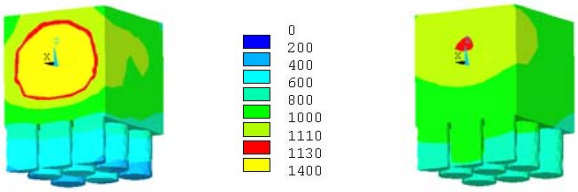

a) in time 1 hour b) in time 5 hours

Fig. 2-8 The calculated iso-zones in the block and in its chills (chills on one side)

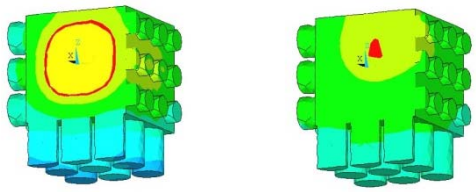

a) in time 1 hour b) 4:30 hours

Fig. 2-9 The calculated iso-zones in the block and in its chills (chills on three sides)

2.5 The relation between the model of the temperature field and the model of structural and chemical heterogeneity

2.5.1 Aims and methodology

The verifying numerical calculation of the local solidification times θ – conducted according to the 3D model proved that, along the height, width and length of these massive castings, there are various points with differences in the solidification times of up to two orders. The aim was to verify the extent to which the revealed differences in the local solidification times affect the following parameters:

a) The average size of the spheroidal graphite particles.
b) The average density of the spheroidal graphite particles.
c) The average dimensions of the graphite cells, and
d) The chemical heterogeneity of the elements in the cross-sections of individual graphite cells.

The relationships – among the given four parameters and the corresponding local solidification times – were determined in the series of samples that had been selected from defined positions of the massive casting.

2.5.2 Experimental material and methods

The ductile cast-iron block (**Fig. 2-1)** was selected to discussion. The bottom part of its sand mould was lined with (a total number of) 15 cylindrical chills of a diameter of 150 mm and a height of 200 mm. The upper part of the mould was not lined with any chills. The average chemical composition of the cast-iron before casting is given in **Tab. 2-1**.

The 500 × 500 × 40 mm plate had been mechanically cut out of the middle of the length by two parallel transversal cuts. Then, further samples were taken from exactly defined points and tested in terms of their structural parameters and chemical heterogeneity. Samples in the form of test-samples

for ductility testing, with threaded ends, were taken from the bottom part of the casting (A), from the middle part (C) and from the upper part (G). The value of 15 mm in diameter and 12 mm high cylindrical samples served to the measurements in order to determine the structural parameters and chemical heterogeneity.

In the points of the defined positions of the samples prepared in this way, the quantitative metallographic analysis was used to establish the structural parameters of cast-iron [L2-3], the in-line point analysis to establish the chemical composition of selected elements [L2-4] and numerical calculation using the 3D model to establish the local solidification time [L1-31].

2.5.3 Quantitative metallographic analysis and chemical heterogeneity of samples

Quantitative analyses of the basic micro-structural parameters in the samples were the subject of a special study [L2-3]. The measurement of the size parameters of the graphite was conducted on the Olympus CUE4 picture analyser under standard conditions, i.e. with a magnification of 100× and on each sample a total number of 49 views were evaluated. On the basis of average values of these results the structural parameters of graphite, i.e. the radius of the spheroids of graphite – R_g, the distances between the edges of graphite particles – L_g and the radius of the graphite cells – R_c have been determined for each sample. These results are given in **Tab. 2-2**.

The concentration of selected elements in each of the samples was measured on the line of Lg between the edges of two particles of spheroidal graphite. The actual measurements of concentrations of ten elements – Mg, Al, Si, P, S, Ti, Cr, Mn, Fe, Ni – was carried out on the JEOL–JSM 840/LINK AN 10/85S analytical complex with an energy dispersed X-ray analyser, an acceleration voltage of the electron beam of 25 kV and exposition time of 50 s.

On each of the samples, the concentrations of all ten elements had been measured in three intervals with each individual step being 3 μm. Before the actual measurement, the regions were selected on an unetched part of the surface and marked with a micro-hardness tester. After the micro-analysis, the samples were etched with nitric acid in alcohol in order to make the contamination of the ground surface visible using an electron beam. Then, using a Neophot light microscope, the interval within which the concentrations were measured was documented. The method of selection of the measurement points is illustrated in **Figs. 2-10** and **2-11**. The results were processed within a special study [L2-4].

Tab. 2-2 Determined structural parameters and the coordinates x, y, z of the measured samples

Sample	R_g	R_c	L_g	x	y	z
	(μm)			(mm)		
A	28	83	110	190	50	507.5
C	36	104	136	190	210	507.5
G	39	109	140	190	450	507.5

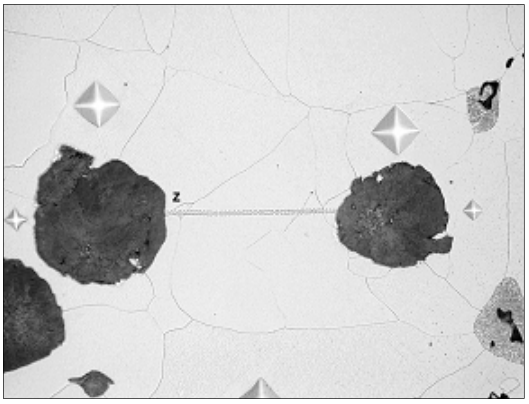

Fig. 2-10 An example of the chemical micro-heterogeneity measurement of ductile cast-iron (z = 165 μm)

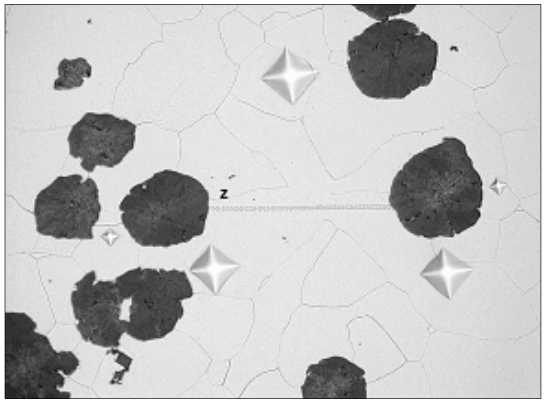

Fig. 2-11 An example of the chemical micro-heterogeneity measurement of ductile cast-iron (z = 167 μm)

The results of the measurements of the chemical heterogeneity were evaluated statistically and entered into **Tab. 2-3** according to the analysed samples. The heterogeneity index of element i.e. I_H is defined by the quotient of standard deviation of element concentration s_x and average element concentration C_{av} in the analysed area, i.e. $I_H = s_x / C_{av}$. The element segregation index I_S is defined by the quotient of element maximum concentration C_{max} and average element concentration C_{av} in the analysed area, i.e. $I_S = C_{max} / C_{av}$.

Tab. 2-3 Results of the chemical heterogeneity measurement

Sample	Para-meter	Element									
		Mg	Al	Si	P	S	Ti	Cr	Mn	Fe	Ni
A	C_{av}	0.0652	0.1002	1.500	0.0151	0.0187	0.0118	0.0615	0.101	97.974	0.156
	I_H	0.984	0.597	0.071	1.805	1.377	1.718	0.571	0.657	0.002	0.538
	C_{max}	0.201	0.235	1.676	0.120	0.103	0.068	0.143	0.242	98.634	0.312
	I_S	3.083	2.345	1.117	7.947	5.508	5.763	2.325	2.393	1.007	2.000
C	C_{av}	0.0387	0.0620	1.562	0.0151	0.0210	0.0065	0.0615	0.0695	97.981	0.184
	I_H	1.550	1.048	0.068	2.306	1.539	2.382	0.751	0.815	0.002	0.453
	C_{max}	0.260	0.200	1.841	0.164	0.107	0.061	0.191	0.193	98.297	0.349
	I_S	6.718	3.226	1.179	10.861	5.065	9.385	3.106	2.777	1.003	1.897
G	C_{av}	0.0872	0.0761	1.396	0.0119	0.0282	0.0068	0.0959	0.107	98.025	0.166
	I_H	1.138	0.815	0.076	1.910	1.264	2.314	0.4867	0.637	0.002	0.513
	C_{max}	0.363	0.216	1.650	0.085	0.124	0.079	0.2222	0.283	98.491	0.417
	I_S	4.163	2.838	1.182	7.143	4.397	11.618	2.315	2.645	1.005	2.512

2.5.4 Local solidification time

The local solidification times of the selected samples of known coordinates within the massive experimental block were calculated by the 3D model explained in the Chapter 2.2, these results are given in **Tab. 2-4**. If the local solidification time is known, then it is also possible to determine the average rate of cooling w_{cool} of the mushy zone as a quotient of the temperature interval and the local solidification time $w_{cool} = \Delta T / \theta$ (K·s^{-1}).

Tab. 2-4 Graphite properties and local solidification time of ductile cast-iron

Sample	Structural parameters (μm)			Local solidification time (s)	Sample coordinates (mm)		
	R_g	R_c	L_g	θ	x	y	z
A	28	83	110	48	190	50	507.5
C	36	104	136	2 509	190	210	507.5
G	39	109	140	4 542	190	450	507.5

2.5.5 Results and their discussion

It is obvious from the results in **Tabs. 2-2 to 2-4** that in the vertical direction from the bottom of the massive casting (sample A: $y = 50$ mm) to the top (gradually samples C: $y = 210$ mm and G: $y = 450$ mm) the characteristic and significant relations are as follows:

a) The average size of the spheroids of graphite, the average size of the cells of graphite and also the average distance between the individual particles of the graphite are all increasing. This relation was confirmed by the quantitative metallographic analysis [L2-3].

b) The chemical heterogeneity within the individual graphite cells is also changing. The increase in the chemical heterogeneity is reflected most significantly in the increase in the indexes of segregation I_S for titanium which are increasing in the direction from the bottom of the massive casting to the top in the following order: 5.763 → 9.385 → 11.618 (**Tab. 2-3**).

The local solidification time increases very significantly – from the bottom of the casting to the top – from 48 s more than 50× (near the centre of the casting) and 95× (at the top of the massive casting).

The relationships between the structural characteristics of graphite in the casting and the local solidification time were expressed quantitatively using a semi-logarithmic dependence, see **Tab. 2-5**. Despite the fact that, for the structural characteristics of graphite R_g, R_c and L_g, there are only three pairs of measured values, i.e. (R_g, θ), (R_c, θ) and (L_g, θ), the given dependences can be considered significant due to the fact that the quantitative metallographic analysis covers 49 measured views (with a magnification of 100×) on each of the three 3D samples. This research can therefore be considered as statistically significant. The relationships between the structural characteristics of graphite and the local solidification time θ had been found using the least-squares method.

The local solidification time θ naturally affects the mechanical properties of cast-iron however with regard to the dimensions of the test pieces; it is not possible to assign the entire body a single local solidification time. To assess relationship among structural parameters, chemical microheterogenity and mechanical properties of analysed cast-iron casting, the selected mechanical properties have been measured, in the **Tab. 2-6** the results for ductility are given. The samples for testing of the tensile strength were taken from the test-sample of the experimental casting in such a way that one had been taken from under the metallographic sample and the second one was taken from above.

The result indicates that the local solidification time θ has significant influence on the ductility. The relationship between the ductility A_5 and the local solidification time (**eq. 2-3**) indicates that the reduction in the ductility of cast-iron in the state immediately after pouring is – in the first approximation – directly proportional to the square of the local solidification time [L2-5].

$$A_5 = 23.339 - 8.1703 \cdot \theta^2 \qquad \text{(eq. 2-3)}$$

Tab. 2-5 The relationships between the structural characteristics of graphite and the local solidification time

Regression equation	Correlation coefficient
$R_g = 19.08 + 2.274 \ln \theta$	0.99
$R_c = 61.33 + 5.567 \ln \theta$	1.00
$L_g = 64.50 + 6.586 \ln \theta$	1.00

Tab. 2-6 Measured ductility of the test-samples

Test-sample		Ductility A_5 (%)	Local solidification time θ (s)
A	1	21.4	48
	2	24.6	
C	1	20.6	2 509
	2	19.4	
G	1	14.0	4 572
	2	6.1	

2.6 Conclusion

It can be seen from previous experiment and the evaluations of the results that – in the general case of the solidification of ductile cast-iron – there could be a dependence of the size of the spheroids of graphite, the size of the graphite cells and therefore even the distance among the graphite particles on the local solidification time, i.e. on the solidification time in which the considered point remains within the mushy zone. The described connection with the 3D model of a transient temperature field, which makes it possible to determine the local solidification time, seems to be the means via which it is possible to estimate the differences in structural characteristics of graphite in cast-iron and also the effect of the local solidification time on ductility in the casting.

The main economic goal observed is the saving of liquid material, moulding and insulation materials, the saving of energy and the already mentioned optimization of pouring and the properties of the cast product.

The solution has been printed in the peer-reviewed journals and presented at prestigious conferences [L2-6 to 2-16].

2.7 Literature

[L2-1] Chvorinov N.: *Crystallisation and heterogeneity of Steels*. NČSAV, Prague 1954, 381 pages.

[L2-2] Smrha L.: *Solidification and Crystallisation of Steel Ingots.* SNTL, Prague 1983, 305 pages.

[L2-3] Belko J. and Stránský K.: Analysing Graphite in Cast-iron. *Research Report (611-57, 811–28) VTUO Brno*, Brno, November 2002.

[L2-4] Winkler Z. and Stránský K. Heterogeneiy of the Compositions of Elements in Ductile Cast-iron Castings. *Research Report (811-11-02) VTÚO Brno*, Brno, December 2002.

[L2-5] Murdoch J. and Barnes J. A.: *Statistical Tables for Science, Engineering, Management and Business Studies.* Macmillan, Cranfield 1970, 40 pages.

[L2-6] Kavička F., Dobrovská J., Heger J., Stránský K., Sekanina B. and Štětina J.: Numerical optimization of the method of cooling of a massive casting of ductile cast-iron. In *Book of Abstracts and CD ROM of the 13th International Heat Transfer Conference,* Sydney, Australia, August 13-18, 2006, p.27.

[L2-7] Stránský K., Dobrovská J., Kavička F., Štětina J., Sekanina B. and Franěk Z.: The character of the solidification structure of massive ductile cast-iron Casting and its prediction. *Materials Science Forum*, 567-568 (2007), 109–112, ©2008 Trans Tech Publications, Switzerland.

[L2-8] Kavička F., Sekanina B., Štětina J., Stránský K., Gontarev V. and Dobrovská J.: Numerical optimization of the method of cooling of a massive casting of ductile cast-iron. *Materiali in tehnologie/Materials and technology*, 43 (2009) 2, 73–78.

[L2-9] Kavička F., Sekanina B., Štětina J. Stránský K. and Dobrovská J.: Numerical optimization of the method of cooling of a massive casting of ductile cast-iron. In *the Proceedings 22nd Canadian Congress of Applied Mechanics*, Dalhousie University Halifax, Nova Scotia, Canada, May 2009, p. 21.

[L2-10] Stránský K., Dobrovská J., Kavička F., Gontarev V., Sekanina B. and Štětina J.: Two numerical models of the solidification structure of massive ductile cast-iron casting. *Materiali in tehnologie/Materials and technology,* 44 (2010) 2, 93–98.

[L2-11] Dobrovská J., Kavička F., Stránský K., Sekanina B. and Štětina J.: Numerical optimization of the method of cooling of a massive casting of ductile cast-iron. In the Book of Abstracts and CD ROM of the *10th International Conference on numerical methods in industrial forming processes NUMIFORM 2010*, Pohang, Republic of Korea, June 2010, p. 113.

[L2-12] Kavička F., Dobrovská J., Stránský K., Sekanina B. and Štětina J.: The Investigation of cooling of a massive casting of ductile cast-iron. In the CD ROM of *18th Annual international conference on composites/nano engineering ICCE-18*, Anchorage, Alaska USA, July 2010, p. 333.

[L2-13] Kavička F., Dobrovská J., Stránský K., Sekanina B. and Štětina J.: The Character of the Solidification Structure of Massive Ductile Cast-Iron Castings and its Prediction *23rd International Symposium on Transport Phenomena (ISTP 23)*, Auckland, New Zealand, 2012, Abstract in the Symposium handbook p. 53, full Peer-Reviewed Paper No.21 on flash disk.

[L2-14] Kavička F., Stránský K., Sekanina B., Štětina J. and Dobrovská J.: Two Numerical Models of a Solydifying Massive Casting of Ductile Cast-Iron. In *Proceedings of the European Congress on Advanced Materials and Process EUROMAT 2007.* Frankfurt, FEMS. 2007. p. 88.

[L2-15] Stránský K., Kavička F., Dobrovská J., Štětina J. and Sekanina B.: Character and Estimation of the Solidification Structure of the Massive Ductile Cast-Iron Casting. In *Abstract Booklet MSMF 5.* Brno, Brno University of Technology. 2007. p. 52.

[L2-16] Kavička F., Štětina J., Stránský K., Dobrovská J. and Heger J.: A numerical model of solidification of a massive casting from malleable cast-iron. In *2004 ASME/JSME Pressure Vessels and Pping Conference*, New York, ASME. 2004. p. 249–255.

3 Chemical and structural heterogeneity of a gravitationally cast ductile- cast-iron roller and its relationship to thermokinetic solidification

3.1 Introduction

Steel and ductile cast-iron rollers, between which train rails (with a hardness of 300 HB) are rolled, are cast into cylindrical iron moulds. Each producer uses their own production technology that must meet the increasingly more demanding requirements concerning length of operational life on the railway – i.e. greater hardness. This means that it is necessary to cast rollers with significantly improved utility properties, mainly high wear-resistance and optimal mechanical and structural properties. It is therefore necessary to find and ensure optimal relationships between the matrix structure and the resultant values of the mechanical properties of the rollers in order to maximize the length of life. The requirements introduced here cannot be met without perfect knowledge of the course of solidification, cooling and heat treatment of the cast rollers as well as the kinetics of the temperature field of the casting and mould [L1-40].

The solidification and cooling of these rollers – partly inside a sand mould and partly inside an iron mould – is a very complicated problem of heat and mass transfer with a phase and structural change. The investigation into the temperature field, which can be described by the 3D Fourier equation, is not possible without the engagement of a numerical model of the temperature field of the entire system – comprising the casting, the mould and ambient. An original application of ANSYS simulated the forming of the temperature field of the entire system. The introduced 3D model of the temperature field is based on the numerical finite-element method. Experimental research and temperature measurement must be conducted simultaneously with numerical calculation in order to make the model more accurate and to verify it [L3-1].

The kinetics of the solidification has a non-negligible influence on the chemical and structural heterogeneity of the cast-iron in question [L3-2]. An original methodology for the measurement of microheterogeneity had been developed – based on the results of the model of the temperature field of the cast rollers. The chemical and structural heterogeneity of the cast roller has proven to be a significant function of the method of melting, modification and inoculation and the successive procedures of risering, casting and crystallization after cooling.

3.2 The assignment and proposal of the calculation of the 3D temperature field

The assignment focused on investigating the transient 3D temperature field of a system comprising a casting, the mould and ambient, using a numerical model. The dimensions of the cylindrical casting and of the iron mould are given in **Fig. 3-1**, the diameter of the actual roller is 1 180 mm and height 2 100 mm. This figure illustrates the entire set-up comprising two parts of the sand mould for the upper and lower spindle ends and the iron mould. The chemical composition is given in **Tab. 3-1**. The initial temperature of the mould was 20 °C.

Tab. 3-1 The chemical composition of ductile cast-iron

Ductile cast-iron										
Element	C	Mn	Si	P	S	Cr	Ni	Mo	Mg	Cu
(wt.%)	3.31	0.65	0.70	0.105	0.005	0.35	2.59	0.59	0.04	1.48

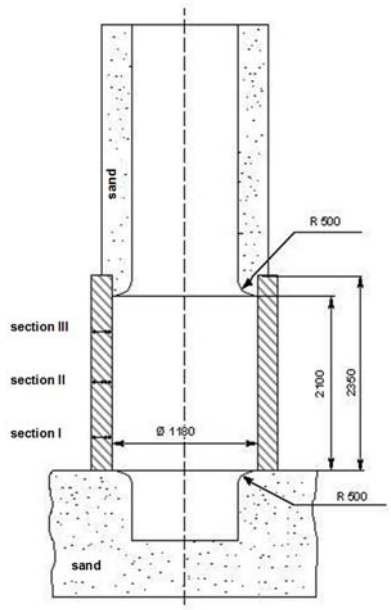

Fig. 3-1 The set-up of a vertically cast roller

Fig. 3-2 The iron mould before a firing off a separator

The working surface of the iron mould is covered with a separating layer – hereafter "separator" (which is a special lubricant applied in various thicknesses to the inside walls of the iron mould and fired at 180 °C prior to casting, see **Fig. 3-2**).

The pouring temperature of the melt was 1 336 °C. The casting was performed from underneath with tangential in-flow. The total time of pouring of the ductile cast-iron was 175 seconds (**Fig. 3-3**).

The mathematical model for the simulation of the temperature field of the roller-mould-ambient system was created by ANSYS, which is described via Fourier equation (**eq. 2-1**), respectively (**eq. 2-2**). Since this is a case of rotational symmetry, it was sufficient to investigate the temperature field of one half of the axial section. The coefficients of heat transfer by radiation and convection in all planes bordering the system into the ambient were defined. Ideal physical contact was presumed between the sand mould and the casting.

Fig. 3-3 The pouring of the roller

The simulation of the release of the latent heats of phase or structural changes is carried out by introducing the thermodynamic enthalpy function [L3-2 and 3-3]. The model enables the evaluation of the temperature field within the actual casting and mould at any point in time within the process of solidification and cooling using contour lines (i.e. so-called iso-lines and iso-zones) or temperature-time curves for any nodal point of the system. It is possible to use all sophisticated sub-programs of ANSYS, such as automatic mesh generation, pre-processing and post-processing.

The program also considers the non-linearity of the task, i.e.:

- The dependence of the thermophysical properties of all materials entering the system on the temperature, and
- The dependence of the heat-transfer coefficients (on all boundaries of the system) on the temperature of the surface – of the casting and mould.

The stability and accuracy of the numerical solution, when applying the explicit method, is sensitive to the size of element of the mesh and the time step. **Figures 3-4** shows the network for the original casting, riser and mould. The initial time step was 10^{-3} s, the minimum step in the following course of the calculation was selected as 10^{-6} s and the maximum step was 120 s.

A series of experimental temperature measurements was conducted for the verification of the model and the closer determining of the boundary conditions of the numerical solution of the temperature field.

Results from experimental measurements were used for verification of the model and correction of the boundary conditions of the numerical solution of the temperature field.

The calculation of the temperature field dealt mainly with the effect of the separator between the casting and the iron mould on the solidification of the roller.

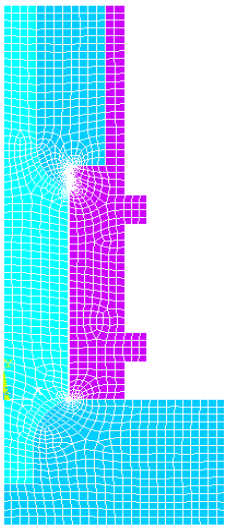

Fig. 3-4 The mesh for the numerical model of the temperature field

3.3 Temperature measurements of the temperatures inside the iron mould and on the surface of the roller

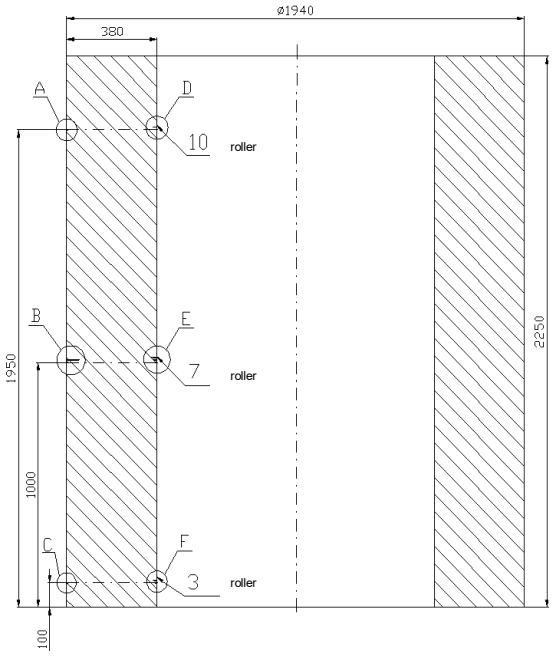

Fig. 3-5 Layout of measurement points

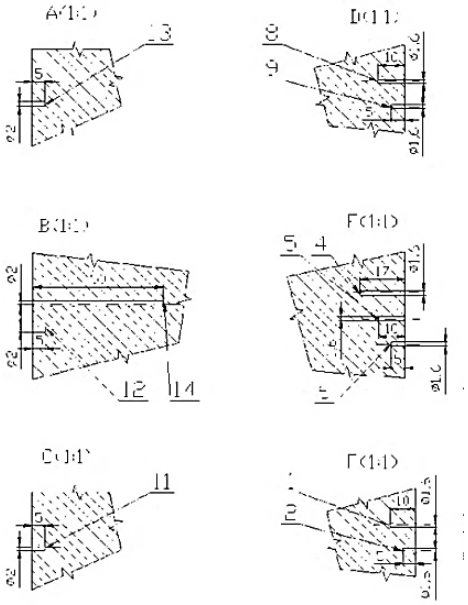

Fig. 3-6 Positions of the thermocouples

The distribution of temperatures along the height of the iron mould and roller was measured in three horizontal planes, 100 mm (section I), 1 000 mm (section II) and 1 950 mm (section III) from the bottom edge of the iron mould (**Fig. 3-1**). **Figures 3-5 and 3-6** show a more detailed diagram of the positioning of the hot junction of the thermocouple. The temperatures of the iron mould were taken beneath the inner surface (at depths of 5 and 10 mm) and outer surface (at a depth of 5 mm). The sensors for measuring the temperature of the roller took the temperatures at a depth of 5 mm beneath the surface in the same horizontal planes as the temperatures of the iron mould.

The temperature was measured in a total number of 14 points where 3 were on the surface of the roller, 7 on the inner surface of the iron mould and 4 points on the outer surface of the iron mould. The thermocouples were interconnected using the compensation leads of the 12-bit GRANT 1250 and 1203 measurement stations with 87 and 46 KB of memory respectively.

3.4 Calculated versus measured temperatures

Section III (**Figs. 3-2**, **3-5 and 3-6** – detail A and D), where thermocouples recorded the temperatures the longest – specifically point 9 (the inner surface of the iron mould) and point 13 (the outer surface of the iron mould) – had been selected for the comparison of the temperatures from the numerical simulation with the experimentally obtained temperatures from inside the iron mould. The results of this comparison are illustrated in **Figs. 3-7 and 3-8**. The interruption of the measurement of the temperatures after 85 hours was caused by the changing of the measurement equipment and, furthermore, the thermocouple in point 13 did not resume work.

The maximum values of the linear density of the heat flow were found to be in section II – based on the temperatures t5 and t6. On average, they are 100 $kW \cdot m^{-1}$ higher than those of section III and section I. The intensity of the heat transfer influenced the formation of the pouring structure monitored on the samples taken from sections I and III (see subchapter **3.6**). The boundary conditions obtained experimentally were successively used to verify the mathematical model.

Figures 3-7 and 3-8 confirm a very close similarity of the calculated and measured temperatures of the iron mould. It appears that the absolute values and histories of experimental and calculated temperatures in the points of the cylindrical casting and iron mould, which had been selected for comparison, are very similar. The determined relationship between the solidification time (of the entire casting or its geometrical centre) and the thickness of the separator applies. The simulation of the temperature field of the roller and the mould can therefore be considered successful.

The results of the mathematical model indicate that the distribution of temperatures and the course of solidification in the vertical direction is quite uneven, which affects the internal quality of the casting. While the body of the roller is solidified along the entire height, the temperatures are still high in the lower spindle and could be the cause of shrinkage porosity in the point where the spindle enters the roller. That is why the lower spindle should solidify in a mould with a higher heat accumulation, i.e. in a mould made of CT-CrMg or in an iron mould. Sooner topping-up of the upper spindle should ensure replenishing of the mould with melt into the body of the roller in order to achieve increased quality.

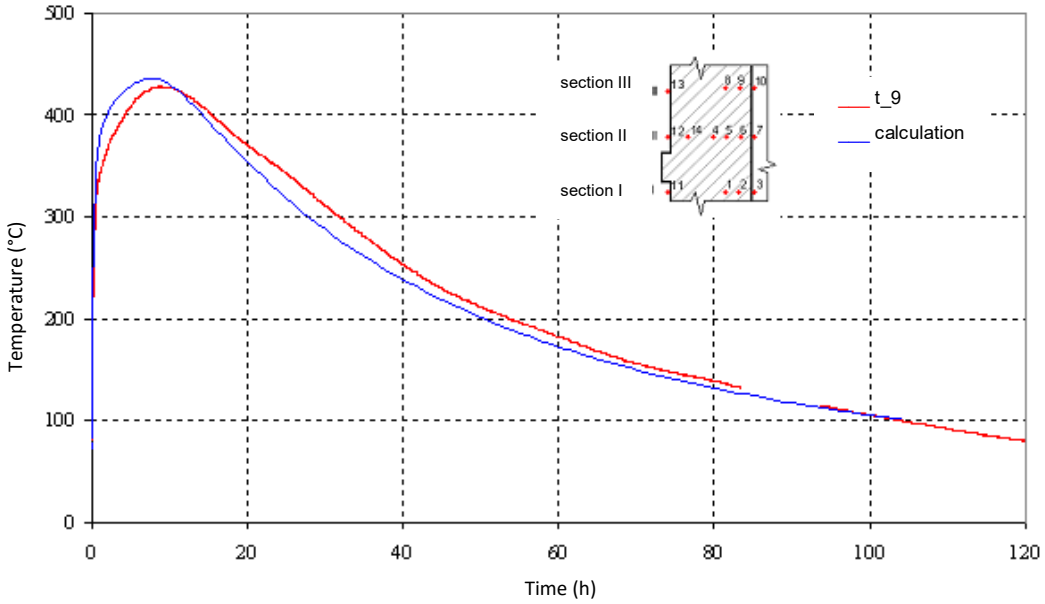

Fig. 3-7 Calculated versus measured temperatures (**Fig. 3-6** - point 9)

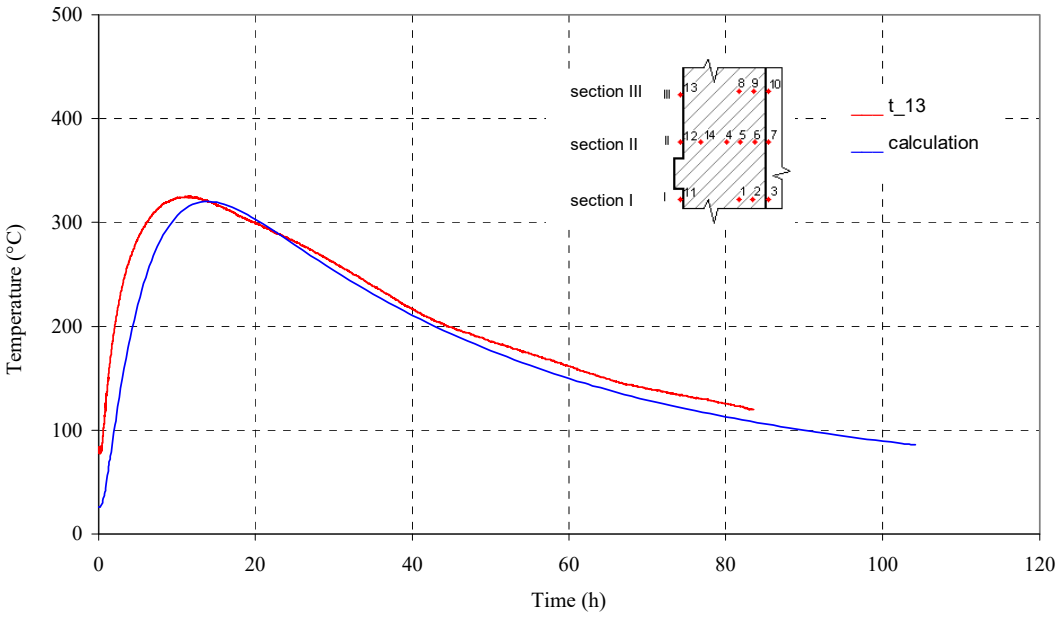

Fig. 3-8 Calculated versus measured temperatures (**Fig. 3-6** - point 13)

3.5 The results of the simulation of the temperature field in dependence on the separator thickness

The thickness of the separator – for individual simulations of solidification and cooling of the roller – was gradually 0, 5, 10 and 15 mm.

The point where the melt solidifies last is the centre – 2 100 mm from the base of the iron mould. The centre of the body of the roller is on the axis at a distance of 1 050 mm from the same base. **Table 3-2** contains the solidification times of the entire roller (including its centre), which are calculated from the simulation.

Tab. 3-2 Solidification times for various separator thicknesses

Separator thickness	Solidification time θ			
	Centre of roller		Entire roller	
(mm)	hours	seconds	hours	seconds
15	8.187	29 473	8.783	31 618
10	7.845	28 242	8.124	29 246
5	7.030	25 310	7.531	27 111
0	6.510	23 437	6.554	23 593

Figures 3-9 to 3-12 illustrate the temperature field along the longitudinal axis of the system for all four thicknesses after 7.845 h, i.e. at the time when the centre of the roller solidifies with a separator of a mean thickness of 10 mm (**Tab. 3-2**).

The area where the maximum temperature occurs is in the riser after 7.845 hours (see the red area) for the no-separator and 5 mm-separator variants (see **Figs. 3-9 and 3-10**). The variants with the 10 mm and 15 mm separators seem to demonstrate directed solidification around the geometric and heat axis (**Figs. 3-11 and 3-12**). It is possible to observe an enlargement of the above-mentioned red area along the vertical axis with an increasing thickness of separator.

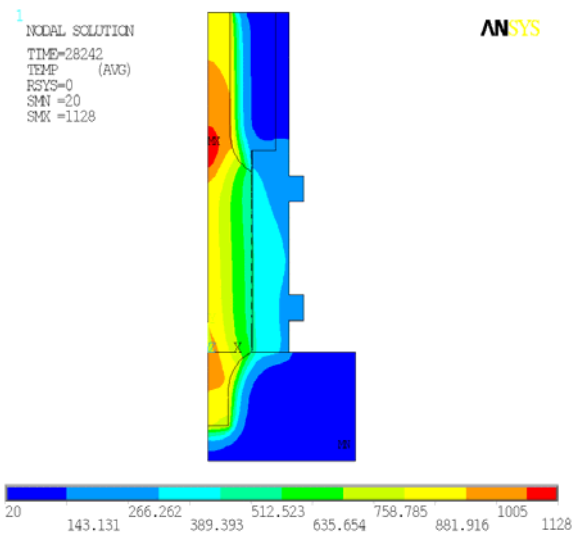

Fig. 3-9 The temperature field along the longitudinal section (without the separator)

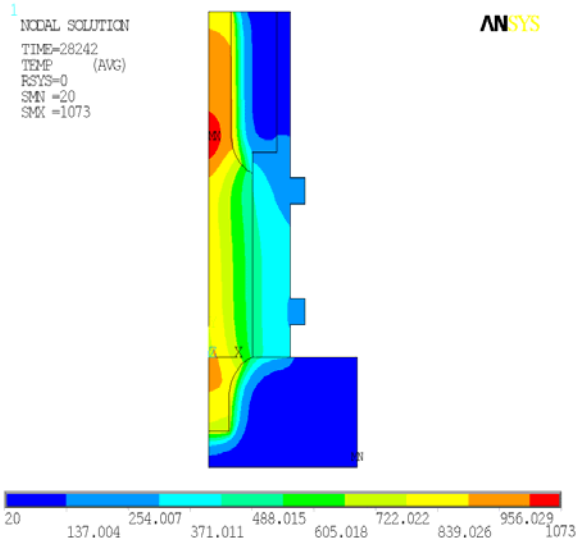

Fig. 3-10 The temperature field along the longitudinal section (with a 5 mm separator)

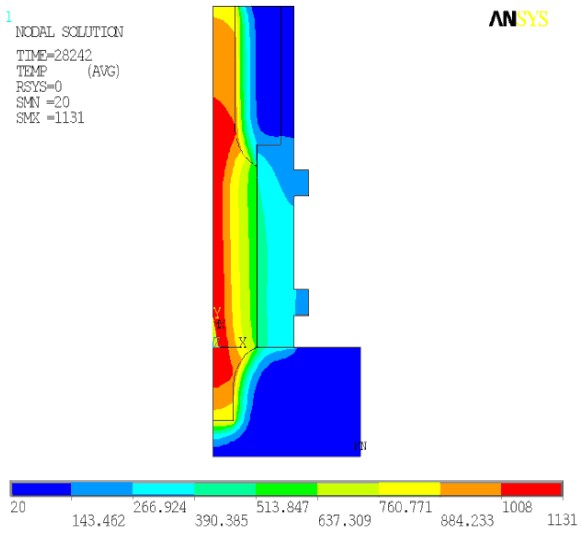

Fig. 3-11 The temperature field along the longitudinal section (with a 10 mm separator)

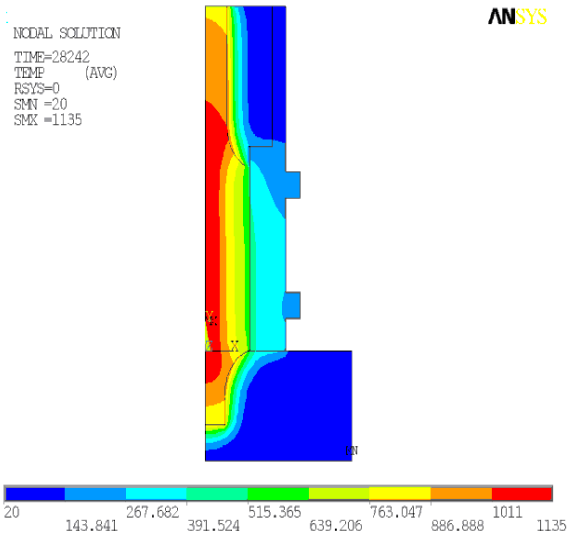

Fig. 3-12 The temperature field along the longitudinal section (with a 15 mm separator)

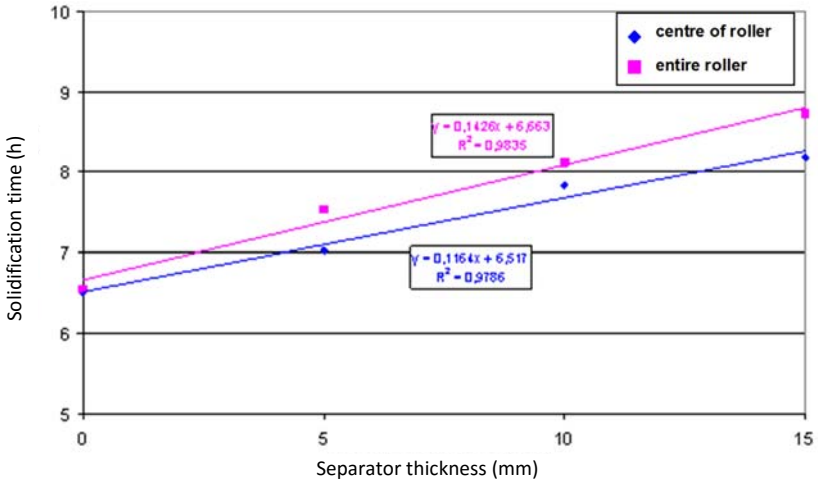

Fig. 3-13 The influence of the separator thickness on the total solidification time

Figure 3-13 shows the dependence of the total solidification time of the centre of the roller and entire roller on the separator thickness. The relationship between the separator thickness and the solidification time can be described in relatively great detail by the linear function – as the reliability coefficient values in **Fig. 3-13** indicate for both straight lines.

The separator has proven to be a good insulator. The solidification time of the roller inside the mould with a 15 mm separator increases by up to 26% compared to that without the separator.

3.6 Structural and chemical heterogeneity of the roller

The final mechanical properties of the rollers – of ductile cast-iron – are determined, not only by the chemical composition but mainly by their structural and chemical heterogeneity, which occurs during casting, crystallization and successive cooling of the material. Some defects occurring in this way can be corrected by heat treatment however the quality of the pouring structure is very important especially with graphite cast-iron.

The samples used for determining the structural and chemical heterogeneity were taken from the ductile cast-iron roller (**Fig. 3-1**) with the chemical composition given in **Tab. 3-1** from the upper part (section III) and from the bottom part (section I). **Figure 3-14** shows how the four samples were taken, with the upper surfaces – marked "X" – being analyzed. Further, they were specified as follows:

- The upper part of the roller on the outer surface (R1 = 540 mm) marked TR1.
- The upper part of the roller on the inner surface (R4 = 400 mm) marked TR4.
- The lower part of the roller on the outer surface marked BR1.
- The lower part of the roller on the inner surface marked BR4.

The actual analyses were conducted at a specialized workplace [L3-3 and 3-4].

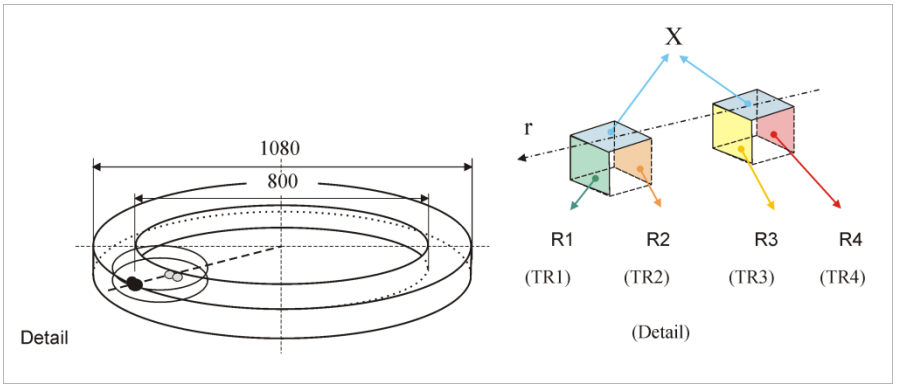

Fig. 3-14 Sampling

The structural analysis of the cast-iron samples was conducted using the Neophot 32 metallographic microscope and an Olympus digital camera C-3030. The measurements of the metallographic parameters of the graphite and the evaluation of the volume part of the structural components were conducted on the Olympus CUE4 image analyzer. The basic statistical parameters of the graphite particles and also the stereological estimate of certain other parameters [L3-5] were calculated from the data files.

The JSM-840 (JEOL) electron scanning microscope was used for determining the chemical heterogeneity together with the LINK AN 10/85S X-ray energy-dispersive microanalyzer. Based on the results of the metallographic analysis [L1-40], two pairs of graphite grains were selected on the ground surface of every sample in order for the line of measurement between the first pair to pass through the perlite (marked "a") and between the second pair vice versa the cementite (marked "b"). The third line was selected through two boundaries created by particles of lamellar graphite, where measurement passes through basic perlite (marked "c"). The individual elements (Si, P, Mo, Cr, Mn, Fe, Ni, and Cu) were analyzed by means of point X-ray microanalysis in a direct line with a step of 3 μm [L3-3].

Figure 3-15 illustrates the material around the selected line of measurement on sample TR1 through the electron scanning microscope and the X-ray energy-dispersive microanalyzer. Following the chemical (element) analysis, the samples were etched using 2% nital in order to make the contamination traces visible and display the line of measured points, incl. their connection to the sample microstructure. The connection of the measured area of the ductile cast-iron to its microstructure can be seen in **Fig. 3-16**, obtained using the light microscope.

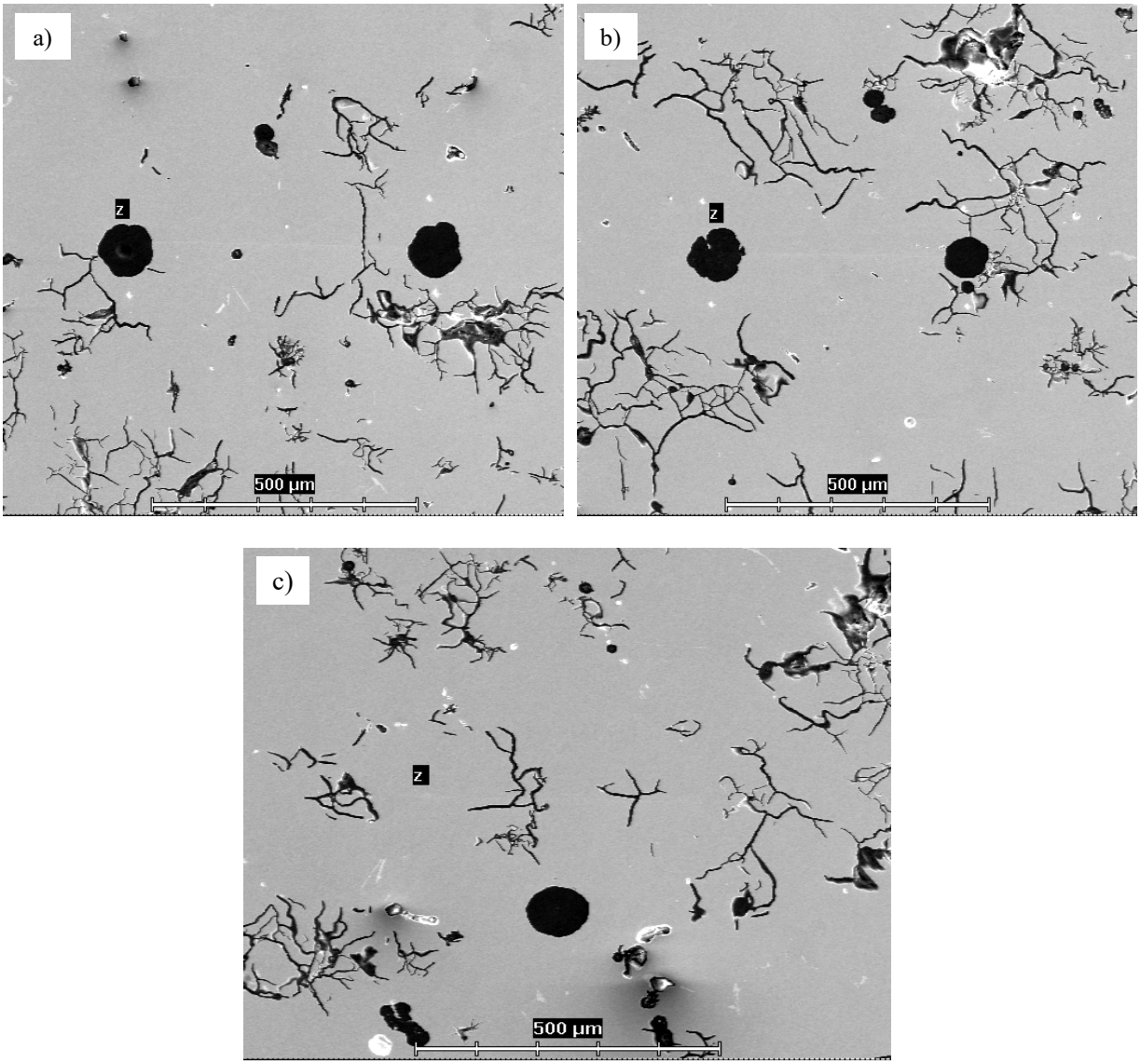

Fig. 3-15 The structures in the area of sample TR1 selected for analysis:

a) between the spherical graphite through perlite
b) between the spherical graphite through cementite
c) through lamellar graphite

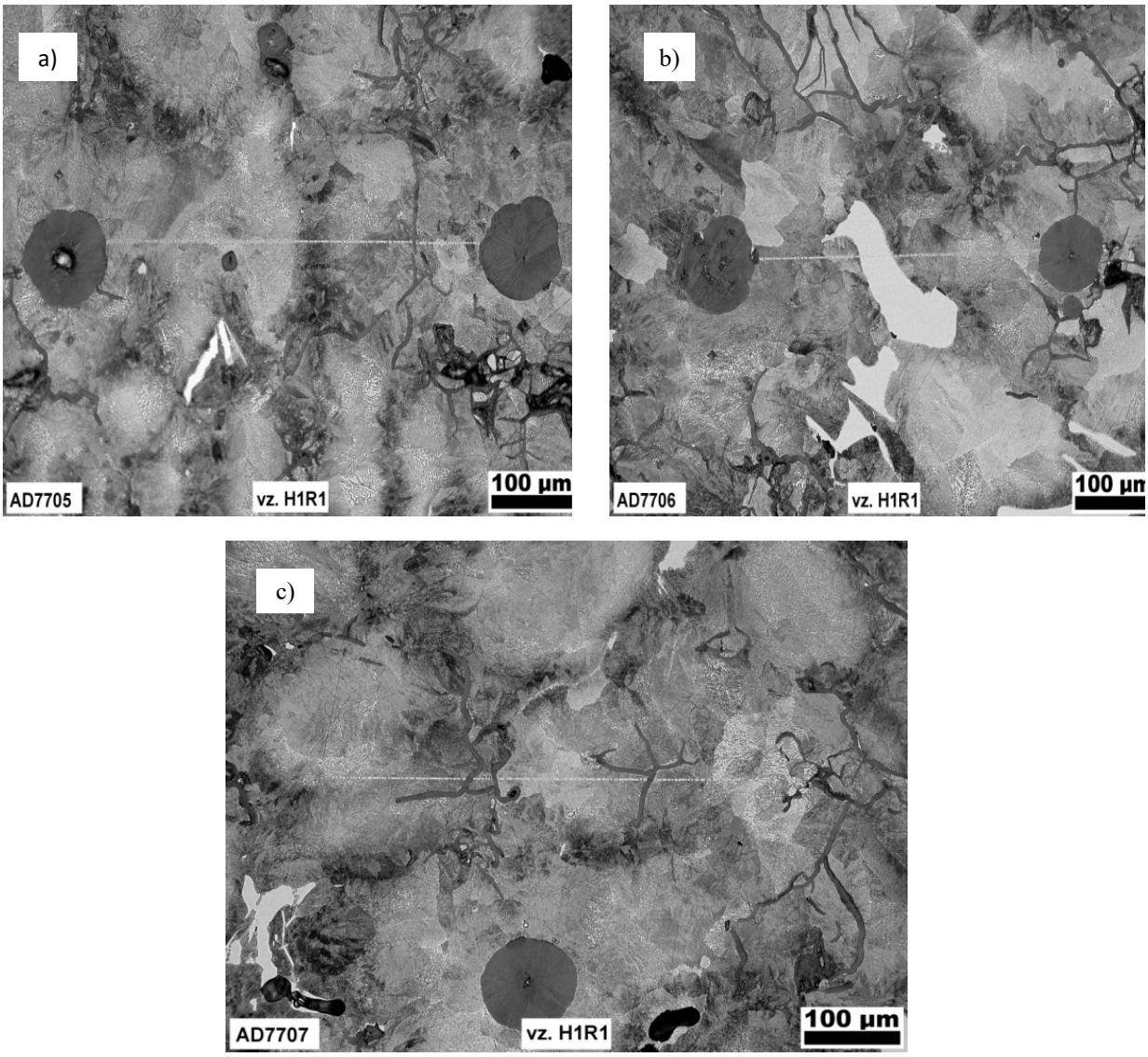

Fig. 3-16 The structures of the measured areas of the TR1 sample with a contamination trace:

a) between the spherical graphite through perlite
b) between the spherical graphite through cementite
c) through lamellar graphite

3.6.1 Structural heterogeneity

Based on experience, it can be assumed that the structure of the material of the casting will, besides globular graphite that is characteristic for ductile cast-iron, also contain a mixture of a certain amount of transition forms of graphite and lamellar graphite found between the globular and lamellar graphite.

The distributions of graphite in the microstructure of samples (**Fig. 3-14**) are shown in the photographs in **Figs. 3-17 to 3-20** taken through the light microscope. **Table 3-3** shows the results from the quantitative metallographic analyses of the structures of the samples in **Fig. 3-14**. The procedure of the quantitative structural measurements, including the results, is described in detail in Ref. [L3-3].

Tab. 3-3 The results from the quantitative measurements of the volume part of the components (in vol. %)

Sample	All graphite, incl. micro-shrinkages	Globular graphite	Transition forms of graphite and lamellar graphite	Cementite	Perlite
BR1	10.5 ± 2.8	1.3	9.2	2.2 ± 1.7	87.3
BR3	13.0 ± 5.4	1.1	11.9	1.2 ± 1.2	85.8
TR1	13.4 ± 5.6	1.1	12.3	2.2 ± 1.8	84.4
TR3	12.6 ± 5.7	1.1	11.5	1.3 ±1.4	86.1

Table 3-3 indicates that the least amount of graphite in the structure can be found in the bottom part of the roller and along the outer edge of the ring – in sample BR1. A greater amount of graphite is segregated near the inner edge of the ring – in sample BR4 – the wall R3 (**Fig. 3-14**). Along the height of the roller, the amount of graphite increases – in samples TR1 and TR4 – measured also on the wall R3 (**Fig. 3-20**) it is greatest, however, simultaneously, the standard deviation of the measurement and the amount of micro-shrinkages also increases. Globular graphite, which makes up the typical structure of the ductile cast-iron, represents the minority phase of this material and its amount is merely 1.3 of the volume percentage, it is highest in the bottom part of the roller along the outer edge of the ring, where the casting cools the quickest, i.e. in sample BR1. The lowest amount of transfer forms of graphite, including lamellar graphite are segregated in this area. Cementite, which is the component of greatest hardness is segregated approximately twice as much as at the outer walls of the ring, which cool faster than the inner walls. The perlite structure of the roller dominates and its volume content is 85.9±1.19%. The relatively greater amount of perlite is in the lower part of the roller however the volume percentage difference of 1.3 is insignificant.

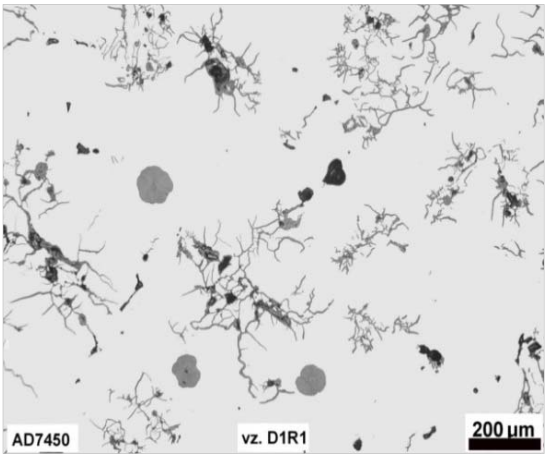

Fig. 3-17 The microstructure of sample BR1

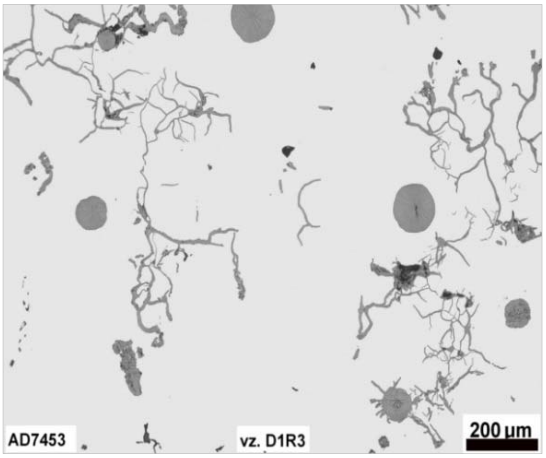

Fig. 3-18 The microstructure of sample BR4

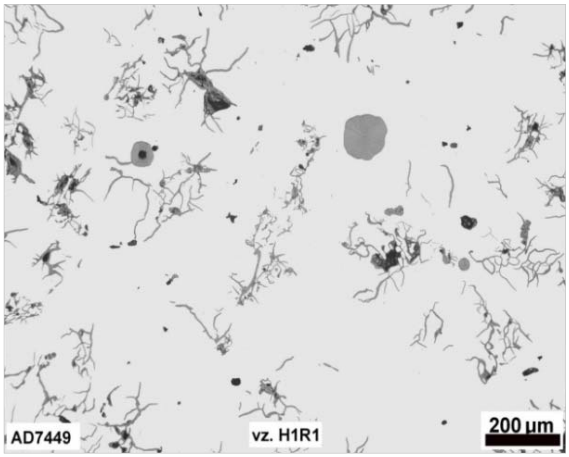

Fig. 3-19 The microstructure of sample TR1

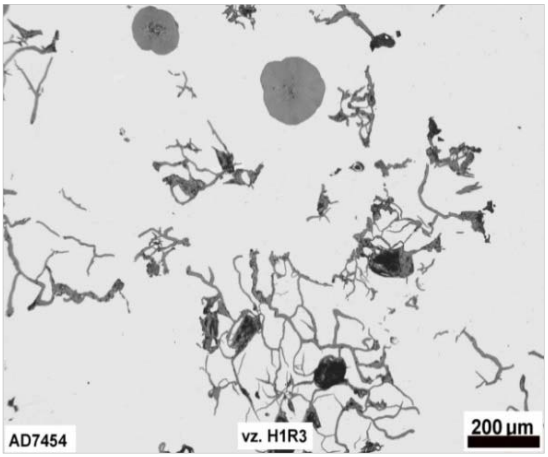

Fig. 3-20 The microstructure of sample TR4

3.6.2 Chemical heterogeneity

The distribution of the concentration of the eight elements, measured three times in one line for each of the samples (**Fig. 3-16: *a*, *b*, *c***) was evaluated using mathematical statistics: the arithmetic mean of the concentration of the element in the selected interval C_{av}, the standard deviation s_x of the measured concentration, the minimum concentration $C_{\min}$ and the maximum $C_{\max}$ – measured each time in the selected interval of the sample (in wt.%). Besides these basic concentration parameters, the segregation index of each measured element was determined and defined as $I_S = C_{\max} / C_{av}$, i.e. as the quotient of the maximum concentration of elements measured on the given interval and the arithmetic mean of its concentration in the same interval. The tendency of the element to segregate – based on experience – is expressed in the values of the segregation indexes. A detailed description of the measurement procedure and the corresponding results can be found in reports [L1-40, L3-3 and 3-4].

Figure 3-21 illustrates the values of this parameter for individual elements and samples measured in one line across the lamellar graphite (**Fig. 3-16c**). Similarly, the segregation index values can be plotted for the area between the globular graphite in a line across perlite (**Fig. 3-16a)**, and also in the area between the globular graphite in a line across cementite (**Fig. 3-16b)**. **Figure 3-22** shows the segregation index values for the elements calculated as the average of the values for all three areas – a, b, c. Furthermore, the graphs in **Figs. 3-21 and 3-22** also indicate that the segregation indexes of the highest values – from the set of measured elements – belong to phosphorus and molybdenum, and the lowest values refer to nickel and iron which make up the matrix.

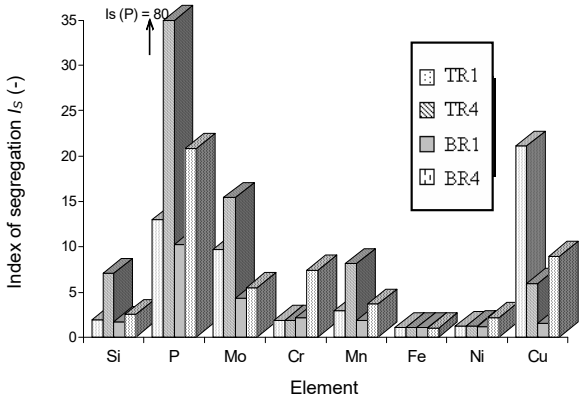

Fig. 3-21 The index of the segregation of elements for individual samples in the area of the transition graphite in the measured area across lamellar graphite

In the segregation of elements during crystallization, solidification and cooling of the roller the sequence of the segregation indexes of element for all three types of measured lines through the different structures (**Fig. 3-16a-c**) remains unchanged – in the order P, Mo, Cr, Mn, Cu, Si, Ni, Fe, i.e. from the element with the highest segregation index to the element with the lowest one. This same sequence applies to the top and bottom parts of the roller. Phosphorus and molybdenum therefore always have the greatest tendency towards segregation and nickel always has the least (if the iron which makes up the matrix is ignored). The elements in the middle of the sequence (Cr, Mn, Cu, Si) can mutually alter the order in which they come depending on certain measured lines – there were as many as 12 lines).

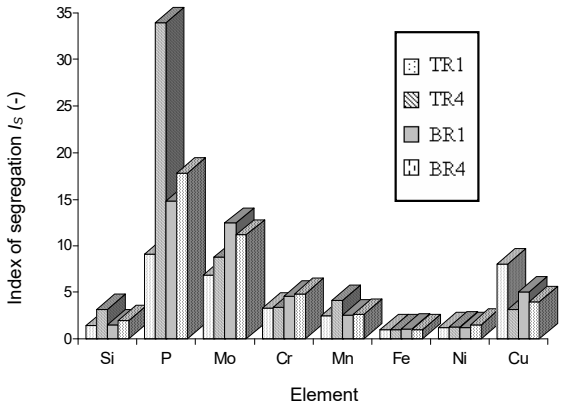

Fig. 3-22 The average index of segregation of the analyzed elements in individual samples

According to the theory of segregation of elements in a melt of pure iron the partition coefficient of the element between the solid and liquid phase determines the intensity of segregation. **Table 3-4** introduces the equilibrium partition coefficients of elements in the order from the smallest to the biggest value [L3-5 and 3-6].

Tab. 3-4 The partition coefficients of elements

Element	P	Si	Mn	Ni	Mo	Cu	Cr	Fe
Partition coefficient	0.13	0.64	0.68	0.69	0.72	0.80	0.90	1

It is remarkable that in the real melt of a roller, it is only the elements on the edges of the sequences relevant for the solidification of pure metals – the solidification of pure iron – that respect the sequence (i.e. phosphorus which segregates the most and iron which makes up the main component of the solution, whose partition coefficient is equal to one). The remaining elements have a completely different position in the sequence according to the previous table. This shows that the crystallization, solidification and cooling of the roller which has a 3.31 wt.% C content, whose chemical composition is given in **Tab. 3-1**, will, as a result of the crystallization of graphite, significantly deviate from the method of crystallization, solidification and cooling of the melt of steel with low carbon content.

The measurement of chemical and structural heterogeneity in the given case is connected to the following production conditions: the cast-iron for the casting of the roller with a mass of 21 800 kg was melted in a flame furnace, then modified using the pouring method (the VL 53 modifier with a quantity of 450 kg at a temperature of 1 380 °C – by pouring from one tundish to another. The graphitizing inoculation took place using 60 kg of the alloy SB 5, where both ends of the roller (**Fig. 3-1**) were moulded into a sand mould. The actual part of the roller was cast into a mould with separator. The time of the melt was 11 hours, the temperature of the melt – after removing the slag – was 1 428 °C and the temperature during tapping was 1 480 °C. The casting took place at a temperature of 1 336 °C, where the pouring time was 120 s and the mould was preheated to 73 °C. The riser, which was protected by IN 6 insulation bricks, was filled 26 minutes after the casting of the entire roller.

3.7 Conclusion

The quality of the working rollers used for shaping metals of different profiles is determined by the chemical and structural composition of the material of the rollers and the production technology. The working rollers are cast from sub-eutectoid and super-eutectoid alloyed steels and special cast-iron. The actual configuration is compact or double-layered. The coat is from high-chrome steel and the core from spherical-graphite cast-iron. The global trend today is for rollers to have a coat of high-speed steel, ensuring long life. The cast-iron rollers with globular graphite are produced slightly hardened with an addition of Cr, and Ni, or hardened and using alloyed Cr, Ni and Mo and also semi-hardened using high-alloy cast-iron. The technology used here is classical, which means stationary (or gravitational) casting, or centrifugal casting guaranteeing a multiple increase in the length of life of the roller.

In the experimental part of Chapter 3, an original methodology for the measurement of the distribution of temperatures and heat flows in the roller-mould system had been developed and verified in the operation. In the design of the original procedure, there were a number of problems connected with the great size of the roller and mould, uneven dilatation of the solidifying roller and mould, the installation and insulation of the thermocouples, the wiring of the thermocouple system – from the measurement points of the thermocouples to the central computer, etc.

The findings regarding the kinetics of the temperature field of the roller and mould, obtained from experimental research, were used for determining the boundary conditions and for the verification of the numerical simulation program. The calculation of the temperature field focused on the analysis of the effect of the mould separator on the course of solidification of the roller. The results of the mathematical modelling indicate that the distribution of temperatures and the solidification in the vertical direction is significantly uneven – this has an effect on the internal quality of the casting. While the body of the roller is solidified along the entire length, the bottom spindle still has areas with high temperatures and this is the cause of contractions and hollows in the area where the spindle enters the roller. It is therefore advisable for the bottom spindle to solidify in a mould made of a mixture of a higher coefficient of heat accumulation, for example from chromium-magnesite, or directly in the

iron mould. Timely topping of the top spindle prevents the formation of shrinkages within the solidifying melt, thus improving the internal quality.

This Chapter 3 introduced an original methodology for the measurement of the chemical heterogeneity of cast-iron of the composition given in **Tab. 3-1**. The structure of this cast-iron is created by a great amount of the transition form of graphite and small amount of globular graphite and also lamellar graphite and cementite, whereas the structure of the metal matrix is perlitic. The volume amounts of the structural components were determined using the quantitative metallographic analysis, which was simultaneously the basis for the selection of the places for the analysis of the element composition using X-ray energy-dispersive spectral microanalysis. Inside the microstructure of four samples, taken from the outer and inner parts of the ring at the top and bottom of the roller (**Fig. 3-14**), in a total of twelve areas, the linear concentration dispersion was measured on the eight elements which make up the basic constitution of the cast-iron: Si, P, Mo, Cr, Mn, Fe, Ni, and Cu. Statistical analysis was used to determine the distribution characteristics of the concentration of the individual elements, including the segregation indexes and the relationships among them. In this way it was possible to assess the influence of the changing kinetics of the temperature field on the resultant structural and chemical heterogeneity of the roller.

The greatest rate of crystallization, solidification and cooling relates to those samples which had been taken from the bottom part of the roller and the outer edge of the ring. The samples from the top part of the roller on the inner side of the ring were cooled by the slowest rate. Simultaneously, during the successive processes of crystallization, solidification and cooling, the constant reducing sequence of the element segregation indexes in the order: P, Mo, Cr, Mn, Cu, Si, Ni, Fe, which corresponds to the greatest heterogeneity in the distribution of P and Mo.

Comparing with the generally known kinetics of the segregation of the same elements in low-carbon steels, it is clear that the conditions connected with the forming of graphite, through which the crystallization, solidification and cooling of the cast-iron of the measured high-carbon-content roller pass, are significantly different from the conditions of solidification of gravitationally cast low-carbon-steel castings. The kinetics of the solidification of the cast-iron roller had a non-negligible influence on the chemical and structural heterogeneity of the investigated type of cast-iron. It is obvious that the chemical and structural heterogeneity of the cast roller is a significant function of the method of melting, modification and inoculation and the successive procedures of risering, casting and crystallization after cooling.

The solution has been printed in the peer-reviewed journals and presented at prestigious conferences [L3-7 to 3-11].

3.8 Literature

[L3-1] Stránský K., Kavička F., Dobrovská J., Sekanina B., Štětina J. and Winkler Z.: Chemical and structural heterogeneity of a gravitationally cast ductile-cast-iron roller. *Slévárenství,* 56 (2008) 11-12, 507–511.

[L3-2] Kavička F., Dobrovská J., Stránský K. and Sekanina B.: The model of temperature field and chemical heterogeneity of solidifying ductile-cast iron roller. *Proceedings of the ASME/JSME 2011 (AJTEC2011*). Honolulu USA, ASME. 2011. p. T44081 (10 p.).

[L3-3] Belko J. and Stránský K.: Structural analysis of cast-iron samples, *Research report*, VTUO Brno, 2005.

[L3-4] Winkler Z. and Stránský K.: Microheterogeneity of the composition of alloyed ductile cast-iron samples Mn, Cu, Ni a Mo, *Research report*, VTUO Brno, 2005.

[L3-5] Kamenský R., Darovnik J. and Stránský K.: The influence of silicon content on the depth of a hardened layer on/in cast-iron castings, *Slévárenství*, 16 (1968) 1, 35–39.

[L3-6] Kuchař L. and Drápala J.: *Metallurgy of pure metals*, Nadacia R. Karnrnela. Košice, 2000.

[L3-7] Kavička F., Stránský K., Sekanina B., Dobrovská J. and Štětina, J.: Numerical and experimental investigation of temperature field of solidifying massive ductile-cast-iron roller. *Materiali in tehnologije / Materials and technology*, 46 (2012) 4, 321–324.

[L3-8] Kavička F., Dobrovská, J., Stránský, K., Sekanina, B. and Štětina, J.: Temperature Field and Solidification Structure of a Ductile-Cast-Iron Roller. *Key Engineering Materials,* 592-593 (2014) 1, 197–200.

[L3-9] Stránský K., Kavička F., Dobrovská J., Sekanina B. and Štětina J.: The model of temperature field and chemical heterogeneity of solidifying ductile-cast-iron roller. *Hutnické listy,* 61 (2008) 6, 37–46.

[L3-10] Kavička F., Stránský K., Sekanina B., Dobrovská J. and Štětina J.: Numerical and experimental investigation of temperature field of solidifying massive ductile-cast-iron roller. In *Program and book of abstracts of 19th conference on materials and technology.* 1. Ljubljana, Institut za kovinske materiale in tehnologie. 2011. p. 49.

[L3-11] Kavička F., Dobrovská J., Stránský K., Sekanina B. and Štětina J.: The temperature field of a gravitationally cast ductile-cast-iron roller and its chemical and structural heterogeneity. In *Fluid structure interaction VII.* C.A. Brebbia, G.R. Rodriguez. UK, WIT Press Southamptom, Boston. 2013. p. 215–226.

4 Numerical optimization of the pouring of a stone-block from ceramic material EUCOR

4.1 Introduction

The corundo-baddeleyit material EUCOR is heat resistant, wear resistant even at extreme temperatures and it is also resistant to corrosion. It belongs to the not too well known system of the Al_2O_3-SiO_2-ZrO_2 oxide ceramics. Throughout the world, it is produced only in several plants—in the Czech Republic under the name of EUCOR [L4-1]. This production process entails solely the utilisation of waste material from re-lined furnaces from glass-manufacturing plants. The melting of this material is done in electric-arc furnaces lined with material of the same chemical composition. The basic approximate chemical composition of CBM (in wt.%) is 13-17% SiO_2, 49-52% Al_2O_3, 30-33% ZrO_2, 0.1% TiO_2, 0.2 CaO, 0.2% FeO and (1-2%) alkaline oxides. Mineralogical composition (i.e. the phase composition) of this ceramic material is given in wt.% as: 48-50% corundum, 30-32% baddeleyit and 18-20% glass phase [L4-1].

From the foundry property viewpoint, EUCOR has certain characteristics that are similar to the behaviour of cast metal materials, especially steel for castings. EUCOR castings can also be risered—to a certain extent in a similar way as steel for castings. In order to ensure their correct functioning, it is necessary to perforate the crust several times during solidification, for the surface layer of the melt solidifies quickly and prevents the further flow of the melt from the riser to the actual casting. Regarding the high volume contraction during solidification (6.5%), it is necessary to select a riser where the ratio of casting-to-riser is 7:3, and count with 70% utilization of melt even when the level (of the riser) is insulated with Sibral and its multiple perforation. With risers that are prone to cracking, it is necessary, within the temperature range from 970 ºC to 560 ºC, to ensure cooling at a rate of less than 50 $ºC \cdot h^{-1}$ [L4-2]. The chapter introduces a numerical model of the kinetics of the temperature field and a successive numerical model of chemical heterogeneity and their application on cast EUCOR.

4.2 The assignment and and proposal of the calculation of the 3D temperature field

The assignment focused on investigating the transient 3D temperature field of a system comprising a casting with a riser, the mould and ambient, using a numerical model. The dimensions of the system casting (the so-called „stone“)-riser-mould are given in **Fig. 4-1**. The initial temperature of the mould was 20 °C. The pouring temperature of the melt was 1 800 °C. That was approximately 300 °C higher, when compared with, for example, the steel pouring temperature. The temperature of the liquidus was 1 775 °C and the solidus 1 765 °C. The temperature field was symmetrical along the axes, i.e. it was sufficient for the investigation of the temperature field of a single quadrant only. The resultant heat flow through both longitudinal sections was equal to zero. **Figure 4-2** shows the network for the original casting, riser and mold. The numerical model for the simulation of the temperature field of this system was created by ANSYS again, which is described via Fourier equation (**eq. 2-1**), respectively equation (**eq. 2-2**) in the Chapter 2. The coefficients of heat transfer by radiation and convection in all planes bordering the system into the ambient were defined. Ideal physical contact was presumed between the sand mould and the casting.

The simulation of the release of the latent heats of phase or structural changes is carried out by introducing the thermodynamic enthalpy function. The model enables the evaluation of the temperature field within the actual casting and mould at any point in time within the process of solidification and cooling using contour lines (i.e. so-called iso-lines and iso-zones) or temperature-time curves for any nodal point of the system. It is possible to use all sophisticated sub-programs of ANSYS, such as automatic mesh generation, pre-processing and post-processing. The program also considers the non-linearity of the task, i.e.: the dependence of the thermophysical properties of all materials entering the system, and the dependence of the heat-transfer coefficients (on all boundaries of the system) on the temperature of the surface – of the casting and mould.

The number of nodal points can be anywhere within the range from 106 to 107 — this density makes it possible to cover castings of more complex shapes. The density also makes it possible to approximate the linear distribution of temperatures between individual points of the 3D mesh and even within time intervals.

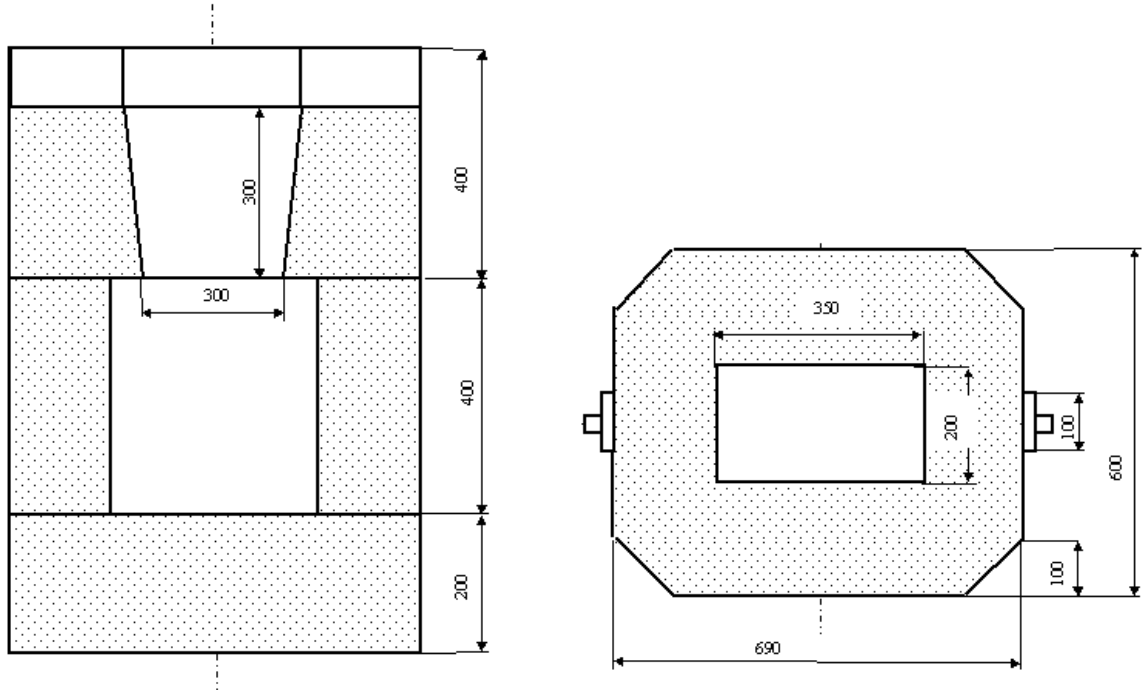

Fig. 4-1 The casting-riser-mould system

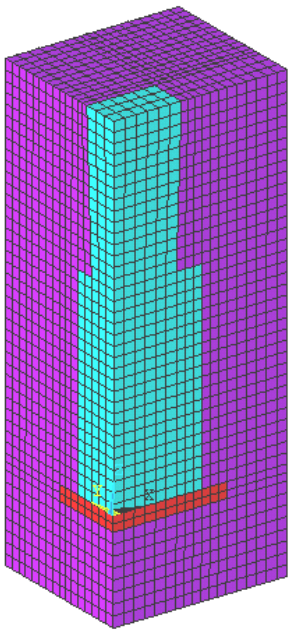

Fig. 4-2 The 3D mesh of the system with the original riser

The thermophysical properties of the ceramic material with their dependence on temperature are given in **Figs. 4-3 to 4-5**. The heat conductivity k is considered of the mould material $k = 3.3\ \mathrm{W{\cdot}m^{-1}{\cdot}K^{-1}}$ within the temperature range 0-100 °C and $k = 0.88\ \mathrm{W{\cdot}m^{-1}{\cdot}K^{-1}}$ above 100 °C; the density ρ is considered $\rho = 600\ \mathrm{kg{\cdot}m^{-3}}$, the specific heat capacity $c = 800\ \mathrm{J{\cdot}kg^{-1}{\cdot}K^{-1}}$ within the temperature range 0-100 °C and $c = 1\,000\ \mathrm{J{\cdot}kg^{-1}{\cdot}K^{-1}}$ above 100 °C.

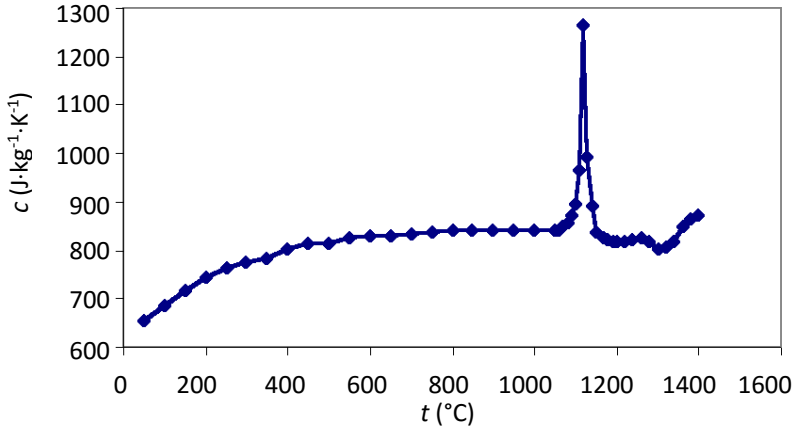

Fig. 4-3 Specific heat capacity *c* of EUCOR and its dependence on temperature

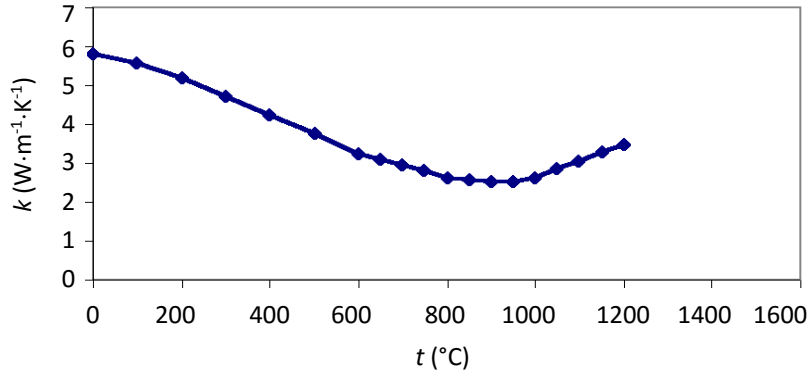

Fig. 4-4 Heat conductivity *k* of EUCOR and its dependence on temperature

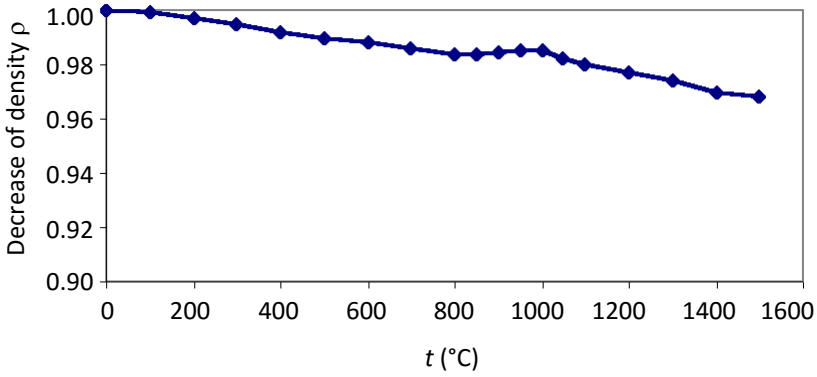

Fig. 4-5 Density ρ of EUCOR and its dependence on temperature

4.3 Temperature measurements of the temperatures inside the system original casting - mould. Calculated versus measured temperatures

The numerical model of the temperature field of the original casting was confronted with experimental measurements and corrected. The temperatures were measured in the actual casting and also in the mold. Special tungsten-rhenium thermocouples had to be used for the measurement within the actual casting, in order to withstand the high pouring temperature, which is approximately 300 °C higher than, for example, the pouring temperature of steel.

The measurement lasted as long as 19 hours. The measurement points (T1-T11) and the unassembled experimental mould are shown in **Fig. 4-6a** and **Fig. 4-6b**. Three GRANT measurement stations were used for the recording of temperatures throughout the process (**Fig. 4-7**).

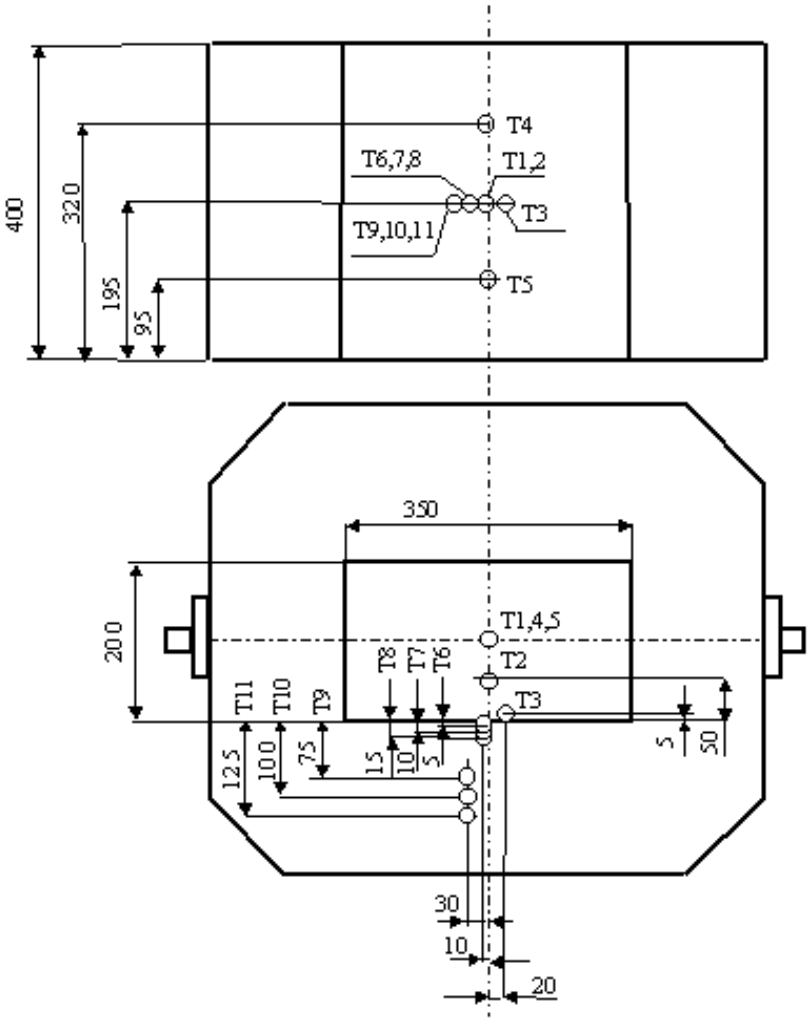

Fig. 4-6a Measurement points

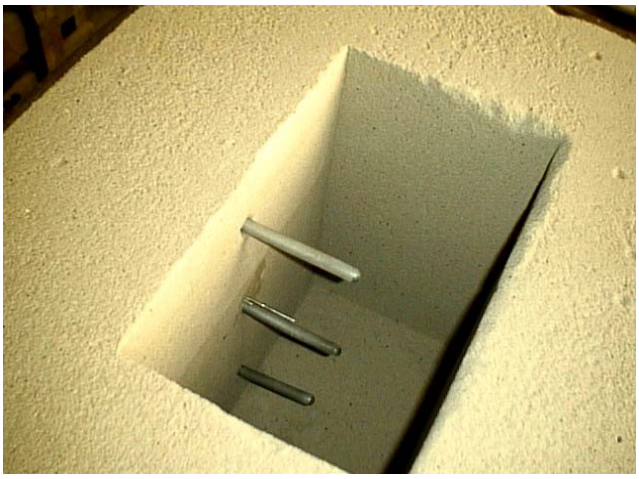

Fig. 4-6b The inside of the unassemled experimental mould

Fig. 4-7 GRANT measurement stations

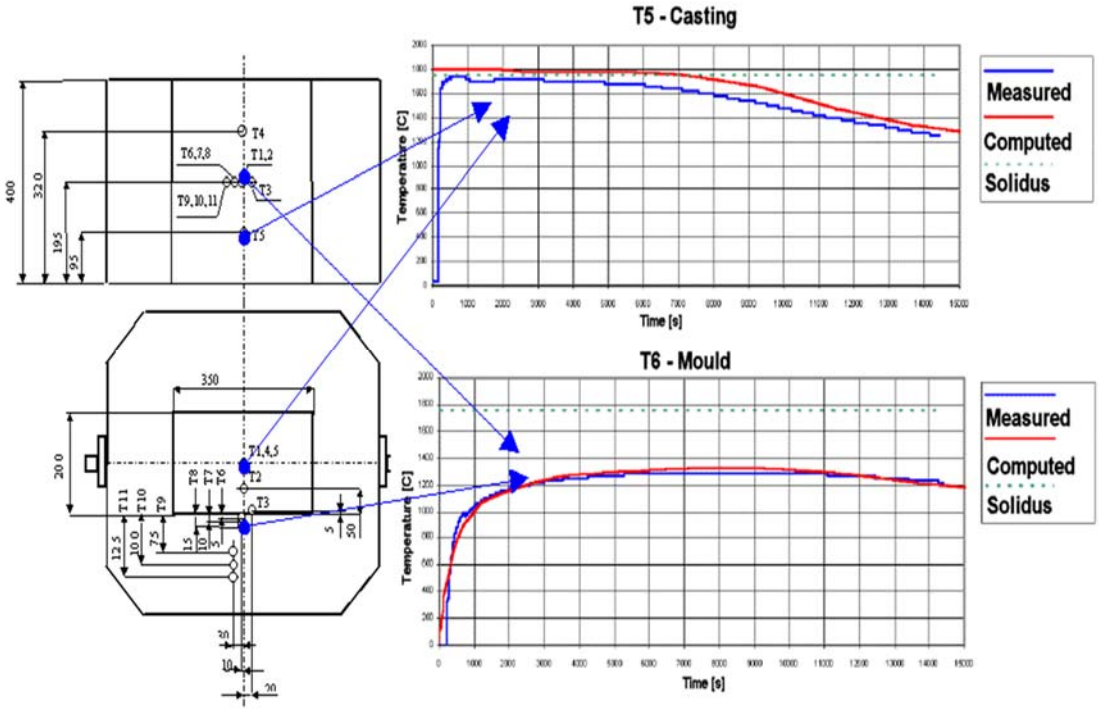

Fig. 4-8 The measurement points and the measured and computed temperature history of the points T5 and T6

In both graphs on **Fig. 4-8**, the blue lines represent the measured and the red lines represent the computed values. The comparison has been satisfactory, however, using the original riser, the directed solidification (which was the primary condition for a "healthy" casting) was not achieved because the riser was 'frozen' (i.e. the 'refilling' of the casting from the riser was cut off) at 5 200 s after pouring (**Fig. 4-9**).

The results attained from the numerical analysis of the temperature field of a solidifying casting and the heating of the mold represent only one quadrant of the system in question. **Figure 4-10** shows the 3D temperature field of the casting with the original riser and the mould at four times (5 400 to 10 800 s) after pouring (still after freezing). The riser-mold interface is an interesting place for monitoring. Once this point solidifies, the riser can no longer affect the process inside the casting. Out of the four charts in **Fig. 4-11**, only the first one shows the temperature field at a moment when the original riser was still functional (3 600 s after pouring).

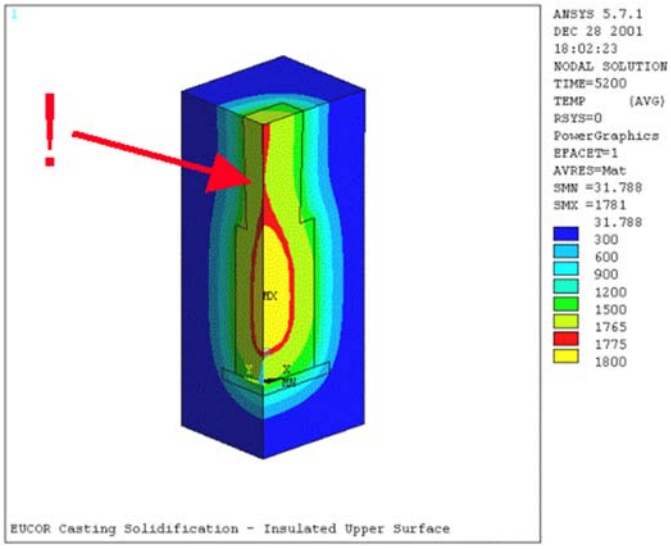

Fig. 4-9 The temperature field of the system comprising the casting, the original riser and mould at 5 200 s

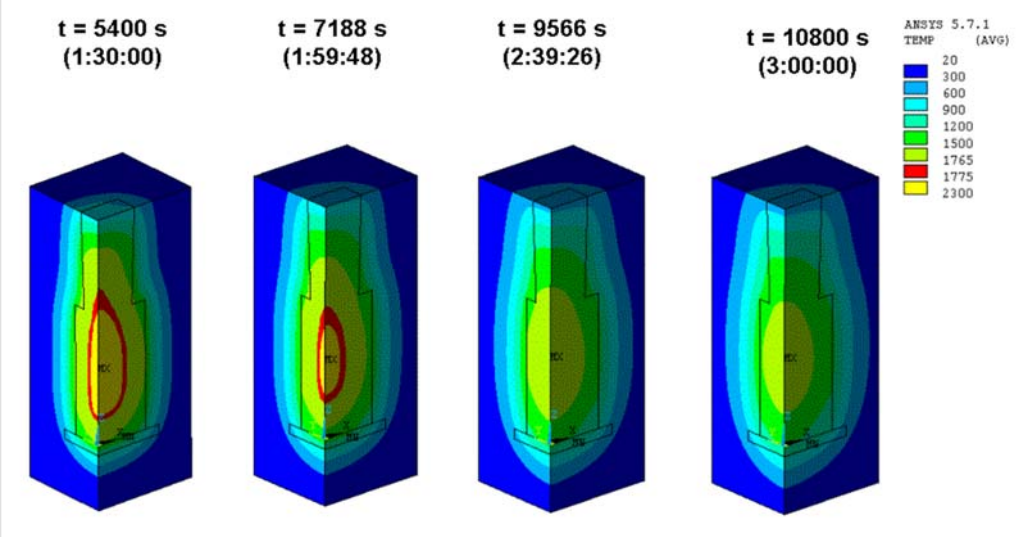

Fig. 4-10 The 3D temperature field of one quadrant of the casting with original riser

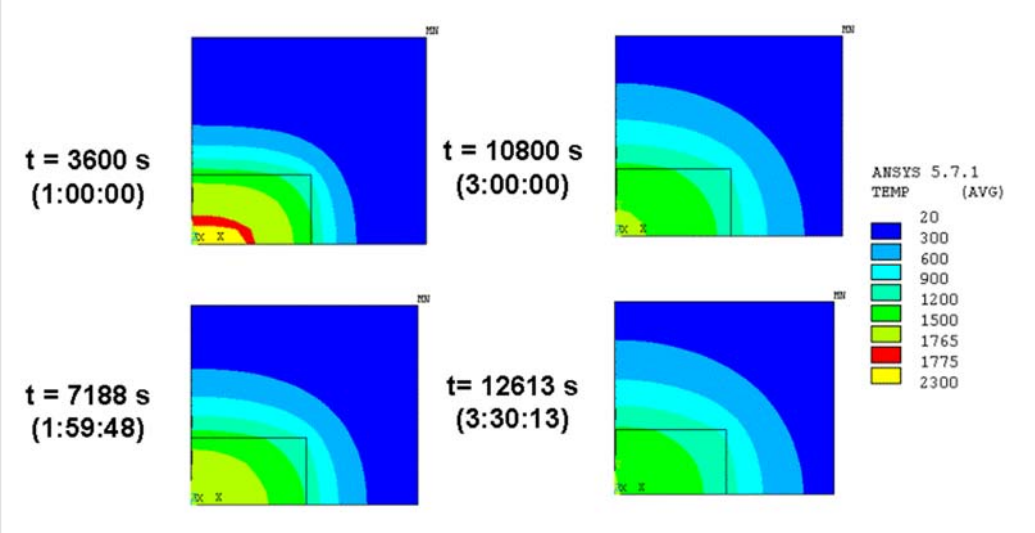

Fig. 4-11 The 2D temperature field on the riser-mould and riser-casting interface

4.4 Optimization of the original riser

The new shape of the riser was selected according to the latest findings. After several modifications, the application with an optimized riser ensured the directed solidification. The 3D mesh of the system with the new riser is presented in **Fig. 4-12 and 4-13**.

Figures 4-14 to 4-16 compare the temperature fields of the casting and riser inside the mold at 6 points in time - from the pouring into the mold to the total solidification. The left-hand figure of each pair represents the original riser and the right one represents the optimized riser. The casting with the new riser has the directed solidification — the casting was still being refilled from the riser.

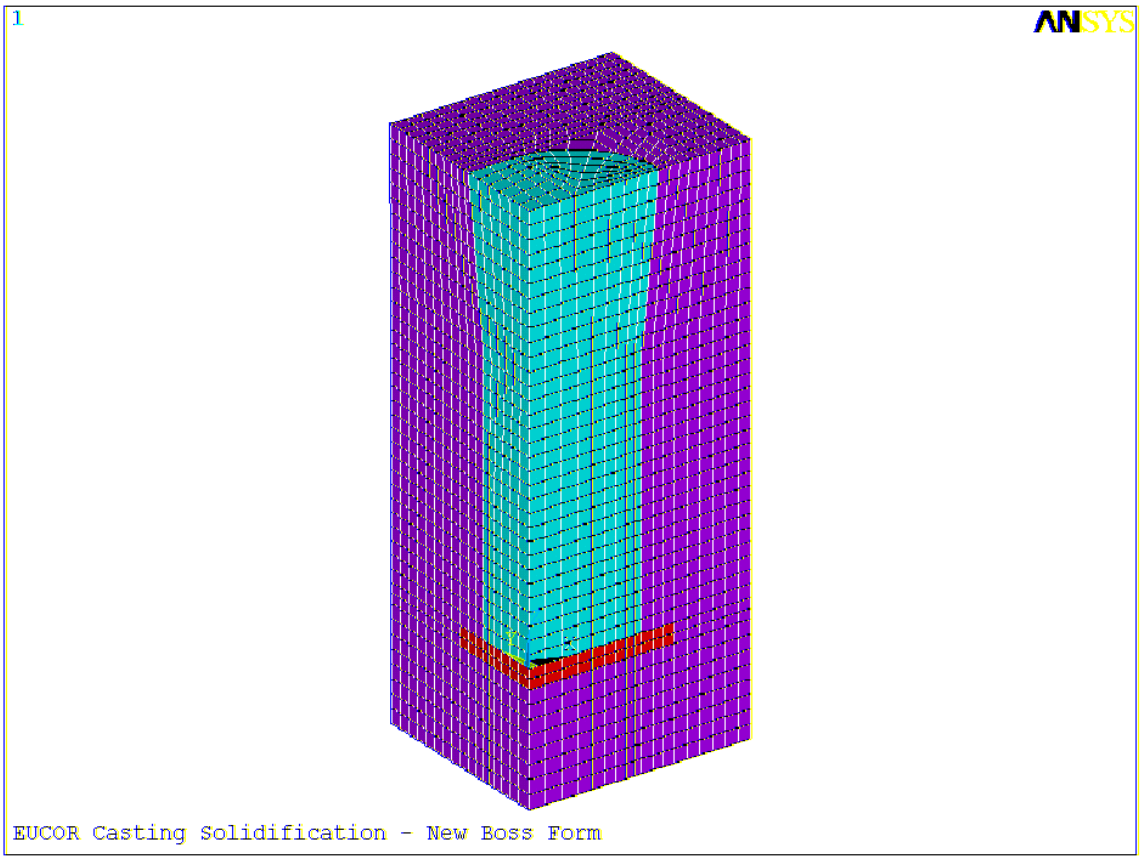

Fig. 4-12 The 3D mesh of the system with the optimized riser

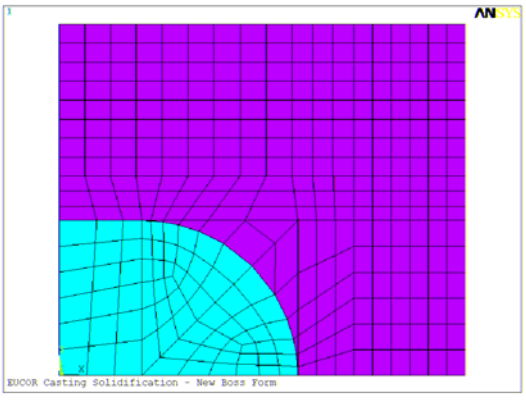

Fig. 4-13 The 2D mesh of the system with the optimized riser

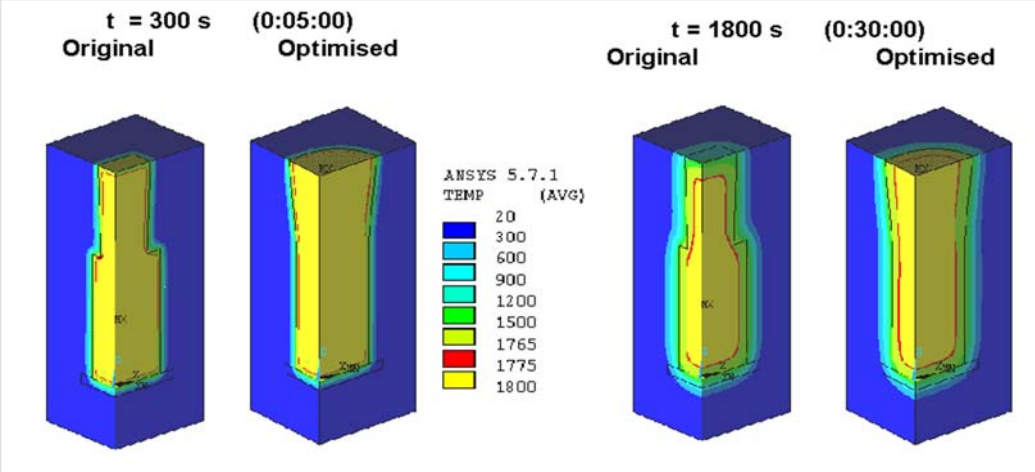

Fig. 4-14 The temperature fields of the system before and after optimization (300 s and 1 800 s after pouring)

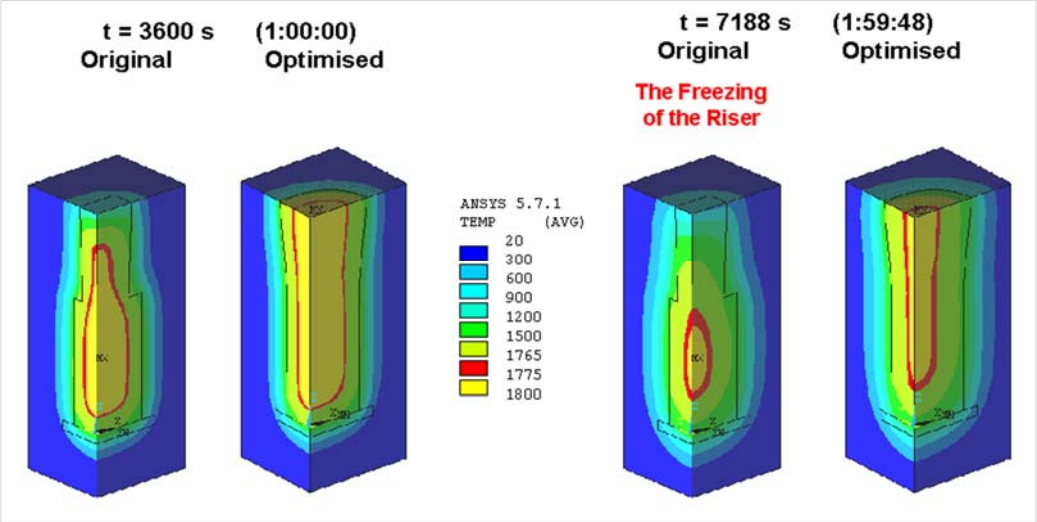

Fig. 4-15 The temperature fields of the system before and after optimization (3 600 s and 7 188 s after pouring)

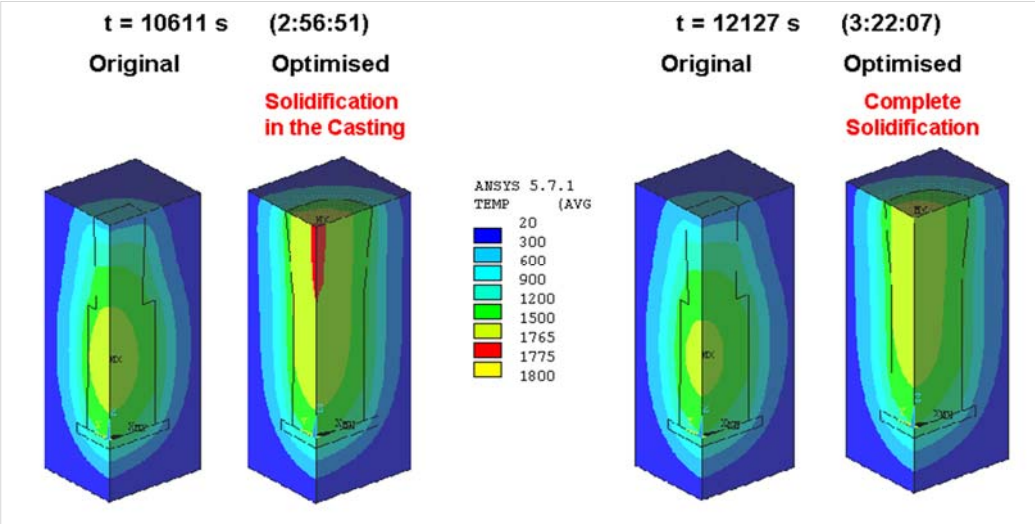

Fig. 4-16 The temperature fields of the system before and after optimization (10 611 s and 12 127 s after pouring)

4.5 The model of the chemical heterogeneity and its application

The concentration distribution of individual oxides, making up the composition of the ceramic material EUCOR, was determined using an original method described in Ref. [L4-3] and applied in the process of measuring the macro- and micro-heterogeneity of elements within ferrous alloys. This method was initially modified with respect to the differences occurring during solidification of the ceramic material, when compared to ferrous alloys.

It was presumed that within EUCOR, the elements had been already distributed, together with oxygen, at the stoichiometric ratio (i.e. the chemical equation), which characterized the resulting composition of the oxides of individual elements after solidification.

The preconditions for the application of the model of chemical heterogeneity on the EUCOR material are as follows:

a) If the analytically expressed distribution of micro-heterogeneity of the oxides of the ceramic material is available, if their effective distribution coefficient is known, and if it is assumed that it is possible to describe the solidification of the ceramic material via analogical models as with the solidification of metal alloys, then it is possible to conduct the experiment on the mutual combination of the calculation of the temperature field of a solidifying ceramic casting with the model describing the chemical heterogeneity of the oxides.

b) If the Brody-Flemings model [L4-3 to 4-5] is applied for the description of the segregation of oxides of the solidifying ceramic material and if an analogy with metal alloys is assumed, then it is possible to express the relationship between the heterogeneity index I_H of the relevant oxide, its effective distribution coefficient k_{ef} and the dimensionless parameter α using the equation

$$[\ln (2\alpha \cdot k_{ef})] / (1 - 2\alpha \cdot k_{ef}) = \{\ln [(1 + n \cdot I_H)/k_{ef}]\}/(k_{ef} - 1), \qquad \text{(eq. 4-1)}$$

the right-hand side based on the measurement of micro-heterogeneity, is already known and through whose solution it is possible to determine the parameter α, which represents so called back-diffusion parameter in the Brody-Flemings model. The quantity n has a statistical nature and expresses what percentage of the measured values could be found within the interval $C_{av} \pm n \cdot s_x$ (where C_{av} is the arithmetic mean and s_x is the standard deviation of the set of values of the measured quantity, i.e. concentration). If $n = 2$, then 95% of all measured values can be found within this interval.

c) If the dimensionless parameter α is known for each oxide, then a key to the clarification of the relationship exists between the local EUCOR solidification time θ, the diffusion coefficient D of the relevant oxide within the solidifying phase and the structure parameter L, which characterizes the distances between individual dendrites (in steels) or cells (in ceramics). The equation of the dimensionless parameter α is

$$\alpha = D \cdot \theta / L^2 . \qquad \text{(eq. 4-2)}$$

It is possible to take the dimension of a structure cell as the structure parameter for the EUCOR material.

The verification of the possibility of combining both methods was conducted on samples taken from the EUCOR blocks – from the edge (sample B) – and from the centre underneath the riser (sample C). Both the measured and computed parameters of chemical micro-heterogeneity and the computed parameters of the local solidification time θ (according to the temperature-field model) were calculated. The local solidification time of sample B is $\theta_B = 112.18$ *s* and of sample C is $\theta_C = 283.30$ *s*. The computed values of parameter α and the local solidification time θ determine, via their ratio, the quotient of the diffusion coefficient D and the square of the structure parameter L, which means that the following relation applies:

$$\alpha / \theta = D / L^2 \quad (s^{-1}) \qquad \text{(eq. 4-3)}$$

The calculated values of relation (**eq. 4-3**) for oxides of the sample B (taken from the edge of the stone) and the sample C (taken from the middle of the wall of the stone under the riser) are arranged in the **Tab. 4-1** together with parameter α.

Tab. 4-1 Calculated values of the equation (**eq. 4-3**)

Oxide	Sample B: α	$\alpha/\theta_B \cdot 10^4$ (s^{-1})	Sample C: α	$\alpha/\theta_C \cdot 10^4$ (s^{-1})
Na_2O	0.0732	6.53	0.0691	2.44
Al_2O_3	0.0674	6.01	0.0662	2.34
SiO_2	0.0741	6.61	0.0663	2.34
ZrO_2	0.00035	0.0312	0.00008	0.0028
K_2O	0.0721	6.43	0.0665	2.35
CaO	0.075	6.69	0.0703	2.48
TiO_2	0.0759	6.77	0.0757	2.67
Fe_2O_3	0.0732	6.53	0.0711	2.51
HfO_2	0.0165	1.47	0.00017	0.006

It comes as a surprise that the values of the parameter $\alpha/\theta = D/L^2$ of the oxides Na, Al, Si, K, Ca, Ti and Fe differ by as much as an order from the value of the same parameter of the oxide of zirconium and hafnium. This could be explained by the fact that zirconium contains hafnium as an additive and, therefore, they segregate together and the forming oxides of zirconium and hafnium have the highest melting temperature. From the melt, both oxides segregate first, already in the solid state. Further redistribution of the oxides of both elements runs on the interface of the remaining melt and the successive segregation of other oxides only to a very limited extent. It is therefore possible that the real diffusion coefficients of zirconium and hafnium in the successively forming crystallites are very small (i.e. $D_{Zr} \rightarrow 0$ a $D_{Hf} \rightarrow 0$). On the other hand, the very close values of the parameters $\alpha/\theta = D/L^2$ of the remaining seven analysed oxides:

$$D/L_B^2 = (6.51 \pm 0.25) \cdot 10^{-4}\ (s^{-1}) \quad \text{and} \quad D/L_C^2 = (2.45 \pm 0.12) \cdot 10^{-4}\ (s^{-1}) \qquad \text{(eq. 4-4)}$$

indicate that the redistribution of these oxides between the melt and the solid state runs in a way, similar to that within metal alloys, namely steels.

According to [L4-5], it would be possible to count – in the first approximation – with the diffusion coefficients of the oxides in the slag at temperatures of 1 765 °C (solidus) and 1 775°°C (liquidus) with an average value of $(2.07 \pm 0.11) \times 10^{-6}$ $cm^{-2} \cdot s^{-1}$ (the data refers to the diffusion of aluminium in the slag with a composition of 39% CaO, 20% Al_2O_3 and 41% SiO_2). For these cases, and using (**eq. 4-3**), it is possible to get the magnitude of the structure parameters that govern the chemical heterogeneity of the values:

$$L_B = \sqrt{[(2.07 \cdot 10^{-6})/(6.51 \cdot 10^{-4}]} = 0.05639\ \text{cm} \quad \text{and} \qquad \text{(eq. 4-5a)}$$

$$L_C = \sqrt{[(2.07 \cdot 10^{-6})/(2.45 \cdot 10^{-4}]} = 0.09192\ \text{cm} \qquad \text{(eq. 4-5b)}$$

which corresponds to 564 μm in sample B and 919 μm in sample C.

From the comparison of the micro-structures of the analyses [L4-6 to 4-8] samples B and C (**Figs. 4-17 and 4-18**) it is obvious that the micro-structure of sample B (L_B) is significantly finer than the micro-structure of sample C (L_C), which semi-quantitatively corresponds to the qualified estimate of the structure parameters L, conducted on the basis of calculations from the data obtained from both models. An analogous comparison can be seen in **Figs. 4-19 and 4-20** too.

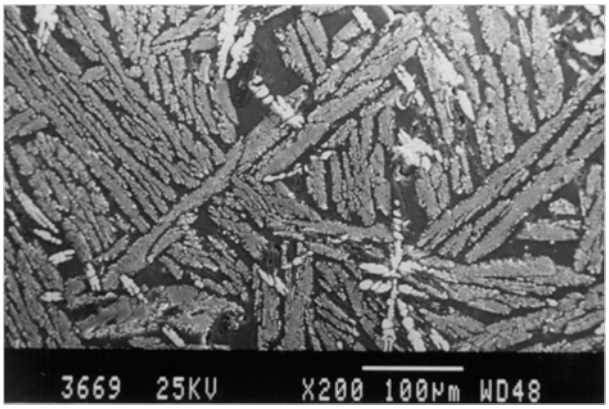

Fig. 4-17 The structure of sample B (L_B = 564.9 μm)

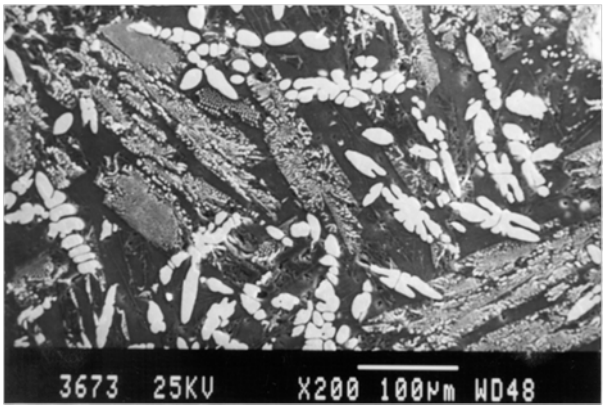

Fig. 4-18 The structure of sample C (L_C = 919.2 μm)

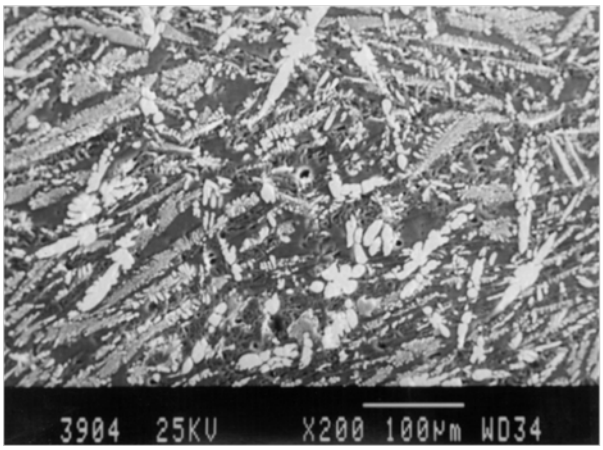

Fig. 4-19 The microstructure of sample B from the the edge of the block

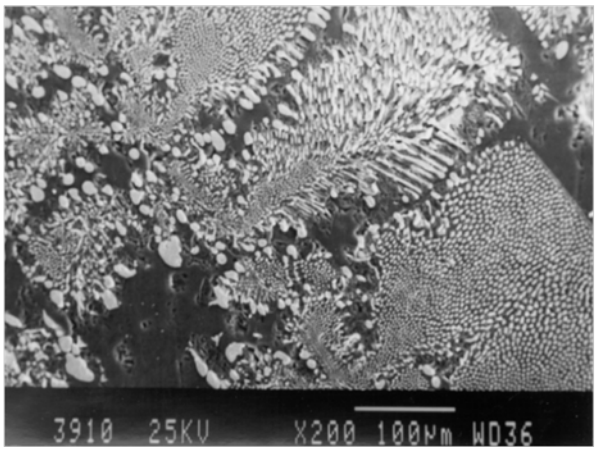

Fig. 4-20 The microstructure of sample C from the middle of the block under its riser

4.5.1 Consequences of the chemical heterogeneity model

The sample B structure in **Fig. 4-17** characterizes higher cooling rate of the EUCOR material from the solidus temperature, when compared with the structure C in **Fig. 4-18**. These two figures show that the higher diameter of the structure parameter L corresponds to the lower cooling rate of the same material. Both structure parameters, L_B and L_C, were calculated using the combination of two models (the numerical model of the temperature field and the model of the chemical heterogeneity). The numerical model of the temperature field of the stone-block solidification provides the information about the local solidification time at any point of the casting, it also means at any critical point of the casting, which has the tendency to crack or to fracture. The model of the chemical heterogeneity creates the chance to estimate the structures parameters in this critical point of castings.

According to fracture mechanics, it was possible, in the first approximation, to write the equation

$$K_{IC} \geq \sigma_B \sqrt{\pi \cdot L_B} = \sigma_C \sqrt{\pi \cdot L_C} \ , \qquad \text{(eq. 4-6)}$$

where K_{IC} is the fracture toughness (MPa·m$^{1/2}$), σ_B, σ_C are the strains on the structure defects' tips (MPa) and L_B, L_C are the the structure parameters (cells) in the samples B and C (m). The occurrence of primary technological defects on the casting grains is highly probable (the micro-shrinkage porosity, micro-shrinkage cavity, and so on). The equation (**eq. 4-6)** implies the following

$$\left(\frac{\sigma_B}{\sigma_C}\right)^2 = \frac{L_C}{L_B} = \frac{919.2}{563.9} = 1.63 \qquad \text{(eq. 4-7)}$$

It means that the relation between the structure parameters L_C and L_B makes (gives) the relation between of quarter of σ_B and the σ_C strain on the tips of potential structure defects of the samples B and C. At the same fracture toughness, the strain on the sample B can be 1.27 times higher, when compared with the strain on the sample C.

4.6 Conclusion

The investigation of the temperature field had two goals: The directed solidification as the primary condition for a healthy casting and the optimization of the casting technology, together with the preservation of optimal utility properties of the product. The achievement of these two goals depended on the ability to analyze and, successively, to control the effect of the main factors which characterize the solidification process or accompany it.The results of the investigation of the quantities should reveal the causes of heterogeneities in castings with respect to the phase and structural changes. It should also focused on the thermo-kinetics of the formation of shrinkage porosities and cavities and on the prediction of their formation and, therefore, on the controlling the optimization of the shape and sizes of the risers, the method of insulation, the treatment of the level, etc.

This Chapter discussed also the numerical model of the transient temperature field and the numerical model of the chemical heterogeneity, their application and combination. The combination of both models makes it possible to estimate the structure parameter, which expresses the size of the crystallites of the resultant material structure.

The combination of both models creates a tool for the estimation of the tendency to the cracks and fractures in critical points of the casting from EUCOR material.

The solution has been printed in the peer-reviewed journals and presented at prestigious conferences [L4-9 to 4-18].

4.7 Literature

[L4-1] Prospectus: EUCOR: *A heat and wear resistant corundo-baddeleyit material*. EUTIT, s. r. o., Stará Voda, Mariánské Lázně, Czech Republic, January 2000.

[L4-2] Kavička F., Buchal A., Bůžek Z., Dobrovská J., Dobrovská V. and Stránský K.: Castings from corundo-baddeleyit ceramics – their properties and utilization for wear resistant materials, piping, etc. *Slévárenství,* 49 (2001) 9, 524–529.

[L4-3] Dobrovská J., Dobrovská V., Rek A. and Stránský K.: Possible ways of prediction of the distribution curves of dendritic segregation of alloying elements in steels. *Scripta Materialia*, 18 (1998) 10, 1583–1598.

[L4-4] Elliott J. F., Gleiser, M. and Ramakrishna V.: *Thermochemistry for steelmaking*. AISI, Reading, Massachusetts, U.S.A., London, England, 1963.

[L4-5] Brody H. D. and Flemings M. C.: *Trans. AIME,* 236 (1966), 615–624.

[L4-6] Winkler Z. and Stránský K.: Microanalysis of the special heat resistant ceramic EUCOR (Part I). *Research report*, No. 78/1050. VTÚO Brno, Czech Republic, 1999.

[L4-7] Winkler Z. and Stránský K.: Microanalysis of the special heat resistant ceramic EUCOR (Part II). *Research report*, No. 78/1064. VTÚO Brno, Czech Republic, 1999.

[L4-8] Winkler Z. and Stránský K.: Microanalysis of the special heat resistant ceramic EUCOR (Part III). *Research report,* No. 78/1096. VTÚO Brno, Czech Republic, 1999.

[L4-9] Kavička F., Dobrovská J., Stránský K., Sekanina B. and Štětina J.: The experimental and numerical investigation of the solidification of a porous ceramic casting. *Frontiers in Heat and Mass Transfer (FHMT).* 3 (2012) 3, 1–9.

[L4-10] Kavička F., Stránský K., Dobrovská J., Sekanina, B. and Štětina J.: Numerical Model of the Temperature Field of the Cast and Solidified Ceramic Material. In *CD-ROM The 10th International Conference on Numerical Methods in Industrial Forming Processes Nuniform 2010.* Pohang, Korea, American Institute of Physics. 2010. p. 571–577.

[L4-11] Kavička F., Sekanina, B.; Heger, J., Ramík, P., Štětina, J. and Dobrovská J.: Numerical optimization of a casting technology of the special ceramics material. In *Proceedings of the 7th world Multiconference on systemics, cybernetics and informatics.* Orlando, USA, International Institut of Informatics and Systemics. 2003. p. 74–79.

[L4-12] Sekanina B., Kavička F., Stránský K., Štětina J. and Dobrovská J.: Two numerical models of solidifying and cooling of a ceramic casting of eucor. In *Program and book of abstracts of 19th conference on materials and technology.* 1. Ljubljana, Institut za kovinske materiale in tehnologie. 2011. p. 142.

[L4-13] Kavička F., Sekanina, B., Stránský K., Štětina J., Dobrovská J. and Franěk Z.: The Experimental and Numerical Investigation of the Solidification of a Porous Ceramic Casting. In *Proceedings of the ASME-ATI-UIT 2010 Thermal and environmental issues in energy systems. Vol. II.* Sorrento, Editioni ETS. 2010. p. 1527–1533.

[L4-14] Stránský K., Dobrovská J., Kavička F., Sekanina B. and Štětina J.: Solidifying ceramics EUCOR and its tendency to the cracks and fractures. In *Proceedings of the International Conference o Crack Paths (CP 2009).* Padua, Italy: University of Padua, 2009. p. 913–919.

[L4-15] Kavička F.: The experimental and numerical investigation of the temperature field of a solidifying ceramic casting. In *Proceedings of the Sixth World Conference on Experimental Heat transfer and, Fluid Mechanics and Thermodynamics.* Japan. 2005. p. 208–209.

[L4-16] Dobrovská J., Kavička F., Stránský K., Dobrovská V., Štětina J. and Heger J.: Two numerical models for optimization of the foundry technology of the ceramics EUCOR. In *2004 ASME Heat Transfer/Fluid Engineering Summer Conference.* Charlotte, ASME. 2004. p. 30–36.

[L4-17] Kavička F., Štětina J., Sekanina B., Ramík P., Heger J. and Dobrovská J.: Calculation of the temperature field of the solidyfying ceramic material EUCOR. In *Proceedings of the 2003 ASME Pressure Vessels and Piping Conference.* Cleveland, US, American Society of Mechanical Engineers. 2003. p. 135–142.

[L4-18] Kavička F., Heger J., Ramík P., Dobrovská J. and Štětina J.: A numerical model of the temperature field of the cast and solidified ceramic material EUCOR. In *Book of Abstracts, CompTest 2003, International Conference.* ENSAM Chalons en Champagne, France, ENSAM. 2003. p. 1.

5 Numerical models of temperature field of a concasting

5.1 Introduction

The production of steels, alloys and metallurgical products in general is constantly developing. Materials with high utility parameters are more in demand and traditional production is being replaced by higher quality steel. More and more sophisticated aggregates using more sophisticated technological procedures are being implemented. In order to maintain competitiveness, diversify production and expand to other markets, it is necessary to monitor technological development.

In the case of concasting, it is not possible to fulfill these requirements without the application of models of all caster processes dependent on thermal-mechanical relationships. These models can be applied both off-line and on-line. An off-line model is one where the calculation takes longer than is the time of the actual casting process. An on-line model runs in real time – taking the data directly from the operation – and its calculation takes the same time (if not less) than the actual process.

These models will support the design of new and redesign of old machines, they will facilitate the identification and quantification of any potential defects and optimization of the various operational conditions in order to increase productivity and minimize (the occurrence) of defects. The process of the solidification of concast steel is influenced by many factors and conditions, among which are the following:

- Complete turbulent transient flow within a comprehensive geometry (input jet and liquid metal in the slab).
- Thermodynamic reactions between the casting powder and the solidifying slab.
- Heat transfer between the liquid and solid powder on the surface of the slab.
- Dynamic movement of the liquid steel inside the mould on the liquid phase-mushy zone interface, including the influence of gravity, oscillations and the casting speed.
- Heat transfer in a superheated melt considering turbulent flow.
- Transition (mixture) composition of the steel during the change of class.
- Heat and mechanical interaction in the area of the meniscus between the solidifying meniscus, the solid powder and liquid steel.
- Heat transfer from the surface of the solidified shell into the space between the shell and the working surface of the mould (including the layers of the casting powder and the air gap) .
- Mass transfer of the powder during its vertical movement through the gap between the shell and the mould.
- Contact of the solidified slab with the mould and support rollers.
- The occurrence of crystals inside the melt.
- The process of micro-segregation and macro-segregation.
- The occurrence of shrinkages as a result of temperature contraction of the steel and the initialization of internal stress.
- The occurrence of stress and strain in the solidified shell as a result of external influence such as friction inside the mould, bulging between rollers, rolling, temperature stress and strain.
- The occurrence of cracks as a result of internal stress.
- The flow of steel as a result electromagnetic stirring and the influence of the stirring on the temperature field and the primary structure.
- The occurrence of stress and strain as a result of unbending of the inside the segments or in the rolling mill.
- Radiation between the various surfaces.
- Cooling as a result of convection beneath the water or water-air jets.

With respect to the complexity of the investigation into the influence of all of the above-mentioned factors, it is not possible to develop a mathematical model that would cover all of them. It is best to group them according to the three main types of influence:

- Heat and mass transfer.
- Mechanical.
- Structural.

The primary and deciding one is the influence of heat and mass transfer because it is the temperature field that gives rise to mechanical and structural influences. The development of a model of the temperature field (of a slab) with an interface for providing data for mechanical stress and strain models and structure models is therefore a top-priority task [L5-1].

5.2 An original off-line model of the temperature field of the concast steel billet 150 × 150 mm

The solidification and cooling of a concasting (for example a slab - profile of a concasting is a rectangle or a billet – profile of a concasting is a square) is a global problem of 3D transient heat and mass transfer. A schema of a billet caster (a concasting machine) is in **Fig. 5-1.**

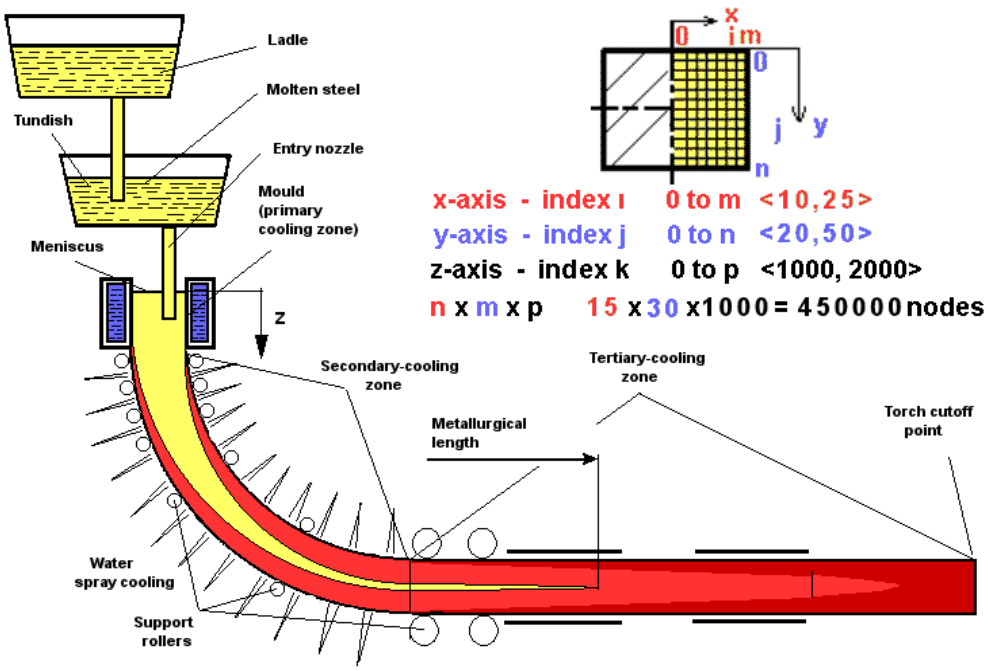

Fig. 5-1 A billet caster

If heat conduction within the heat transfer in this system a billet-mould (in a primary cooling zone-a crystallizer) or a billet-ambient (in a secondary and tertiary cooling zone) is decisive, then the heating up of the mould is described by the Fourier equation **(eq. 5-1)** and the solidification and cooling of the billet is described by the Fourier-Kirchhoff equation **(eq. 5-2)**, which contains the components describing the heat flow from the melt flowing with a casting speed w and the component including the internal source of latent heats of phase or structural changes $\dot{Q}_{source}$. It describes the temperature field of the solidifying billet in all three of its states: at the temperatures above the liquidus (i.e. the melt), within the interval between the liquidus and solidus (i.e. in the mushy zone) and at the temperatures below the solidus (i.e. the solid state).

$$\rho \cdot c \frac{\partial T}{\partial \tau} = \frac{\partial}{\partial x}\left(k \frac{\partial T}{\partial x}\right) + \frac{\partial}{\partial y}\left(k \frac{\partial T}{\partial x}\right) + \frac{\partial T}{\partial z}\left(k \frac{\partial T}{\partial z}\right) \qquad \text{(eq. 5-1)}$$

$$\rho \cdot c \frac{\partial T}{\partial \tau} = \frac{\partial}{\partial x}\left(k \frac{\partial T}{\partial x}\right) + \frac{\partial}{\partial y}\left(k \frac{\partial T}{\partial y}\right) + \frac{\partial y}{\partial z}\left(k \frac{\partial T}{\partial z}\right) + \varrho \cdot c \left(w_x \frac{\partial T}{\partial x} + w_y \frac{\partial T}{\partial y} + w_z \frac{\partial T}{\partial z}\right) + \dot{Q}_{source} \qquad \text{(eq. 5-2)}$$

The presented in-house model of the transient temperature field of the billet is unique in that, in addition to being entirely 3D, it can work in real time. It is possible to adapt its universal code and implement it on any billet caster. The numerical model covers the temperature field of the complete length of the blank (i.e. from the meniscus inside the mould all the way down to the cutting torch) with up to one million nodes.

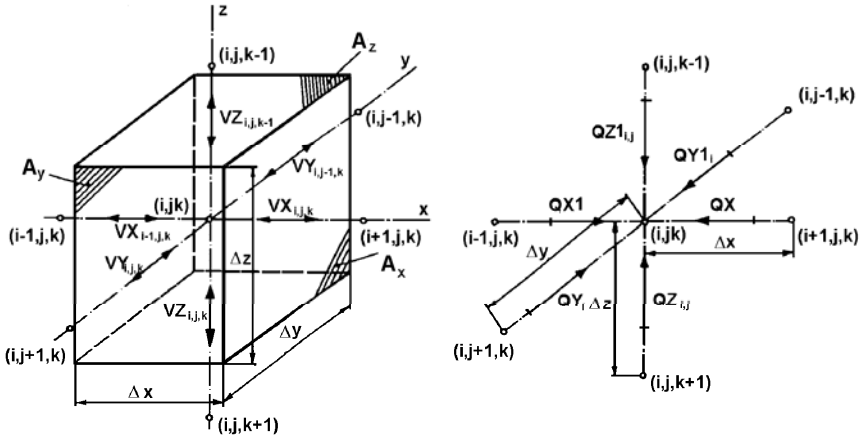

Fig. 5-2 The thermal balance diagram of the general nodal point of the network

Figure 5-2 shows the temperature balance of an elementary volume representing a general node of the mesh *(i,j,k)* inside the mould. The heat conductivities *VX*, *VY* and *VZ* (W·K^{-1}) along the main axes are:

$$VX_{i,j,k} = k_i \frac{A_x}{\Delta x} \qquad VX_{i-1,j,k} = k_{i-1} \frac{A_x}{\Delta x} \qquad \text{(eq. 5-3a)}$$

$$VY_{i,j,k} = k_j \frac{A_y}{\Delta y} \qquad VY_{i,j-1,k} = k_{j-1} \frac{A_y}{\Delta y} \qquad \text{(eq. 5-3b)}$$

$$VZ_{i,j,k} = k_k \frac{A_z}{\Delta z} \qquad VZ_{i,j,k-1} = k_{k-1} \frac{A_z}{\Delta z} \qquad \text{(eq. 5-3c)}$$

The heat flows $\dot{Q}X$, $\dot{Q}Y$ a $\dot{Q}Z$ (W) through the elementary volume along the main axes are:

$$\dot{Q}X = VX_{i,j,k}\left(T^{(\tau)}_{i+1,j,k} - T^{(\tau)}_{i,j,k}\right) \qquad \dot{Q}X1 = VX_{i-1,j,k}\left(T^{(\tau)}_{i-1,j,k} - T^{(\tau)}_{i,j,k}\right) \qquad \text{(eq. 5-4a)}$$

$$\dot{Q}Y_i = VY_{i,j,k}\left(T^{(\tau)}_{i,j+1,k} - T^{(\tau)}_{i,j,k}\right) \qquad \dot{Q}Y1_i = VY_{i,j-1,k}\left(T^{(\tau)}_{i,j-1,k} - T^{(\tau)}_{i,j,k}\right) \qquad \text{(eq. 5-4b)}$$

$$\dot{Q}Z_{i,j} = VZ_{i,j,k}\left(T^{(\tau)}_{i,j,k+1} - T^{(\tau)}_{i,j,k}\right) \qquad \dot{Q}Z1_{i,j} = VZ_{i,j,k-1}\left(T^{(\tau)}_{i,j,k-1} - T^{(\tau)}_{i,j,k}\right) \qquad \text{(eq. 5-4c)}$$

The temperature balance of the general node is:

$$\left(\dot{Q}Z1_{i,j} + \dot{Q}Z_{i,j} + \dot{Q}Y1_i + \dot{Q}Y_i + \dot{Q}X1 + \dot{Q}X\right) = \frac{\Delta x \cdot \Delta y \cdot \Delta z \cdot \varrho \cdot c}{\Delta \tau}\left(T^{(\tau+\Delta\tau)}_{i,j,k} - T^{(\tau)}_{i,j,k}\right) \qquad \text{(eq. 5-5)}$$

where the right hand side expresses the accumulation (or loss) of heat in the node *i,j,k* during the time step $\Delta\tau$. The unknown temperature of the general node of the mesh inside the mould in the following instant *(τ+$\Delta\tau$)* is therefore given by the explicit formula:

$$T^{(\tau+\Delta\tau)}_{i,j,k} = T^{(\tau)}_{i,j,k} + \left(\dot{Q}Z1_{i,j} + \dot{Q}Z_{i,j} + \dot{Q}Y1_i + \dot{Q}Y_i + \dot{Q}X1 + \dot{Q}X\right)\frac{\Delta\tau}{c \cdot \varrho \cdot \Delta x \cdot \Delta y \cdot \Delta z} \qquad \text{(eq. 5-6)}$$

The temperature field of the billet passing through a radial caster of a large radius can be simplified by the Fourier-Kirchhoff equation where only the w_z component of the velocity is considered. Equation **(eq. 5-2)** is therefore reduced to:

$$\rho \cdot c \frac{\partial T}{\partial \tau} = \frac{\partial}{\partial x}\left(k \frac{\partial T}{\partial x}\right) + \frac{\partial}{\partial y}\left(k \frac{\partial T}{\partial y}\right) + \frac{\partial y}{\partial z}\left(k \frac{\partial T}{\partial z}\right) + \varrho \cdot c \cdot w_z \frac{\partial T}{\partial z} + \dot{Q}_{source} \qquad \text{(eq. 5-7)}$$

Equation **(eq. 5-7)** must cover the temperature field of the billet in all three stages: above the liquidus temperature (i.e. the melt), in the interval between the liquidus and solidus temperatures (i.e. the so-called mushy zone) and beneath the solidus temperature (i.e. the solid phase. It is therefore convenient to introduce the thermodynamic function of specific volume enthalpy $H_v = c \cdot \rho \cdot T$ (J·m^{-3}), which is dependent on temperature, and also includes the phase and structural heats (**Fig. 5-3**).

Heat conductivity k, specific heat capacity c and density ρ are thermophysical properties that are also functions of temperature. Equation **(eq. 5-7)** therefore takes on the form:

$$\frac{\partial H_v}{\partial \tau} = \frac{\partial}{\partial x}\left(k\frac{\partial T}{\partial x}\right) + \frac{\partial}{\partial y}\left(k\frac{\partial T}{\partial y}\right) + \frac{\partial y}{\partial z}\left(k\frac{\partial T}{\partial z}\right) + w_z\frac{\partial H_v}{\partial z} \qquad \text{(eq. 5-8)}$$

The heat balance of the elementary node is:

$$\left(\dot{Q}Z1_{i,j} + \dot{Q}Z_{i,j} + \dot{Q}Y1_i + \dot{Q}Y_i + \dot{Q}X1 + \dot{Q}X\right) = \frac{\Delta x \cdot \Delta y \cdot \Delta z}{\Delta \tau}\left(H_{v_{i,j,k}}^{(\tau+\Delta\tau)} - H_{v_{i,j,k}}^{(\tau)}\right) \qquad \text{(eq. 5-9)}$$

where the heat flow $QZ_{i,j}$ now must also include the enthalpy of the incoming second volume of melt:

$$\dot{Q}Z_{i,j} = VZ_{i,j,k}\left(T_{i,j,k+1}^{(t)} - T_{i,j,k}^{(t)}\right) - A_z \cdot w_z \cdot H_{v_{i,j,k}}^{(\tau)} \qquad \text{(eq. 5-10)}$$

The unknown enthalpy of the general node of the billet in the following instant $(\tau + \Delta\tau)$ is given by the explicit formula, similar to equation (**eq. 5-6**):

$$H_{v_{i,j,k}}^{(\tau+\Delta\tau)} = H_{v_{i,j,k}}^{(\tau)} + \left(\dot{Q}Z1_{i,j} + \dot{Q}Z_{i,j} + \dot{Q}Y1_i + \dot{Q}Y_i + \dot{Q}X1 + \dot{Q}X\right)\frac{\Delta\tau}{\Delta x \cdot \Delta y \cdot \Delta z} \qquad \text{(eq. 5-11)}$$

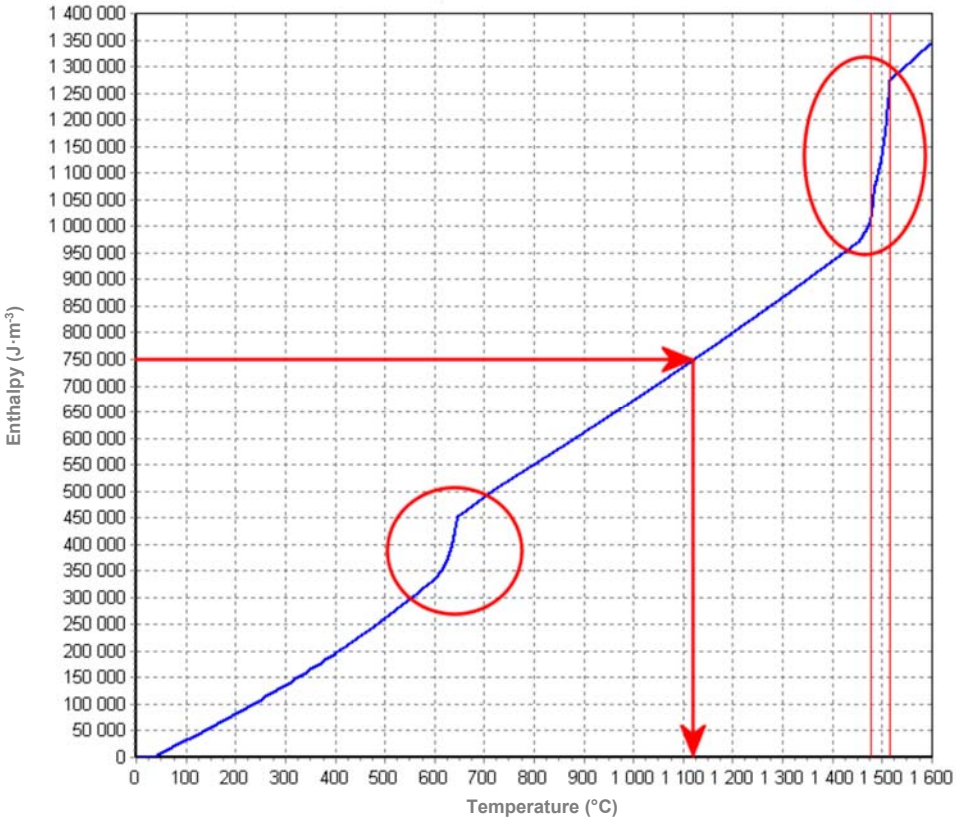

Fig. 5-3 The enthalpy function for steel showing the phase and structural changes

Figure 5-3 indicates how the temperature model for the calculated enthalpy in equation (**eq. 5-11**) determines the unknown temperature. The enthalpy function is not known as an analytical function but as a set of table values, and therefore the inverse calculation of the temperature is a very demanding problem numerically. In the dynamic model where the calculation must run at least as fast as is the flow of the process in real time, the method in which the interpolation values are calculated at 0.1 °C

intervals even before the actual calculation was chosen. The temperature for the relevant enthalpy is then determined using modern search methods.

The next task is to choose a suitable coordinate system and mesh. This paper deals with the symmetrical half of one cross-section of a blank from the meniscus inside the mould down to the cutting torch. The origin of the coordinate system is positioned on the small radius in the centre of the width (**Fig. 5-4a**). This enables all coordinates to be positive, which facilitates software programming. In the region of the radius, the Cartesian coordinates are transformed into cylindrical (i.e. y is the radius and z is the angle). The mesh is generated automatically and the model supports all densities of the mesh introduced in **Fig. 5-4a**. All results presented in this paper are based on a mesh of 573 594 nodes (11 in the x-direction, 21 in the y-direction and 1861 in the z-direction) and a 7.5 × 7.5 × 15 mm elementary volume.

All thermodynamic properties of the cast steel, dependent on its chemical composition and cooling rate, enter the calculation as functions of temperature [L5-2]. This is therefore a significantly non-linear task because, even with the boundary conditions, their dependence on the surface temperature of the billet is respected here.

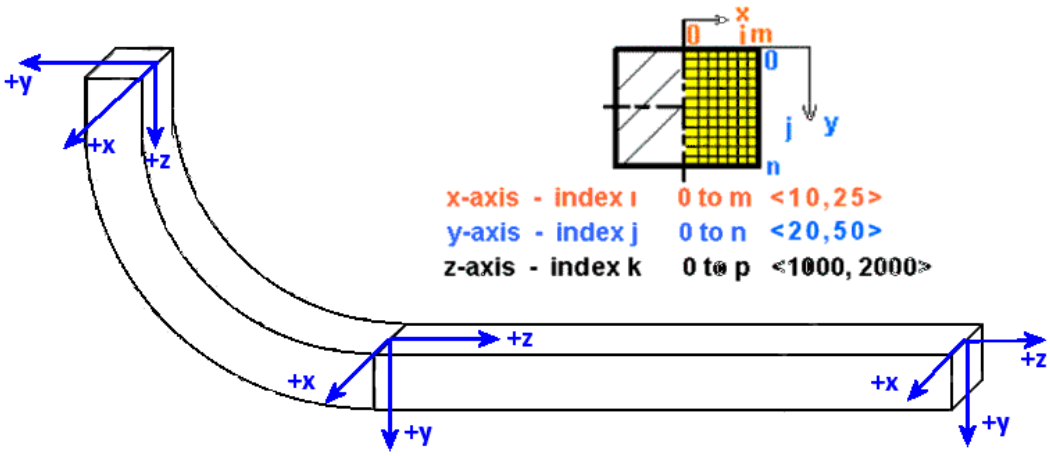

Fig. 5-4a The mesh and definition of the coordinate system

Regarding the fact that the task can be considered symmetrical along the axis (**Fig. 5-4a**), it is sufficient to deal with only one half of the cross-section. The boundary conditions are therefore as follows:

1. $T = T_{cast}$ — the level of the steel (eq.5-12a)

2. $-k\frac{\partial T}{\partial n} = 0$ — the plane of symmetry (eq. 5-12b)

3. $-k\frac{\partial T}{\partial n} = htc \cdot \left(T_{surface} - T_{amb}\right)$ — inside the mould (eq. 5-12c)

4. $-k\frac{\partial T}{\partial n} = htc \cdot \left(T_{surface} - T_{amb}\right) + \sigma \cdot \varepsilon \cdot \left(T_{surface}^4 - T_{amb}^4\right)$ — within the secondary and tertiary zones (eq. 5-12d)

5. $-k\frac{\partial T}{\partial n} = \dot{q}$ — beneath the rollers (eq. 5-12e)

The courses of the temperatures of the same points of the cross-section were selected as the basic graphical representation for comparison along the entire length of the caster, in combination with the graph showing the increase in the thickness of the shell.

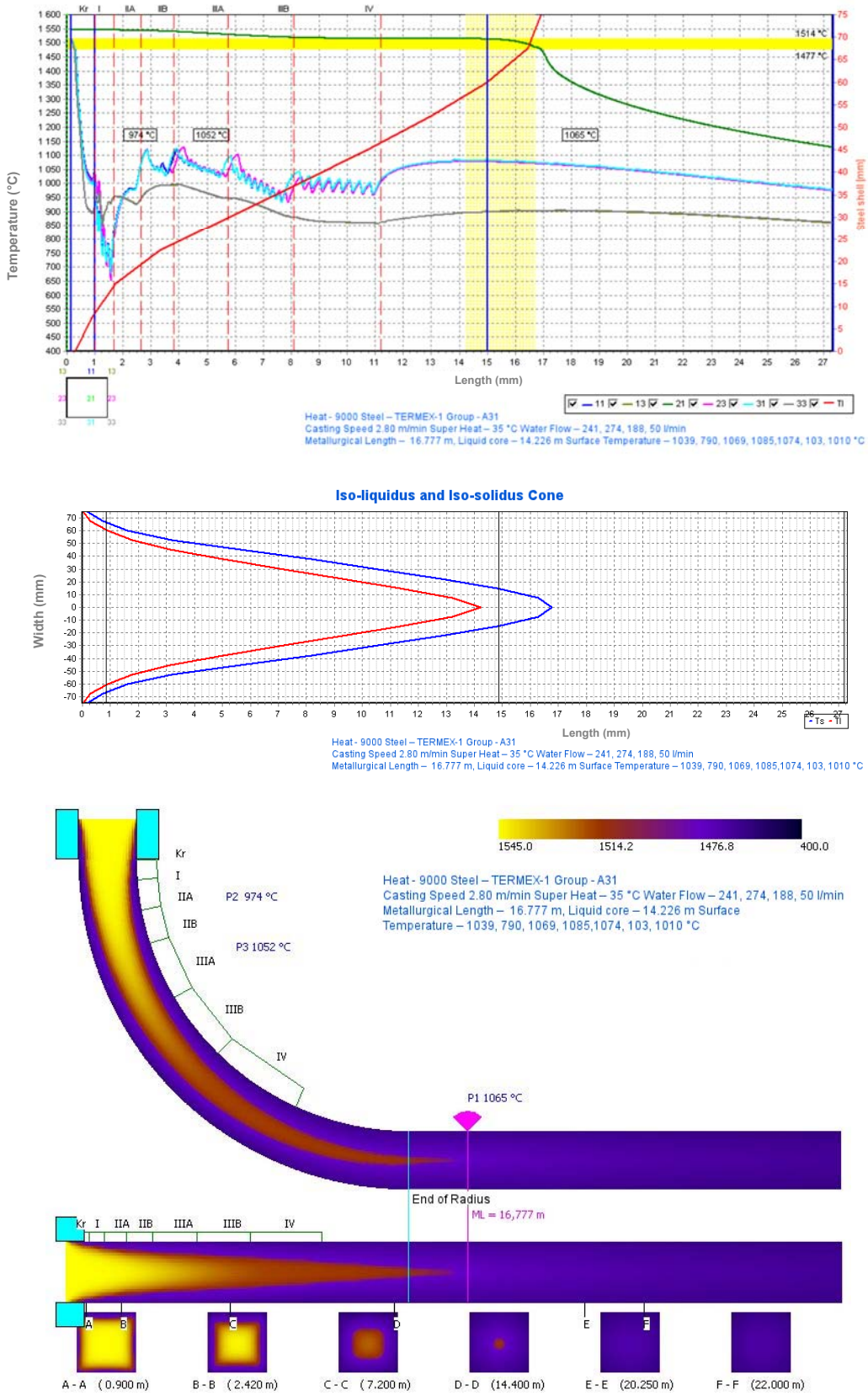

Fig. 5-4b Temperature field of the steel billet

There are three types of graphs drawn in order to illustrate the results as clearly and as completely as possible. **Figure 5-4b** shows the temperature history of six points of the cross-section of the steel slab (i.e. in the centre of the slab, in its corners and in the middle of the sides of the surface) in the way that

the cross-section passes through the caster (from the meniscus of the steel in the mould all the way down to the cutting torch). The distance from the meniscus inside the mould is plotted on the horizontal axis. The width of the horizontal yellow strip illustrates the temperature interval for the relevant class of steel. The width of the vertical yellow strip illustrates the distance between the isoliquidus and isosolidus (i.e. the width of the mushy zone) in its maximum values. Furthermore, the graph indicates three surface temperatures where the pyrometers were positioned (974 °C, 1 052 °C and 1 065 °C). The red vertical dashed lines are the boundaries between individual segments and, the blue vertical lines represent the meniscus of the steel inside the mould, the bottom edge of the mould, the unbending point and the end of the caster cage. The next graph describes the course of the isoliquidus and isosolidus unrolled along the longitudinal section through the entire concasting. This picture gives a clear idea of the shape of the mushy zone, which closely corresponds to the structure and any potential internal defects. The last graph illustrates the temperature field in the diagram of the caster, where the shades of blue represent solidified steel, the shades of yellow represent liquid steel and the red represents the mushy zone.

The 3D model had first been designed as an off-line version and later as an on-line version so that it could work in real time. After correction and testing, it will be possible to implement it on any CCM thanks to the universal nature of the code. The numerical model takes into account the temperature field of the entire blank (from the meniscus of the level of the melt in the mould to the cutting torch) using a 3D mesh containing more than a million nodal points.

5.3 An original off-line model of the temperature field of the concast steel slab 1 530 × 250 mm (width × thickness)

A schema of a caster for a slab is in **Fig. 5-5**.

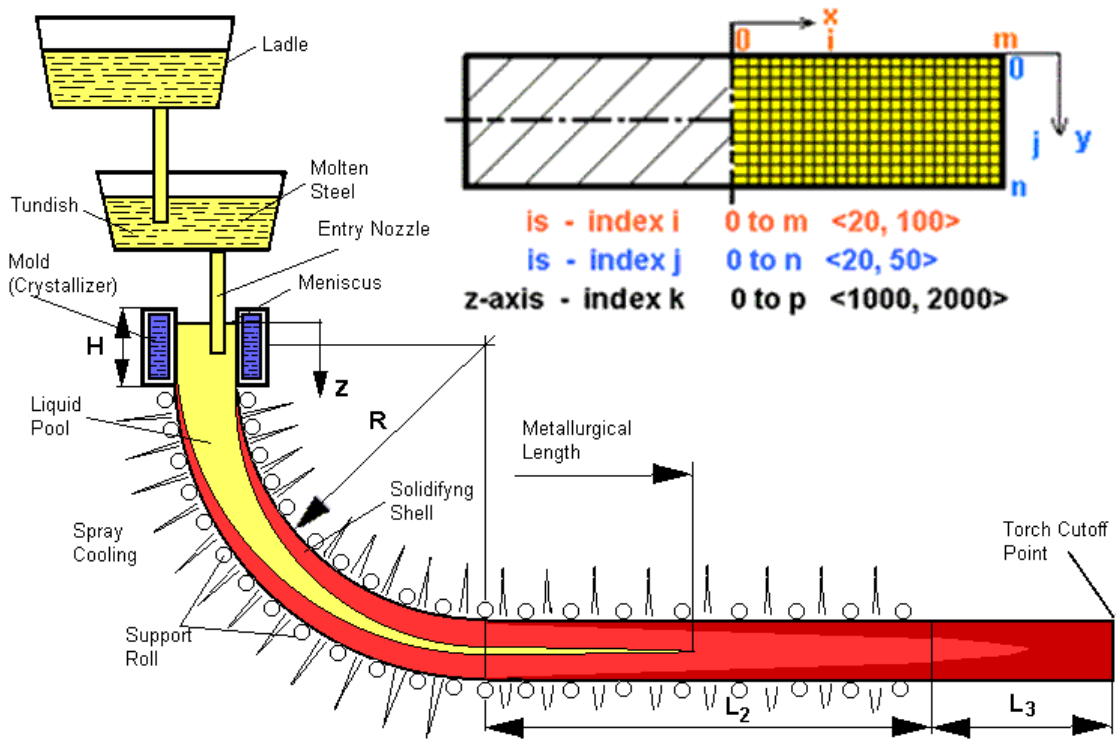

Fig. 5-5 A slab caster and the mesh and definition of the coordinate system.

Figure 5-6 shows three types of graphs drawn in order to illustrate the results of simulation of the temperature field of the concast steel slab 1 530 × 250 mm, which are analogous to the results of the temperature field of the steel slab (the 11325 class steel - **Tab. 5-1**).

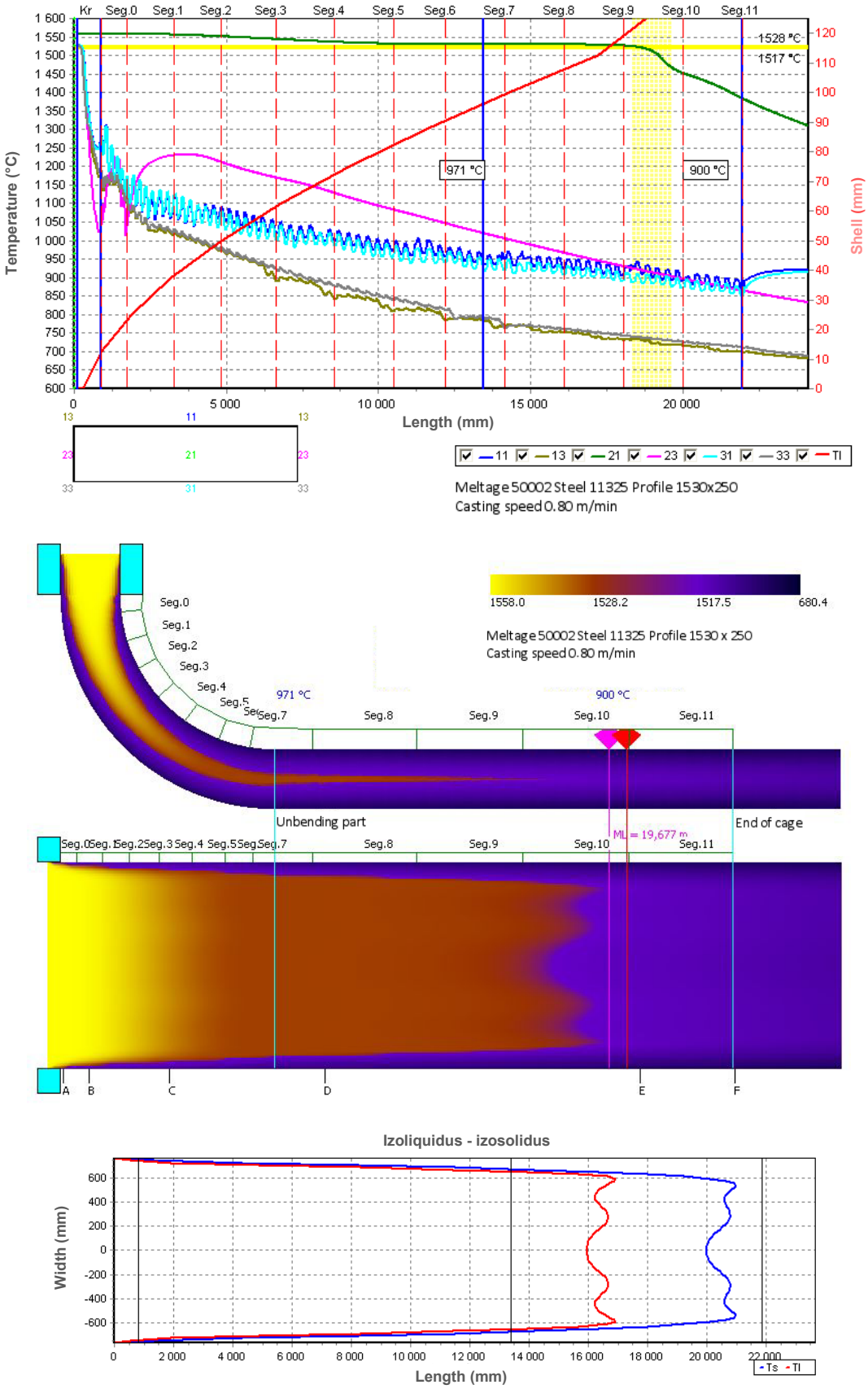

Fig. 5-6 Temperature field of the 11325 class steel slab (first row of **Tab. 5-1**)

The graph indicates two surface temperatures where the pyrometers were positioned (971 °C, 900 °C).

5.4 A parametric study of casting of the slab 1 530 × 250 mm (width × thickness)

5.4.1 A study on the effect of the chemical composition on the resultant temperature field

The original off-line model of the temperature field and its calculation speed makes it possible to perform so-called parametric studies, i.e. the analysis of the effect of individual input technological parameters and properties on the resultant temperature field [L5-3 and 5-4]. The results of these parametric studies could serve for the verification of the empirical relationships used, for establishing technological procedures for the caster operators, for the carrying out of comprehensive optimization and for the setting up of the dynamic model. Regarding the fact that the result of the modelling process is a 3D temperature field, it is necessary to select such output parameters that can be uniquely defined and compared or to select the graphics output of the compared output parameter, in order to assess the effect of the chemical composition. The most suitable for the comparison seems to be the maximum metallurgical length, the maximum length of the liquid phase, the surface temperature at the unbending point and the surface temperature the point just before leaving the caster cage.

A real concasting operation casts up to several hundred classes of steel. It would therefore be difficult to set the concasting and other relevant technological parameters for all of them. That is why steels are subdivided into groups, mostly according to their carbon content, preferably according to the so-called equivalent carbon content, given by:

$$C_{eq} = C - 0.1 \cdot Si + 0.04 \cdot Mn - 0.04 \cdot Cr + 0.1 \cdot Ni - 0.1 \cdot Mo \qquad \text{(eq. 5-13)}$$

Tab. 5-1 Selected classes of steel with their compositions (in wt.%) used for calculation

Class	Group	C_{eq}	C	Mn	Si	P	S	Cu	Ni	Cr	Mo	V	Ti	Al	Nb	T_S	T_L
11325	2	0.067	0.050	0.225	0.025	0.010	0.010	0.150	0.150	0.150	0.040	0.050	0.0025	0.045	0.030	1 499.8	1 529.8
21026	5	0.235	0.150	1.075	0.300	0.0175	0.010	0.150	0.200	0.100	0.040	0.045	0.001	0.040	0.015	1 451.4	1 514.2
31087	3	0.275	0.190	1.450	0.200	0.015	0.010	0.100	0.150	0.100	0.040	0.010	0.001	0.040	0.030	1 438.7	1 510.6
11500	4	0.326	0.270	0.550	0.275	0.015	0.010	0.150	0.150	0.125	0.040	0.050	0.025	0.040	0.030	1 423.2	1 507.4
13180	6	0.826	0.75	1.050	0.250	0.0175	0.010	0.125	0.200	0.150	0.050	0.100	0.050	0.040	0.025	1 322.7	1 467.7

A single class of steel was selected from each group for the analyses below. **Table 5-1** contains the recommended compositions of these steels, together with the temperatures of the liquidus and solidus. For an example it was selected 11325 class steel. **Figure 5-7** illustrates the dependence of the thermophysical properties on the temperature for this steel [L5-2]. **Figure 5.6** presents the calculated temperature field of the slab 1 530 × 250 mm for this class of steel. The calculation of the temperature field of the same slab was performed also for other steels. In order to analyse the influence of the chemical composition on the temperature field more clearly, the other concasting parameters were used identical, i.e. the casting speed 0.8 $m \cdot min^{-1}$, the superheating temperature 30 °C and the profile of the slab, just like the flow of water through the secondary-cooling zone. In practice, a different cooling mode is selected for each different class of steel.

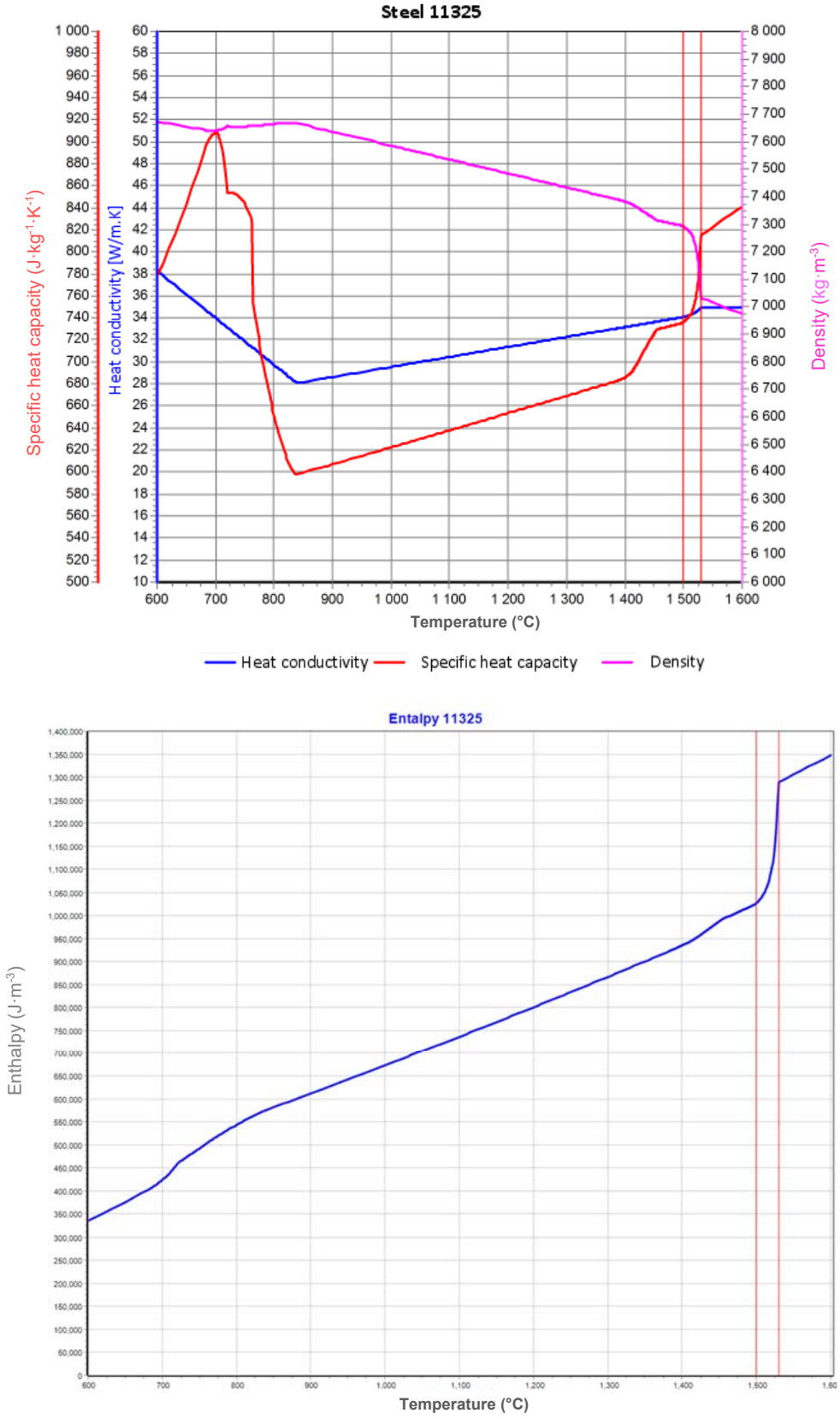

Fig. 5-7 Thermophysical properties of the 11325 class steel (first row of **Tab. 5-1**)

Figures 5-8 and 5-9 prove that the effect of the chemical composition on the resultant temperature field evaluated by the above-mentioned output parameters is significant.

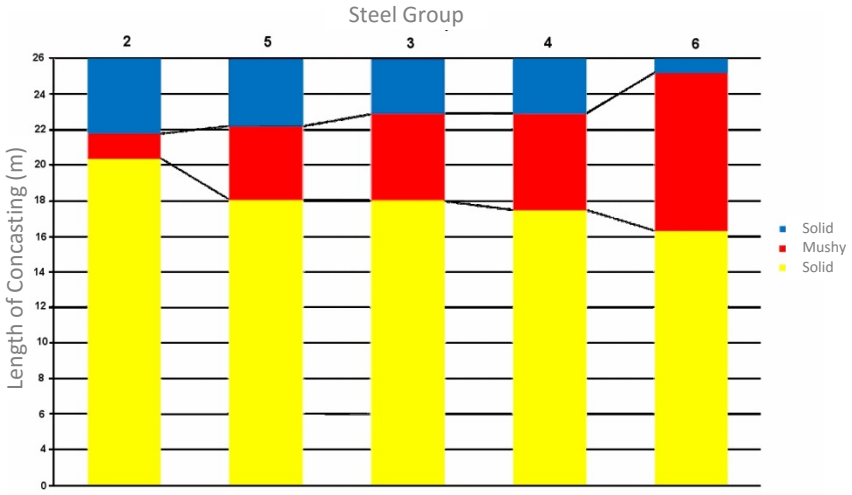

Fig. 5-8 Comparison of the length of the liquid phase and the metallurgical length for various classes of steel

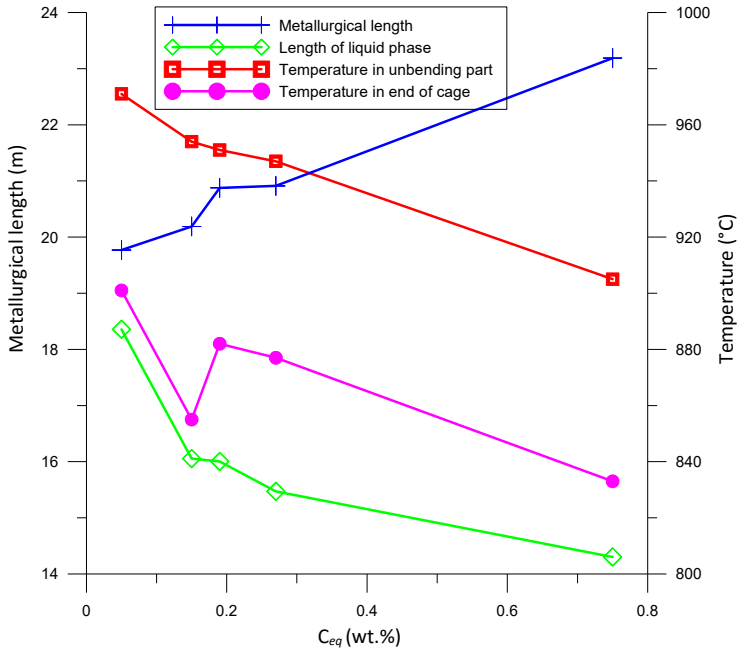

Fig. 5-9 The effect of the chemical composition on the resultant parameters

5.4.2 A study on the effect of the casting speed (11325 class steel)

The casting speed is a basic technological parameter. In calculations, whose results are represented here (for the 11325 class steel), the operating range of the speed is considered 0.7 to 0.85 m·min^{-1}. The flow of water through the secondary-cooling zone, according to the technological regulations, increases linearly. The other input parameters are again left constant, i.e. especially the superheating temperature of 30 °C. A higher speed need not be investigated because the metallurgical length exceeds the length of the cage, which is unacceptable. On the other hand, lower casting speeds are used only short-term, e.g. in the case that there is the risk of breakdown or when the tundish is being exchanged.

The graphs in **Figs. 5-10 and 5-11** show that there is a linear dependence of all of the monitored parameters (the metallurgical length, the length of the liquid phase, the temperature of the unbending part and the temperature at the end of the cage) on the casting speed. A slight deviation can be seen for lower speeds, which corresponds with the setting of secondary cooling. A casting speed of 0.82 m·min^{-1} seems to be the optimum for all of these parameters.

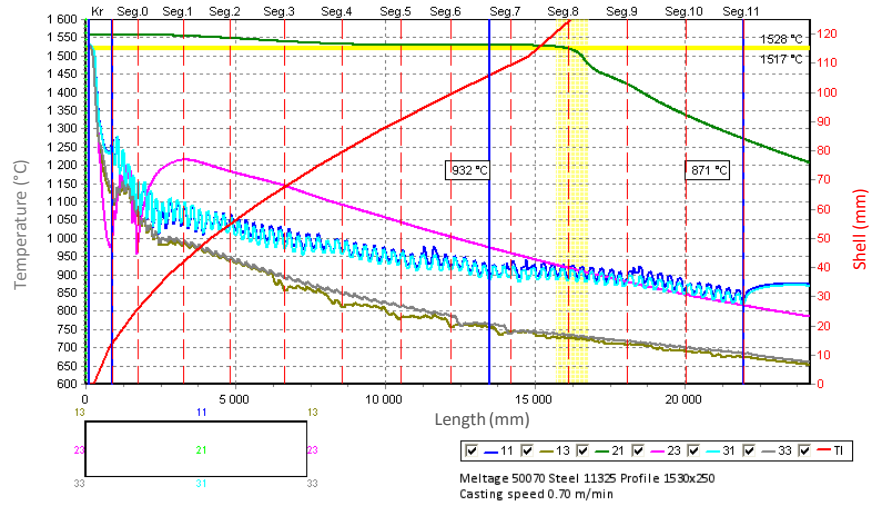

a) Casting speed 0.7 m·min^{-1}

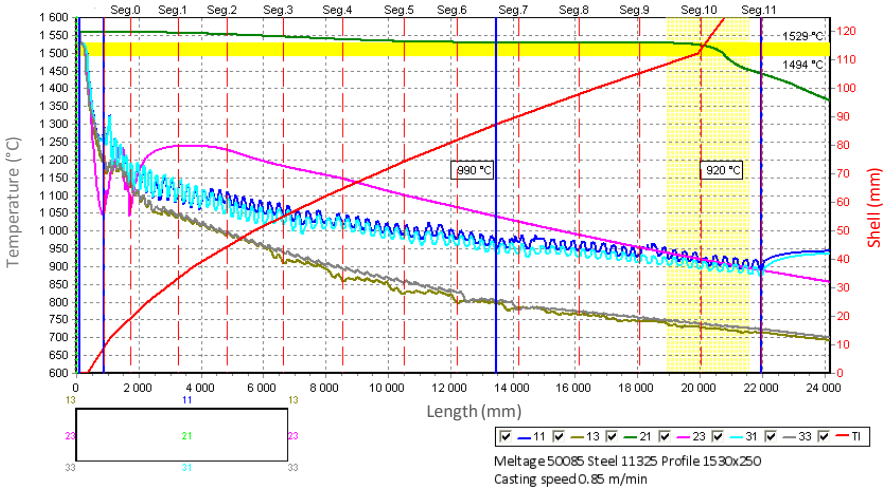

b) Casting speed 0.85 m·min^{-1}

Fig. 5-10 Comparison of the temperature fields for various casting speeds, superheating 30 °C (temperatures 832 °C, 871 °C, 990 °C, 920 °C - measured by the pyrometers)

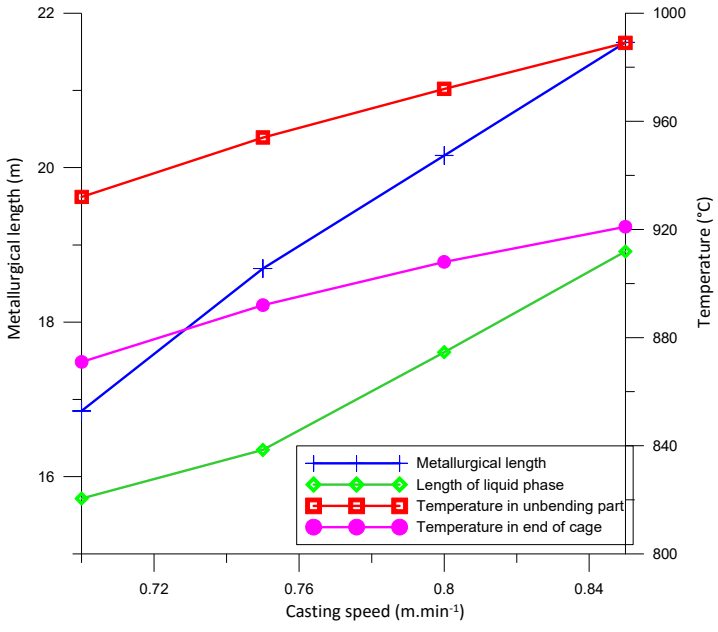

Fig. 5-11 Effect of the casting speed on the selected parameters, superheating 30 °C

5.4.3 The influence of the superheating temperature (11325 class steel)

The casting temperature must always be higher than the temperature of the liquidus, in order to ensure sufficient transport of liquid steel through the casting nozzle. From the operation point of view, it is desirable to increase the casting speed when the superheating temperature is lower in order to empty the tundish. **Figure 5-12** summarise information on the input parameter. They show how the level of the superheating of the melt above the temperature of the liquidus influences the metallurgical length. The lower the superheating, the shorter the metallurgical length – this enables the introduction of a higher casting speed.

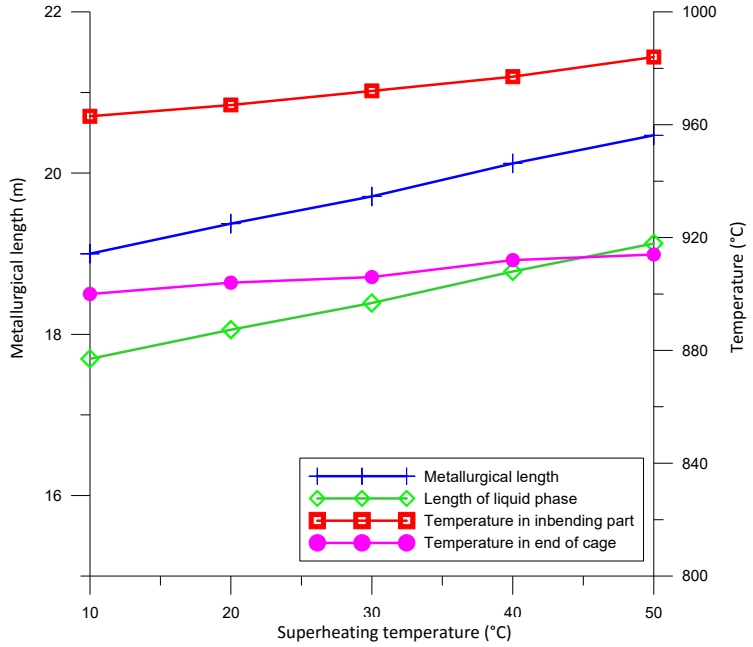

Fig. 5-12 Influence of the superheating temperature, 11325 class steel, speed 0.8 m·min^{-1}

This finding is in accordance with the requirement for ensuring timely emptying of the tundish. Calculations proved that the effect of the superheating on the surface temperatures is limited.

5.4.4 The influence of the slab thickness

On some casters it is possible to alter the thickness of the slab when the width 1 500 mm is constant. The mould of the CCM in question can be set to three different slab thicknesses i.e. 145, 180 and 250 mm (**Fig. 5-13a,b,c**). In this study, the calculations have been carried out for the same class of steel and superheating temperature. However, the casting speed and cooling mode are set to the usual values for each profile because there is no sense in calculations using the same speed and cooling.

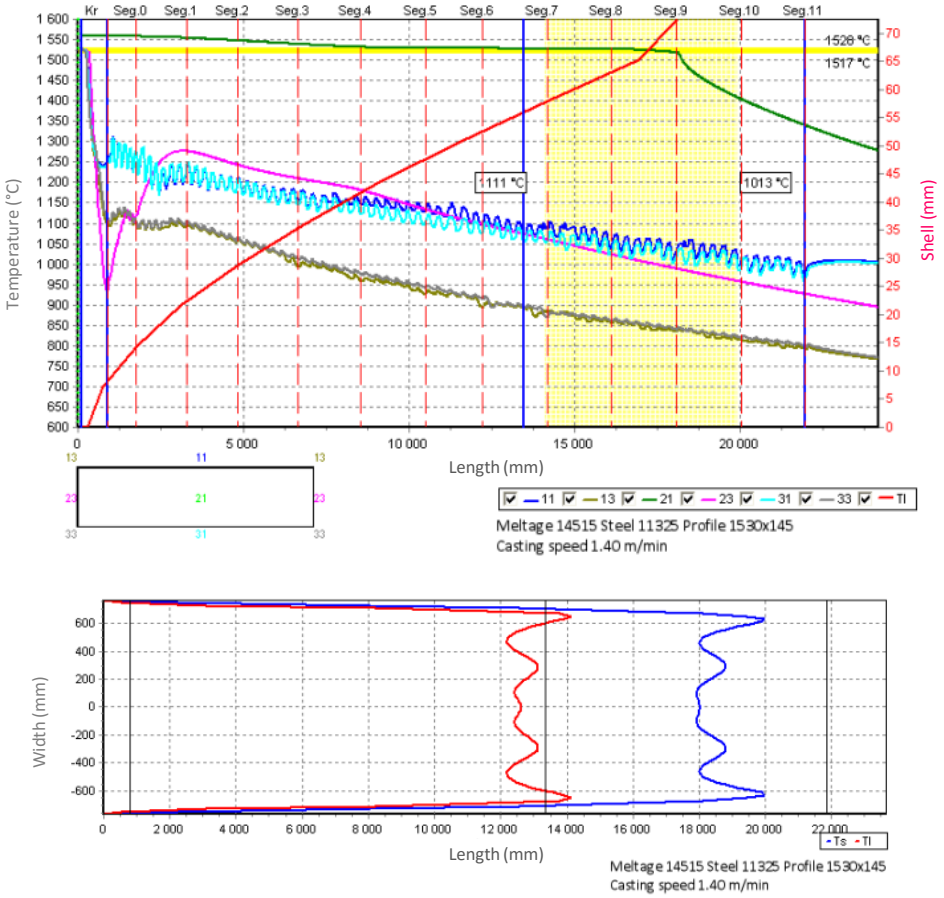

a) thickness 145 mm (temperatures 1 111°, 1 013 °C - measured by the pyrometers)

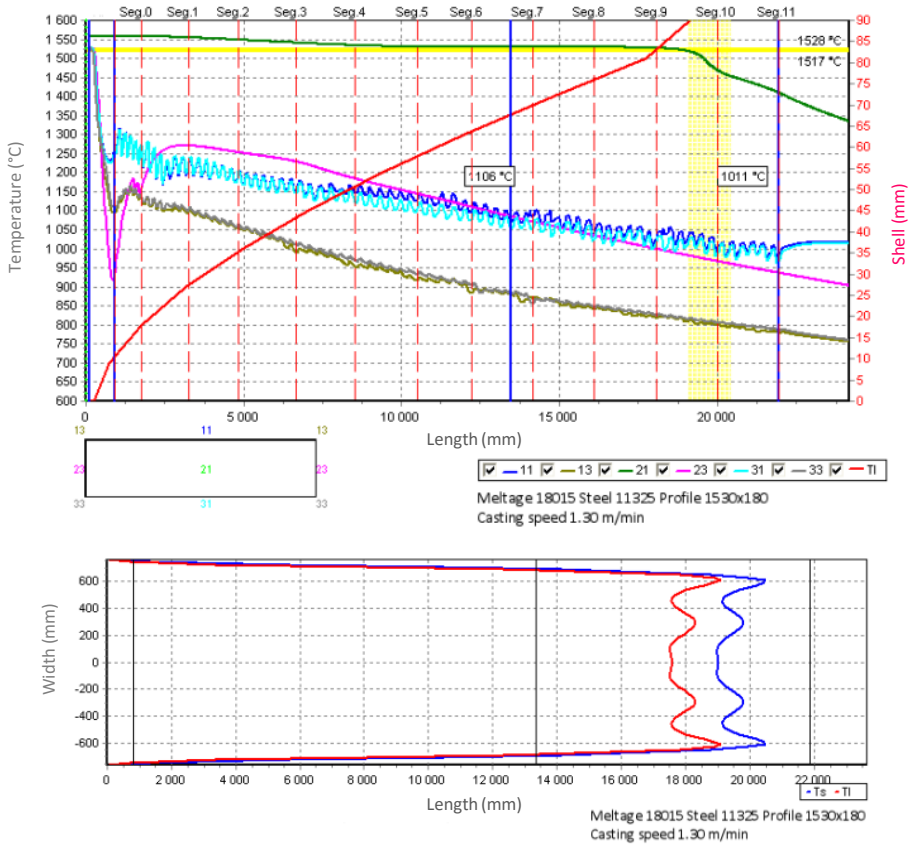

b) thickness 180 mm (temperatures 1 106°, 1 011 °C - measured by the pyrometers)

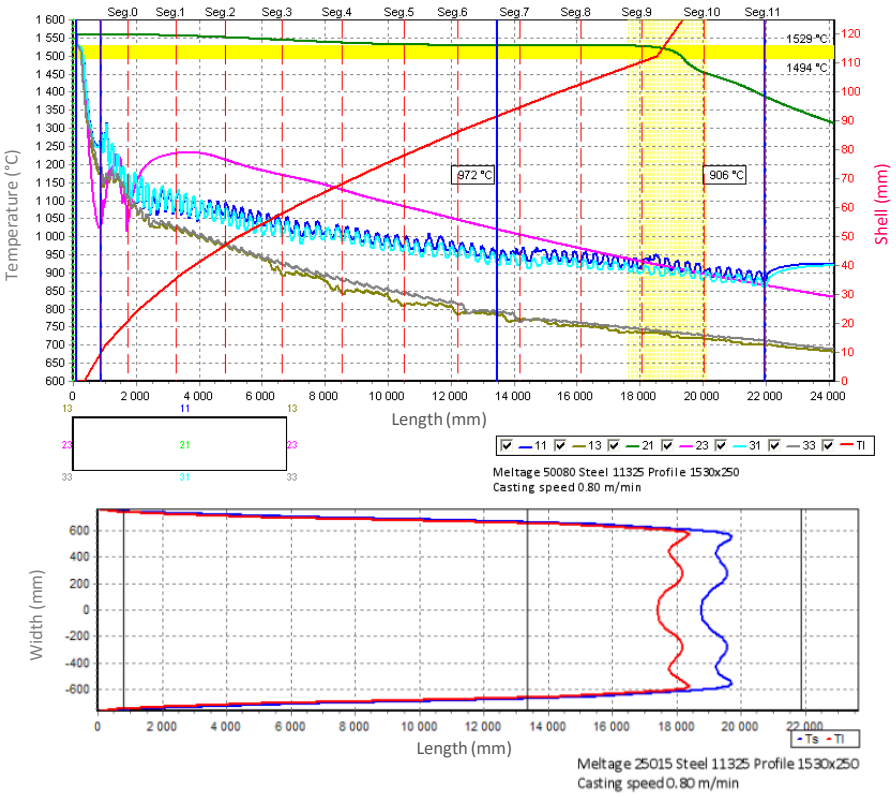

c) thickness 250 mm (temperatures 9 720°, 9 060 °C - measured by the pyrometers)

Fig. 5-13 Temperature field for the slab thickness 145 to 250 mm

5.4.5 Importance of the off-line model

Off-line model analyses the temperature field of the actual concasting while it passes through the primary-, secondary- and tertiary-cooling zone, i.e. through the entire caster, as well as through the most important – or problematic – parts of the caster. Simultaneously, this enables the analysis of the temperature field of the mould and, therefore, the optimisation of its operational parameters, such as cooling, oscillations and the casting flux used. The numerical model fully considers the non-linearity of the task, i.e. the dependence of the thermophysical properties, especially of the concasting material and the mould on the temperature, as it does the dependence of the boundary conditions on surface temperature and other influences (shift rate, cooling intensity, etc.). The numerical model is equipped with an interactive graphics environment for facilitated entry of the input parameters with the successive automatic generation of the mesh (i.e. pre-processing), as well as modern graphics output that displays the temperature field using contour lines in the various sections, time curves, etc. (i.e. post-processing). The software, based on this model must be user-friendly and it is possible to change the parameters by the trained steelworks staff. In this way it is ready for immediate application in the appropriate offices as an off-line system.

The model is fully functional and accurately conducts general analyses of the influences of the various technological measures on the formation of the temperature field of the entire concasting. In a similar way, it helps the staff to analyse the failure state of the caster. Furthermore, it enables the user to design even a non-traditional file or combination of technological interventions for the optimal formation of the temperature field with the aim of enhancing the quality of the concasting while maintaining or even raising the volume of production. The results of this analysis and the corresponding optimisation measures are confronted with experimental results and the achieved quality of the semi-finished product. A comparison of several designed variants of technological measures could provide solutions to possible problems. A disadvantage of the off-line system is mainly a considerable delay – from the occurrence of the failure to the identification of the cause and the corrective action – and the tedious process of obtaining input data for computation [L5-5 and 5-6].

5.5 An on-line (dynamic) model of a temperature field of the concast steel slab

If a manufacturer wishes to remain competitive in the field of concasting, they must continue to introduce and enhance the control of casters. Improved monitoring and control increase the quality of steel and meet the needs of customers in terms of dimensions, brands, quantity and qualities of prefabricated products at lower costs. As in other areas, an important tool in this effort is a set of computer models that are used for on-line prediction and process control. They introduce flexibility to the process in that they give the operator the possibility of changing the casting speed while maintaining the important process parameters (e.g. the surface temperature of the slab and the end of the solidification cone) within the required limits. Such a possibility in the control of a process brings improved evenness of the properties of the cast material during the course of the entire process. The off-line version of this dynamic model makes it possible to look into the variable behavior of the process quantities and parameters and understand the casting process in greater detail. The presented on-line model for a slab caster is original [L5-3 and 5-7].

A temperature model can be considered successfully implemented if it integrated into the existing information and control systems of a caster. **Figure 5-14** illustrates a specific case of integration of models into the casting technology control system of a caster for the casting of steel and the quality system for slab casting at VÍTKOVICE STEEL, a.s. The caster control room is equipped with a two-processor workstation where the on-line dynamic model is running nonstop and which receives data from the 1st and 2nd levels of control via an interface program. The input data are verified, the erroneous data being filtered out and the temperature field is calculated. On the computer monitor, the operator can select from the various forms of output. According to the results, the on-line model makes recommendations for the operator in order to facilitate the control of the concasting process. The computer in question is simultaneously a web server and therefore the technologists and other users of the steelworks web can observe all of the data coming from the on-line temperature model. The results from the calculated temperature field of the concasting of each melt are stored on an archive server for a period of six months.

All filtered input data and their relevant aggregated quantities pertaining to the temperature field are stored into the database of an application server, where they are re-calculated for a specific slab and linked to the information on the quality of the slab and, successively, the quality of the sheet steel produced from this slab. The data from the application server are then passed on to the prediction system.

The users (i.e. technologists) can record the real-time data from the on-line model into their off-line model of the temperature field, carry out any necessary changes in the input parameters (e.g. to alter the secondary cooling or the casting speed). After simulation on the off-line model, it is possible to determine how the temperature field changes after carrying out these changes. Another application of the off-line version is in the occurrence of defects on/in the actual slab or sheet steel. The user can read the temperature field from the archive server using the dynamic model and – using the off-line model – analyse any likely causes of defects and prepare the necessary measures for the defects never to occur again. The off-line model will (in future) enable the reading of quantities and their dependences from the application server and, using statistical methods and the relationships among these quantities and defects, will look for the cause in the original temperature field of the concasting from a specific melt. This however will be the task of the mathematical-stochastic prediction model.

The dynamic model therefore recommends the input casting parameters. That is why it must contain the basic rules – limitations – always for the dimensions of a specific slab. For example, the casting of a 1 530 × 250 mm slab must keep within the following rules:

- **Casting speed:**
  - Technological range: 0.5–1.0 $m \cdot min^{-1}$.
  - Most frequently used range: 0.7–0.85 $m \cdot min^{-1}$ (for which the existing cooling is designed).
  - The optimum value from the quality viewpoint: 0.75 $m \cdot min^{-1}$.
  - From the production output point of view as high as possible, limited by the metallurgical length.
  - Must respect the superheating temperature and the quantity of steel in the tundish.

- **Metallurgical length:**
  - Direct proportionality applies: the higher the speed, longer the metallurgical length.
  - Acceptable values lie between the unbending point and the end of the cage (i.e. 13–22 m).
  - Optimum value approximately 20 m.
- **Secondary cooling:**
  - Surface temperatures should have a constantly decreasing tendency – i.e. the temperature at the end of each cooling section of the relevant circuit should always be lower than at the beginning.
  - The temperatures at the end of the cage (22 m) should never fall below 800 °C.
  - At the unbending point, the surface temperatures should be within the interval 900–1 050 °C (the higher the temperature the better).
  - The reheating (i.e. the local increase in temperature between the jets) should not exceed 120 °C.
  - The maximum flow of water through individual circuits is limited by the powers of the pumps.

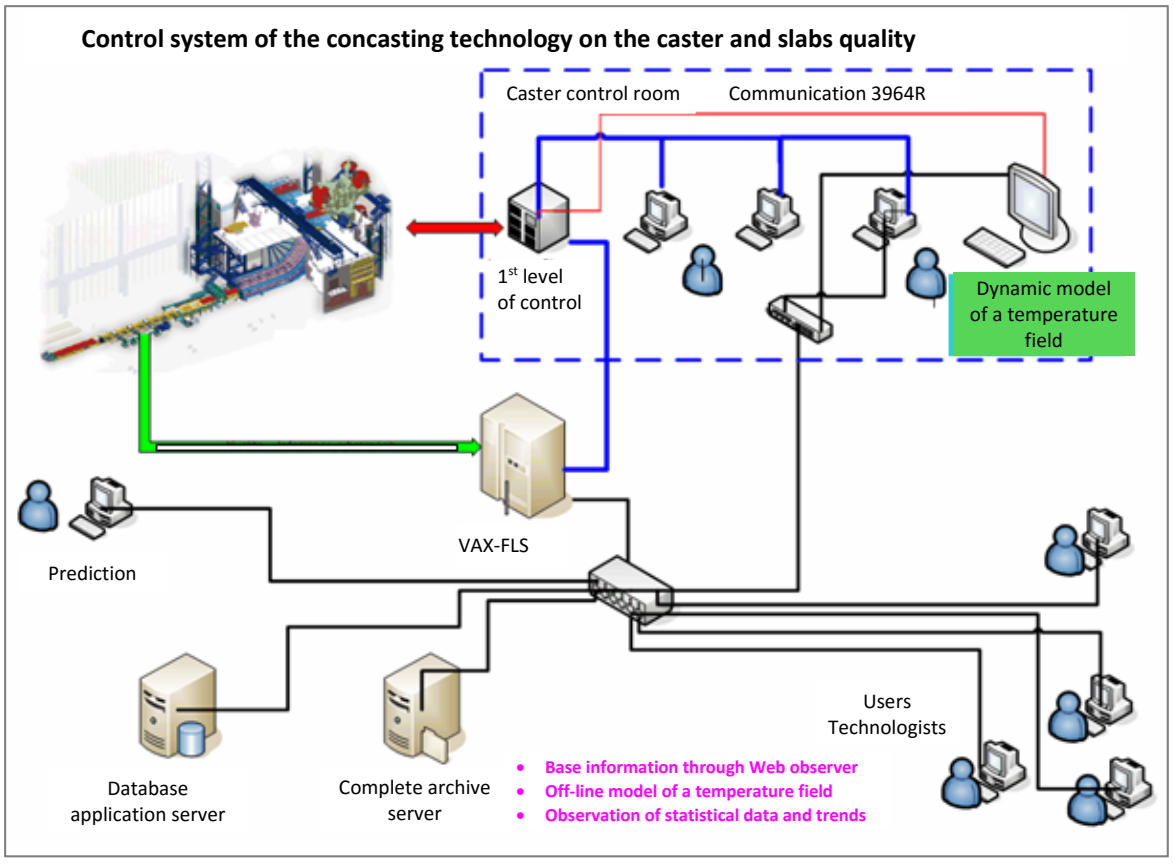

Fig. 5-14 The casting technology control system

Based on these rules and parametric studies, it is possible to split the problem of the control of the casting parameters into two separate parts:

- The control of the casting speed according to the superheating temperature and the actual (calculated) metallurgical length.
- The control of the water flow according to the required surface temperatures as in **Fig. 5-15**, where the courses of the cooling curves (**Fig. 5-16**) are used. The set of cooling curves was proposed and optimized using the off-line model.

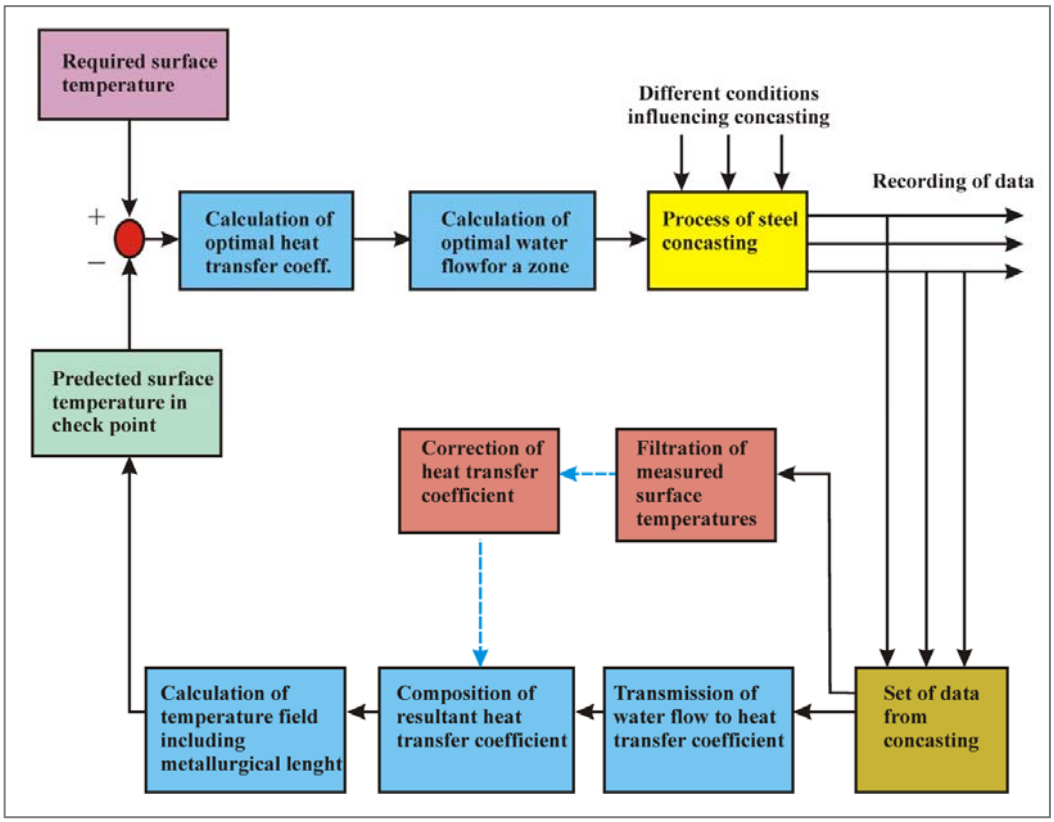

Fig. 5-15 Dynamic control of the secondary cooling

The dynamic model does not control the water flow in the individual circuits directly, but only recommends the operator to switch to another cooling curve. Here, the model is tuned according to the measured surface temperatures with the aid of pyrometers in two places of the caster (**Fig. 5-15**). Both pyrometers measure the upper surface of the slab. The first pyrometer is positioned very close to the unbending point. Originally, it served as a reference for checking the function of the secondary cooling. The value given by this pyrometer now serves for the comparison of the temperatures calculated by the model with the actually measured ones. The measured temperature must be higher than the prescribed (i.e. a concasting which is too cold must not be unbent). On the other hand, the temperatures measured upon output from the cage by the second pyrometer should be lower than those prescribed in the technological procedure.

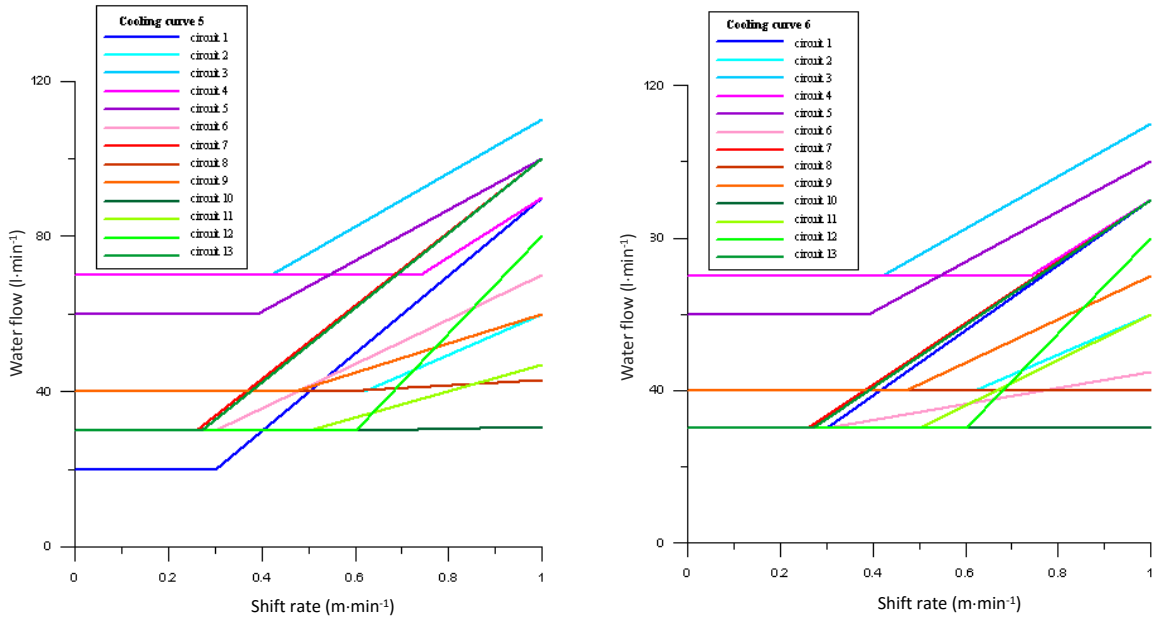

Fig. 5-16 Cooling curves of the 1 530 × 250 mm slab

This approach is possible due to the fact that changes in the casting speed within the range 0.75 to 0.82 m·min^{-1} during normal casting are very small and therefore the dynamic model controls the process and predicts it. This example when there is a change in the casting speed as a result of an intervention by the breakout system, a change in the casting speed while changing the tundish in an uninterrupted casting process or a failure in any circuit of the secondary cooling.

Figure 5-17 illustrates a testing case of a step change in the casting speed from 0.8 to 0.5 m·min^{-1} and back. Such step decreases in speed can be caused by an intervention of the breakout system, the return to the original speed in reality happens more slowly and it the dynamic model that makes it possible to find the optimal method for controlling the speed and secondary cooling.

Figures 5-18 and 5-19 show the output from a simulation of a failure in the secondary cooling (e.g. of the pumps in circuits 8 and 9) using the dynamic model on the analysis of the functioning of the secondary cooling. If there had really been such a failure, the temperature model would have warned the operator in time for him/her to decide what action to take.

Figure 5-20 shows the quantities from a real melt (#20577) and the data from the dynamic model. Towards the end of the casting process there is an increase in the casting speed as a result of a reduction in the superheating temperature.

Figure 5-21 shows an example of real data from the dynamic model of a 1 530 ×180 mm slab upon the intervention of the breakout system. This intervention brought about a drop in the casting speed from 1.22 to 0.5 m·min^{-1} and an increase back to the original value.

It is interesting to observe the course of the measured temperatures in the unbending point and at the end of the cage where the drop in the casting speed is visible. It is quite obvious that the calculated temperature history will facilitate any decision-making by the operator regarding the control of the caster.

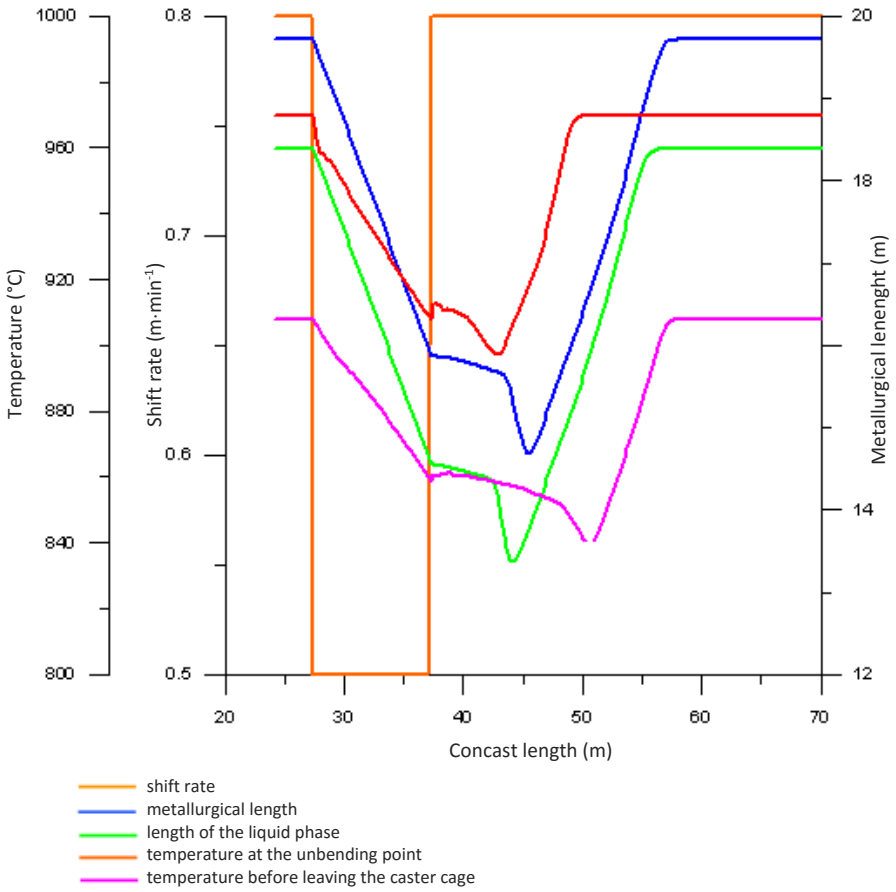

Fig. 5-17 A simulated change in speed and the response of the calculated quantities

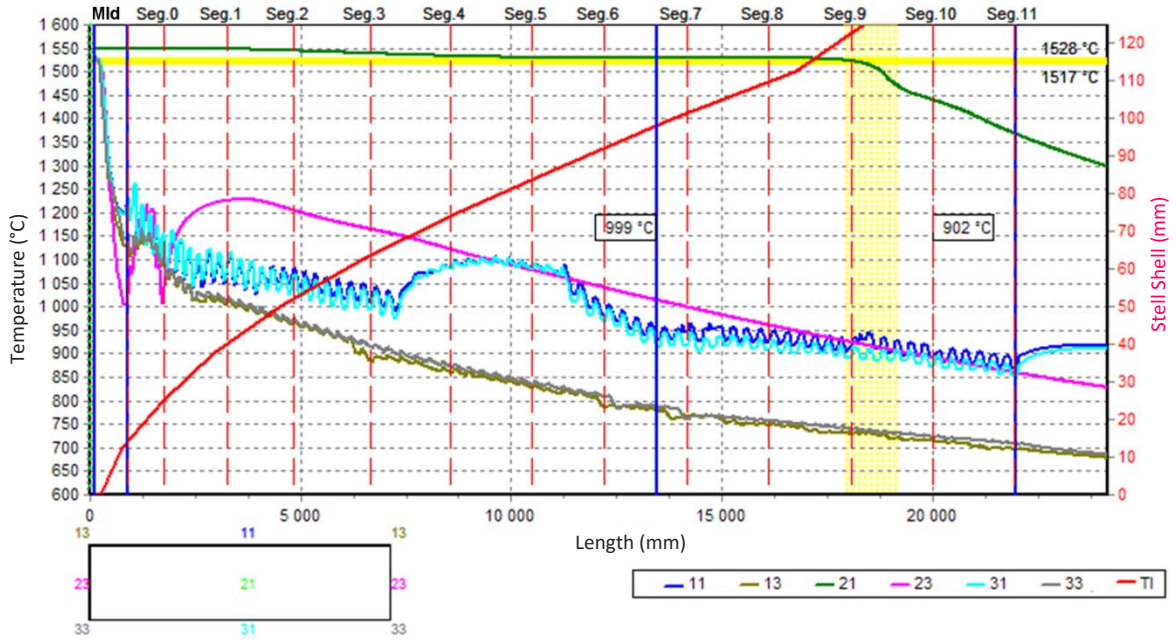

Fig. 5-18 Calculation results from the simulated failure in the secondary cooling incircuits 8 and 9 (temperatures 999° , 902 °C - measured by the pyrometers)

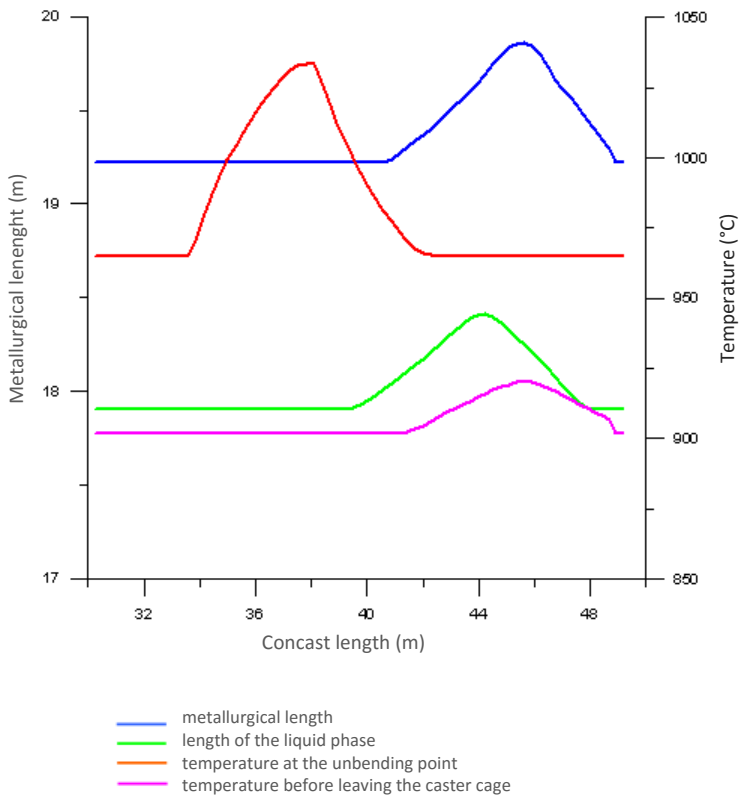

Fig. 5-19 The history of the selected quantities during the simulated failure in the secondary cooling in circuits 8 and 9

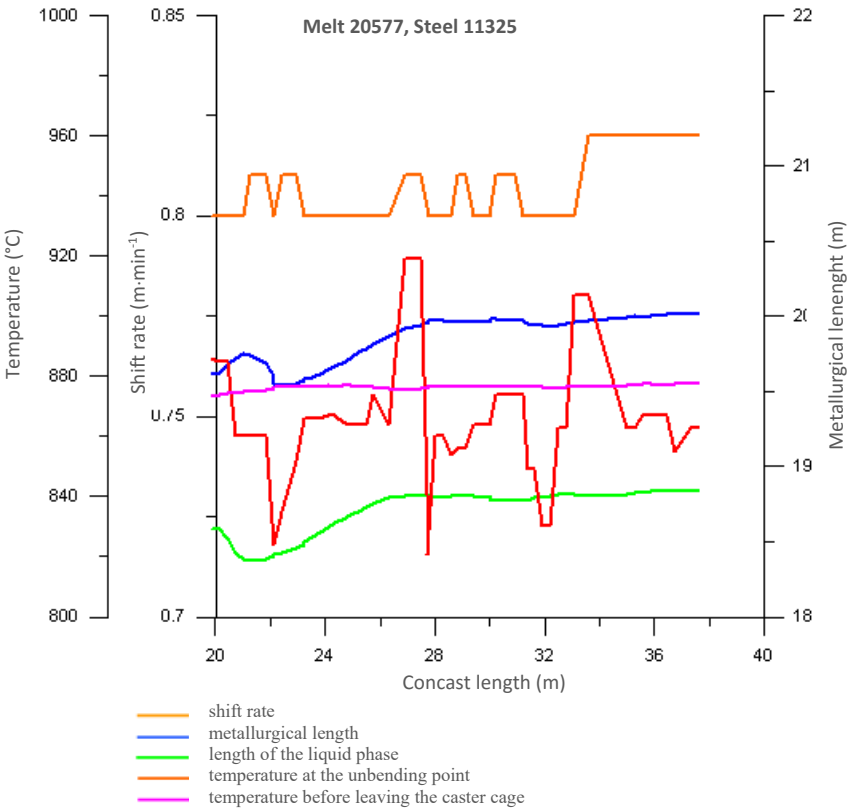

Fig. 5-20 The history of the selected quantities relating to melt #20577

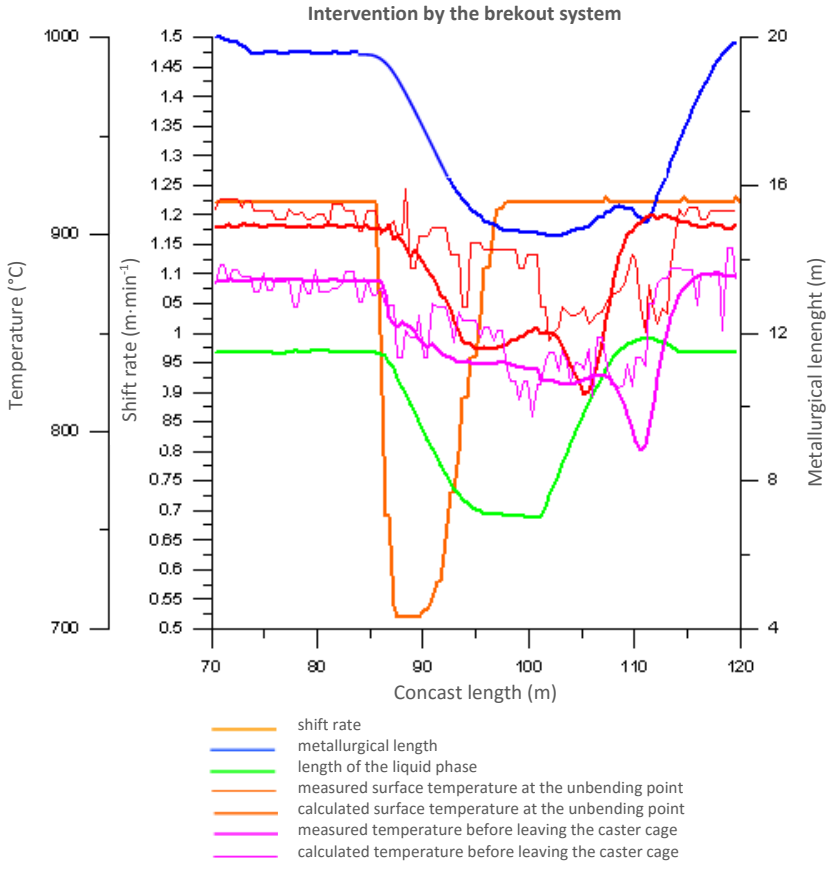

Fig. 5-21 An example of the drop in the casting speed upon the intervention of the breakout system

5.5.1 Importance of the on-line model

The on-line version of the model of the temperature field of a concastig is currently undergoing a non-stop trial run in one operation because steel slabs or billets are produced 24 hours per day. The off-line version will be utilised further – for various analyses within the caster operation, independently of the real melting process, product range, cooling intensity, shift rate, etc.

The on-line model enables a multiple increase in the speed with which the temperature field of the concasting is computed – both with the application of more sophisticated software as well as hardware. As a result of this, it will be possible to monitor the formation of the temperature field – in real time – within the mould, the secondary- and maybe even the tertiary-cooling zones, and also to utilise this information for the optimisation of the control of the caster as a whole as well as its individual parts. Furthermore, it can be used in the re-design (modernisation) of the actual caster or the range of its products [L5-8 and 5-9].

The model adjusts the caster parameters (especially the shift rate, the oscillations of the mould, the cooling of the mould, the cooling intensity of the cooling jets) according to the real time data acquired and the calculated values.

Furthermore, the system enables the archiving of the calculations of the real melts (depending on the size of the data storage) and their potential traceability. With melts where there are defects, it will be possible to re-play their history, simulate them again with the off-line system and to propose certain technological measures (e.g. a change in the shift rate or the spraying plan) in order for these defects not to recur in the future melts.

Another capability of the on-line system is the raised quality and the accuracy of the input data, their mutual connections and qualitative parameters, including the setting of the limit values. This creates a system, which, not only quickly but also very accurately, displays the actual temperature field of the concasting during the process, including all necessary technological data concerning the caster.

The basic condition for the successful running of the system is the suitable hardware and its optimal connection to the existing information system of the caster as well as the connection to the lowest control level of the caster. The functioning of the on-line model of the temperature field is conditioned by the availability of the following on-line input data, as is in the case of billet casting: the pouring temperature, the dimensions of the concasting, the chemical composition of the poured steel, the shift rate, the position of the level within the mould, the temperatures within the walls of the mould, the oscillations of the mould, the temperature difference on the entry and output of cooling water within the mould, the flow of water through the mould, the pressure of the water through the secondary-cooling zone, the temperature from the pyrometers within the secondary-cooling zone.

This data is passed on to the temperature field model through a newly developed interface programme designed in accordance with industrial standards such as SQL and OPC. It is not suitable for the temperature model to read the data from the technology directly, because the technology is heterogeneous and there are possible changes that would always require a change in the software of the temperature model. The interface programme is based on object-oriented technology, which enables, through various models, to solve the connections to various technologies and, simultaneously, communicates with the temperature model via standard objects.

The values are obtained at various time intervals. However, in order for this data to be processable further, it is necessary for the communication programme to be able to:

- Eliminate all irregular values using filters for all quantities, which would find out whether the value of the quantity is valid, i.e. whether it lies within the given interval.
- Interpolate these points and establish continuous functions for each quantity.
- Establish a common time base.
- Read the interpolated value of the function of each relevant quantity within each (equal) time step.

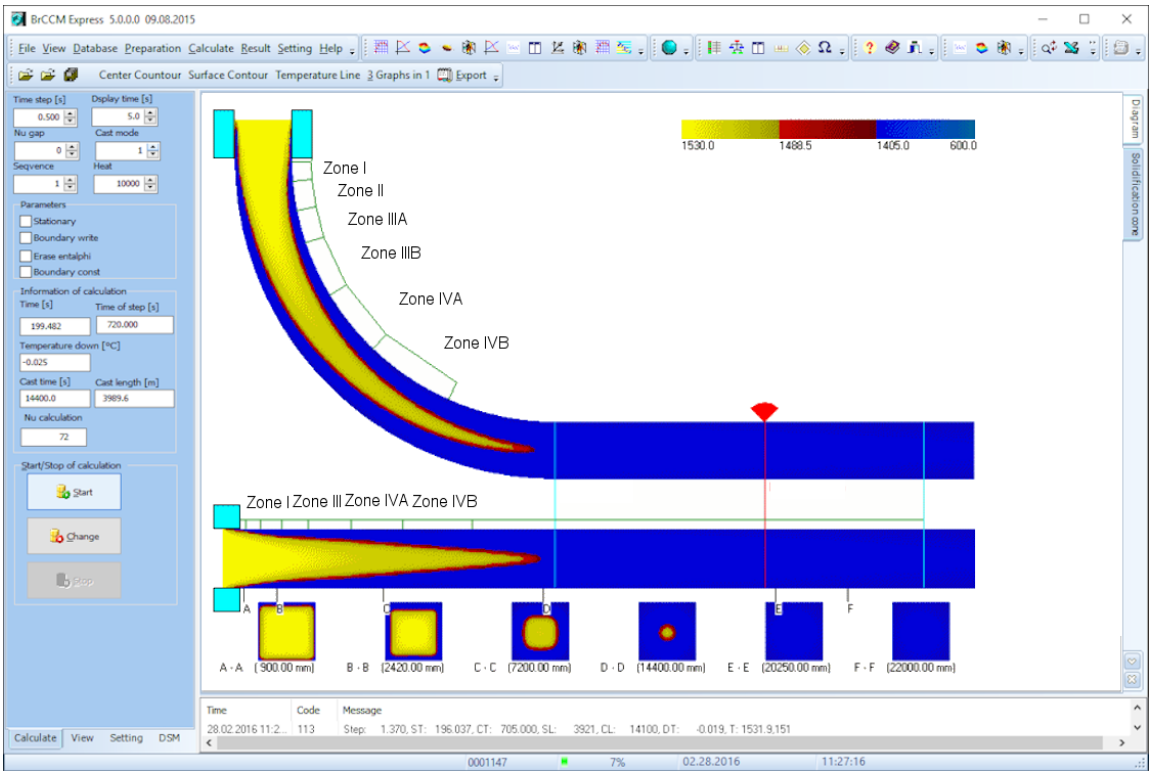

Figure 5-22 The main screen of the dynamic solidification model

The basic evaluated parameters are: the courses of the surface temperatures along the length of the caster, the thickness of the shell while it passes through the caster, the length and shape of the liquid centre of the concasting, the course of the iso-solidus and iso-liquidus lines along the caster, the distributions of temperatures – the temperature field – in an arbitrary cross-section and moment in time. For example **Fig. 5-22** shows the main screen of the on-line model of a billet caster.

The on-line model will automatically set the technological parameters of the casting process in order to achieve the required quality of the cast steel.

5.6 Experimental measurement for the application of the model of the temperature field of a steel slab 1 530 × 250 mm

The successful application of a numerical model (for example of a steel slab) and its continuous improvement is necessarily conditioned by carrying out demanding experiments and their evaluation [L5-1 and 5-10]. The measured parameters serve either as direct input data for the numerical model or they are used for the creation of this input data. This is, for example, the case of determining the heat transfer coefficients beneath the cooling jets that has to be carried out in the laboratory (see below). The range of the measurements carried out and applied was relatively considerable. They can therefore be divided into experimental research carried out on an operational device (caster) and experimental research carried out in laboratory conditions [L5-3]. Research conducted on the operational device comprises permanent monitoring of the necessary physical and technological quantities during the entire process. Some of them are part of a so-called breakout system. This entails relatively extensive files of values containing individual data as well as time records – for example temperature in the walls of the mould, surface temperatures of the slab in the place of the bend, the pouring temperature, the casting speed, the temperature of the cooling water, etc. Furthermore, other experiments were also conducted for the purposes of research. This includes, for example, measurement of the surface temperatures in other places of the secondary-cooling zone (i.e. the cage), after exiting the cage (in the so-called tertiary-cooling zone) [L5-11] and more. Experimental work in the operation is very expensive and complicated even from the organisational standpoint because this must not influence in any way the actual production. It is therefore necessary, for the setting up of the model, to utilise the

quantities that have been measured within the existing caster control system. Due to the volume of data and the variety of the experimental work and its results, the procedure will be discussed only briefly, together with an example of the values measured. The most common measured quantities are the temperature of the steel, the flow of water through the mould and its heating up, the temperatures of the plates of the mould and the surface temperatures in the unbending point.

5.6.1 Measuring temperatures in the mould (crystallizer) and in the secondary-cooling zone

Figure 5-23 illustrates the positions of 44 thermo-couples in two lines along all walls of the mould. The results of these measurements are indicated in **Fig. 5-24**, together with the course of the mean value and distribution, and are entered into the numerical model of the mould.

Figure 5-24 shows an example of real immediate temperatures on the mould. **Figure 5-25** illustrates the temperatures from the breakout system, which uses the dynamic model of the temperature field. The upper part of the diagram shows the temperature map that arises from the measured temperatures and the bottom part shows the so-called floating graph obtained from the upper line of thermocouples in time.

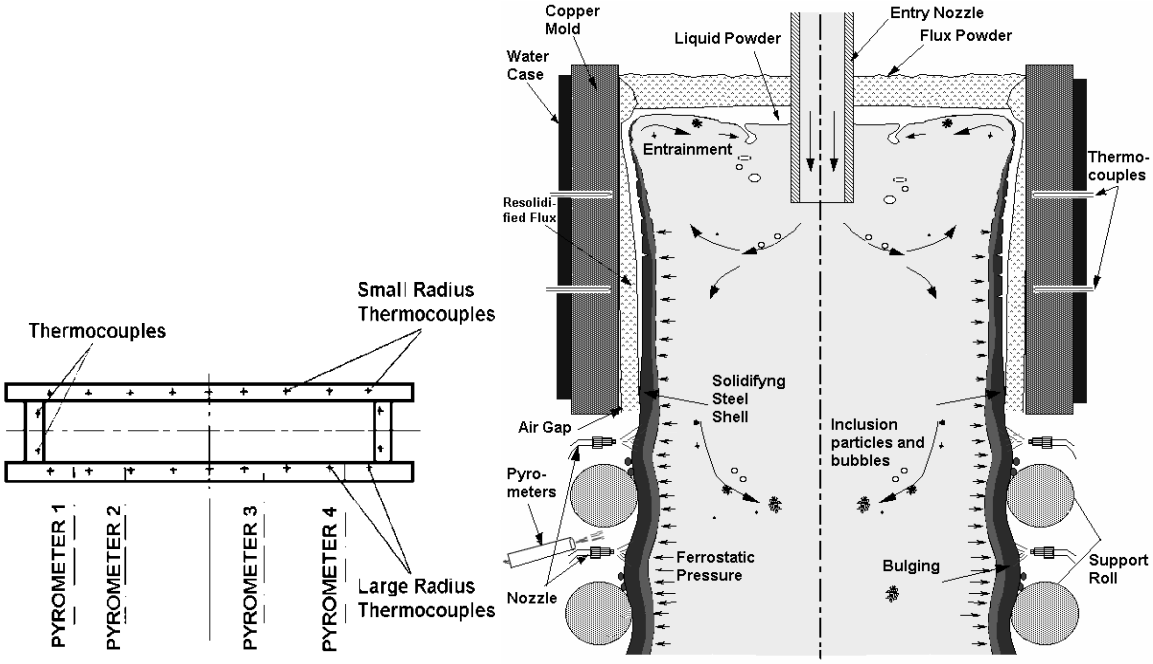

Fig. 5-23 Arrangement of measurement sensors

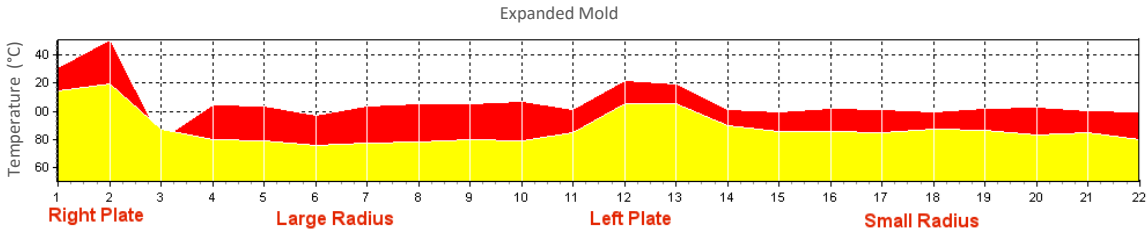

Fig. 5-24 Immediate temperatures of the breakout system (red – upper line, yellow – bottom line)

In order to make the model of the temperature field of the mould more accurate and to verify it, it is useful to carry out experimental measurement of the surface temperatures immediately below the mould, i.e. in the area of the retaining rollers. The measurement is carried out using optical pyrometers

positioned at the centre of the slab, half-way between the centre and the edge and near the corner (**Fig. 5-23**). This measurement also makes it possible to assess whether the temperature field is symmetrical along the axis of the cross-section. **Fig. 5-26** shows the measurement of the surface temperatures along the large radius in the area of the retaining rollers. The graph illustrates that it is necessary to process the data before it is used, i.e. it is necessary to find a suitable method of filtering. The generally used method of filtering is floating averaging. Its disadvantage is that large deviations are spread along a larger area. The median recursive filter brings the strongest filtration – its output is, for example, usable for the regulation of the secondary cooling. It is possible to consider that interference of the signal from the pyrometer is caused by a quality surface of the slab (scales and solidified casting powder). That is why the maximal values provided by the maximum filter are considered as correct.

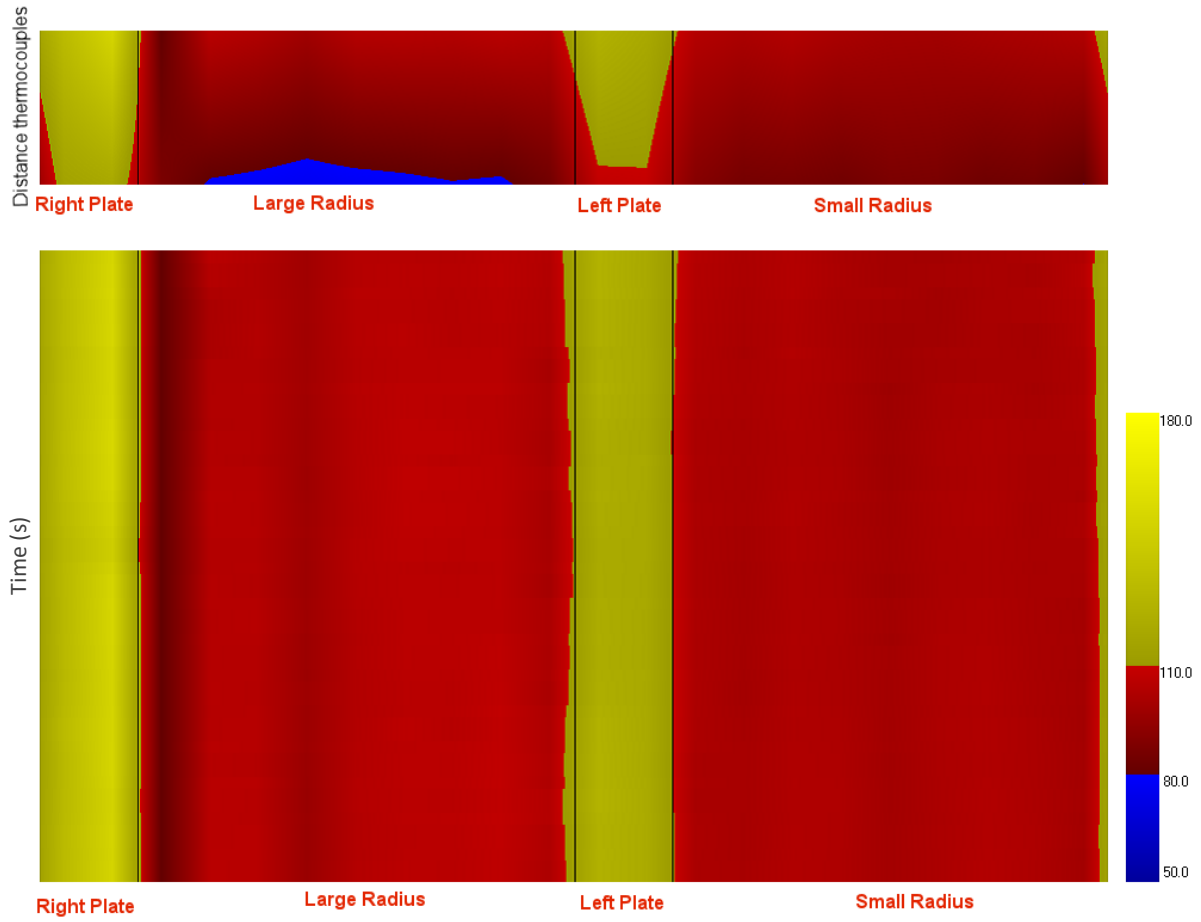

Fig. 5-25 Temperatures in the dynamic model

The course of the temperatures measured immediately below the mould is not symmetrical along the longitudinal axis of the wider wall of the slab. This also means that even the heat released through the walls of the mould is not symmetrical. This is confirmed by the courses of the temperatures recorded by the breakout system, which means that if it was desirable to use the calculated temperature field in the model of the structure formation, i.e. the heterogeneity or in the model of temperature stress and strain, it would be necessary to investigate the entire slab and not only one symmetrical half of the cross-section. The experimental temperatures could be used from the breakout system (and not the data from the pyrometers), which, with respect to the densely arranged thermocouples in two horizontal planes (**Fig. 5-23**) covers the asymmetry better. In order to apply the dynamic model of the temperature field, the investigation of only one half of the slab is sufficient. **Fig. 5-26** illustrates the favourable comparison of temperatures measured by three pyrometers with a calculated curve of the surface temperatures of the slab after 4 000 s.

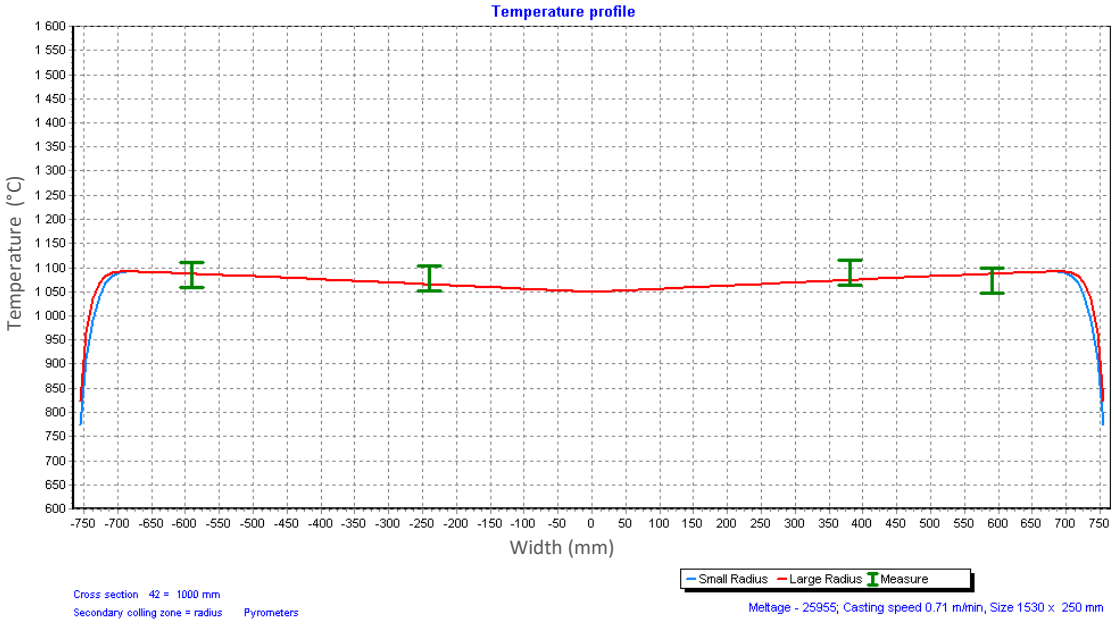

Fig. 5-26 A comparison of the course of the calculated and measured temperatures after 4 000 s

In order to make the model of the temperature field more accurate and to verify it, it was necessary to use two permanently installed pyrometers with both measuring the upper surface of the slab along the small radius. The first was installed by Mannesmann Demag already at the stage of starting up the caster. It is positioned just before the unbending point. This pyrometer was originally used for checking the function of the process secondary cooling. During the integration of the on-line model into the system, it is now used for comparing the temperatures calculated by the model with the real ones. Furthermore, it was joined by another pyrometer of the same type at the exit from the cage. This arrangement of both models also includes a processing unit that filters the measured data. This facilitates their utilisation because the software of the temperature model no longer has to deal with the filtering of the signal. The pyrometers measure within the range from 750 to 1 200 °C and in the case of a measurement failure it shows a temperature of 700 °C. The positioning of the pyrometers in the two mentioned points is necessary for the purposes of checking. The temperature of the slab in the point of the first pyrometer at the beginning of the unbending (point) must be higher than the temperature prescribed for this point (i.e. a slab that is too cold must not be straightened out). On the other hand, the temperature at the exit of the cage should be lower than the prescribed temperature.

5.6.2 Measuring of cooling effect of nozzles

One of the possibilities of how to determine the heat-transfer coefficient beneath the cooling nozzles inside a laboratory [L5-12 and 5-13] is via measurement on a hot plate (**Fig. 5-27**). A steel plate with installed thermocouples is clamped and electrically heated. The plate can be raised to the required horizontal heating position and after achieving the required temperature, the electrical heating element is removed. The space between the heating element and the plate is filled with argon. During the entire heating process, the flow of argon is maintained constant, which prevents degradation of the quality of the surface of the plate. The reason for using an inert gas was to ensure the same conditions for all experiments and to prevent oxides forming on the heating element and plate. The surface of the investigated plate was “rolled” and covered with a layer of oxides formed during spraying. The oxides were removed from the surface before each successive heating but the surface was not polished.

While the experiment is conducted, there is a nozzle with a moving mechanism inserted beneath the plate (the heating element is removed at this stage). During the experiment, the water is pumped through the nozzle from a tank. The air is brought in from the pressure vessel of a compressor. The pressure of the water and air is measured before entering the nozzle. The temperature of the water and the temperature inside the plate are monitored by a data acquisition system. The size of the hot plate is 600 × 320 mm and thickness is 24 mm. The plate contains 18 thermocouples (1.5 mm in diameter, type K).

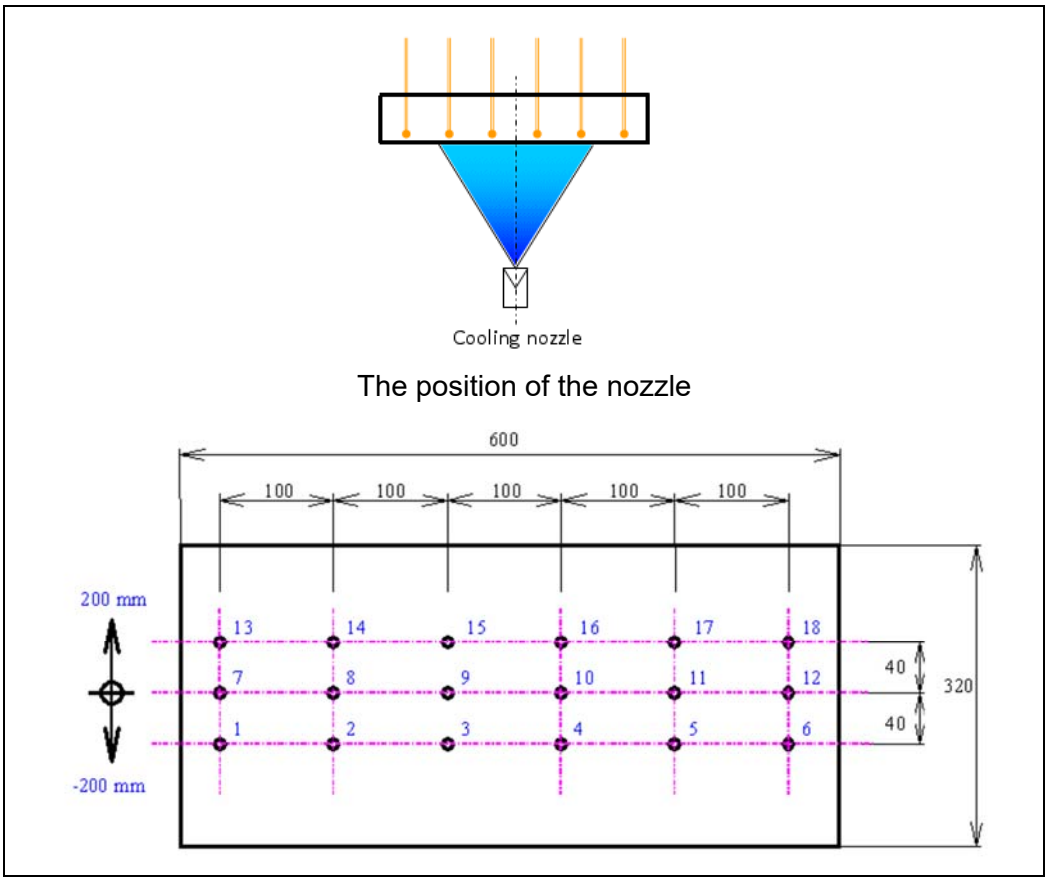

Fig. 5-27 The dimensions of the plate and the positions of the measured points

The set of thermocouples measures the temperature at a depth of 2.5 mm (from the bottom surface which is sprayed). The top surface of the plate is insulated. Water-air nozzles with a flat spray were used for the measurements. The nozzles are positioned on a moving carriage (**Fig. 5-28**).

This makes it possible for the nozzle to move parallel to the plate in the direction of the axis running through for example points 1, 7, 13.

Before the actual measurement, the heating element is inserted beneath the plate and the plate is lowered into the heating position. The heated space is filled with argon (set to a constant flow). The plate is electrically heated up to the prescribed temperature (1 240 °C). The entire process of heating and cooling is monitored by a measurement system. Once the prescribed temperature is reached, the plate is raised, the heating element is removed and the unit with the mechanism the drives the nozzle is set to the cooling position.

Fig. 5-28 The laboratory device in use

After the heating element is replaced by the unit that drives the nozzle, the temperature begins to decrease as a result of radiation and natural convection. When the initial temperature of the experiment is reached, the nozzle begins to spray the plate and the motor that drives the plate starts up. The nozzle moves from the left (position – 200 mm) to the right (position 200 mm) at a speed of 0.8 or 1.3 m·min^{-1}, and in the opposite direction at a speed of 1.6 or 2.6 m·min^{-1}.

The records on the course of the temperature and the information on the position of the nozzle with respect to the plate are stored in digital form. The position of the nozzle is measured using an opto-electronic unit. This data is used as the input information for the inverse task that evaluates the conditions of the heat transfer. The surface temperatures and the heat transfer coefficients are calculated using the inverse task.

A real caster is mounted with four Lechler water-air nozzles and three types of water nozzles. The water nozzles take turns simultaneously with the adaptation of the mould to the given profile. For each slab width (145 mm, 180 mm and 250 mm) there is only one water nozzle mounted. The water-air nozzles in the area of the retaining rollers are mounted in two configurations, i.e. either five nozzles in a row or only four nozzles in a row. Regarding the fact that the caster is operated in only two casting speeds, the experiments were conducted for the casting speed of 0.8 m·min^{-1} and 1.3 m·min^{-1}. Regulation of air pressure has not been considered as yet. Therefore, all experiments had been carried out at an operational pressure of 0.2 MPa. As many as 4 to 8 experiments for various water flows were conducted for each nozzle. The overall number of experiments exceeded 100. All results can therefore not be presented here. This chapter contains only a selection corresponding to the casting profile of 1 530 × 250 mm at a casting speed of 0.8 m·min^{-1}.

For example **Figs. 5-29a,b** present the measured values of the heat transfer coefficients processed by the temperature model software [L5-14]. This entails merely the selection of the results for the limit water flows. For each nozzle configuration, there is a graph of the maximal value of the heat transfer coefficient dependent on the surface temperature, the course of the heat transfer coefficient across and through the centre of the nozzle, the course of the heat transfer coefficient in the direction of motion in the centre of the nozzle and the 3D graph of the heat transfer coefficient beneath the nozzle. These graphs are plotted for a surface temperature of 1 000 °C.

Together with the information on the dependence of the heat transfer coefficients on the temperature of the surface of the slab, it is necessary to remember the so-called Leidenfrost temperature [L5-14]. This is the surface temperature at which the character of the heat transfer changes significantly. A continuous layer of vapour, forming at the surface at high temperatures is disrupted and the heat transfer coefficients leap to higher values. Significantly more intensive drops of the surface temperature while passing under the nozzles also correspond to this state. The graphs indicate that with the water-air nozzles that used on the slab caster the influence, this influence is not so significant and arises usually at temperatures lower than 800 °C, which do not occur within the operating range of the caster.

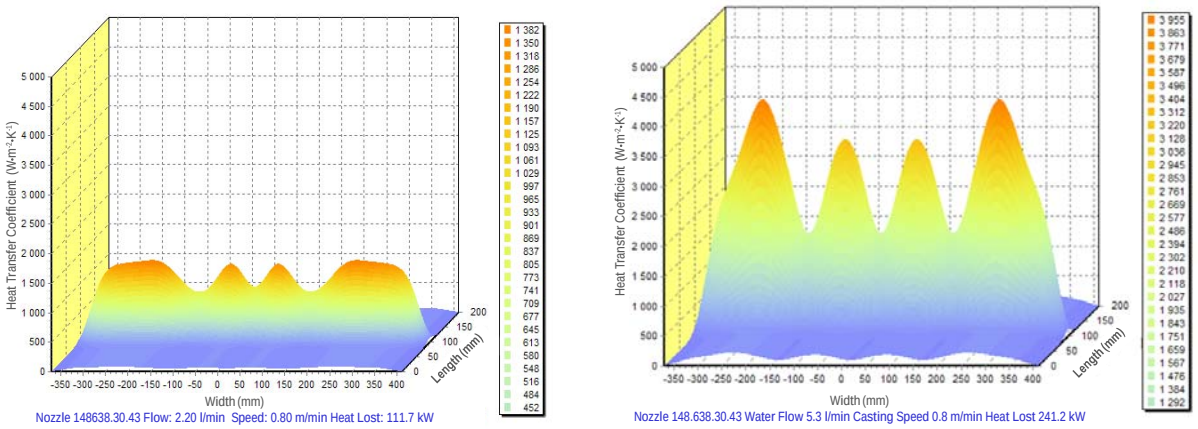

a) Flow through one nozzle at 2.2 l·min^{-1} b) Flow through one nozzle at 5.3 l·min^{-1}

Fig. 5-29 The heat transfer coefficient for the 148.638.30.43 nozzle – 4 nozzles in a row

5.6.3 Measuring of slab surface temperatures in the tertiary cooling zone

Three 2 mm insulated thermocouples had been used for the measurement. The hot end of each thermocouple was fixed inside the hollow tip of a stud, carefully positioned on the surface of the slab after cooling (**Fig. 5-30**) and all were hammered into the same depth during the torch-cutting process. The measurement was initiated on a separated slab, 5-to-6 m from the exit of the cage, and continued until the slab was cold – in the cooling field. The correction of the error of the measurement result, from the heat transfer through the thermocouple insulation and the protruding end, is conducted via comparison measurements (**Fig. 5-30**).

The measured temperatures of three surface points are in **Fig. 5-31**.

5.6.4 Measuring of the metallurgical length

Determining the metallurgical length via the radioisotope method is more demanding (technically, economically, as well as administratively) than temperature measurement using thermocouples or pyrometers.

The determination of the farthest solidifying point – from the level – could be facilitated by contaminating the liquid metal using a radioactive indicator (e.g. a lead body inside a protective casing, enabling its melting at a safe distance from the mould) and its successive revealing using radiograms. This method, however, is not permitted by safety and legislative regulations. A solution is the combination of two indicators:

- A point gamma-radiation source in the geometric centre of a lead body that will not melt and which will be cut out and stored safely in the radioisotope laboratory after the slab is measured.
- Inactive lead bodies for determining how far into the solidification cone they penetrate, using chemical analysis.

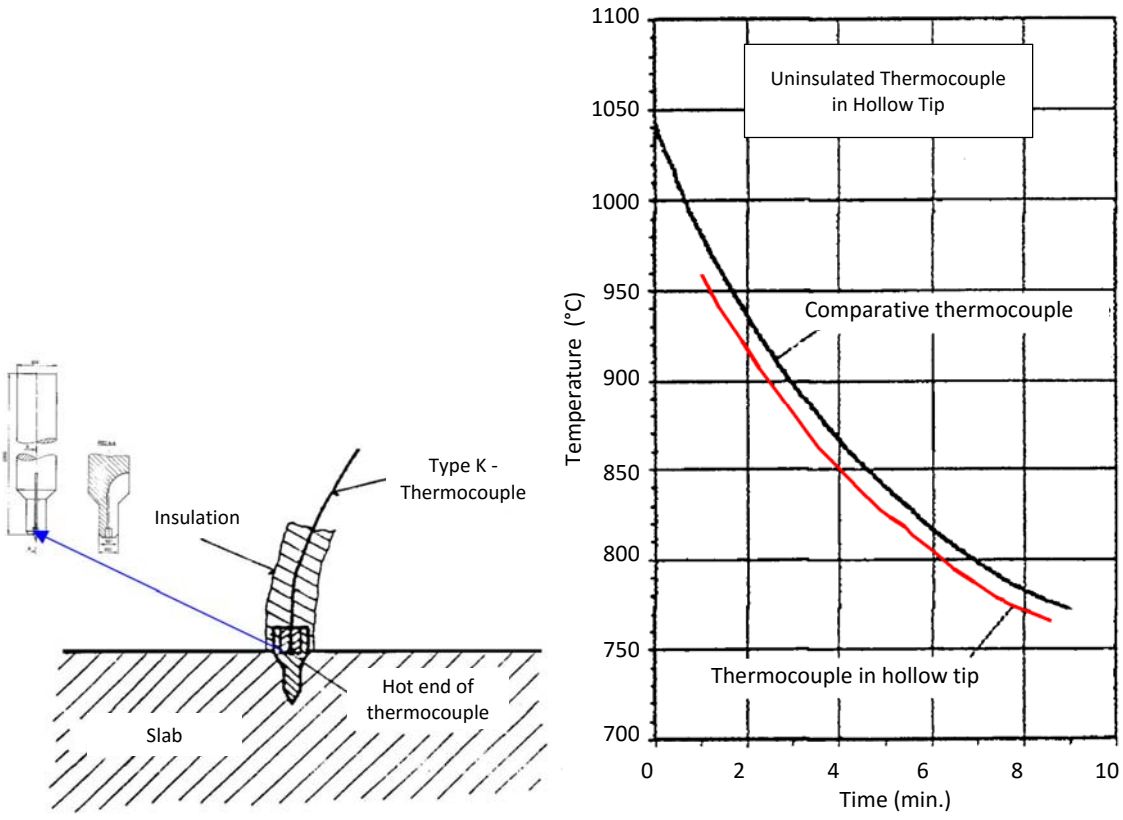

Fig. 5-30 The positioning of the thermocouple for surface measurement

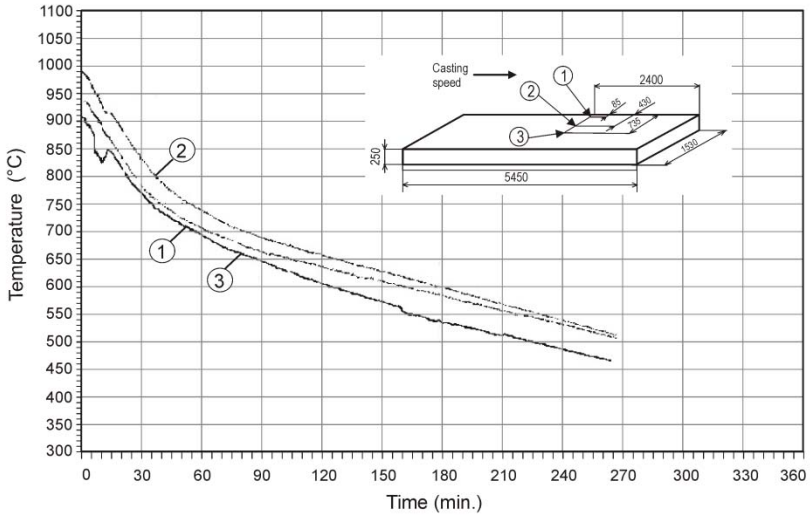

Fig. 5-31 Temperatures of the three surface points

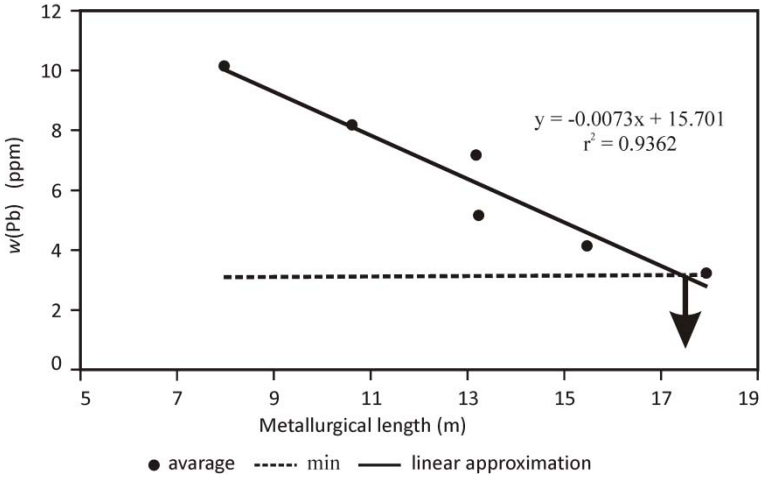

Fig. 5-32 Determining the metallurgical length (graphical extrapolation)

The point sources (low-carbon-content steel cylinders containing the radionuclid Fe 59, 20 MBq, 22 mm long, with diameters of 10 mm) were cast in inactive lead, in the centres of 120 mm cylindrical sheet-metal containers with external diameters of 100 mm.

A total of four attempts were made at measuring the metallurgical length. The first was a trial, in order to overcome problems concerning the detection of the passage of the emitters, i.e. the premature catching of the lead bodies on the dendrites of the shell of the solidifying slab, where the lead does not reach the apex of the solidification cone. The metallurgical length was determined as 17.4 m (**Fig. 5-32**) using mathematical and graphical extrapolation [L5-15]. The calculation revealed that there are really two solidification cones. Experimentation confirmed this fact (see **Fig. 5-6**).

5.7 Experimental measurement for the application of the model of the temperature field of a steel billet 150 × 150 mm

5.7.1 Measuring temperatures in the mould (crystallizer) and in the secondary-cooling zone

It is necessary to tune the model and verify it according to measurement results from a real caster [L5-15]. In this case, the temperature of the wall of a pipe crystallizer and the surface temperatures were measured (using pyrometers) in the secondary- and tertiary-cooling zones (**Fig. 5-33**).

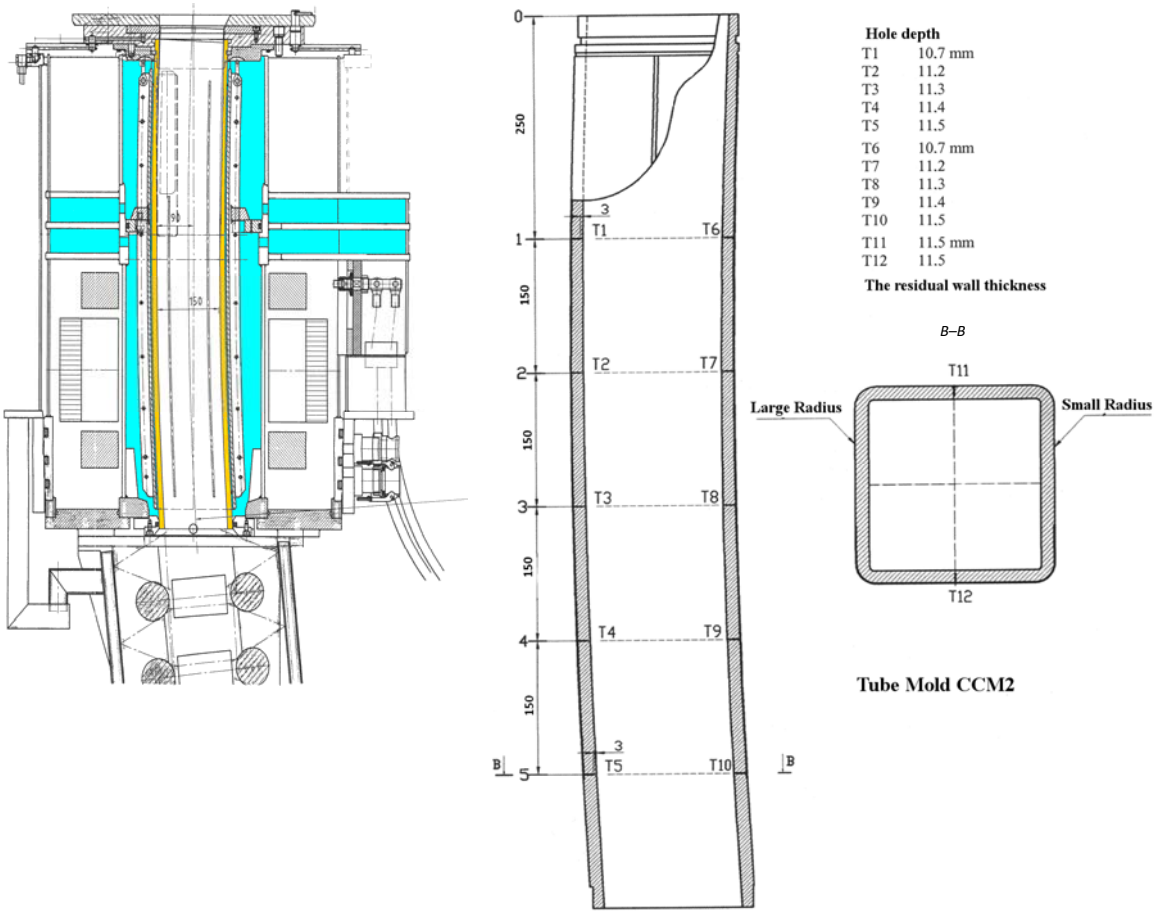

Fig. 5-33 Schema of the pipe crystallizer and thermocouples position

For example the course of temperatures in the wall of the pipe crystallizer is given in the **Fig. 5-34**. **Figure 5-35a** shows the positions of pyrometers in the secondary- and tertiary-cooling zones of the real caster, **Fig. 5-35b** schema of the positions of four pyrometers. **Figure 5-36** brings an example of the temperature history graph.

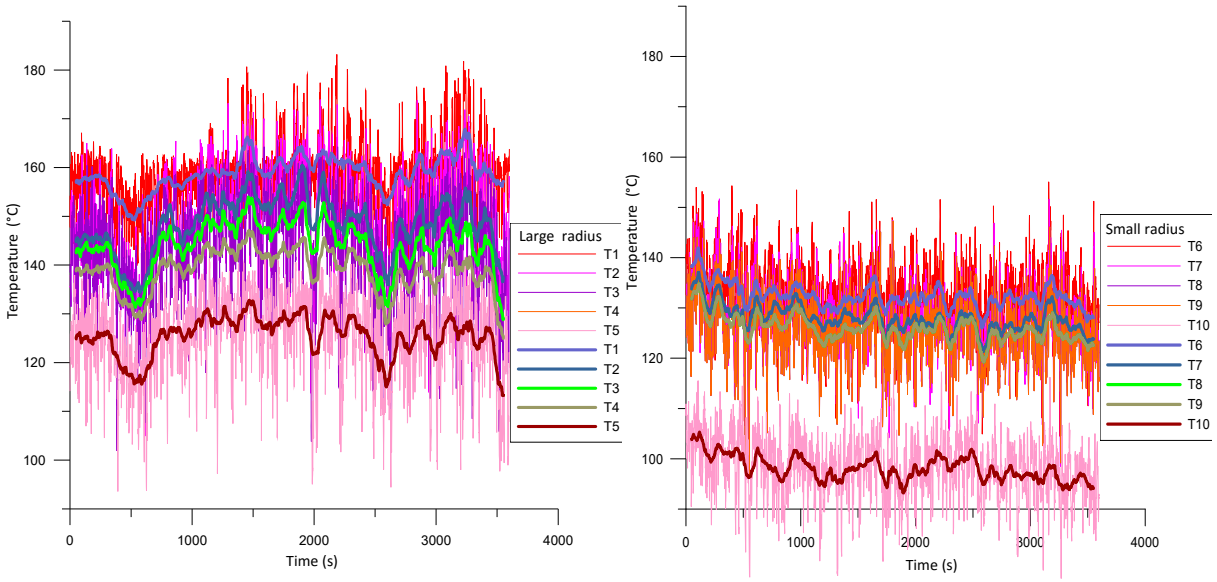

Fig. 5-34 The course of temperatures in the wall of the pipe crystallizer

Fig. 5-35a The place of temperature measurement

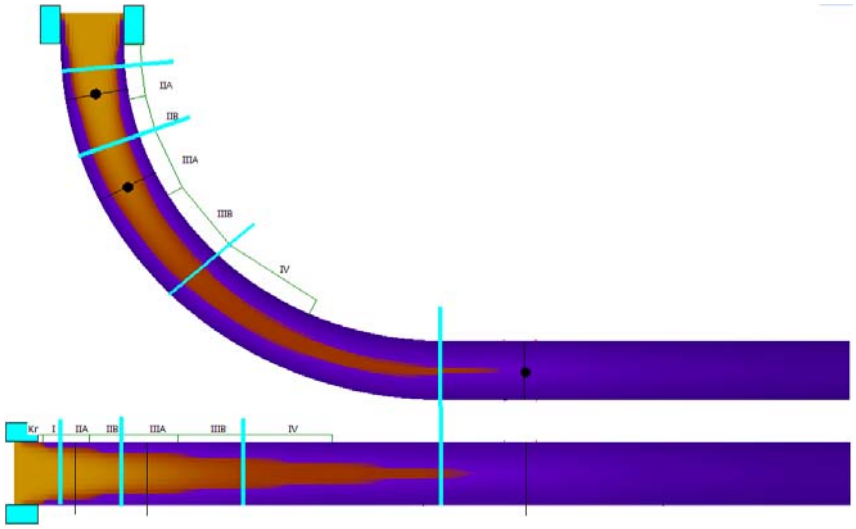

Fig. 5-35b The positions of the pyrometers in the secondary- and tertiary-cooling zones

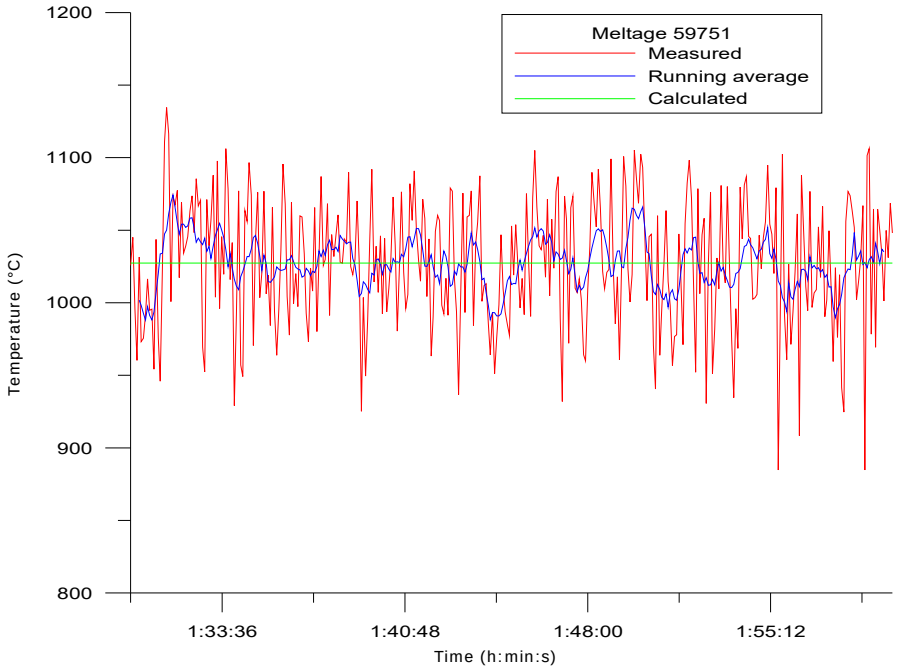

Fig. 5-36 Temperature history graph

5.7.2 Measuring of cooling effect of nozzles

The second most important part of the mould which affects the correct solidification of the billet during pouring are the cooling water-jets positioned inside the secondary-cooling zone. In order for the model to function correctly, it is necessary to determine the correct value of the *htc* underneath the jet. There exist a number of empirical equations for calculating the *htc*, however, these have proven to be inaccurate for the 3D model. Therefore, extensive experimentation had been conducted on a laboratory device simulating the process of solidification within the secondary-cooling zone (**Fig. 5-37** see also **Fig. 5-28**).

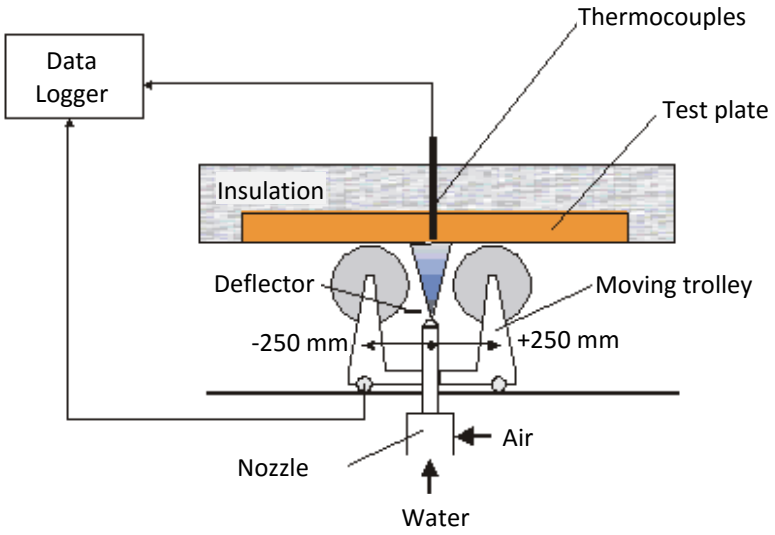

Fig. 5-37 Laboratory device simulating the process of cooling

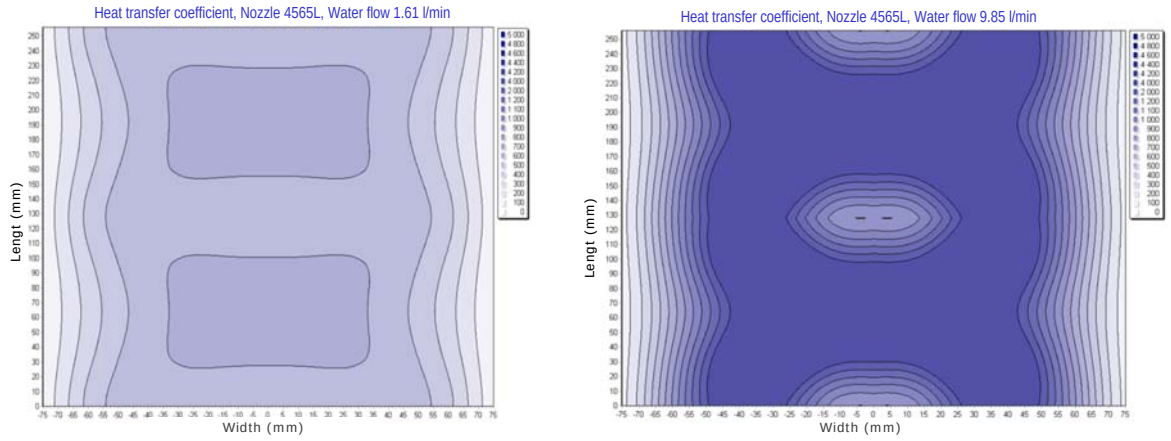

a) Flow through one nozzle at 1.61 l·min^{-1} b) Flow through one nozzle at 9.85 l·min^{-1}

Fig. 5-38 The 2D heat transfer coefficient htc for the 4565L nozzle

The values of the *htc´s* underneath the water jets were obtained via an inverse task which used the temperatures measured in the cooled surface. (The calculated *htc´s* are a function of the surface temperature.) These measurements were conducted for various operation conditions, i.e. the pressure of the water and the shift rate. The numerical model contains a function which, based on the entered water pressure, shift rate, positions of the jet and the surface temperature, calculates the current HTC. For example **Fig. 5-38** shows 2D *htc* for the 4565L nozzle for two flow quantities.

5.7.3 Conclusion

Research into the thermokinetics of solidification and cooling of concast slabs or billets requires systematic experimental measurement on a real caster. Its results are utilised not only for improving

the numerical model, of the temperature field, but also for assessing the exactness of this model. This dynamic model, which works non-stop in real time, ensures continuous correction of the real process of the caster in question. The main measured quantities are the temperature in the walls of the mould, the surface temperatures of the slab upon exit from the mould, at the unbending point of the slab and upon exit from the cage of the secondary cooling. Furthermore, it is the casting temperature, the casting speed, the temperature of the cooling water, the metallurgical length, etc. A specialised laboratory conducts measurements of the spraying characteristics of individual cooling nozzles. Its output establishes the heat transfer coefficients beneath each of the water or water-air nozzles.

The solution has been printed in the peer-reviewed journals and presented at prestigious conferences [L5-16 to 5-31].

5.8 Literature

[L5-1] Brimacombe J. K.: The Challenge of Quality in Continuous Casting Process. *Metallurgical and Materials Trans*, B, Volume 30B (1999), 553–566.

[L5-2] Miettinen J., Louhenkilpi S. and Laine J.: Solidification analysis package IDS. *Proceeding of General COST 512 Workshop on Modelling in Materials Science and Processing*, M.Rappaz and M. Kedro eds., ECSC-EC-EAEC, Brussels, Luxembourg, 1996.

[L5-3] Štětina J.: The dynamic model of the temperature field of concast slab. *Ph.D. Thesis*, Technical University of Ostrava, Czech Republic, 2007.

[L5-4] Štětina J., et al.: The numerical and Experimental investigation of a concasting process, *The Book of Abstracts of the ASME/JSME Thermal Engineering Joint Conference*, Kohala Coast, Hawaii USA, March 2003, p. 103.

[L5-5] Štětina J., et al.: Optimization of a concasting technology via a dynamic solidification model of a slab caster. *Materials Science Forum.* 475-479 (2005) 5, 3831–3834.

[L5-6] Štětina J., et al.: Optimization of technology and control of a slab caster. I. Off-line numerical model of temperature field of a slab and a parametric studies. *Hutnické listy*, 63 (2010) 1, 43–52.

[L5-7] Štětina J.: *Optimization of a billet caster parameters by means of the model of the temperature field*. Associate professorship and habilitation thesis, Technical university of Ostrava, Czech Republic, 2008.

[L5-8] Štětina J., et al.: Operational experiences with the optimization of secondary cooling. *Proceedings of the 8th European continuous casting conference ECCC 2014.* Leoben, Austria: Austrian Societ for Metallurgy and materials (ASMET), 2014, p. 1181–1190.

[L5-9] Štětina J., et al.: New challenges in modelling and secondary cooling control of continuous steel casting. In *METEC&2nd ESTAD 2015 Proceedings*. 1. Dusseldorf Steel Institute VDEh, 2015, p. 1–8 .

[L5-10] Richard R.A., Harding R., Kai Liu and Beckermann Ch.: A transient simulation and dynamic spray cooling control model for continuous steel casting, *Metallurgical and materials transactions*, 34B (2003), 297–306.

[L5-11] Thomas B. G., O'Malley R. J. and Stone D. T.: Measurement of temperature, solidification, and microstructure in a continuous cast thin slab. *Paper presented at Modeling of Casting, Welding and Advanced* Solidification Processes VIII, San Diego, CA, TMS. 1998.

[L5-12] Horský J. and Raudenský M.: Measurement of heat transfer characteristics of secondary cooling in continuous casting. In the Proceedings of the *14th International Metallurgical & Materials Conference METAL 2005*, Hradec nad Moravicí, Czech Republic, May 23-25, 2005, p. 1–8.

[L5-13] Horský J., et al.: Heat Transfer study of secondary cooling in continuous casting, *AISTech 2005*, Iron&Steel technology Conference and exposition, May 2005, Charlotte, USA.

[L5-14] Raudenský M. and Horský J.: Secondary cooling in continuous casting and Leidenfrost temperature. *Ironmaking and Steelmaking,* 32 (2005) 2, Maney, UK.

[L5-15] Štětina J., Kavička F. and Dobrovská J.: Mathematical model for the calculation of the temperature field of a billet in real time. In *Book of Abstracts and CD ROM of the 13th International Heat Transfer Conference*, Sydney, Australia, August 13-18, 2006, p. 26.

[L5-16] Kavička F., Sekanina B., Štětina J. and Masarik M.: Definition of boundary conditions for the numerical model of transient temperature field of a concast steel slab. *Communications.* 4A2012 (2012) 14, 13–17.

[L5-17] Kavička F., Štětina J., Sekanina B., Stránský K., Dobrovská J. and Heger J.: The optimization of a concasting technology by two numerical models. *Journal of Materials Processing Technology.* 185 (2007) 1-3, 152–159.

[L5-18] Kavička F., Franěk Z. and Štětina J.: Software Analytical Instrument for Assessment of the Process of Casting Slabs. In *CD ROM The 10th International Conference on Numerical Methods in Industrial Forming Processes Nuniform 2010.* Pohang, Korea, American Institute of Physics. 2010. p. 586–592.

[L5-19] Štětina J., Kavička F., Stránský K., Heger J. and Dobrovská J.: Optimisation of a concasting technology via a dynamic solidification model of a slab caster. In *Computational Methods and Experimental Measurements XII.* Cambridge, WIT Press. 2005. p. 749–756.

[L5-20] Štětina J., Kavička F., Dobrovská J., Čamek L. and Masarik M.: Optimization of a concasting technology via a dynamic solidification model af a slab caster. In *PRICM 5. Proceedings of the 5th Pacific Rim International Conference on Advanced Materials and Processing.* Zuerich, Trans Tech Publications. 2004. p. 3831–3836.

[L5-21] Kavička F., Sekanina B., Štětina J. and Ramík P.: An original numerical model of heat and mass transfer in a concasting machine. In *3rd International conference on advances in fluid mechanics AFM 2000.* Montreal (Canada), WIT Press. p. 705–714.

[L5-22] Kavička F., Štětina J., Ramík P. and Sekanina B.: Solidification of continuously cast steel. In *CHT01: Advances in computational heat transfer II1.* Palm Cove (Australia), Graham de Vahl Davis. Eddie Leonardi. 2001. p. 1209–1218.

[L5-23] Štětina J., Kavička F. and Mauder T.: The influence of chemical composition of steels on the numerical simulation of a concasting process. In *Thermal and Environmental Issues in Energy Systems (id 18262).* Sorrento, Edizioni ETS. 2010. p. 963–968.

[L5-24] Štětina J., Kavička F. and Mauder T.: Transfer phenomena beneath the water cooling jets transfer phenomena beneath the water cooling jets of a billet caster. In *ISTP-20 Proceedings.* Victoria, BC, Canada, University of Victoria IESVic. 2009. p. 122–129.

[L5-25] Štětina J., Kavička F., Sekanina B. and Dobrovská J.: Optimization parameters of continuously casting apply 3D numerical model. In *Proceedings of SCANMET III Volume 2.* Lulea, Sweden, MEFOS. 2008. p. 189–198.

[L5-26] Kavička F., Štětina J., Stránský K., Dobrovská J. and Heger J.: The numerical and experimental investigation of a concasting technology. In *Abstracts of the Fourth International Conference on Computational Fluid Dynamics in the Oil and Gas, Metallurgical and Process Industries.* Trondheim, SINTEF. 2005. p. 58.

[L5-27] Štětina J., Kavička F., Heger J., Dobrovská J., Ramík P. and Sekanina B.: The numerical and experimental investigation of a concasting process. In *Proceedings of the 6th ASME-JSME Thermal Engineering Joint Conference -AJTEC 2003.* Hawaii Island, USA, Japan Society of Mechanical Engineers. 2003. p. 103.

[L5-28] Štětina J., Kavička F., Dobrovská J. and Heger J.: The importance of thermophysical properties for the accuracy of the numerical simulation of a concasting process. In *Book of Abstracts of The Sixteenth European Conference on Thermophysical Properties.* London, Imperial College and the National Physical Laboratory London. 2002. p. 319–320.

[L5-29] Kavička F., Štětina J., Stránský K., Dobrovská V., Dobrovská J. and Heger J.: Numerical analysis and optimization of an industrial concasting process. In *Proceedings of ASDA2002 Engineering systems design and analysis conference.* Istambul, ASME International Turkey Section. 2002. p. 24–25.

[L5-30] Kavička F., Štětina J., Sekanina B. and Ramík P.: Solidification of continuously cast steel. In *Proceedings of the 2001 National Heat Transfer Conference.* Anaheim (California, USA), The American society of mechanical engineers. 2001. p. 123–128.

[L5-31] Kavička F., Ramík P. and Štětina J.: Continuous casting of steel semiproducts and its optimization. In *Research and Development i Net Shape Manufacturing Programme and Abstracts.* IRC in Materials, The University of Birmingham, Birmingham, UK. 2001. p. 18.

6 The connection of the models of temperature field (model A) and chemical heterogeneity (model B)

6.1 Characterization of continuously cast steel slab solidification by means of chemical micro-heterogeneity assessment

6.1.1 Introduction

Structure of metallic alloys is one of the factors, which significantly influence their physical and mechanical properties. Formation of structure is strongly affected by production technology, casting and solidification of these alloys. Solidification is a critical factor in the materials industry, e.g. [L2-1]. Solute segregation either on the macro- or micro-scale is sometimes the cause of unacceptable products due to poor mechanical properties of the resulting non-equilibrium phases. In the areas of more important solute segregation there occurs weakening of bonds between atoms and mechanical properties of material degrade. Heterogeneity of distribution of components is a function of solubility in solid and liquid phases. During solidification a solute can concentrate in inter-dendritic areas above the value of its maximum solubility in solid phase. Solute diffusion in solid phase is a limiting factor for this process, since diffusion coefficient in solid phase is lower by three up to five orders than in the melt [L2-2].

When analysing solidification of steel so far no unified theoretical model was created, which would describe this complex heterogeneous process as a whole. During the last fifty years many approaches with more or less limiting assumptions were developed. Solidification models and simulations have been carried out for both macroscopic and microscopic scales. The most elaborate numerical models can predict micro-segregation with comparatively high precision. The main limiting factor of all existing mathematical micro-segregation models consists in lack of available thermodynamic and kinetic data, especially for systems of higher orders. There is also little experimental data to check the models [L6-1].

Many authors deal with issues related to modelling of a non-equilibrium crystallisation of alloys. However, majority of the presented works concentrates mainly on investigation of modelling of micro-segregation of binary alloys, or on segregation of elements for special cases of crystallisation – directional solidification, zonal melting, one-dimensional thermal field, etc. Moreover these models work with highly limiting assumption concerning phase diagrams (constant partition coefficients) and development of dendritic morphology (mostly one-dimensional models of dendrites); e.g. overview works [L6-1 to 6-4]. Comprehensive studies of solidification for higher order real alloys are rarer. Nevertheless, there is a strong industrial need to investigate and simulate more complex alloys because nearly all current commercial alloys have many components often exceeding ten elements. Moreover, computer simulation have shown that even minute amounts of alloying elements can significantly influence microstructure and micro-segregation and cannot be neglected [L6-1].

6.1.2 Methodology of chemical heterogeneity investigation

Original approach to determination of chemical heterogeneity in structure of poly-component system is based on experimental measurements made on samples taken from characteristic places of the casting, which were specified in advance. In selected sections of these samples concentration of main constitutive elements and impurities is determined at regular steps. Length of the measured section depends on dendrite arms spacing, and e.g. in steels we are interested most of all in secondary dendrite arms spacing, which can be made visible by suitable etching. Line segment, along which concentration of elements is measured, should moreover intersect appropriately great number of these dendritic arms (at least five and even more). Depending on chemical heterogeneity and structure of casting there are usually selected the sections with length of 500 to 1 000 μm, and total number of steps, in which concentration is determined, is set to 101.

Method of quantitative energy dispersion (ED), or wave dispersion (WD) X-ray spectral micro-analysis is used for determination of concentration of elements.

After termination of measurement suitable etching is applied on the sample surface in order to visualise contamination of surface by electron beam, and the measured trace is documented photographically. In this manner correspondence of the measured concentrations of elements and the structure of the given alloy is documented and at the same time there is metallographically determined average dendrites arm spacing within the frame of the measured section.

Next procedure is based on statistical processing of concentration data sets and application of the original mathematical model for determination of distribution curves of dendritic segregation of elements, characterising the most probable distribution of concentration of element in the frame of dendrite [L6-5 and 6-6], and the original mathematical model for determination of effective partition coefficients of these elements in the analysed alloy.

6.1.3 Application of methodology of chemical heterogeneity investigation – investigation into chemical micro-heterogeneity of concast steel slab

A continuously cast steel slab with dimensions 1 530 × 250 mm was chosen for presentation of results, with the following chemical composition in (wt.%): 0.14 C; 0.75 Mn; 0.23 Si; 0.016 P; 0.010 S; 0.10 Cr; 0.050 Cu; 0.033 Al_{total}.

After solidification and cooling of the cast slab a transversal band was cut out, which was then axially divided into halves. Nine samples were taken from one half for determination of chemical heterogeneity according to the schema in **Fig. 6-1**. The samples had a form of a cube with an edge of approx. 20 mm, with recorded orientation of its original position in the slab. **Figure 6-2** shows an example of microstructure of the analysed slab.

On each sample a concentration of seven elements (*aluminium, silicon, phosphor, sulphur, titanium, chromium and manganese*) were measured along the line segment long 1 000 μm. The distance between the measured points was 10 μm.

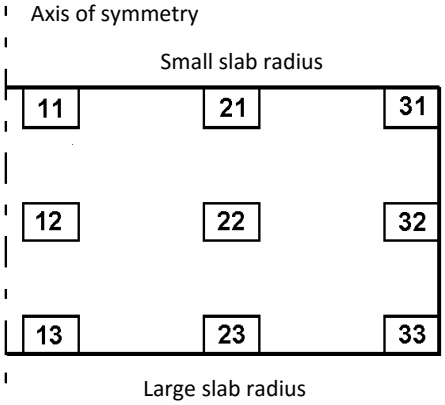

Fig. 6-1 Schema of sampling from a slab and marking of samples

Analytical complex unit JEOL JXA 8600/KEVEX Delta V Sesame was used for determination of concentration distribution of elements, and concentration was determined by method of energy dispersive X-ray spectral micro-analysis. As an example, **Figs. 6-3 and 6-4** present the basic concentration spectrum of Mn, Si, P and S.

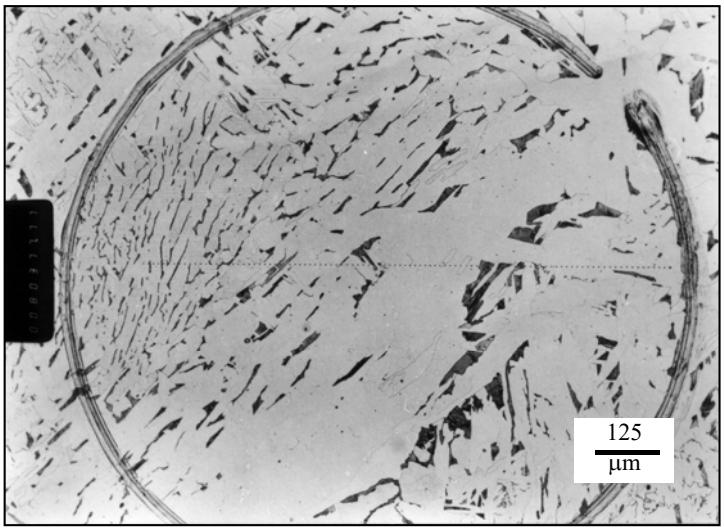

Fig. 6-2 Example of structure of the sample 21 with a microscopic trace of 1 000 μm long

Chemical micro-heterogeneity, i.e. segregation of individual elements at distances, order of which is comparable to dendrite arms spacing, can be quantitatively evaluated from the basic statistical parameters of the measured concentrations of elements in individual samples. These parameters comprise: C_{av} average concentration of element (arithmetic average) in the selected section, s_x standard deviation of the measured concentration of element, $C_{\min}$ minimum concentration of element and $C_{\max}$ maximum concentration of element measured always on the selected section of the sample.

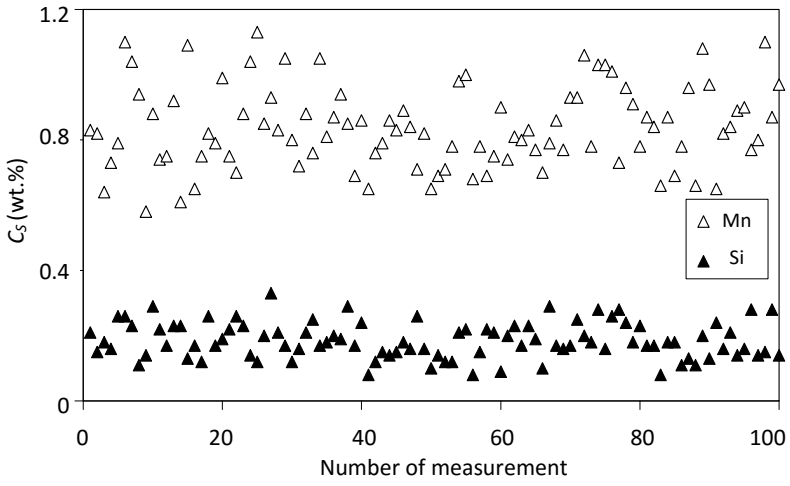

Fig. 6-3 Basic concentration spectrum of Mn and Si (sample 21)

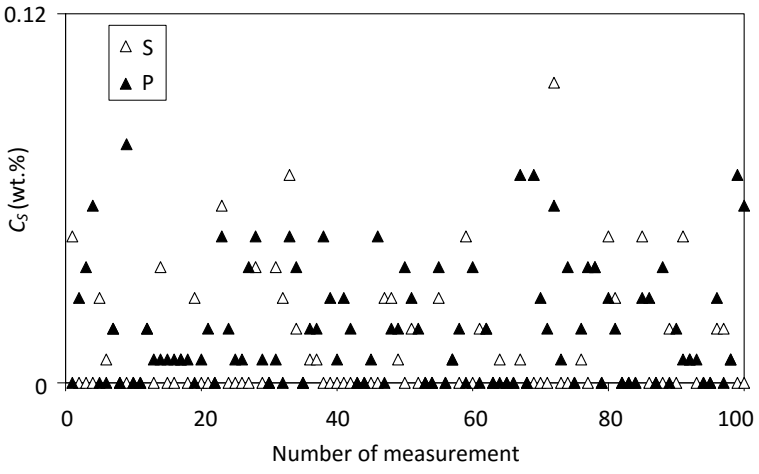

Fig. 6-4 Basic concentration spectrum of S and P (sample 21)

It is possible to calculate from these data moreover indexes of dendritic heterogeneity I_H of elements in the measured section of individual samples as ratio of standard deviation s_x and average concentration C_{av} of the element.

Then the element distribution profiles can be plotted according to the Gungor's method [L6-7] from the concentration data sets measured by the method ED along the line segment 1000 μm long. Data plotted as the measured weight percent composition versus number of data (**Figs. 6-3 and 6-4**) were put in an ascending or descending order and *x*-axis was converted to the fraction solid (f_S) by dividing each measured data number by total measured data number. The element composition versus fraction solid, i.e. element distribution profile (distribution curve of dendritic segregation) was then plotted; **Figs. 6-5 and 6-6** represent such dependences for manganese, silicon, phosphor and sulphur. The slope of such curve (ascending or descending) depended on the fact, whether the element in question enriched the dendrite core or the inter-dendritic area in the course of solidification.

From these statistical data it is also possible to determine with use of original mathematical model for each analysed element from the given set of samples the values of effective partition coefficients k_{ef}. The procedure of this coefficient calculation will be outlined here as follows:

The sequence of such arranged concentrations (**Figs. 6-5 and 6-6**) was seen as a distribution of concentrations of the measured element in the direction from the axis ($f_S = 0$) to the boundary ($f_S = 1$) of one average dendrite.

The effective partition coefficient k_{ef} was in this case defined by the relation

$$k_{ef}(f_S) = \frac{C_S(f_S)}{C_L(f_S)}, \qquad \text{(eq. 6-1)}$$

where C_S is the solute concentration in the solid phase and C_L is its concentration in liquid phase and argument (f_S) expressed the dependence of both concentrations on the solid fraction.

A perfect mixing of an element in the interdendritic melt was then assumed (this assumption is the same as e.g. in Scheil [L6-8] and Brody-Flemings [L4-5] model of solidification). It was therefore possible to substitute the equation (**eq. 6-1**) by the formula

$$k_{ef,i} = \frac{C_i}{C_{R,i}}, \qquad \text{(eq. 6-2)}$$

where C_i is the concentration in $i^{\text{-th}}$ point of the sequence (i.e. in the $i^{\text{-th}}$ point of the curve in **Figs. 6-5 and 6-6**) and $C_{\text{R,i}}$ is the average concentration of the element in the residual part of the curve (i.e. for $f_S \in \langle i, 1\rangle$), expressed by the relation:

$$C_{\text{R,i}} = \left[\frac{1}{(n-i+1)}\right] \cdot \sum_{j=i}^{n} C_j\,, \qquad \text{(eq. 6-3)}$$

where n was the number of the measured points. In this way it was possible to determine the values of effective partition coefficients for all $i \in \langle 1, n\rangle$, i.e. for the entire curve characterising the segregation during solidification. The effective partition coefficients of all the analysed elements were calculated by this original method. The average values of the determined effective partition coefficients are listed in **Tab. 6-1**. No segregation occurs when $k_{ef} = 1$; the higher is the deviation from the number 1, the higher is the segregation ability.

The effective partition coefficients calculated in this way inherently include in themselves both the effect of segregation in the course of alloy solidification and the effect of homogenisation, occurring during the solidification as well as during the cooling of alloy.

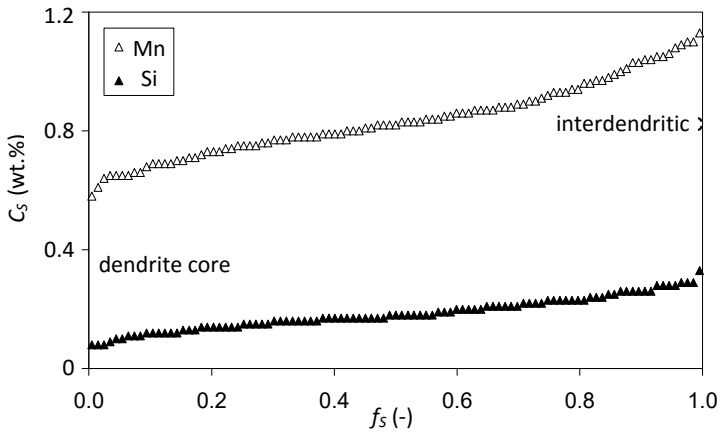

Fig. 6-5 Experimentally determined distribution curve of dendritic segregation for Mn and Si (sample 21)

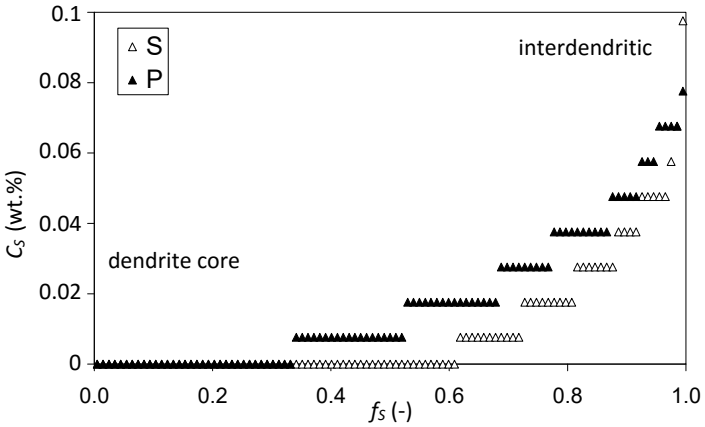

Fig. 6-6 Experimentally determined distribution curve of dendritic segregation for P and S (sample 21)

Tab. 6-1 The average values of the heterogeneity index I_H and the effective partition coefficient k_{ef} of elements in the individual samples

Sample		Element						
		Al	Si	P	S	Ti	Cr	Mn
11	I_H	1.24	0.28	1.22	1.45	0.30	0.22	0.14
	k_{ef}	0.32	0.78	0.33	0.26	0.76	0.83	0.88
12	I_H	1.54	0.30	1.12	1.74	0.29	0.27	0.15
	k_{ef}	0.24	0.77	0.36	0.20	0.78	0.79	0.88
13	I_H	1.44	0.30	1.25	1.48	0.30	0.29	0.15
	k_{ef}	0.27	0.78	0.32	0.26	0.77	0.78	0.88
21	I_H	1.33	0.29	1.58	1.49	0.31	0.24	0.13
	k_{ef}	0.29	0.78	0.24	0.25	0.76	0.81	0.89
22	I_H	1.14	0.28	1.31	1.41	0.30	0.26	0.14
	k_{ef}	0.35	0.78	0.30	0.27	0.77	0.80	0.88
23	I_H	1.56	0.29	1.34	1.86	0.26	0.28	0.13
	k_{ef}	0.24	0.78	0.29	0.18	0.80	0.78	0.89
31	I_H	1.11	0.28	1.22	2.34	0.31	0.23	0.16
	k_{ef}	0.37	0.78	0.33	0.18	0.76	0.82	0.87
32	I_H	1.44	0.27	1.16	1.49	0.34	0.25	0.14
	k_{ef}	0.27	0.79	0.34	0.25	0.74	0.80	0.88
33	I_H	1.32	0.29	1.24	1.64	0.35	0.26	0.13
	k_{ef}	0.30	0.78	0.32	0.22	0.74	0.80	0.89

Tab. 6-2 Average values of the measured and calculated quantities in the set of all samples

Element	C_{av} ± s_x	I_H ± s_I	k_{ef} ± s_k	$k_{ef}^{(ref)}$ according to [Ref.]
Al	0.0136 0.0029	1.352 0.162	0.294 0.046	0.12–0.92 [L6-9]
Si	0.1910 0.0068	0.285 0.011	0.781 0.005	0.66–0.91 [L6-9 and 6-10]
P	0.0141 0.0023	1.270 0.133	0.314 0.035	0.06–0.50 [L6-9 and 6-10]
S	0.0136 0.0030	1.657 0.297	0.232 0.035	0.02–0.10 [L6-9]
Ti	0.0951 0.0032	0.306 0.027	0.765 0.019	0.05–0.60 [L6-9]
Cr	0.1758 0.0076	0.255 0.023	0.799 0.017	0.30–0.97 [L6-9]
Mn	0.8232 0.0169	0.143 0.009	0.873 0.033	0.72–0.90 [L6-10]

6.1.4 Results and discussion

Data represented in **Tabs. 6-1 and 6-2** make it possible to evaluate dendritic heterogeneity (micro-heterogeneity) of elements, as well as their effective partition coefficients in individual samples, and also in the frame of the whole analysed half of the slab cross-section. It is obvious from these tables that dendritic heterogeneity of accompanying elements and impurities is comparatively high. This is demonstrated by the index of dendritic heterogeneity I_H. It follows from **Tabs. 6-1 and 6-2**, that distinct differences exist between micro-heterogeneity of individual elements. **Fig. 6-7** brings the dependence of the index of dendritic heterogeneity I_H on the effective partition coefficient of the monitored elements. **Figures 6-8a,b** show distribution of indexes of micro-heterogeneity of sulphur (the most segregating element) and manganese (the least segregating element) on slab cross-section. Average value of the heterogeneity index I_H and the effective partition coefficient k_{ef} of elements in the individual samples is given in **Tab. 6-1**. It follows from this table that dendritic heterogeneity of slab decreases in this order of elements: sulphur, aluminium, phosphor, titanium, silicon, chromium and manganese, which has the lowest index of heterogeneity.

Dendritic heterogeneity of the analysed elements is expressed also by the values of their effective partition coefficients, arranged for individual samples in **Tab. 6-1** and for the set of samples in **Tab. 6-2**. It is obvious from the tables that pair values of the index of dendritic heterogeneity and effective partition coefficient for the same element do mutually correspond. The higher the value of the heterogeneity index, the lower the value of effective partition coefficient and vice versa. The lowest value of the effective partition coefficient is found in sulphur and the highest value is found in manganese. It follows from the **Tab. 6-2**, that effective partition coefficient increases in this order of elements: sulphur, aluminium, phosphor, titanium, silicon, chromium and manganese. All the analysed elements segregate during solidification into an inter-dendritic melt, and their partition coefficient is smaller than one.

For comparison, the **Tab. 6-2** contains also the values of partition coefficients found in literature. It is obvious that our values of effective partition coefficients, calculated according to the original model, are in good agreement with the data from literature, only with the exception of sulphur (and titanium). The reason for this difference is probably the means of calculation of the effective partition coefficient – the value of this parameter is calculated from concentration data set measured on solidified and cooled casting. Consequently, the effective partition coefficients calculated in this way inherently include in themselves both the effect of segregation in the course of alloy solidification and the effect of homogenisation, occurring during the solidification as well as during the cooling of alloy.

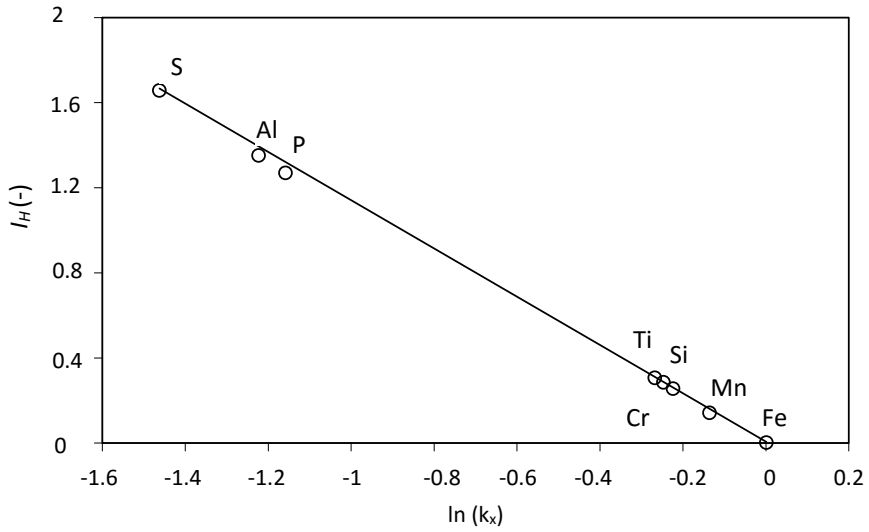

Fig. 6-7 The dependence of the index of dendritic heterogeneity I_H on the effective partition coefficient k_{ef} of the monitored elements

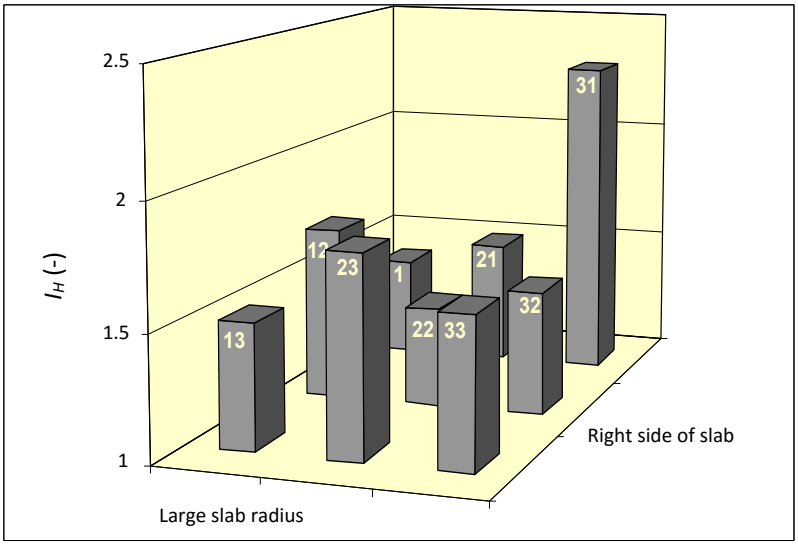

Fig. 6-8a Differences in sulphur micro-heterogeneity in samples taken from one-half of slab cross-section

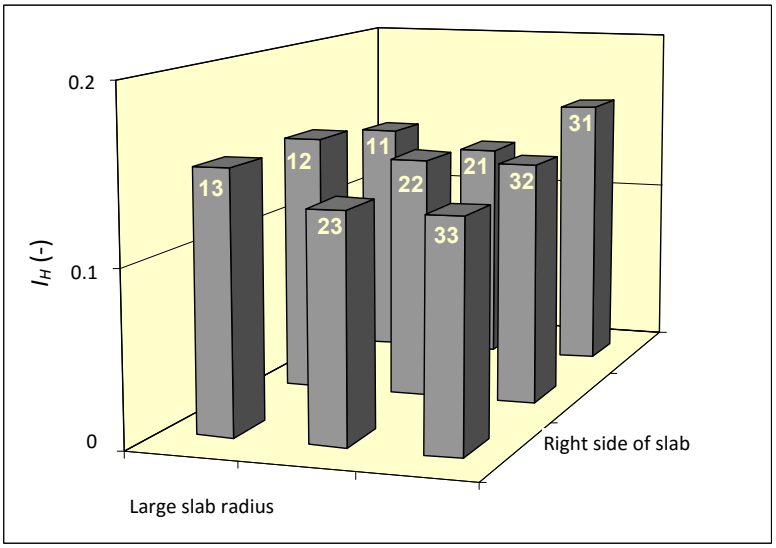

Fig. 6-8b Differences in manganese micro-heterogeneity in samples taken from one-half of slab cross-section

6.1.5 Conclusion

The chapter presents new approach to measurement and evaluation of chemical heterogeneity of elements in poly-component systems. The method is based on experimental measurements made on samples taken from characteristic places of the casting. In selected sections of these samples the concentration of elements in question is determined in regular steps. Line segment, along which the concentration of elements is measured, should moreover intersect appropriately large number of dendritic arms. Number of the measured concentrations should also be appropriately large. Method of quantitative energy dispersion (ED), or wave dispersion (WD) X-ray spectral micro-analysis is used for determination of concentration of elements [L6-11].

Next processing of concentration data sets is based on application of the original mathematical model for determination of distribution curves of dendritic segregation of the analysed elements, characterising the most probable distribution of concentration of element in the frame of dendrite, and the original mathematical model for determination of effective partition coefficients of these elements in the analysed alloy.

The paper describes also application of this method at research of chemical heterogeneity on cross-section of CC steel slab and presents selected results (indices of heterogeneity and effective partition coefficients of seven analysed elements) characterising chemical micro-heterogeneity on one half of cross-section of this CC steel slab.

The following main results were obtained:

- dendritic heterogeneity of accompanying elements and impurities is comparatively high;
- all the analysed elements segregate during solidification into an inter-dendritic melt, and their partition coefficient is smaller than one;
- the dendritic heterogeneity decreases in this order of elements: sulphur, aluminium, phosphor, titanium, silicon, chromium and manganese;
- the effective partition coefficients calculated in this new way inherently include in themselves both the effect of segregation in the course of alloy solidification, and the effect of homogenisation, occurring during the solidification, as well as during the cooling of an alloy.

Presented methodology of investigation into chemical micro-heterogeneity makes it possible to study and to describe the micro-segregation behaviour of selected elements in representative areas of steel slab. Since a microprobe was used for experimental investigation, the results have high accuracy (even though assessment by microprobe is time-intensive and costly). The results, acquired in this way, can also serve for creating standards for other faster and cheaper method for investigation into (micro) heterogeneity of CC steel slab [L6-12].

6.2 Interconnection of the models

The developed original numerical model A for the simulation of the temperature field of a concasting (see the subchapter 1.1) evolves and specifies constantly [L2-3 and L6-13 to 6-21]. The model is based on the numerical method of finite differences with explicit formula for the unknown temperature of the mesh node. Model takes into account non-linearity of the task; it means dependence of thermo-physical properties of all materials of the systems on temperature and dependence of heat transfer coefficients on temperature of all external surfaces.

Another model, which has also been already mastered is the model of chemical heterogeneity B. The model enables description and measurement of dendritic segregation of constitutive elements and admixtures in crystallising and cooling continuously cast casting [L6-22 and 6-23]. Majority of parameters necessary for application of the model A is known, but parameters necessary for use of the model B had to be determined by measurements on the work itself, i.e. on suitably chosen samples from solifified castings (see subchapter 6.1).

It was verified that the basic set of measured concentration data of elements (8 to 11 elements) makes it possible to obtain a semi-quantitative to quantitative information on chemical heterogeneity of the

cast, and that it is possible to apply at the same time for evaluation of distribution of elements in the cast structure the methods of mathematical- statistical analysis. It is possible to determine the distribution curve of the element concentration in the measured segment of the analysed blank and their effective partition coefficient between the solid and liquid phase during crystallisation. In this way the crucial verified data necessary for creation of the conjugated model AB of crystallising, solidifying and cooling down concasting were obtained. It was verified that re-distribution of constitutive, additive elements and admixtures can be described by effective partition coefficient.

At the moment of completed crystallization, at surpassing of an isosolidic curve in the concasting (a slab or a billet), it is possible to express for dendritically segregating element the ratio of the concentration C_S of a given solute at the solid-liquid interface to the initial liquid concentration C_0 by the relation

$$C_S = k_{ef} \cdot C_0 \left[1 - \left(1 - 2\alpha \cdot k_{ef} \right) f_S \right]^{\left(k_{ef} - 1 \right) / \left(1 - 2\alpha \cdot k_{ef} \right)}, \qquad \text{(eq. 6-4)}$$

where k_{ef} is effective partition coefficient, f_S is solid fraction of the solidified phase, and α is dimensionless Fourier's number of the 2nd kind for mass transfer, which is given by the relation

$$\alpha = D_S \cdot \theta / L^2, \qquad \text{(eq. 6-5)}$$

in which D_S is diffusion coefficient of the segregating element in solid phase, θ is local solidification time (i.e. time of persistence of the assumed dendrite between the temperature of liquidus and solidus) and L is the secondary dendrite arm spacing.

In the next step it is necessary to express the ratio of concentrations C_S/C_0 as a function of heterogeneity index I_H and of statistical distribution of the measured element, expressed by distributive curve of dendritic segregation (given e.g. in **Fig. 6-5 or 6-6**). In this manner the following equation is available for each measured element:

$$C_S / C_0 = I_H \qquad \text{(eq. 6-6)}$$

which expresses by concrete numbers the parameters, defined by the equation (**eq. 6-4**). By solving the first two equations it is then possible to determine for each analysed element (i.e. for its measured index of dendritic heterogenity, effective partition coefficient and distribution curve of dendritic segregation, i.e. for the established statistic character of distribution of the analysed element in structure of the blank) certain values of dimensionless criterion α. Afterwards on the basis of semi-empiric relations and rates of movement of the crystallisation front, calculated from the thermal field model A in confrontation with the results of experimental metallographic analysis, the secondary dendrite arm spacing L can be determined. The values θ and L for determination of the criterion α are calculated from the model for each sample, which were determined for individual measured elements in each sample of the concasting. It is possible to make from the equation (**eq. 6-5**) an estimation of the diffusion coefficient of each analysed element in individual samples of the concasting. At the moment, when temperature of any point of the mesh drops below the liquidus temperature, it is valid that the share of the forming solid phase f_S grows till its limit value $f_S = 1$ (i.e. in solid phase). In this case segregation of the investigated element achieves in the residual inter-dendritic melt its maximum.

The calculated coefficients of diffusion can be compared with their literary values, to assess the differences and verify the legitimacy of the connection of the two models *AB***.** A steel slab with dimensions 1 530 × 250 mm was chosen for this comparison of diffusion coefficients, with the following chemical composition in (wt.%): 0.11 C; 0.61 Mn; 0.18 Si; 0.009 P; 0.015 S; 0.15 Cr; 0.04 Ni; 0.01 Mo; 0.06 Cu; 0.006 Al_{total}; 0.01 Nb; 0.01 V; 0.08 Ti.

Graphical results of the temperature model are on **Figs. 6-9a** to **6-9g** [L1-26 and L6-24].

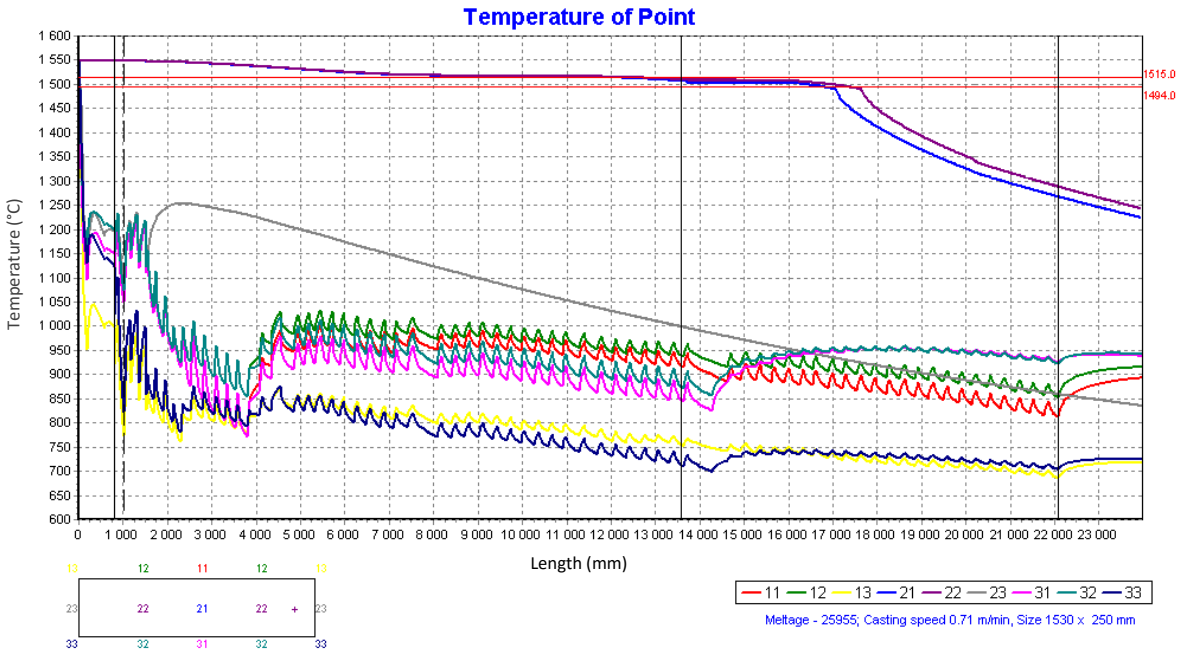

Fig. 6-9a The temperature history of the nodes of the slab cross-section

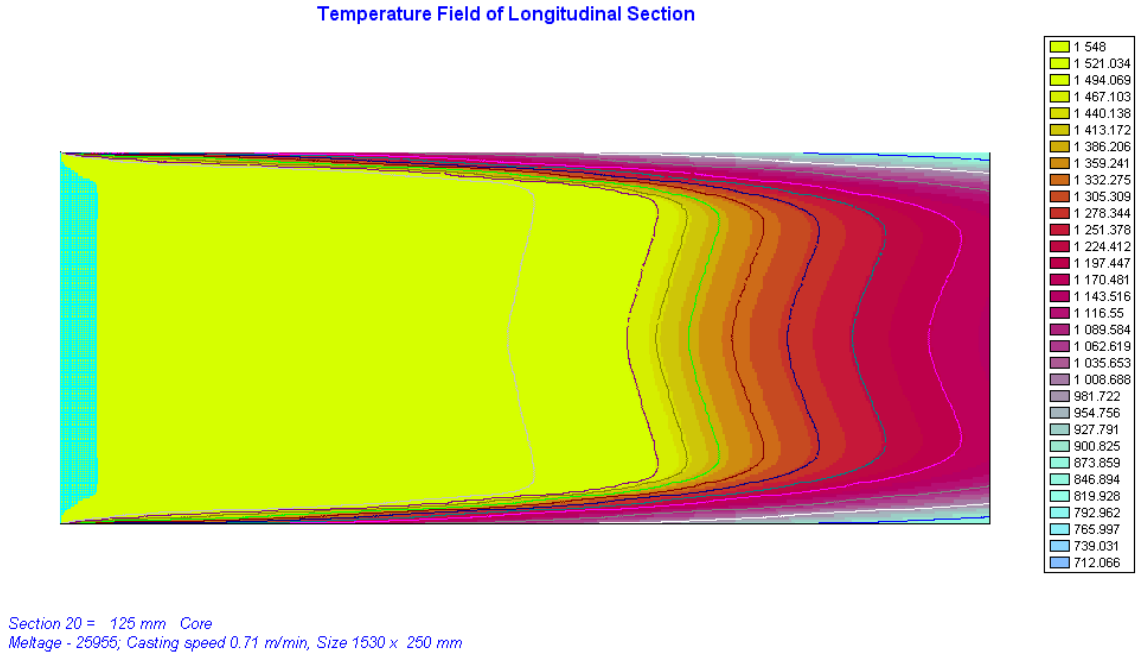

Fig. 6-9b 2D graph of temperature iso-zone in the 1st axial longitudinal section of the slab

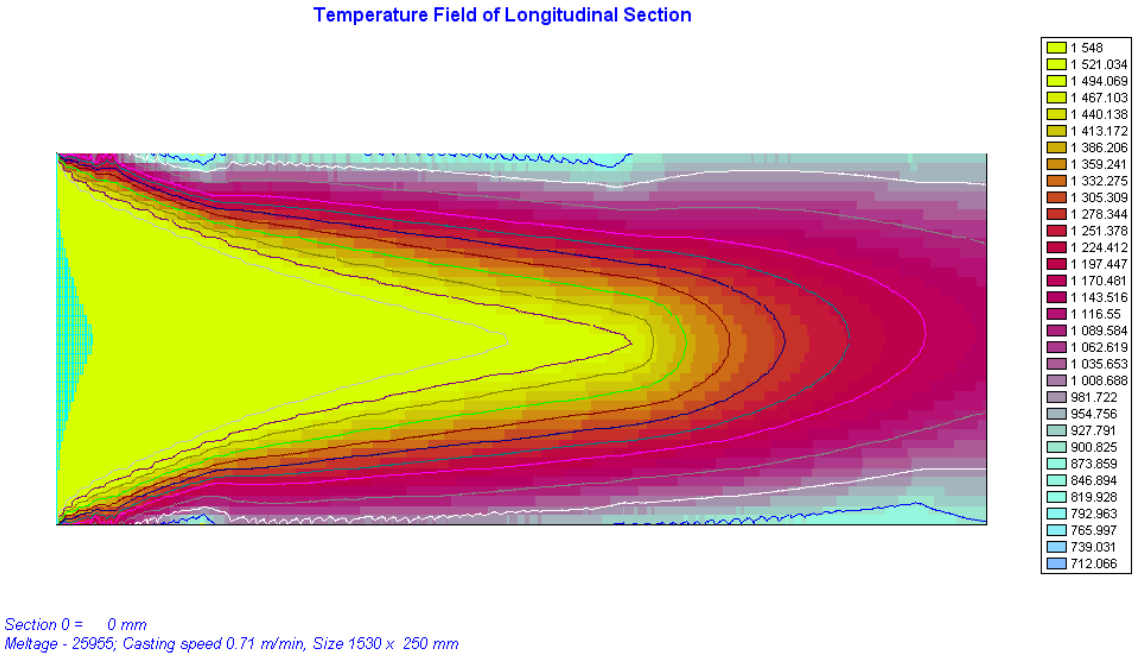

Fig. 6-9c 2D graph of temperature iso-zone in the 2nd axial longitudinal section of the slab

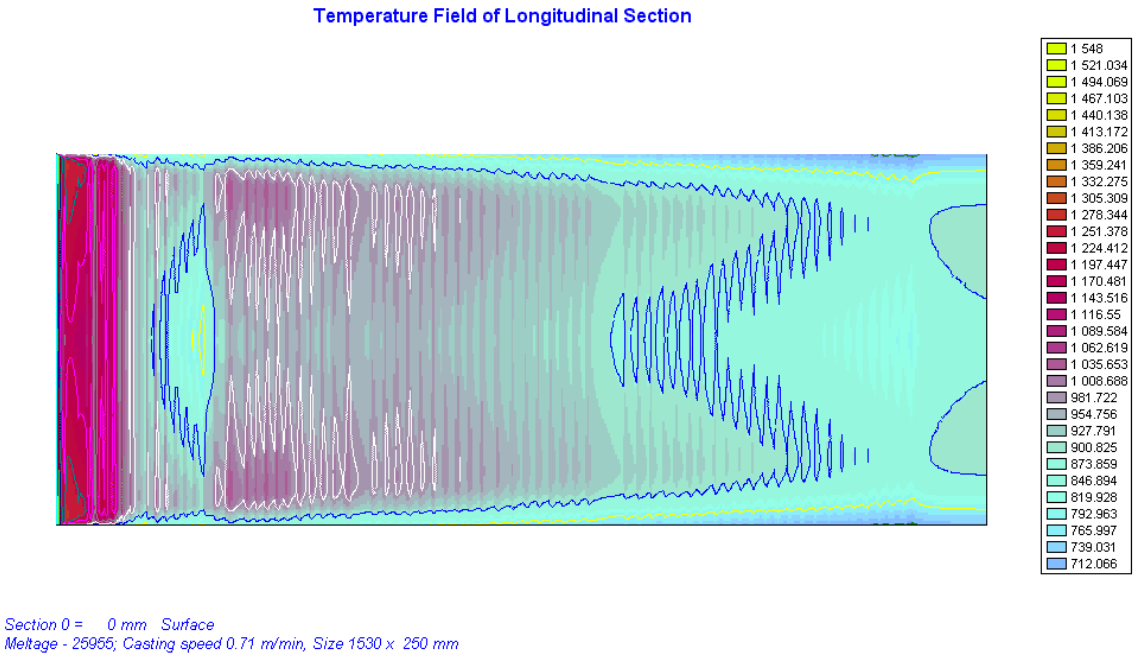

Fig. 6-9d 2D graph of temperature iso-zone on the longitudinal surface of the slab

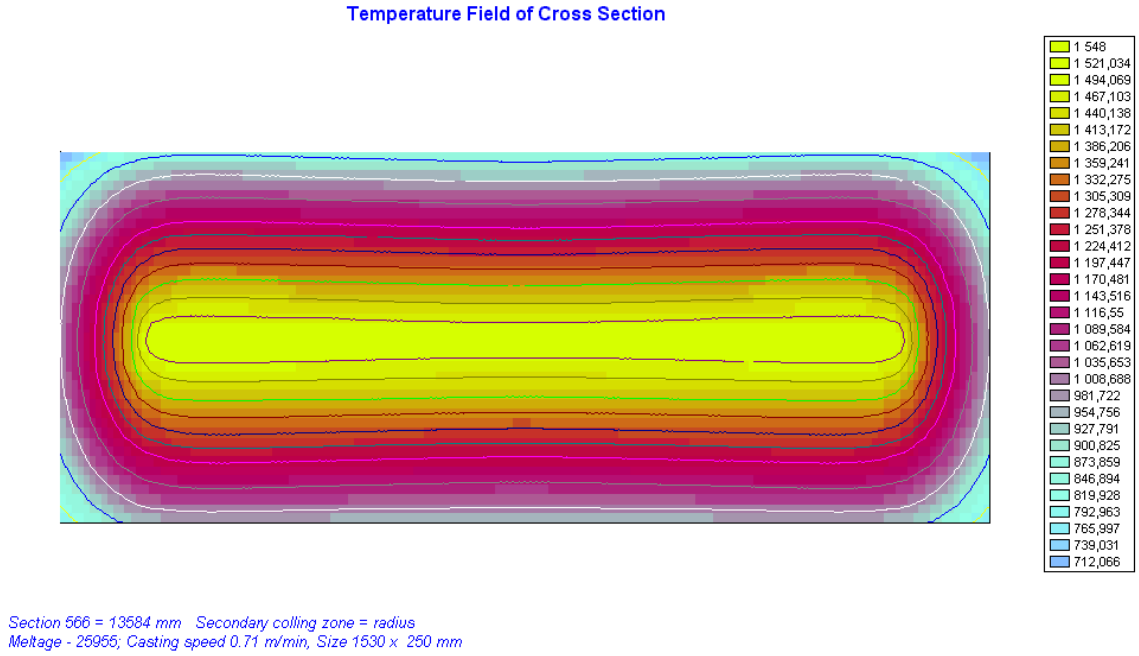

Fig. 6-9e 2D graph of a temperature iso-zone in the cross-section of the slab (in a place of the end of a arc)

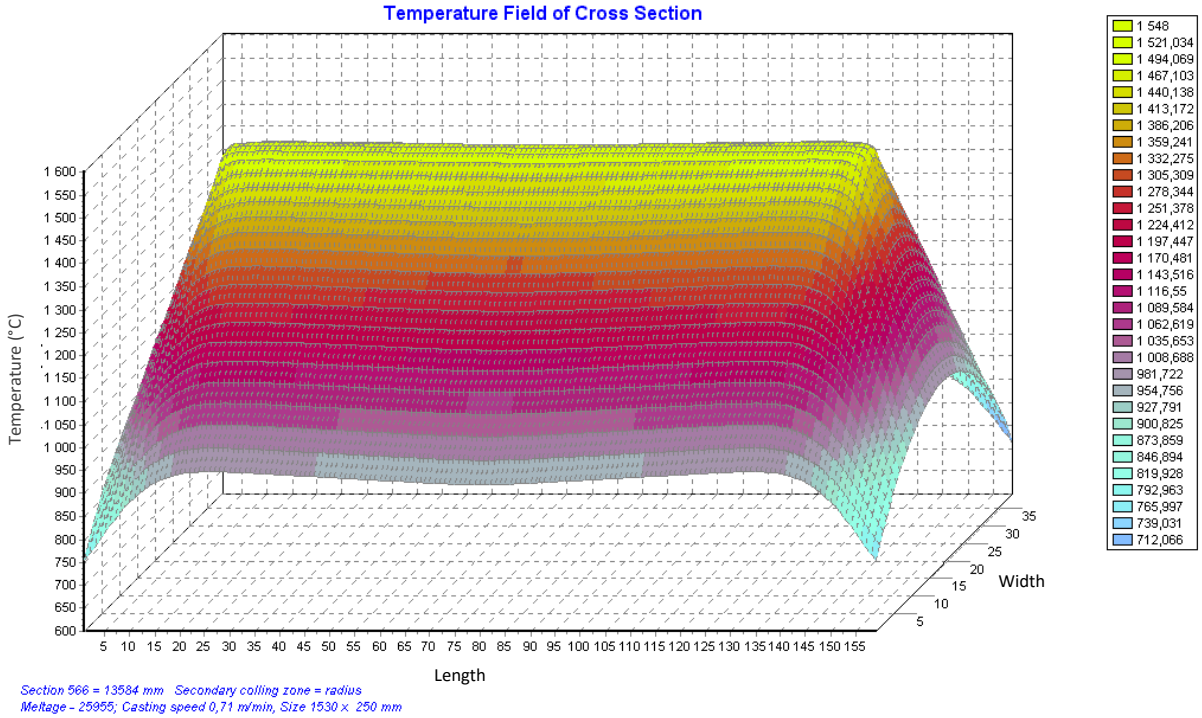

Fig. 6-9f 3D graph of a temperature iso-zone in the cross-section of the slab (in a place of the end of a arc).

The local time solidification θ of each point of the computational network of the slab have been calculated. 3D graph of this parameter is given in **Fig. 6-9g.**

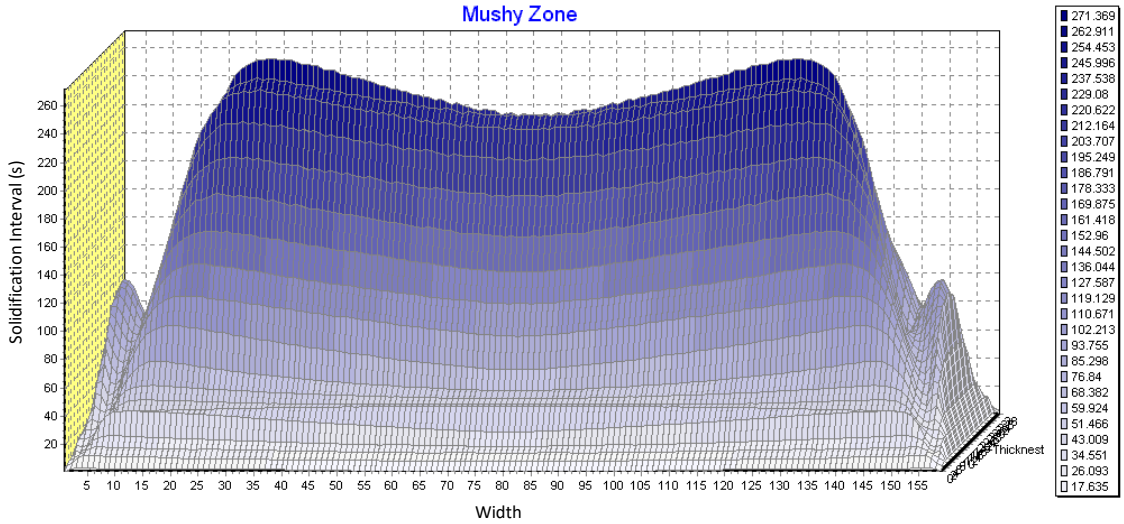

Fig. 6-9g 3D graph of the calculated local solidification time

An example of verification of the validity of the connection of both models is demonstrated:

- in **Tab. 6-3**, which contains the experimentally measured parameter L (the secondary dendrite arm spacing) and calculated parameter θ (the local solidification time) for each sample of the slab (sample No.11, 12, 13, 21, 22, 23, 31, 32 and 33) – on the basis of the numerical model of the temperature field [L6-25],
- in **Tab. 6-4**, which contains the corresponding parameters k_{ef}, α , D_S , for each sample of the slab and for each of the analysed element (Al, Si, P, S, Ti, Cr, Mn and Fe),
- in **Tab. 6-5 and Fig. 6-10** which the correlation between the calculated (D_S^{exp}) and literary (D_S^{lit}) diffusion coefficients contains.

Tab. 6-3 Calculated values of local solidification time θ and experimentally measured secondary dendrite arm spacing L.

Parameter	Sample								
	11	12	13	21	22	23	31	32	33
θ (s)	11.440	653.824	11.440	13.477	710.646	13.477	11.491	34.243	11.491
L (μm)	107.252	565.286	107.252	114.710	586.441	114.710	107.449	168.107	107.449

Tab. 6-4 Parameters characterizing the connection of two numerical models

Sample	Parameter	Element							
		Al	Si	P	S	Ti	Cr	Mn	Fe
11	k_{ef}	0.18	0.81	0.23	0.30	0.73	0.81	0.86	1.00
	I_H	1.90	0.25	1.60	1.31	0.35	0.24	0.17	0.0013
	α	0.02068	0.0188	0.02207	0.03965	0.0245	0.0106	0.0113	0.00719
	$D_S \cdot 10^8$	5.198	4.728	5.548	9.967	6.154	2.665	2.833	1.807
12	k_{ef}	0.21	0.80	0.18	0.28	0.75	0.78	0.85	1.00
	I_H	1.73	0.25	1.98	1.38	0.33	0.28	0.18	0.0016
	α	0.02583	0.0138	0.01704	0.02864	0.0183	0.0112	0.0159	0.00908
	$D_S \cdot 10^8$	3.156	1.686	2.082	3.499	2.236	1.375	1.942	1.109
13	$D_S \cdot 10^8$	0.21	0.83	0.18	0.18	0.78	0.79	0.83	1.00
	I_H	1.78	0.22	1.86	2.44	0.29	0.28	0.22	0.0017
	α	0.01700	0.0246	0.02154	0.00814	0.0168	0.0044	0.0009	0.00003
	$D_S \cdot 10^8$	4.273	6.184	5.415	2.046	4.233	1.099	0.221	0.007
21	k_{ef}	0.20	0.80	0.21	0.25	0.76	0.80	0.87	1.00
	I_H	1.79	0.25	1.72	1.52	0.32	0.26	0.16	0.0012
	α	0.02713	0.0186	0.02051	0.02947	0.0243	0.0197	0.0166	0.02114
	$D_S \cdot 10^8$	6.622	4.540	5.006	7.193	5.944	4.811	4.062	5.160
22	k_{ef}	0.18	0.81	0.27	0.30	0.76	0.79	0.87	1.00
	I_H	1.95	0.24	1.42	1.30	0.31	0.27	0.16	0.0013
	α	0.02411	0.0185	0.02424	0.02484	0.0177	0.0273	0.0134	0.01216
	$D_S \cdot 10^8$	2.917	2.243	2.933	3.005	2.146	3.303	1.618	1.471
23	k_{ef}	0.17	0.81	0.14	0.28	0.76	0.79	0.88	1.00
	I_H	2.01	0.26	2.29	1.37	0.31	0.26	0.15	0.0012
	α	0.01745	0.0202	0.02152	0.02990	0.0134	0.0088	0.0087	0.00666
	$D_S \cdot 10^8$	4.259	4.926	5.253	7.298	3.278	2.143	2.131	1.626
31	k_{ef}	0.21	0.79	0.21	0.27	0.71	0.78	0.88	1.00
	I_H	1.77	0.28	1.72	1.43	0.39	0.28	0.15	0.0012
	α	0.01432	0.0151	0.03063	0.02239	0.0150	0.0133	0.0248	0.00750
	$D_S \cdot 10^8$	3.597	3.790	7.694	5.624	3.770	3.338	6.224	1.884
32	k_{ef}	0.17	0.81	0.22	0.15	0.74	0.78	0.87	1.00
	I_H	2.00	0.25	1.67	3.12	0.33	0.28	0.16	0.0014
	α	0.02702	0.0092	0.02859	0.00643	0.0076	0.0140	0.0021	0.00018
	$D_S \cdot 10^8$	5.575	1.906	5.899	1.327	1.566	2.886	0.435	0.037
33	k_{ef}	0.25	0.79	0.18	0.27	0.76	0.79	0.88	1.00
	I_H	1.53	0.26	1.87	1.44	0.32	0.27	0.15	0.0012
	α	0.03252	0.0091	0.02457	0.02210	0.0192	0.0101	0.0213	0.01047
	$D_S \cdot 10^8$	8.168	2.281	6.172	5.551	4.823	2.542	5.353	2.630

Tab. 6-5 Comparison of the calculated and literary [L6-25 and 6-26] diffusion coefficients ($m^2 \cdot s^{-1}$)

Parameter	Element							
	Al	Si	P	S	**Ti**	**Cr**	**Mn**	**Fe**
$D_S^{exp} \cdot 10^8$	4.612	3.253	4.799	4.264	3.451	2.465	1.844	0.688
$D_S^{lit} \cdot 10^8$	61.942	0.624	5.340	59.800	0.585	1.649	0.327	0.204

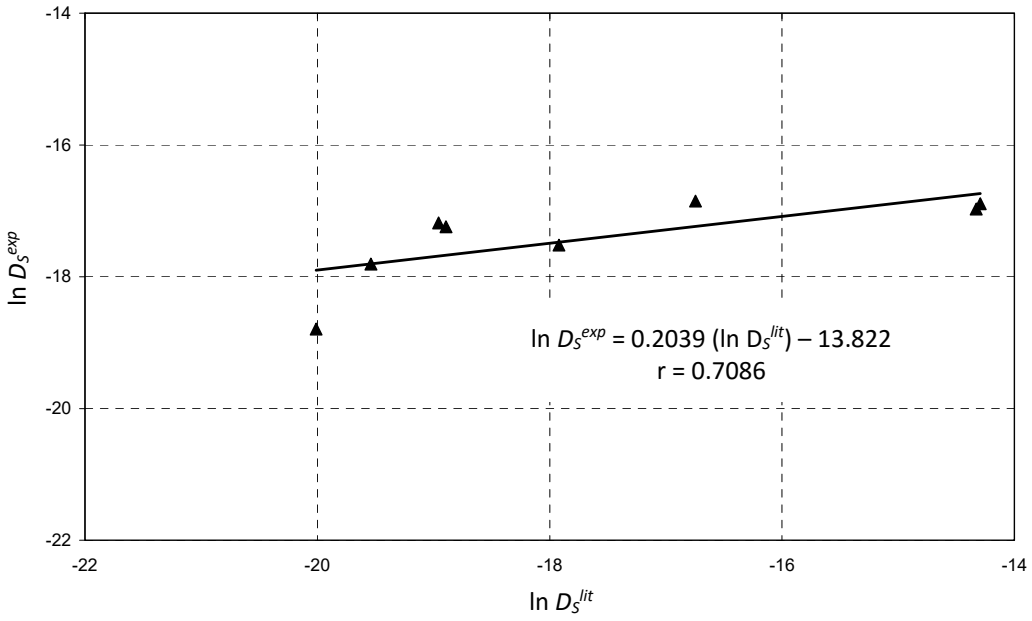

Fig. 6-10 Correlation between the calculated values of the diffusion coefficients of elements $D_S^{\exp}$ (from **eq. 6-5**) and their literary values D_S^{lit}

It is possible to substantiate that the probability of mistake of the connection of both models is less than five percent.

When we calculate further the ratio of both values of diffusion coefficients, i.e. the ratio of D_S^{exp}/D_S^{lit} (see data in **Tab. 6-5**), and if we establish the geometric average of both values of diffusion coefficients we obtain the value in equation (**eq. 6-7**):

$$\frac{D_S^{exp}}{D_S^{lit}} = 1.007\ ^{+4.754}_{-0.831} \qquad \text{(eq. 6-7)}$$

D_S^{lit} are average values from [L6-25 and 6-26]. Equation (**eq. 6-7**) shows that there is the agreement between the calculated and literary diffusion coefficients.

Chemical heterogeneity of elements is predominant cause of defects of cast and formed steel products. During crystallisation and solidification of metals and alloys chemical non-homogeneities occur, i.e. chemical heterogeneities of individual elements, since the elements, both constitutive and tramp elements and admixtures, segregate [L2-1 and L6-27]. Crystallisation occurs in real castings and ingot in comparatively broad zone, in which solid phase separates out in the form of lattices from axes or arms, which form frames of dendrites.

Lattice frames of dendrites do not interrupt continuity of the liquid phase, so diffusion can be running in it. This diffusion is, however, much smaller in comparison with diffusion in free melt, since arms of dendrites prevent convection. Under these conditions it is possible to consider the diffusion exchange of admixtures between more distant areas of crystallisation zone as limited or possibly negligible.

As a result of incomplete diffusion of admixture in solid phase concentrations of admixtures in solid crystals are not getting balanced and admixtures remain segregated in spaces between arms of dendrites and cause thus dendritic segregation. Due to the fact that mechanism of dendritic segregation is controlled by diffusion processes at the phase boundary liquidus-solidus, its magnitude depends significantly on kinetics of crystallisation.

6.3 Investigation of influence of cooling rate on back diffusion at solidification of concast steel billet 150 × 150 mm

6.3.1 Theoretical basis – modelling of non-equilibrium micro-segregation

Tables 6-6 and **6-7** give an overview of selected analytical micro-segregation models for non-equilibrium crystallisation. Authors Scheil [L6-8] and Pfann [L6-28] assume the state with no diffusion in solid phase, directional solidification, heat removal and unidirectional growth of crystals. Brody and Flemings [L4-5] for the first time analysed the model, which assumed a complete diffusion in liquid and incomplete back diffusion. Application of their result is limited by slow diffusion. This general form of Brody-Flemings model introduces β as a back diffusion parameter, which has been quantified by many researches in different ways. In the original Brody-Flemings model for a plate dendrite $\beta = 2\alpha$, where parameter α is given by (**eq. 6-5**).

The quantity α is the mass Fourier number (back diffusion parameter) and it characterises intensity of diffusion of elements in solid phase in respect to the secondary dendrite arms spacing (L) and to the local time of solidification (θ). It has been verified experimentally that with increasing value of this parameter segregation of elements at solidification increases, interval of solidification increases and tendency of steel to cracking between dendrites increases considerably [L6-9].

Tab. 6-6 Main assumptions used in analytical micro-segregation models [L4-5, 6-3, 6-8 and 6-9, 6-25, 6-28 to 6-30]

Model	Geometry	Solid Diffusion	Liquid Diffusion	Partition Coefficient	Growth	Coarse-ning
Scheil	No restriction	No	Complete	Constant	No restriction	No
Brody-Flemings	No restriction	Incomplete	Complete	Constant	No restriction	No
Clyne-Kurz	No restriction	Spline fit	Complete	Constant	No restriction	No
Ohnaka 1, 2	Linear, Columnar	Quadratic Equation	Complete	Constant	Linear, Parabolic	No
Won-Thomas	No restriction	Incomplete	Complete	Constant	No restriction	Yes

Tab. 6-7 Mathematical expression of models in **Tab. 6-6**

MODEL	EQUATION (eq. 6-8)	EXPRESSION OF BACK DIFFUSION
Scheil	$C_S = kC_0\left[1-(1-\beta k)f_S\right]^{(k-1)/(1-\beta k)}$	$\beta = 0$
Brody-Flemings	$C_S = kC_0\left[1-(1-\beta k)f_S\right]^{(k-1)/(1-\beta k)}$	$\beta = 2\alpha = 8D_S\theta/L^2$
Clyne-Kurz	$C_S = kC_0\left[1-(1-\beta k)f_S\right]^{(k-1)/(1-\beta k)}$	$\beta = 2\alpha\left[1-\exp(-1/\alpha)\right]-\exp(-1/2\alpha)$
Ohnaka 1 (Linear)	$C_S = kC_0\left[1-(1-\beta k)f_S\right]^{(k-1)/(1-\beta k)}$	$\beta = 2\alpha/(1+2\alpha)$
Ohnaka 2 (Parabolic)	$C_S = kC_0\left[1-(1-\beta k)f_S\right]^{(k-1)/(1-\beta k)}$	$\beta = 4\alpha/(1+4\alpha)$
Won-Thomas	$C_S = kC_0\left[1-(1-\beta k)f_S\right]^{(k-1)/(1-\beta k)}$	$\beta = 2\alpha^{+}\left[1-\exp\left(-\frac{1}{\alpha^{+}}\right)\right]-\exp\left(-\frac{1}{2\alpha^{+}}\right)$, where $\alpha^{+} = 2\left(\alpha+\alpha^{c}\right)$ and $\alpha^{c} = 0.1$ (effect of coarsening)

Note to **Tab. 6-7**: C_S is the concentration of a given solute at the solid-liquid interface, C_0 is the initial liquid concentration, k is the equilibrium partition coefficient for the given solute and f_S is the solid fraction.

Authors Clyne and Kurz [L6-30] derived more suitable mathematical expression, which approaches asymptotically the Scheil's equation and equilibrium solidification model for infinitely small and infinitely big diffusion coefficient. Ohnaka's model [L6-25] (Ohnaka 1) is based on comparison with an approximate solution of the diffusion equation for the plate dendrite, assuming a quadratic solute profile in the solid. Further modification (Ohnaka 2) was proposed in order to account for irregular-

shaped microstructures, such as columnar dendrites. Won a Thomas [L6-29] derived semi-empirical model, which is again based on Brody-Flemings' model, and parameter of back diffusion comprises also coarsening of dendrite branches.

The mathematical formulation of several analytical micro-segregation models and the main assumptions of their use are treated in the monograph [L6-31].

6.3.2 Results of investigation of cooling rate influence on back diffusion of selected elements at solidification of the steel billet and their discussion

Parameters of back diffusion of the determined elements (C, Si, Mn, P and S) in selected cross-sections of concast steel billet 150 × 150 mm (chemical composition of the melt is given in **Tab. 6-8**) were calculated on the basis of mathematical models mentioned in the previous chapter. Our own experimental data were used of calculations, as well as tabulated data and also outputs from temperature model [L6-35] simulating temperature field of the billet at solidification and cooling. The results of the simulation of the billet temperature field bring **Figs. 6-11 to 6-13**.

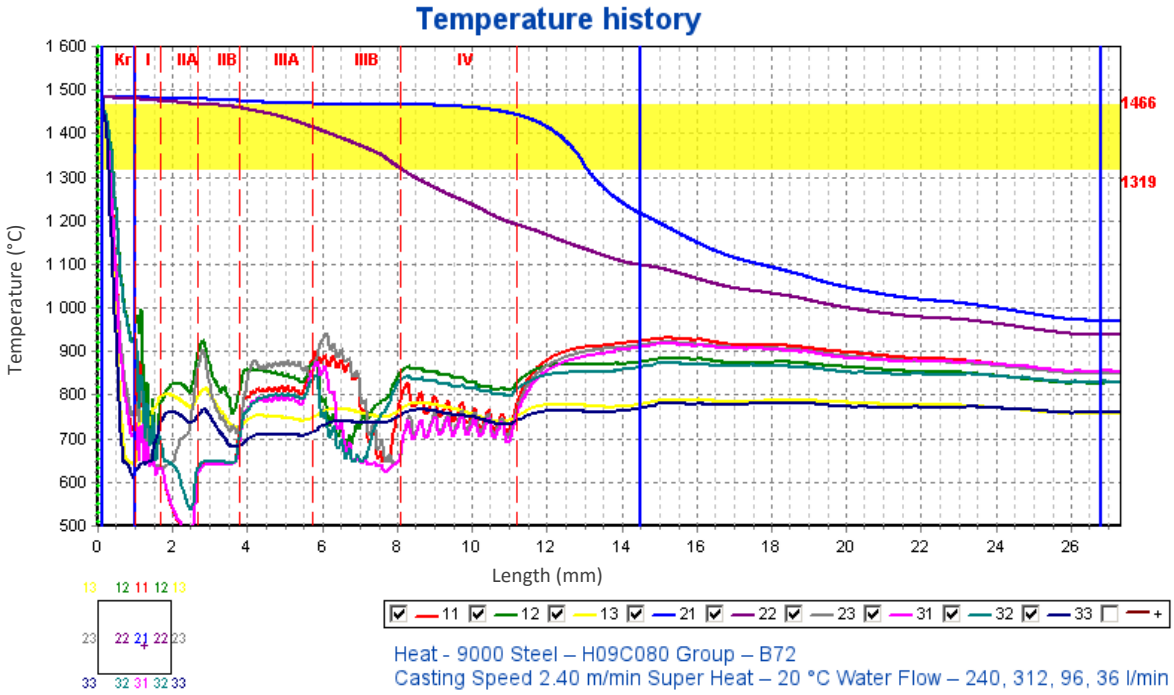

Fig. 6-11 Temperature history of six points of the cross-section of the steel billet

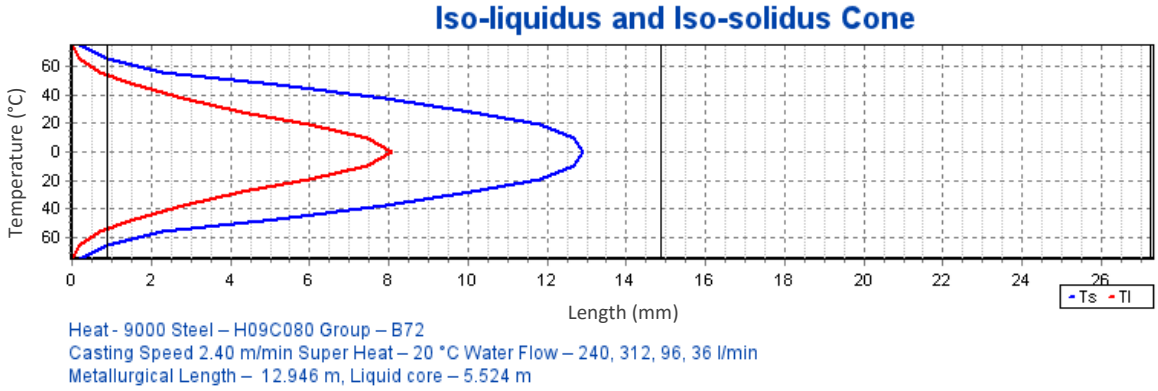

Fig. 6-12 Isoliquidus and isosolidus unrolled along the longitudinal section through the entire caster

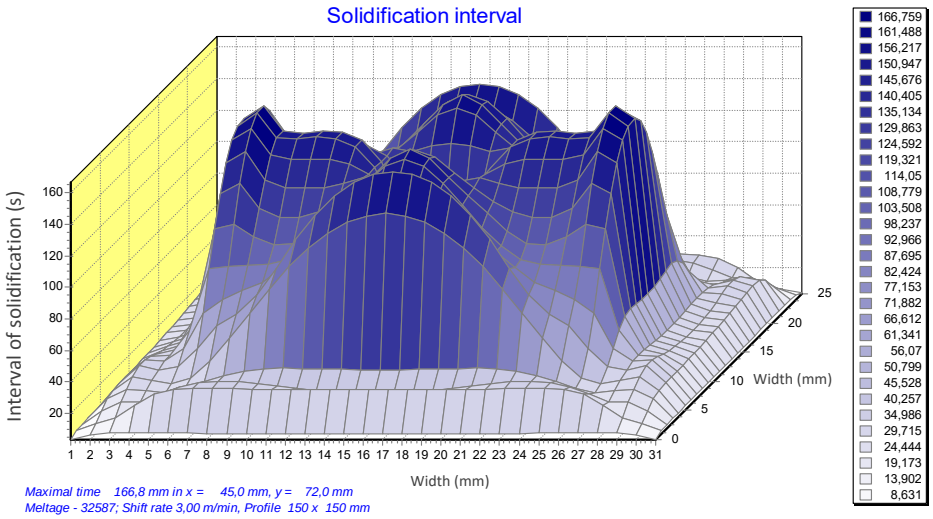

Fig. 6-13 Solidification time in cross section of the billet

The following processes were investigated:

- influence of cooling rate w_{cool} on back diffusion parameter α of selected elements,
- influence of cooling rate w_{cool} on back diffusion parameter β calculated on the basis of individual models,
- influence of cooling rate w_{cool} on maximum concentration of investigated elements $C_{S,i}$ predicted by individual models given in **Tab. 6-7**.

Tab. 6-8 Chemical composition of steel (in wt.%)

C	Mn	Si	P	S	Cu	Cr	Ni	Al_{total}	Mo
0.73	0.50	0.23	0.008	0.013	0.02	0.04	0.02	0.003	0.005

The following relations were used for calculation of back diffusion parameter α_i of the solute i (i = C, Mn, Si, S and P) according to the equation (**eq. 6-5**):

Determination of liquidus temperature T_L based on the relation:

$$T_L = T_{cast} - \sum_i m_i \cdot C_{0,i} \qquad \text{(eq. 6-9)}$$

where T_{cast} is the melting point of pure iron, m_i is the slope of the liquidus line of i^{th} element in the pseudobinary Fe-i phase diagram, and $C_{0,i}$ is the initial liquid concentration of the element.

Determination of concentration of i^{th} element in the melt $C_{L,i}$ according to the relation (**eq. 6-10**) for i = C, Mn, Si, S and P under assumption that $f_S = 1$.

$$C_{L,i} = \frac{C_{0,i}}{1-(1-k_{ef,i})f_S}, \qquad \text{(eq. 6-10)}$$

if $f_S = 1$, then relation (**eq. 6-10**) is transformed to the form of

$$C_{L,i} = \frac{C_{0,i}}{k_i}. \qquad \text{(eq. 6-11)}$$

Determination of solidus temperature T_{sol} according to the relation

$$T_S = T_{cast} - \sum_i m_i \cdot C_{L,i}, \qquad \text{(eq. 6-12)}$$

Calculation of cooling rate w_{cool} at known value of the local solidification time θ:

$$\theta = \frac{T_L - T_S}{w_{cool}} . \qquad \text{(eq. 6-13)}$$

Calculation of the secondary dendrite arm spacing L according to the relation [L6-29]

$$L = 143.9\, w_{cool}^{-0,3616} \cdot C_C^{(0.5501 - 1.996\, C_C)} , \qquad \text{(eq. 6-14)}$$

C_C is carbon content (wt.%). Values of local solidification time θ (s) were calculated with use of original temperature model B enabling simulation of temperature field of solidified casting. For the steel billet with dimensions 150 × 150 mm and chemical composition specified in **Tab. 6-8** local solidification times for the chosen technological conditions of concasting were determined within the range from 20 s (border parts of the billet) to 120 s (central part). 3D graph of this parameter is given in **Fig. 6-13.**

Tab. 6-9 Calculated values of the parameter β according to different models

θ (s^{-1})	w_{cool} ($K \cdot s^{-1}$)	Scheil	Brody-Flemings	Clyne-Kurz	Ohnaka 1	Ohnaka 2	Won-Thomas
carbon							
120	1.07	0	9.51	$9.03 \cdot 10^{-1}$	$9.05 \cdot 10^{-1}$	$9.50 \cdot 10^{-1}$	$9.51 \cdot 10^{-1}$
20	6.41	0	5.79	$8.50 \cdot 10^{-1}$	$8.53 \cdot 10^{-1}$	$9.21 \cdot 10^{-1}$	$9.22 \cdot 10^{-1}$
silicon							
120	1.07	0	$6.34 \cdot 10^{-3}$	$6.34 \cdot 10^{-3}$	$6.30 \cdot 10^{-3}$	$1.25 \cdot 10^{-2}$	$3.21 \cdot 10^{-1}$
20	6.41	0	$3.86 \cdot 10^{-3}$	$3.86 \cdot 10^{-3}$	$3.85 \cdot 10^{-3}$	$7.66 \cdot 10^{-3}$	$3.19 \cdot 10^{-1}$
manganese							
120	1.07	0	$1.36 \cdot 10^{-3}$	$1.36 \cdot 10^{-3}$	$1.36 \cdot 10^{-3}$	$2.71 \cdot 10^{-3}$	$3.16 \cdot 10^{-1}$
20	6.41	0	$8.27 \cdot 10^{-4}$	$8.27 \cdot 10^{-4}$	$8.26 \cdot 10^{-4}$	$1.65 \cdot 10^{-3}$	$3.16 \cdot 10^{-1}$
phosphorus							
120	1.07	0	$3.46 \cdot 10^{-2}$	$3.46 \cdot 10^{-2}$	$3.34 \cdot 10^{-2}$	$6.47 \cdot 10^{-2}$	$3.44 \cdot 10^{-1}$
20	6.41	0	$2.11 \cdot 10^{-2}$	$2.11 \cdot 10^{-2}$	$2.06 \cdot 10^{-2}$	$4.04 \cdot 10^{-2}$	$3.33 \cdot 10^{-1}$
sulphur							
120	1.07	0	$4.07 \cdot 10^{-1}$	$3.18 \cdot 10^{-1}$	$2.89 \cdot 10^{-1}$	$4.49 \cdot 10^{-1}$	$5.41 \cdot 10^{-1}$
20	6.41	0	$2.48 \cdot 10^{-1}$	$2.30 \cdot 10^{-1}$	$1.99 \cdot 10^{-1}$	$3.31 \cdot 10^{-1}$	$4.72 \cdot 10^{-1}$

Table 6-9 predicts values of the parameter β calculated according to the micro-segregation models from **Tab. 6-7**. The following facts follow from comparison of values of the parameter β in **Tab. 6-9** for non-equilibrium models of Brody-Flemings, Ohnaka, Clyne-Kurz and Won-Thomas:

1. For the given cooling rate carbon has the highest values β, which is interrelated with its biggest diffusion coefficient (in comparison with Si, Mn, P and S). It has the strongest tendency to back diffusion in solid phase, i.e. the biggest predisposition for homogenization in solid phase. Contrary to that manganese has the lowest value of this parameter, which again is related to its lowest diffusion coefficient. Value of this parameter β generally decreases with the increasing cooling rate, i.e. rate of diffusion homogenization in concentrations in solid phase decreases. However, it is necessary to take into account that both the local time of solidification and the secondary dendrite arm spacing decreases with increasing cooling rate, which means that homogenization occurs at smaller distance.
2. For Mn, Si and P the models of Brody-Flemings and Clyne-Kurz predict the same value β for all cooling rates, for S the values slightly differ and this difference increases with decreasing cooling rate. Difference of prediction of the parameter β for carbon according these two models is of one order and it slightly increases with the increasing cooling rate. These trends confirm the fact that model of Clyne-Kurz passes to the model of Brody-Flemings, when influence of diffusion is small.
3. Model Ohnaka 1 predicts for Mn, Si and P almost the same values of the parameter β as Brody-Flemings' model. The differences are slightly bigger for S and decreases with the decreasing cooling rate; the differences for C are again of one order and they increase with the increasing cooling rate.

4. Won-Thomas' model predicts for all investigated constitutive elements (Mn, Si, P and S) higher value of β than other models. For Si, Mn and P its values are approximately the same. Furthermore, prediction of the parameter β for Mn and Si is not influenced by cooling rate; for P and S is slightly influenced – with the increasing cooling rate the influence of back diffusion decreases. These effects may be caused by the fact that this model assumes coarsening of dendrites in the course of solidification and it includes into the parameter β this influence by the value 0.1 (see the formula for β calculation in Tab. 6-7, Won-Thomas Model). It means that if the value of the parameter β without assumption of coarsening is smaller than 0.1, then influence of cooling rate on predicted micro-segregation is according to this model negligible.
5. Influence of cooling rate on back diffusion is manifested the most in the elements with higher value of diffusion coefficient – carbon, sulphur.

Predicted maximum concentrations for the solid fraction $f_S \rightarrow 1$ are given in **Tab. 6-10**, from it follows that change of cooling rate in the assumed extent has only small influence on of predicted segregation.

Tab. 6-10 Predicted values of max. concentration of elements ($f_S \rightarrow 1$) according to individual models

θ (s)	w_{cool} (K·s^{-1})	Scheil	Brody-Flemings	Ohnaka 1	Ohnaka 2	Clyne-Kurz	Won-Thomas
carbon (wt.%)							
120	1.07	2 260	0.351	0.762	0.746	0.763	0.746
20	6.41	2 260	0.393	0.783	0.757	0.785	0.756
silicon (wt.%)							
120	1.07	90.3	1.867	1.872	1.356	1.867	0.334
20	6.41	90.3	2.361	2.365	1.707	2.361	0.335
manganese (wt.%)							
120	1.07	8.1	1.763	1.763	1.516	1.763	0.587
20	6.41	8.1	1.965	1.965	1.689	1.965	0.587
phosphorus (wt.%)							
120	1.07	172.6	0.117	0.120	0.069	0.117	0.018
20	6.41	172.6	0.179	0.182	0.102	0.179	0.018
sulphur (wt.%)							
120	1.07	280.5	0.029	0.040	0.027	0.037	0.022
20	6.41	280.5	0.046	0.057	0.035	0.050	0.025

6.3.3 Conclusion

The chapter investigates influence of cooling rate on back diffusion of selected elements (C, Si, Mn, P and S) at solidification of continuously cast steel billet. Back diffusion was characterised by back diffusion parameter β used in numerous micro-segregation models. The following main facts were established for the chosen conditions of investigation:

- Carbon has generally the highest values of this parameter, i.e. it has the strongest tendency to back diffusion in solid phase; contrary to that manganese has the lowest value of this parameter.
- Value of this parameter generally decreases with the increasing cooling rate, i.e. rate of diffusion balancing of concentration decreases.
- Cooling rate changes along the cross-section of the billet 150 × 150 mm only very little, under these conditions the influence of cooling rate on the parameter β is manifested only in the models, which do not take into account coarsening of dendrite branches.
- Change of cooling rate in the assumed extent (approx. 1 to 6.4 K·s^{-1}) has only small influence on change of magnitude of the maximum segregation of elements.

The results were also presented in the peer-reviewed journals and at prestigious conferences [L6-33 to 6-40].

6.4 Literature

[L6-1] Kraft T. and Chang Y. A.: Predicting microstructure and microsegregation in multicomponent alloys, *JOM*, December 1997, 20–28.

[L6-2] Rappaz M.: Modelling of microstructure formation in solidification processes", *Int. Mater. Rev*., 34 (1989), 93–123.

[L6-3] Stefanescu D.M.: Methodologies for modelling of solidification microstructure and their capabilities, *ISIJ Int.,* 35 (1995), 637–650.

[L6-4] Boettingen W. J., et al.: Solidification microstructures: recent development, future directions, *Acta Mater*., 48 (2000), 43–70.

[L6-5] Dobrovská J., Dobrovská, V., Rek A. and Stránský, K.: Possible ways of prediction of the distribution curves of dendritic segregation of alloying elements in steels, *Scripta Mat*., 38 (1998), 1583–1588.

[L6-6] Dobrovská V., Dobrovská J., Rek A. and Stránský K.: The dendritic segregation of impurities in steel and its distribution curves prediction, *Kovove Mater*., 33 (1995), 462–472.

[L6-7] Gungor M.N.: A statistically significant experimental technique for investigating micro-segregation in cast alloys, *Metall. Trans*. *A*, 20A (1989), 2529–2538.

[L6-8] Scheil E.: Uber die eutektische kristallisation, *Z. Metallkd.*, 34 (1942), 70–80.

[L6-9] Levíček P. and Stránský K.: *Metallurgical defects of steel castings (causes and their elimination) In Czech*. SNTL, Praha 1984, p. 257.

[L6-10] Eckstein H.J.: *Wärmebehandlung von Stahl*. VEB, DVG, Leipzig 1971, p. 139.

[L6-11] Dobrovská J., Stránský K., Dobrovská V. and Kavička F.: Characterization of continuously cast steel slab solidification by means of chemical micro-heterogeneity assessment, *Hutnické listy*, 62 (2009) 5, 4–9.

[L6-12] Preßlinger H., et al.: Methods for assessment of slab centre segregation as a tool to control slab continuous casting with soft reduction, *ISIJ Int*., 46 (2006), 1845–1851.

[L6-13] Kavička F., Štětina J., Stránský K., Heger J., Dobrovská J. and Dobrovská V.: Optimization of an Industrial Concasting Technology via Two Numerical Models. In *Proceedings of the International Conference CCCT 03.* Orlando, USA, International Institute of Informatics and Systemics, Orlando. 2003. p. 423–428.

[L6-14] Kavička F., Štětina J., Sekanina B., Ramík P. and Dobrovská J.: Numerical and experimental investigation of heat and mass transfer of a concasting. In *Computational Methods and Experimental Measurements X.* Boston (USA), WIT Press Southampton, Boston. 2001. p. 779–788.

[L6-15] Kavička F., Štětina J., Stránský K., Dobrovská J., Dobrovská V. and Heger J.: Two numerical models for prediction of an industrial concasting process. In *Proceedings of the 2003 ASME Pressure Vessels and Piping Conference.* Cleveland, US, The American Society of Mechanical Engineers. 2003. p. 109–118.

[L6-16] Kavička F., Štětina J., Sekanina B. and Ramík P.: An original numerical model of heat and mass transfer in a concasting machine. In *Proceedings of the 3rd International conference on advances in fluid mechanics AFM 2000*, Montreal, Canada, May 2000, p. 705–714.

[L6-17] Kavička F., Štětina J., Stránský K., Dobrovská J., Dobrovská V. and Velička B.: Original numerical simulation of heat and mass transfer in a concasting technology. In *Proceedings of the 6th International Conference Semi-Solid*, Italy, Turin, September 2000, p. 813–818.

[L-6-18] Kavička F., Štětina J., Sekanina B., Ramík P., Heger J., Stránský K., Dobrovská J., Dobrovská V., Velička B., Kožušník Z., Masarik M. and Kozelský V.: Mathematical and experimental investigation of the transient field of a concast slab. I. The numerical model. *Hutnické listy*, 54 (2001) 6-7, 46–53.

[L6-19] Kavička F., Štětina J., Sekanina B., Ramík P., Heger J., Stránský K., Dobrovská J., Dobrovská V., Velička B., Kožušník Z., Masarik M. and Kozelský V.: Mathematical and experimental investigation of the transient field of a concast slab. II. Experimentation and measurement. *Hutnické listy*, 54 (2001) 6-7, 54–60.

[L6-20] Štětina J., Kavička F., Sekanina B., Ramík P., Heger J., Stránský K., Dobrovská J., Dobrovská V., Velička B., Kožušník Z., Masarik M. and Kozelský V.: Mathematical and experimental investigation of the transient field of a concast slab. III. Results and their discussion. *Hutnické listy*, 54 (2001) 8, 44–50.

[L6-21] Štětina J., Kavička F., Stránský K., Dobrovská J. and Dobrovská V.: The use of two numerical models in industrial concasting technology. In *ICCE/8 - International Community for Composites Engineering.* Tenerife (Spain), David Hui. 2001. p. 889–891.

[L6-22] Dobrovská J., Dobrovská V., Stránský K., Kavička F., Štětina J., Ramík P. and Velička B.: The temperature field and chemical heterogeneity of CC steel slab. I. The mathematical modelling of chemical heterogeneity over the section area of a CC slab. *Hutnické listy,* 54 (2001) 8, 31–38.

[L6-23] Dobrovská J., Dobrovská V., Stránský K., Kavička F., Štětina J., Ramík P. and Velička B.: The temperature field and chemical heterogeneity of CC steel slab. II. The fundamental parameters and interconnection of models. *Hutnické listy,* 54 (2001) 8, p. 39–43.

[L6-24] Štětina J., Kavička F., Stránský K., Dobrovská J. and Heger J.: The numerical and experimental investigation of a concasting process. In *Computational Methods and Experimental Measurements XI.* Neuvedeno. Halkidiki, Geece, WIT Press. 2003. p. 721–730.

[L6-25] Kobayashi S.: A Mathematical Model for Solute Redistribution during Dendritic Solidification. *Trans. ISIJ*, 28 (1988), 535.

[L6-26] *Smithells Metals Reference Book*, Butterworth-Heinemann, Seventh Edition, 1998.

[L6-27] Kubíček L.: *Segregation of admixture elements at dendritic crystallisation of aluminium alloys (in Czech).* Investigation report of ČSAV, ACADEMIA Praha, 10, 1972. 121 p.

[L6-28] Pfann W.G.: Principles of Zone-Melting. *J. Metals*, (1952) 4, 747–755.

[L6-29] Won Y-M. and Thomas B.G.: Simple Model of Microsegregation during Solidification of Steels. *Met. Metall Mater Trans A*, 32A (2001), 1755–1767.

[L6-30] Clyne T. W. and Kurz W.: Solute redistribution during solidification with rapid solid state diffusion. *Metall. Trans. A*, 12A (1981), 965–972.

[L6-31] Dobrovská J.: *Chemical heterogeneity of metal alloys*. (In Czech) Monography. MONTANEX, Ostrava, 2005.

[L6-32] Kavička F., Štětina J., Stránský K., Heger J., Dobrovská J. and Dobrovská V.: Optimization of an Industrial Concasting Technology via Two Numerical Models. In *Proceedings of the International Conference CCCT 03.* Orlando, USA, International Institute of Informatics and Systemics, Orlando. 2003. p. 423–428.

[L6-33] Dobrovská J., Kavička F., Francová H. and Dobrovská V.: Study of cooling rate effect on back-diffusion during solidification of continuously cast steel billet. In the CD ROM of 19th Annual international conference on composites/nano engineering ICCE-19, Shanghai, China, July 2011.

[L6-34] Dobrovská J., Kavička F., Štětina J. and Stránský K.: Numerical models of the temperature field and chemical heterogeneity of a concast steel slab. In *Proceedings of the 21st Canadian Congress of Aplied Mechanics CANCAM 2007.* Toronto, CANCAM. 2007. p. 384–385.

[L6-35] Kavička F., Štětina J., Stránský K., Dobrovská J. and Heger J.: Optimization of a concasting technology by two numerical models. In *ICAMT 2004. Third International Conference on Advanced Manufacturing Technology.* Kuala Lumpur, International Islamic University Malaysia. 2004. p. 647–653.

[L6-36] Kavička F., Štětina J., Sekanina B., Heger J. and Velička B.: Simulation of heat transfer under air-water cooling jets. In *Abstracts 4th ECCE, Topics 9.0.* Granada, Spain, Albolote, Granada. 2003. p. 9–10.

[L6-37] Štětina J., Ramík P., Kavička F., Stránský K., Dobrovská V. and Dobrovská J.: Industrial application of two numerical models in concasting technology. In *Practical Aspects of Particle Technology Proceedings.* Budapest (Hungary), HUN-Pra-PARTEC. 2001. p. 95–100.

[L3-38] Kavička F., Stránský K., Štětina J., Dobrovská J., Dobrovská V. and Velička B.: Original numerical simulation of heat and mass transfer in a concasting technology. In *6th International Conference Semi-Solid.* 2000 Turin (Italy), Politecnico di Torino. p. 813–818.

[L3-39] Dobrovská J., Kavička F., Dobrovská V., Stránský K. and Francová H.: A new approach to evaluating the chemical micro-heterogeneity of a continuously část steel slab. *Materiali in tehnologie/Materials and technology* 47 (2013) 1, 79–83.

[L6-40] Kavička F., Štětina J., Sekanina B., Stránský K., Dobrovská J. and Heger J.: The optimization of a concasting technology by two numerical models. *J. Mater. Process. Technol.* 185 (2007) 1-3, 152–159.

7 The possibilities of verifying the cross cracking mechanism in the concast steel slab 1 300 × 145 mm

7.1 Introduction

The crack was found inside a low-carbon steel slab with l 300 × l45 mm cross-section, after cutting. This, almost 600 mm tortuous crack, passed through the middle part of the slab thickness, and was displaced asymmetrically towards one edge of the slab (**Fig. 7-1**). The chemical composition of the slab steel – low-alloyed manganese-steel – is (in wt.%): 0.16 C, 1.39 Mn, 0.37 Si, 0.015 P, 0.007 S, 0.06 Cr, 0.030 Cu, 0.048 Al(sum), 0.010 Nb, 0.010 Mo and 0.10 V.

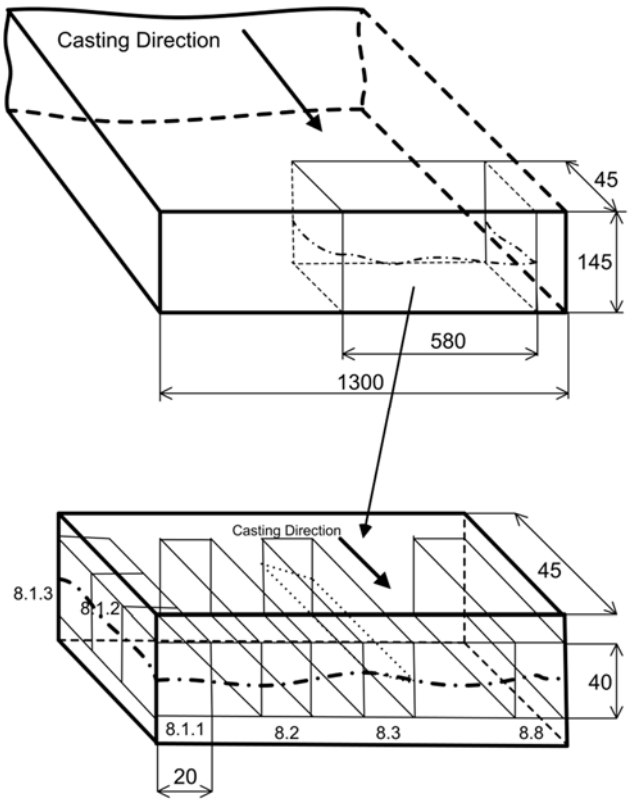

- The distances between the samples 8.1, 8.2 and 8.3 are 200 mm.
- Samples 8.3 – 8.8 were extracted consecutively.
- The size of the samples represented by double numbers (i.e. number-point-number) were 41 × 20 × 45 mm.
- The size of the samples represented by triple numbers (i.e. number-point-number-point-number) were 41 × 20 × 13 mm.

Fig. 7-1 The cracking corpus extraction schema, and the estimation of metallographic samples to the heterogeneity measuring

Two original models have been used [L7-1 to 7-3] for the investigation into the mechanism and causes of cross cracking in mentioned steel slab – the 3D numerical model of the nonstationary temperature field of a concasting and the model of chemical heterogeneity of a concast slab. The first one is capable of simulating the temperature field of a caster. Experimental research and data acquisition have to be conducted simultaneously with the numerical computation – not only to confront it with the actual numerical model, but also to make it more accurate throughout the process. The utilization of the numerical model of solidification and cooling of a concasting plays an indispensable role in practice. The potential change of technology – on the basis of computation – is constantly guided by the effort to optimize, i.e. to maximize the quality of the process. After computation, it is possible to obtain the temperatures at each node of the network, and at each time of the process. The user can choose any appropriate longitudinal or cross-section of a slab and display the temperature field in a 3D or 2D graph.

The second model – the original model of chemical heterogeneity – assesses critical points of slabs from the viewpoint of their increased susceptibility to crack and fissure. In order to apply this model, it is necessary to analyze the heterogeneity of the constituent elements (Mn, Si and others) and impurities (P, S and others) in characteristic places of the solidifying slab. The model, based on measurement results obtained by an electron micro-probe, generates distribution curves showing the dendritic segregation of the analyzed element, together with the partition coefficients of the elements between the liquid and solid phases.

The combination of both models enables the prediction of cracks and fissures in critical points of the continuously cast carbon-steel slab. The first results of the investigation into mechanism and causes of the initiation of a transversal crack of the low alloy manganese steel slab were given in [L7-1 and 7-2].

There has been found out that the cross cracking is characterized of high macro-heterogeneity of manganese, carbon and sulphur. The causes of cross cracking have been explained by means of a thermokinetic calculation of a slab transient temperature field and by mean of an application of the theory of physical similarity and dimensionless criteria. There has been confirmed that two solidification cones are formed asymmetrically in the course of slab solidification and it is probable that the asymmetrically passing crack initiated on one of these two apexes.

The chapter deals with hypothesis of initiation and propagation of cross (transverse) crack verified by behaviour of tensile test samples taken from continuously cast slab of similar chemical composition within the temperature range from 25 °C to 1 450 °C. Tensile tests completed with use of 18 test bars were progressively torn under defined conditions with appropriately selected temperature differences. At the same time the following main parameters have been investigated quantitatively: tensile force (N), work to rupture (J) and contraction (%). Relief of the resulting rupture area in dependence on temperature was simultaneously investigated and documented in detail. In this manner we have obtained relations between relief of rupture area, tensile force, work to rupture and contraction of test bars taken within the specified temperature range from continuously cast slab of similar chemical composition as the slab with cross crack.

On the basis of comparison of rupture areas of cross crack ascertained in the work [L7-2] and rupture area obtained in the given interval of testing temperatures from 25 °C to 1 450 °C during this investigation (for which relationships between slab material properties and its behaviour at rupture under the relevant temperature are known) we have afterwards analogically assessed possible behaviour of slab material affected by cross crack.

In this way it is possible to particularise and verify mechanism of initiation and subsequent discrete propagation of cross crack, to evaluate temperature interval in which initiation of cross crack was of the highest probability and to assess also to what degree anomalies in applied continuous casting technology could have influenced initiation of cross crack.

7.2 The results of the simulation of the temperature field of the slab

The conditions of pouring were characterized by the temperature in the tundish (1 543 °C), by the liquidus temperature T_L = 1 519 °C, by the solidus temperature T_S = 1 479 °C, and by the shift rate of the slab (w = 1.3 m·min^{-1}).

The definition of boundary conditions is the most difficult part of the investigation of the thermokinetics of this process. The boundary conditions of the numerical model of the temperature field of the concasting are defined as the transfer of heat by convection. The heat transfer coefficient *htc* includes the so-called reduced convection coefficient corresponding to heat transfer by radiation [L1-31].

The only, but extremely important, coefficient, after leaving the crystallizer, is the *htc* on the surface of the concasting, and is mainly dependent on the temperature of the surface, the shift rate and the intensity of spraying. This subchapter therefore focuses mainly on a mantion about heat transfer coefficients under air-water cooling jets, which spray the slab in the so-called secondary-cooling zone. Regarding the fact that on a real caster, where there are many types of jets with various settings positioned inside a closed cage, it is practically impossible to conduct measurement of the real boundary conditions. Therefore, a laboratory device was introduced in order to measure the cooling characteristics of the jets. In order to cover all types of jets and their layouts (incl. their settings) on specific caster, it was necessary to conduct 22 experimental measurements. **Figures 7-1a** and **7-1b** illustrates for example the courses of the *htc* for one jet in direction of moving and direction of cross.

Despite the fact that the laboratory device provides a very good basis for numerical modeling of the temperature field of a slab, it is suitable to expand the experimentation with additional measurements on a real caster.

Regarding the above-mentioned, the measurements can be conducted only in a limited number of points. Therefore, the position, which affects the quality of the surface of the slab the most, was selected, i.e. the region closest to the crystallizer—the first section of the secondary-cooling zone. A total of four pyrometers were positioned within the cage. The pyrometers were placed inside

a special casing in order to be able to withstand extreme temperatures. Furthermore, it is necessary to use compressed air to disperse the arising water vapor, which would otherwise distort the results attained by the optical measurement of the surface temperatures.

The course of the reduced heat transfer coefficient is illustrated in **Fig. 7-2**. It is obvious that radiance is dependent on the surface temperature.

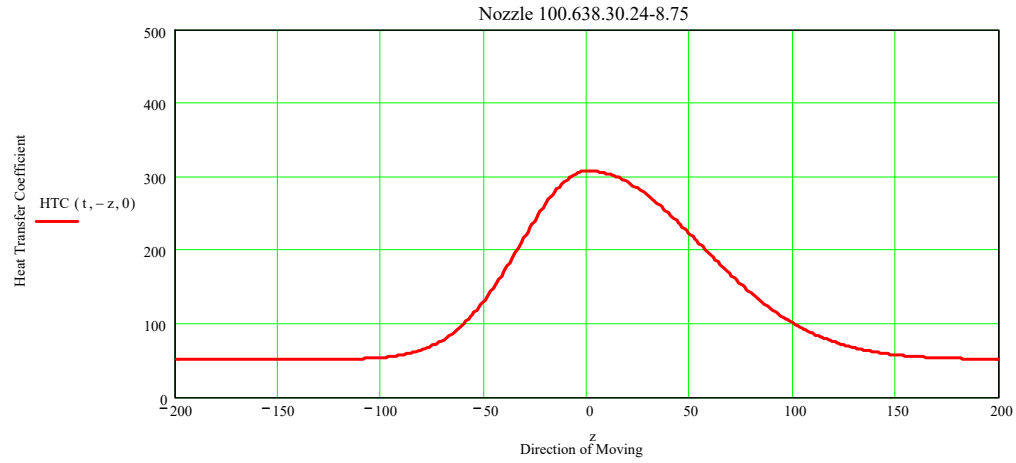

Fig. 7-1a The htc for one of the many jets – Direction of moving

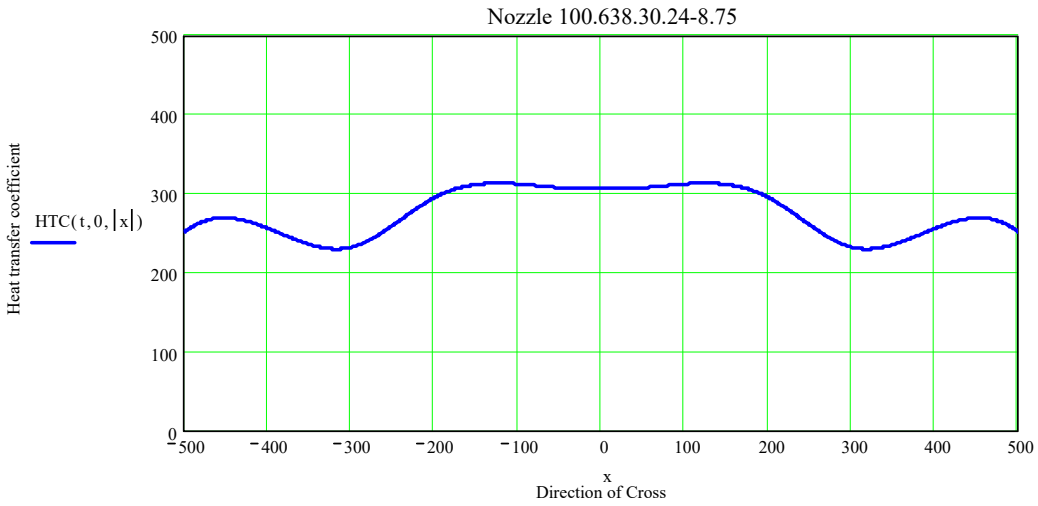

Fig. 7-1b The htc for one of the many jets – Directon of cross

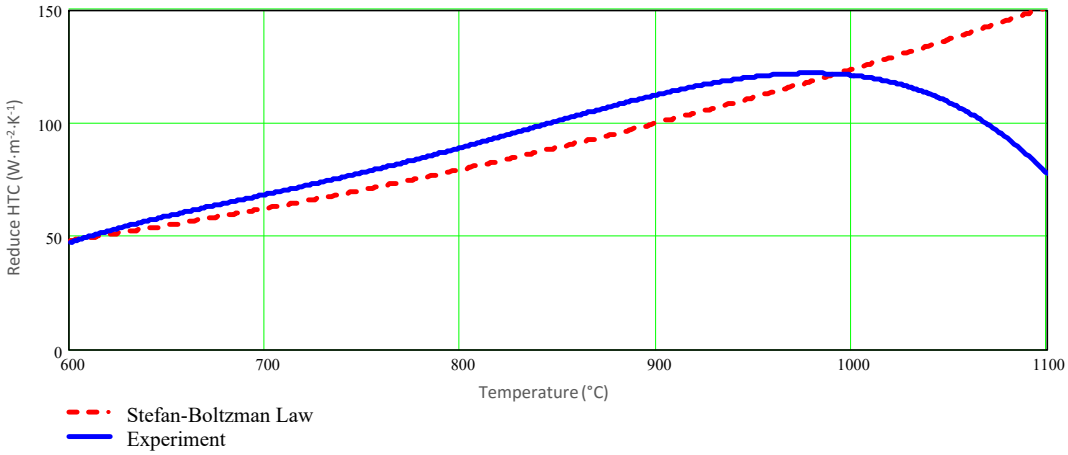

Fig. 7-2 The dependence of the reduced *htc* on temperature

After computation, it is possible to obtain the temperatures at each node of the network, and at each time of the process. The graph in **Fig. 7-3** is very useful because it shows the temperature history in selected points of the cross-section of the slab. The course of the temperature can be displayed in any user-defined point. The user can therefore choose for example any appropriate longitudinal of a slab and display the temperature field in a 2D or 3D graph whenever necessary. **Figure 7-4** shows the 2D temperature field of the 1 300 × 145 mm steel slab in its axial longitudinal section and **Fig. 7-5** the 3D temperature field in the axial longitudinal section of the slab. **Figure 7-6** represents the 3D temperature filed of the axial longitudinal section of the slab.

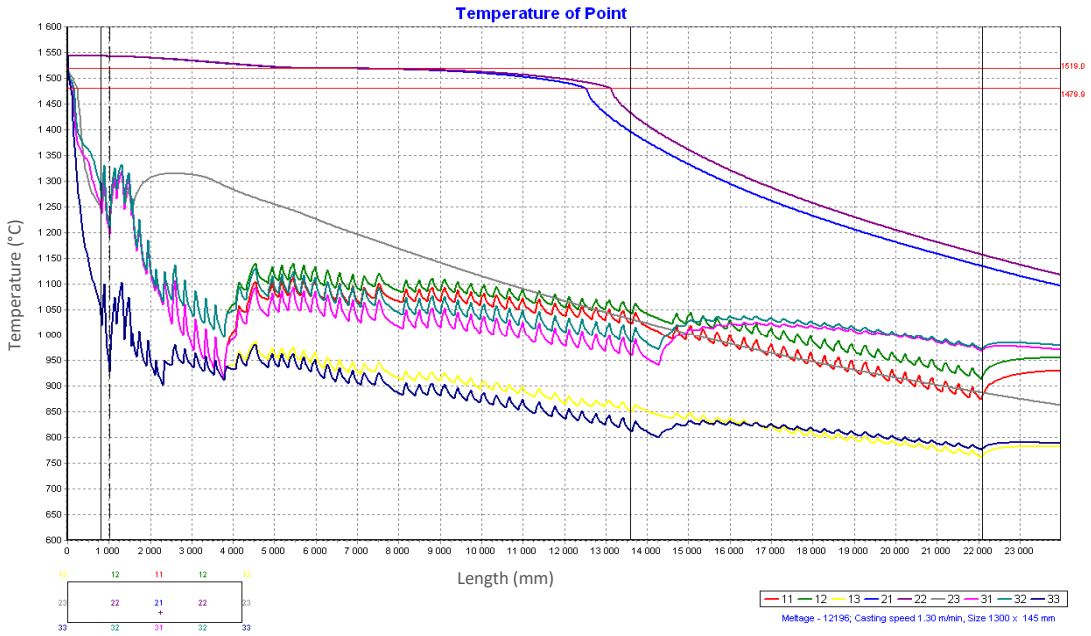

Fig. 7-3 The temperaturew history in selected points of the cross-section

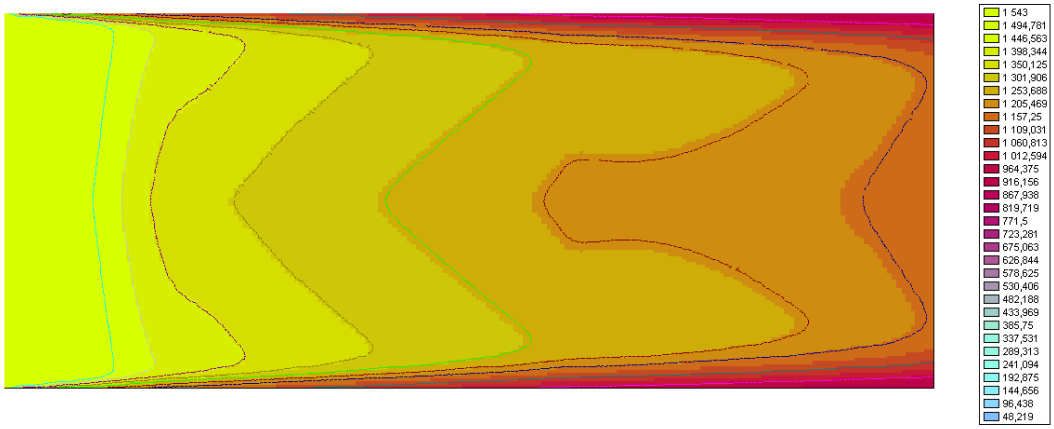

Fig. 7-4 The 2D temperature field of the axial longitudinal section of the slab

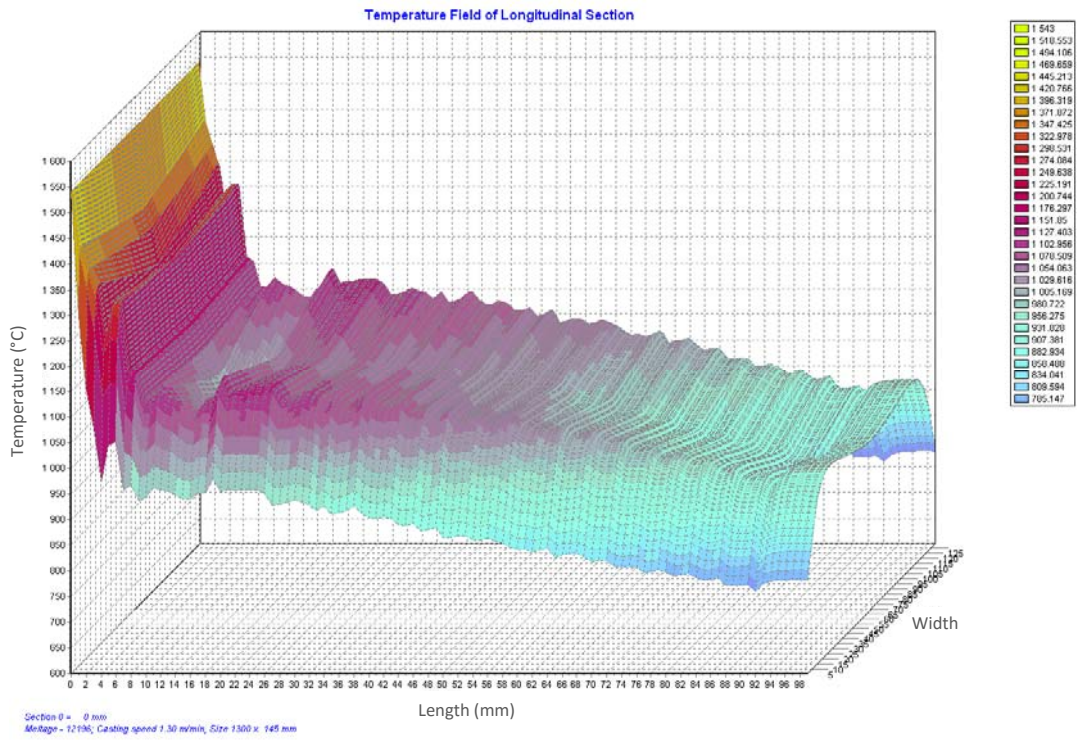

Fig. 7-5 The 3D temperature field of the axial longitudinal section of the slab

7.3 Morphology and heterogeneity of a transversal crack in the slab

The aim of the measurements was to evaluate the course of the crack, the character of the structure in which the crack was propagating, the heterogeneity of the chemical composition of the elements in the matrix in the vicinity of the crack, and even the concentration of elements at the crack surface. Investigations were also made into the phenomena of initiation and propagation of the crack, as well as evaluation of the main cause for such phenomena [L7-4 and 7-5].

Measurement of the chemical heterogeneity first required a certain part of the crack with its surrounding to be extracted mechanically from the slab. The total sectional area with the course of the crack is shown in **Fig. 7-1**, which also illustrates the method of extraction of the samples. The course of the crack—shown by a dot-and-dash line towards the sample, marked 8.8 in **Fig. 7-5** — shows discontinuity. The samples were prepared from the section of the slab, whereby the samples 8.1.1, 8.1.2, 8.2, 8.3 and 8.8 were selected for the measurement of the heterogeneity of elements.

The thickness of the samples varied around 13 mm. No sample with an evident crack fell apart, despite the fact that the crack was quite obvious both on the thin-section side as well as on the reverse side. The thin sections were wet-ground with abrasive paper and polished by means of a diamond paste with a granularity of less than l μm.

7.3.1 Measurement of the concentration series of elements within the steel matrix

Concentration of elements is measured using energy-dispersing (ED) X-ray spectral microanalysis and with the help of the micro-analytic complex JEOL JXA-8600/KEVEX Delta V-Sesame (see subchapter 6.2) The prepared metallographic thin sections were first slightly etched by 2%-nital to make the microstructure more visible; with the help of the light microscope a zone suitable for analyzing was selected and marked by a micro-hardness tester. Then, the samples were re-polished using the diamond paste in order to remove the etched layers and the microanalysis was carried out on each sample. The working conditions were the same for all samples and were chosen as follows: the accelerating voltage of the primary electron beam was 15 kV, the current of the primary electron beam was 1 nA and the collecting time (i.e. measurement) of one X-ray spectrum lasted 50 s. The KEVEX

Quantex VI software was applied here and the quantitative evaluation of the measured concentration of elements was conducted using pure-metal standards. The ZAF-correcting system was applied, including corrections to the atomic number, absorption and fluorescence, whereby the concentrations of eight elements were determined, namely Al, Si, P, S, Ti, Cr, Mn and Fe. The measurements of concentration of elements was carried out with each sample in 101 points along a section of 1 000 μm, the distance between two consecutive points being l0 μm [L7-6].

The measurement results from five concentration series (samples 8.1.1, 8.1.2, 8.2, 8.3 and 8.8) are in the **Tab. 7-1** (column 'Matrix').

Tab. 7-1 Results of concentration microanalysis (in wt.%) in the matrix (five samples 8.1.1, 8.1.2, 8.2, 8.3 and 8.8) and on the surface cracking (sample 8.3)

Elements	Matrix*) (Arithm. mean and std. dev.)	Regions				
		A	B	C	D	E
Al	0.03 ± 0.01	0.11	0.03	0.09	0.04	0.20
Si	0.32 ± 0.03	0.55	0.30	0.32	0.31	0.37
P	0.03 ± 0.01	0.07	0.03	0.01	0.01	0.02
S	0.03 ± 0.00	0.14	0.91	0.07	0.15	0.46
Ti	0.009 ± 0.001	0.02	0.26	0.03	0.07	0.14
Cr	0.03 ± 0.00	0.09	0.26	0.12	0.16	0.32
Mn	1.65 ± 0.10	1.71	4.72	1.43	1.96	3.26
Fe	97.91 ± 1.26	97.31	93.50	97.94	97.30	95.24
O	without oxides	without oxides	oxides	without oxides	oxides	oxides
Crack	-	Cleavage	Dendritic	Cleavage	Dendritic	Dendritic

*Note: *) The concentrations of elements in the matrix were determined as the arithmetic mean of analyses of five metallographic samples*

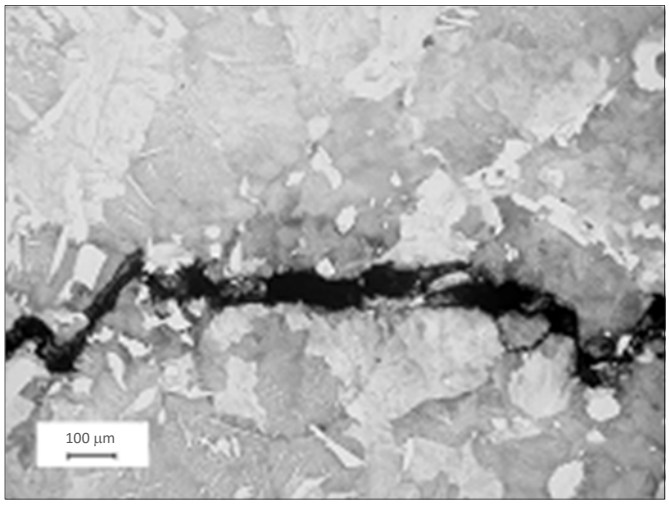

Fig. 7-6 The perlitic structure of matrix rounding the cracking in the samples No. 8.3.1. The cracking has the interdenritic coarse. Etched by nital.

The tortuous inter-dendritic course of the crack in sample 8.3.1, and the almost pure pearlitic matrix surrounding the crack, is shown in **Fig. 7-6**.

7.3.2 Measurement of the concentration of elements at the crack-surface

Since none of the metallographic samples broke up in two parts, it was necessary to open each crack. The approximately 13 mm sample 8.3.1, where the course of the crack on both sides was most evident, was selected for investigation. The sample was first milled down to a thickness of 8 mm, then cooled to the temperature of liquid nitrogen (approximately –196 °C), clamped into a vice and broken into two by a hammer. After breaking, the fracture surfaces were briefly dipped into ethanol and immediately reheated to room temperature. The original surface of the crack was oxidized, compared to the freshly prepared fracture surface. Measurements show that the original surface of the crack was approx. 22% of the overall fracture surface. This indicates that the crack is not continuous across the section, but in several parts.

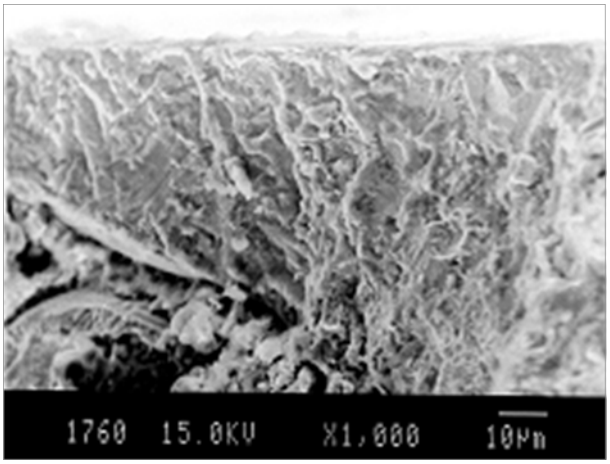

Fig. 7-7 The detail of an origin cracking surface. Scanning microscope – secondary electrons.

A detail of the oxidized surface of the original crack is illustrated in **Fig. 7-7**. The fracture area reveals a relief feature and is covered by a thin layer of oxides. **Figure 7-8** illustrates a detail of a fresh crack—the result of cooling in liquid nitrogen and breaking in two parts.

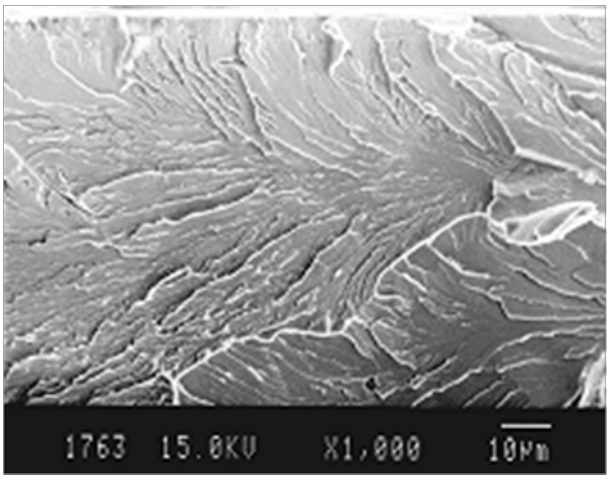

Fig. 7-8 The detail of a liquid nitrogen cracking surface. Scanning microscope – secondary electrons.

The fracture surface reveals cleavage transcrystalline morphology with a distinct stream feature. Its morphology indicates considerable brittleness of the matrix of the slab at the temperature of liquid nitrogen. A profound examination of the surface of the original crack revealed shrinkages at the surface of the original crack, as is illustrated in **Fig. 7-9**. Shrinkages at the surface of the original crack prove that initiation of the crack was associated with the presence of microshrinkages and microcavities.

Microanalysis of the same elements, as in the matrix, was also carried out at the fracture surface. The distribution of elements was scanned on the surface of the fracture on an area of approx. 1 mm^2 for 300 s. The remaining measured parameters and the method of processing were the same as with the measurement of concentration of elements in the matrix.

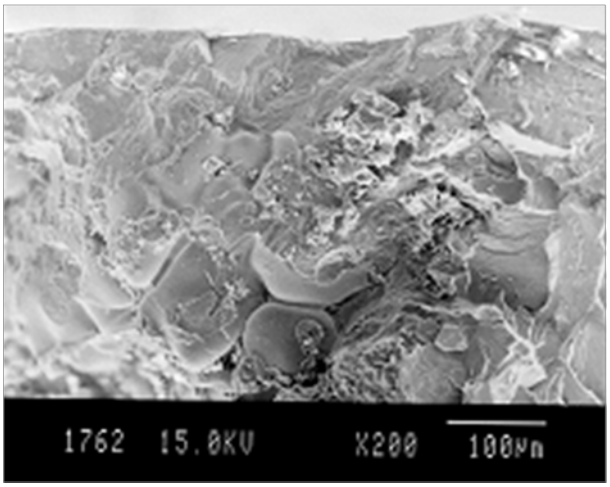

Fig. 7-9 The detail of an origin cracking surface with the porosity. Scanning microscope – secondary electrons.

The measurements of concentration of elements (**Tab. 7-1**) were performed in the following regions of sample 8.3:

- Region A – at the edge of the sample at the surface of the fresh crack.

- Region B – on the oxidized surface of the original crack, with shrinkage porosity as shown in **Fig. 7-9**.
- Region C – on the fresh crack surface in the middle of the sample.
- Region D – on the oxidized surface of the original crack.
- Region E – on the oxidized surface of the original crack, with a sporadic shrinkage porosity.

Tab. 7-1 contains the measurement results, together with the average chemical composition of the matrix—as measured in the vicinity of the crack and in the form of an arithmetic mean of the analyses of all of the five metallographic samples 8.1.1, 8.1.2, 8.2, 8.3 and 8.8.

7.3.3 Measurement of the concentration of elements in the steel matrix

It is obvious from the results of the investigation of the crack (**Tab. 7-1**), completed by the metallographic examination (**Fig. 7-1**), that the crack occurred very close to in the middle of the slab thickness.

The crack was not completely continuous in its plane and, therefore, it is considered to be a zone of discontinuous local planar cracks. The individual cracks propagated inter-dendritically (**Fig. 7-6**).

The original cracks were found by metallographic examination only in places where the pearlitic structure had uniquely prevailed. Nevertheless, in the places of occurrence of almost pure pearlitic structure, the cracks were mutually separated by strips of compact and solid slab material. Furthermore, it was obvious from the samples that any material discontinuity in the slab disappears in the zone where the proportion of ferrite increases at the expense of pearlite. In samples, where the proportions of ferrite and pearlite in the structure were almost identical—in this case it was in the prolongation of the examined crack in sample 8.8—the crack disappeared.

The measurements of concentration of elements have shown that the areas with prevailing pearlitic structures (in which this type of crack propagates) have a higher concentration of Mn and also—slightly—Si, S and P (**Tab. 7-1**) than in the zones where ferrite and pearlite occur in the same ratio. The almost pure pearlitic structure indicates that the occurrence of cracks is also associated with a higher concentration of C.

Thus, the measurements of the concentration series of elements in the matrix have shown that the occurrence of the transversal crack is associated mostly with significant zonal (macroscopic) and also dendritic (microscopic) segregation of Mn and C. Segregation of the remaining analyzed elements, which are of very low concentrations (Al, Si, P, Ti and Cr, with the exception of S), is not so significant.

7.3.4 Measurement of the concentration of elements at the original crack-surface

Tab. 7-2 Concentrations of elements (in wt.%) at the original-crack surface and at the fracture surface in liquid nitrogen

Element	Surface of original crack (regions B, D and E)		Fracture surface in liquid nitrogen (regions A and C)		Concentration difference %X(B,D,E) – %X(A,C)
	C_{av}	s_x	C_{av}	s_x	
Al	0.090	0.095	0.094	0.068	-0.004
Si	0.327	0.038	0.435	0.163	-0.108
S	0.477	0.391	0.105	0.049	+0.372
P	0.020	0.010	0.040	0.03	-0.020
Ti	0.157	0.096	0.025	0.007	+0.132
Cr	0.247	0.081	0.105	0.021	+0.142
Mn	3.313	1.381	1.570	0.198	+1.743
Fe	95.347	1.902	97.625	0.445	-2.278

Table 7-1 indicates that the concentrations of Mn and S at the surface of the original crack are significantly higher than those in the matrix. The results of these measurements therefore confirm that the crack passes through places with a high segregation of Mn and, furthermore, in contrast to the measurements of concentrations of elements in the matrix, a high segregation of S. **Table 7-2** contains the results of the measurements of concentrations of elements at the surface of the original crack (regions B, D and E). It compares the concentrations of elements, measured at the surface of the original crack, with the concentrations of the same elements measured at a clean cleavage fracture (regions A and C), which initiated as a result of opening the original crack after freezing in liquid nitrogen.

7.3.5 Discussion

As given in **Tab. 7-2**, a significantly increased concentration of Mn (+1.743 wt.%) and S (+0.372 wt.%), and also a higher concentration of Ti (+0.132 wt.%) and Cr (+0.142 wt.%), are obvious at the surface of the original transversal crack (compared with the surface of the clean fracture). On the other hand the concentrations of Al, Si, P and Fe are somewhat reduced.

There are differences in concentrations of elements in the matrix of the same slab with the crack (**Tab. 7-1** - in the 'Matrix' column). Comparing these concentrations with those given in **Tab. 7-2** and marked as the surface (regions B, D and E) crack and the surface in liquid nitrogen (regions A and C), then it is obvious that—with the exception of P (and Fe)—that the average concentration of the remaining elements (i.e. Al, Si, S, Ti, Cr and Mn) analyzed in the matrix in a certain distance from the crack is smaller than that in the zones measured directly at the surface of the crack or fracture. Accordingly, the concentrations of Al, Si, S, Ti, Cr and Mn increase towards the crack that reveals and inter-dendritic course.

The results of these analyses, as well as of the fundamental investigations, show quite clearly that the crack has an inter-dendritic course, whereby, most probably, it initiates in zones with segregation of the elements that are associated with the presence of shrinkage microporosity.

The zonal segregation takes place during slow solidification of the melt. On the basis of the thermokinetic calculation of a transient temperature field of a 1 300 ×145 mm slab [L7-5], two solidification cones are formed within a solidifying slab. **Figure 7-4** shows that the apexes are symmetrically distributed over the sectional area of slab. It is probable that the asymmetrically passing crack initiated in one of these two apexes. The concentrations and metallographic analyses suggest that—in the case of zonal segregation—there could be significant positive co-operation of C and Mn.

7.3.6 Conclusion

a) The transversal internal cracks of the described type in a concast slab initiate consecutively and are mutually discontinuous.

b) The course of transversal cracks is inter-dendritic and is characterized by a significantly increased concentration of Mn, S and C, and also by an increased concentration of Cr and Ti, i.e. with a high zonal segregation of the mentioned elements.

c) The cracks originate in the vicinity of the solidus temperature, and with a certain amount of the inter-dendritic melt.

d) Propagation of cracks takes place mostly within the solidus region and, with decreasing temperature, it gradually comes to a halt, thus causing no interconnection.

e) The causes of zonal segregation of elements are most probably associated with very slow solidification at one of the two solidification cones.

7.4 Fracture behaviour of analysed slabs

The chapter deals with hypothesis of initiation and propagation of cross (transverse) crack verified by behaviour of tensile test samples taken from continuously cast slab of similar chemical composition within the temperature range from 25 °C to 1 450 °C. Tensile tests completed with use of 18 test bars were progressively torn under defined conditions with appropriately selected temperature differences. At the same time the following main parameters have been investigated quantitatively: tensile force (N), work to rupture (J), and contraction (%). Relief of the resulting rupture area in dependence on temperature was simultaneously investigated and documented in detail. In this manner we have obtained relations between relief of rupture area, tensile force, work to rupture and contraction of test bars taken within the specified temperature range from continuously cast slab of similar chemical composition as the slab with cross crack.

On the basis of comparison of rupture areas of cross crack ascertained in the work [L7-3] and rupture area obtained in the given interval of testing temperatures from 25 °C to 1 450 °C during this investigation (for which relationships between slab material properties and its behaviour at rupture under the relevant temperature are known) we have afterwards analogically assessed possible behaviour of slab material affected by cross crack.

In this way it is possible to particularise and verify mechanism of initiation and subsequent discrete propagation of cross crack, to evaluate temperature interval in which initiation of cross crack was of the highest probability and to assess also to what degree anomalies in applied continuous casting technology could have influenced initiation of cross crack.

7.4.1 Fracture behaviour of continuously cast slab A in the temperature interval from 25 °C to 1 450 °C

Test specimens for tensile tests were taken from cross section of the slab (marked as the slab A) with dimensions of 250 ×1 530 mm. Chemical composition of this slab is the following (in wt.%): 0.12 C, 0.38 Mn, 0.26 Si, 0.010 P, 0.012 S, 0.06 Cr, 0.064 Cu, 0.033 Al(sum), 0.03 Ni. It is close to chemical composition of the slab with cross crack, which was discussed in subchapters 7.1 to 7.3. For further analysis this slab will be marked as the slab B. Test specimens were taken from the slab after its solidification and cooling down to a room temperature. Mechanical tensile tests were made on test bars with thread of total length of 245 mm. Nominal diameter of test bars was 6mm and their measured length was 100mm. The tests as such were completed in the laboratory on special tensile machine [L7-3]. The equipment used for tests and conditions of tests are in detail described in the work [L7-7].

Overview of results of all torn test bars taken from continuously cast slab is given in the **Tab. 7-3**. Afterwards a sub-set of ten test bars was chosen from the set of registered torn test bars for fractographic analysis of rupture (see the second column in the **Tab. 7-3**).

Electronic scanning microscope JEOL JSM 840 has been used for fractographic analysis of rupture. Complete fractographic analysis of the selected set of torn test bars is contained in the work [L7-8].

7.4.2 Influence of temperature on morphology of rupture of the slab A

The following behaviour has been ascertained by tests: at temperatures 25, 312, 536, 632 and 732 °C ruptures of test bars are trans-crystalline and ductile and they are realised by cavity mechanism. Ruptures are free of defective signs. Ruptures at temperatures 798 and 841 °C show on test bars significant drop of contraction (down to 11%). At the temperature of 988 °C there prevails an interdendritic fracture.

Tab. 7-3 Basic parameters of test bars at tensile tests within the temperature range from 25 to 1 450 °C

Serial No.	Fractographic analysis	Test temperature T (°C)	Tensile force F (N)	Contraction Z (%)	Work to rupture A (J)
1	yes	25	9 570	31.1	139
2	yes	312	11 395	46.0	158
3	yes	536	4 813	17	28
4	yes	632	3 519	37	23
5	yes	732	2 086	76	14
6	-	798	1 315	31	15
7	-	841	1 315	32	7
8	yes	988	1 179	11	5
9	-	1 093	817	58	7
10	yes	1 134	663	100	8
11	-	1 265	398	100	4
12	-	1 394	238	100	2
13	-	1 415	196	100	2
14	-	1 418	192	100	2
15	yes	1 420	182	100	2
16	yes	1 423	178	53	1
17	-	1 447	24	0	<<1
18	yes	1 450	15	0	<<1

Zone of temperatures, in which there occurs almost complete contraction of test bars (**Fig. 7-10**), lies in the temperature interval from 1 134 to 1 420 °C. It is possible to observe formation of cavities in the central part of almost complete narrowing (**Fig. 7-11**).

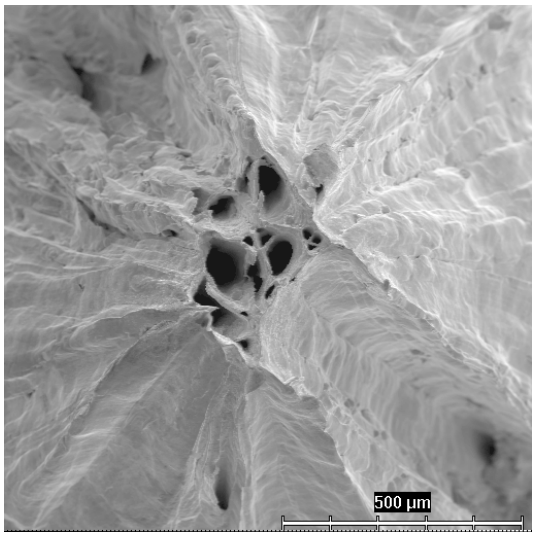

Fig. 7-10 (slab A) Rupture at 1 420 °C, contraction 100%

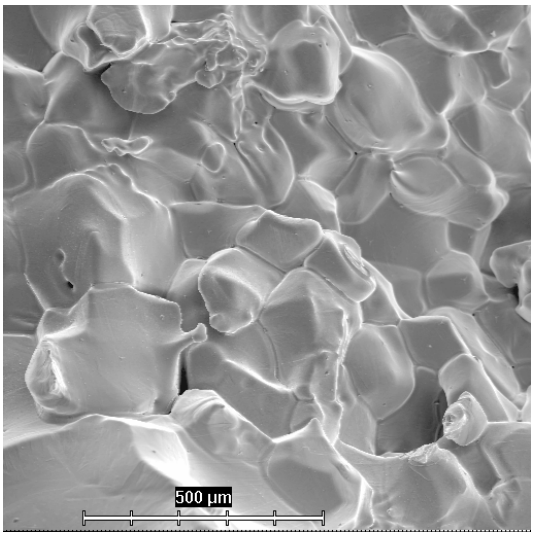

Fig. 7-11 (slab A) Rupture at 1 450 °C, contraction 0%

At temperature of testing of 1 423 °C, which is close to a solidus temperature proportion of interdendritic fracture increases. Next increase of testing temperature to 1 450 °C is accompanied by overall attenuation of boundaries and dendrites and their prevailing melting in. Before rupture of test bar there occurs an interdendritic fracture with almost zero contraction (**Fig. 7-11**). It follows from result of fractographic analyses that rupture behaviour of continuously cast slab is in the investigated temperature interval characterised by two extremes of contraction values: complete, total contraction under the solidus temperature (**Fig. 7-10**) and zero contraction, which occurs right before rupture of test bar in the area of co-existence of solid and liquid phases (**Fig. 7-11**).

Morphology of ruptures of steel with low carbon contents had already been investigated in dependence on their plastic characteristics up to temperatures of solidus by authors Longauerová et al. [L7-9].

They mention three temperature areas of embrittlement in carbon steels. If we, however, proceed in direction of descending temperatures, we find the following areas: the first area of embrittlement of steel is in proximity of temperature of solidus, the second area of embrittlement is in high-temperature area of stable austenite (1 200 to 900 °C), the third area of embrittlement is in the interval of transformation of gamma to alpha, or alpha to gamma (900 to 600 °C). Presence of liquid films at interdendritic interfaces or at grains boundaries is given as cause of embrittlement in the first area. Embrittlement in the second area is caused mainly by precipitation of fine particles of sulfitic type, or other phases at grain boundaries. The following reasons are given as causes of embrittlement in the third area: formation of pro-eutectoid ferrite at boundaries of austenitic grains, shifting of grain boundaries, precipitation of secondary phase particles, etc.

7.4.3 Progress of rupture of continuously cast slab B with cross crack

Results of analyses of cross crack made after laboratory opening of the crack on its surface have proved that crack is propagated preferentially at dendrite boundaries [L7-3]. It was ascertained that it nucleates in areas with increased zonal segregation of segregated elements, which are at the same time connected with presence of micro-shrinkages (**Fig. 7-12**). Legibility of fractographic photos taken from the surface of transverse crack is deteriorated due to oxidation of the rupture surface. It is, nevertheless, possible to find in relief signs of rupture along dendrite boundaries (**Fig. 7-13)**, as well as signs of trans-crystalline ductile failure (**Fig. 7-14**). Interface of surface of original transverse crack and final rupture in laboratory made under liquid nitrogen (i.e. at temperature of approx. –196 °C) by brittle fracture, is shown in **Fig. 7-15**.

Afterwards on the basis of model of non-stationary temperature field for the slab B with transverse crack there were calculated durations of dwell of selected areas of slab between the temperature of liquidus and solidus, i.e. values of local time of solidification θ. Calculation described e.g. in the work [L7-10] was made for the top edge of the mold (10 mm from the top edge of the slab B with dimensions 1 300 ×145 mm^2) and for the area of central part of the slab (72.5 mm also from the top edge of the same slab), in nodal points given in the **Tab. 7-4**. Due to the fact that dendrite arms spacing is a function of the local time of solidification [L7-11], it is possible to establish that the coarsest dendritic structure of slabs is at the distance about 170 mm from the right edge.

Tab. 7-4 Values of local time of solidification θ (s) calculated in nodal points of the slab B with cross crack

Distance from the top edge (mm)	Time (s)	Distance from the right edge of the slab (mm)						
		650	530	410	290	170	50	10
10	θ	25.4	25.4	25.4	25.4	25.4	22.7	9.03
72.5	θ	341.8	347.2	354.8	355.0	372.9	217.7	12.3

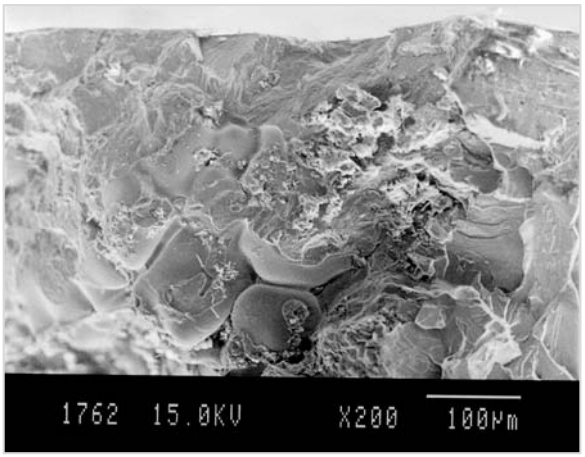

Fig. 7-12 (slabB) Surface of cross crack with distinct micro-shrinkages

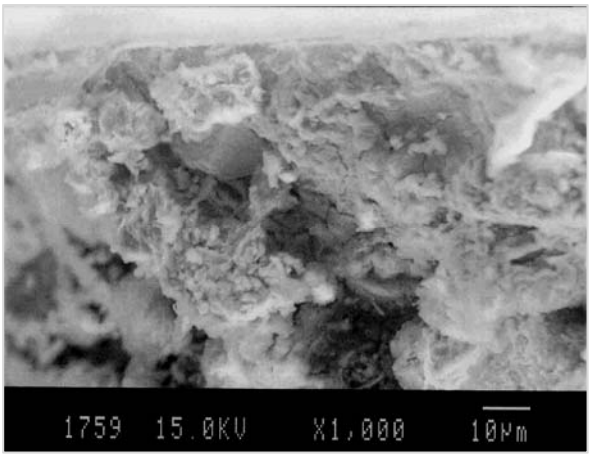

Fig. 7-13 (slabB) Oxidised surface of cross crack with signs of development between dendrites

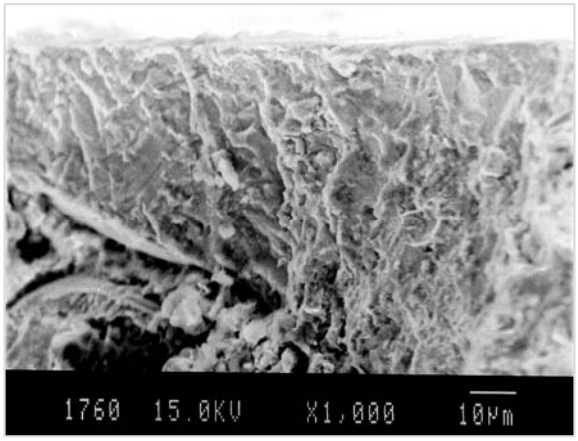

Fig. 7-14 (slabB) Partly oxidised, ductile trans-crystalline fracture of cross crack

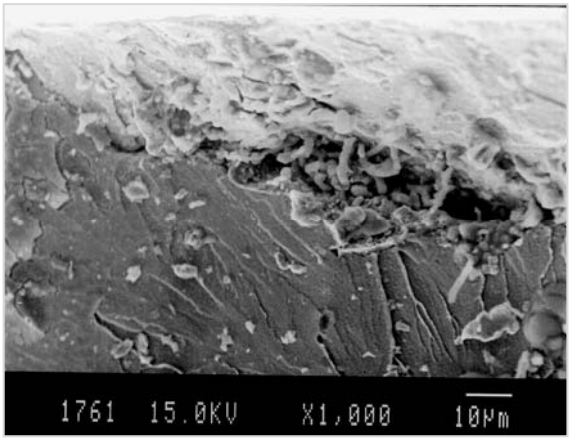

Fig. 7-15 (slabB) Interface of trans-crystalline fracture of cross crack with brittle final fracture

7.4.4 Discussion of obtained results – comparison of fractures of analysed cast slabs

Seven characteristic surfaces were available for mutual comparison of morphology of fractures taken from surface of cross crack (slab B) after its opening in liquid nitrogen. These surfaces were afterwards compared with ruptures of the slab A obtained within the temperature range from 25 to 1 450 °C. Total set of 72 characteristic pictures of rupture relief were available. It was possible to draw the following conclusions on the basis of mutual comparison of micro-relief of rupture surface of cross crack on the slab B with micro-reliefs of rupture of the slab A:

a) On the rupture of cross crack of the slab B there have not been established any morphological signs, which characterise total contraction occurring on the bars from the slab A at the temperature from 1 134 °C to 1 420 °C (**Fig. 7-10**). On the rupture of cross crack there have also been found no signs that are typical for a sharp drop of contraction of test bars taken from the slab A at temperature of 1 423 °C or also signs characteristic for a zero contraction, which accompanies ruptures of tensile test bars taken from the slab A at temperature of 1 450 °C (**Fig. 7-11**). It is possible to exclude with high probability a possibility of initiation of cross crack within the given temperature range.

b) Identical signs of micro-reliefs of the cross crack surface of the slab B with micro-relief of ruptures of tensile test bars from the slab A were found on slab ruptures, which were torn at the temperature from 732 °C to 988 °C (see relief of ruptures in **Figs. 7-12 to 7-15** from the surface of cross crack and relief of ruptures in **Figs. 7-16 and 7-17** from tensile test specimen taken from the slab A). It is therefore possible to presume that initiation and subsequent propagation of transverse crack occurs with high probability within the temperature interval from 990 to 730 °C. At temperatures below 730 °C no identical signs of micro-relief and cross crack were fully reliably found.

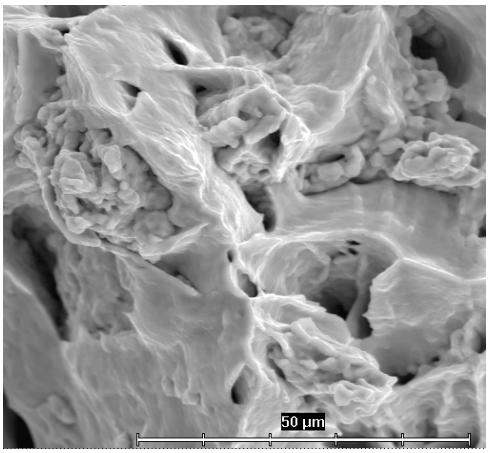

Fig. 7-16 (A) Rupture at 732 °C, contraction 76%

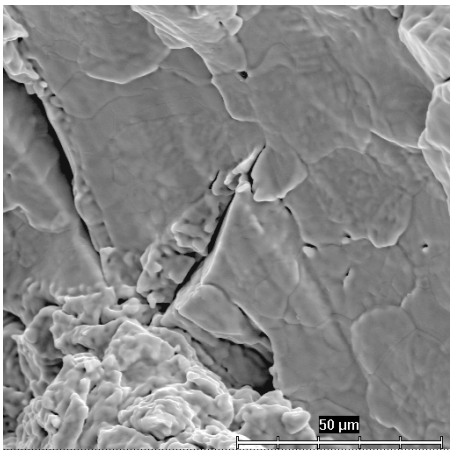

Fig. 7-17 (A) Rupture at 988 °C, contraction 11%

c) During cooling of tensile test bars in the temperature interval from 990 to 730 °C there occur the following values: work to rupture A from magnitude of approx. 5 J to 14 J, tensile force F from magnitude 1 179 N to 2 086 N, and also contraction Z from magnitude 11% to the magnitude of 76%. This means that there increases not only strength of slab material, but also its plasticity.

The preceding facts ensuing from comparison of ruptures demonstrate that initiation of cross crack can be expected in high-temperature area of stable austenite, i.e. in the second area of embrittlement, which is usually characterised by the temperature range from 1 200 to 900 °C. In our case it is possible to presume initiation of partial transverse crack rather at the temperature of 990 °C, which is in case of test bars from the slab A characterised as absolutely the lowest work to rupture (A = 5 J, see **Tab. 7-3**). With respect to discrete progress of cross crack (consisting of individual partial cracks), it is possible to assume that its initiation occurs in such points of the slab, which solidify as the last ones, have comparatively the most coarse dendritic structure and at the same time it is possible to expect in them higher frequency of shrinkage porosities and micro-shrinkages. Shrinkage porosities really do occur on the transverse crack surface (**Fig. 7-12**).

On the basis of analyses of ruptures and fractured surface of transverse crack it is possible to presume that progressive propagation of individual partial cracks and their mutual local inter-connection occurs in the second and third area of embrittlement. The third area of embrittlement is in the interval of transformation of iron gamma to alpha, i.e. in the interval from 900 to 600 °C and it can comprise also eutectoid transformation. In our case it is possible to assume propagation of cross crack, connected with gradual inter-connection of individual partial cracks up to temperature of approx. 730 °C. Below this temperature propagation of partial cracks and thus also their mutual inter-connection already stops. That's why the second transverse crack is characterised even after complete cooling down of the slab to temperature of surrounding temperature by partial discontinuity. In spite of the fact that crack covers comparatively large surface of the central part of the slab, it is continuous only on larger parts of this surface (in other words – on smaller parts of surface it is discontinuous - discrete).

7.4.5 Conclusion

On the basis of preceding considerations it is possible to reconstruct initiation and propagation of cross crack in continuously cast slab B in the following way [L7-6]:

a) Initiation of partial cracks occurred below temperature of 990 °C, which is – according to analogy with fracture behaviour of the compared slab A – characterised by minimum work to rupture and at the same time by low plasticity.

b) Initiation of the first partial cracks has occurred with high probability in centre of the slab, in its right half (if we consider it from position against direction of movement of the slab in continuous casting machine = CCM) at the distance of 170 mm from its right edge. This area of the slab B is characterised by the coarsest dendritic structure, the longest interval of solidification between temperature of liquidus and solidus, and also the top of the solidification cone in this half of the slab (**Tab. 7-4** and Fig. 1 in [L7-3]).

c) Initiation of next partial cracks occurred in direction towards the central part of the slab, and also in direction towards its right edge. Dendritic structure coarsening decreases in both directions. Coarsening of dendrites in direction towards the central part of the slab decreases slowly (**Tab. 7-4**), that's why initiation and other propagation of partial cracks occurred here more easily than in the opposite direction.

d) Refining of dendritic structure in direction to the right edge of the slab (**Tab. 7-3**) has lead to substantial decrease of probability of initiation of partial cracks and their further propagation subsequently also stopped approx. 60 mm from the slab edge.

e) Initiation of partial cracks was supported by existence of micro-shrinkages and internal state of stress, when direction of main stresses was perpendicular to the cross (transverse) crack, the extent of which kept growing, which was, however, only partly inter-connected.

f) Progressive propagation of partial cracks, connected with their partial inter-connection occurred during cooling of the slab down to the temperature of approx. 730 °C, when there occurred a complete braking of their further propagation, and the size and position of cracks were stabilised up to ambient temperature.

g) It also follow from this study that with use of the model of non-stationary temperature field it is possible in connection with the model of chemical heterogeneity to determine size (coarsening) of dendritic structure.

h) In the given case it is possible to assume that segregation together with high local concentration manganese gradient (the concentration of which on surface of transverse crack was measured at the same time as the highest – 3.31 wt.% [L7-3]), was the factor that had influenced growth of dendrites.

The solution has been printed in the peer-reviewed journals and presented at prestigious conferences [L7-11 to 7-18].

7.5 Literature

[L7-1] Kavička F., et al.: The optimization of concasting using two numerical models (In: *The VI International Conference Moving Boundaries–Computational Modelling of Free and Moving Boundary Problems*, WIT Press, Lemnos, Greece 2001), 31.

[L7-2] Dobrovská J., Dobrovská V., Kavička F., Stránský K., Štětina J., Heger J., Camek L. and Velicka B.: Industrial application of two numerical models in concasting technology. *Proc. of the 7th Int. Conf. on Damage and Fracture Mechanics*, eds. C.A. Brebbia & S.I. Nishida, WITpress Southampton: Boston, pp. 183–192, 2002.

[L7-3] Dobrovská J., Dobrovská V., Stránský K., Kavička F., Štětina J., Velička B. and Heger J.: On the mechanism and causes of cross cracking in concast low alloy manganese steel slab. *Proc. of the 1st Int. Conf. on Fatigue Damage of Materials, Experiment and Analysis*, eds. eds. C.A. Brebbia & S.I. Nishida, WITpress Southampton: Boston, pp. 171–180, 2003.

[L7-4] Rek A. and Stránský K.: Heterogeneity of a CC-slab with failed central compactness (*Research report no. 618-08-01*, The 1st part, VTÚO Brno 2001).

[L7-5] Rek A. and Stránský K.: Heterogeneity of a CC-slab with failed central compactness (Analysis of the fracture area of crack. *Research report no. 618-08-01*, The 2nd part, VTÚO Brno 2001)

[L7-6] Dobrovská J., et al.: On the possibilities of verifying the cross cracking mechanism in the concast steel slab. Proceedings of the 8th International Conference on Structure Under Shock and Impact, *SUSI 2004*, Creta Greece, March 31-April 2, p. 119–128.

[L7-7] Havlíček F., Kozelský P., Kořený R., Szromek P., Hanus A., Kubatý J., Stránský K. and Blažíková J.: The temperature cracking condition in the cast materials. *Report of GAČR GA106/99/1537*. Technical University of Ostrava, 2002 (in Czech).

[L7-8] Blažíková J. and Stránský K.: The Fractography of a con-cast steel slab after high temperature probes. *Report of the VTÚO*, Brno 2002 (in Czech).

[L7-9] Longauerová M., Fujda M., Longauer S., Kozelský P. and Bodnar M.: Morphology of fractures of low carbon steels with different Cu contents in dependence on their high temperature plastic characteristics in proximity of solidus temperature. In *Fractography 2000*, ed. M. Longauerova, Košice 2000, pp. 235–242.

[L7-10] Kavička F., Štětina J., Sekanina B. and Ramík P.: An original numerical model of heat and mass transfer in a concasting machine. *Proceedings of the 3rd International Conference on Advances in Fluid Mechanics AFM 2000*, Montreal, Canada, 2000, pp. 705-714.

[L7-11] Dobrovská J., Stránský K., Kavička F. and Štětina J.: Analysis of transversal crack in steel slab. *Materials Science Forum.* (2008) 567-568, 105 - 108.

[L7-12] Dobrovská J., Dobrovská V., Stránský K., Kavička F., Štětina J., Čamek L., Masarik M. and Heger J.: Prediction of cracs of the continuously cast carbon-steel slab. In *Proceedings of the Seventh international conference on computer methods and experimental measurements for surface effects and contact mechanics.* Cambridge, WIT Press. 2005. p. 111–120.

[L7-13] Kavička A., Dobrovská J., Dobrovská V., Stránský K., Štětina J., Velička B. and Heger J.: On the machanism and causes of cross cracking in concast low alloy manganese steel slab. In *Proceedings of the First International Conference Fatigue Damage of Materials.* Toronto, Canada, WIT PRESS. 2003. p. 171–180.

[L7-14] Kavička F., Dobrovská J., Stránský K., Sekanina B. and Štětina J.: Numerical analysis of a transversal crack in a steel slab. In *CD ROM of 19th Annual international conference on composites/nano engineering ICCE-19.* Shanghai, David Hui. 2011. p. 13–20.

[L7-15] Stránský K., Dobrovská J., Kavička F., Štětina J. and Sekanina B.: A transversal crack in a steel slab and its analysis. In *Proceedings of the International Conference o Crack Paths (CP 2009).* Padua, Italy, University of Padua. 2009. p. 751–758.

[L7-16] Kavička A., Dobrovská J., Stránský K. and Štětina J.: Study of a transversal crack in a steel slab from the chemical heterogeneity point of view. In *Proceedings 22nd Canadian congress of applied mechanics.* CANCAM. Halifax, Canada, Dalhouse university. 2009. p. 159–160.

[L7-17] Stránský K., Dobrovská J., Dobrovská V., Kavička F., Štětina J., Velička B. and Heger J.: The analysis of the causes of cross cracking in concast slab via two numerical models. In *Proceedings of the XIII international scientzific conference Iron and Steelmaking.* Szczyrk, Poland, Wydawnictwo PRIOR, Chorzow. 2003. p. 215–218.

[L7-18] Kavička F., Sekanina B., Štětina J. and Ramík P.: An original numerical model of heat and mass transfer in a concasting machine. In *3rd International conference on advances in fluid mechanics AFM 2000.* Montreal (Canada), WIT Press. p. 705–714.

8 Analysis of atypical breakout during radial continuous casting of a slab 250 × 1 530 mm in the straightening zone

8.1 Numerical simulation of temperature field of a slab

8.1.1 Introduction

Oscillation marks are transverse grooves forming on the surface of the solidifying shell of a continuously cast slab. The course of individual marks is rough and perpendicular to the direction of the movement of the slab. The formation of the marks is sometimes the result of the bending of the solidifying shell during the oscillation of the mould, which depends on the frequency and the amplitude of the oscillation and on the casting speed. The hooks are solidified microscopically thin surface layers of steel [L8-1 to 8-3]. They are covered with oxides and slag from casting powder. Their microstructure is different from that of the base material of the solidifying shell. Formation of the oscillation marks is related to formation of hooks. The depth of the oscillation marks and also the shape, size and the microstructure of the hooks, vary irregularly. An increasing extent of these changes leads to a defect in the shape of a crack, which reduces the thickness of the solidified shell of the slab upon its exit from the mould and causes a dangerous notch. In the secondary-cooling zone, where the slab is beginning to straighten out, the breakout of the steel can occur in the points of the increased local chemical and temperature heterogeneity of the steel, from increased tension as a result of bending of the slab and also of high local concentration of non-metallic slag inclusions. Especially dangerous are the changes in the chemical composition of the steel during the actual continuous casting. The consequences of this operational immediate change in the chemical composition of the steel, which are not prevented by a breakout system directly inside the mould, could lead to an immediate interruption of continuous casting and to a breakout at a greater distance from the mould than usual, thus leading to significant material loss and downtime of the caster.

8.1.2 Interruption of continuous casting

This case was recorded during the process of continuous casting of 250 ×1 530 mm steel slabs of the grade A with a 0.416 wt.% carbon content and 0.95 wt.% chromium content (melts 1 to 3) and the grade B with 0.174 wt.% carbon content and 0.070 wt.% chromium content (melt 4). The casting of the first two melts of the grade A took place without any significant issues, after the casting of the third melt of the grade A, the fourth melt of the grade B followed. The change in the chemical compositions of the steels of both grades was carried out very quickly by changing the tundish. Inside the mould, the steel B mixed with the steel A from the previous melt. The casting continued for another 20 minutes but then, at the point of straightening of the slab, at a distance of 14.15 m from the level of the melt inside the mould, a breakout occurred between the 7^{th} and 8^{th} segment and the caster stopped. The difference in height between the level inside the mould and the breakout point was 8.605 m. This tear in the shell occurred on the small radius of the caster. A 250 mm thick plate was taken from the breakout area using a longitudinal axial section (**Fig. 8-1a**). The structure of this plate was analyzed and the distribution of sulphur was also analyzed with use of the Bauman print. In the **Fig. 8-1b** the numbers 1 to 11 indicate also the positions of the samples in the places around the breakout intended for analysis. Simultaneously, significant 25 mm sulphide segregations were discovered – very heterogeneous areas created by the original base material of the slab (melt 3), by new material of the slab (melt 4) and between them, and also by the areas of mixed composition. Beneath the surface of the slab, at a depth of 75-to-85 mm, there were cracks and a zone of columnar crystals oriented towards the surface of the slab on the small radius. This was identical to the orientation of the groove, which gradually turned into a crack (**Fig. 8-1b** – direction 4 – 6) and, on the opposite surface of the slab, the hook, which was covered by melt (position 8).

Fig. 8-1a A plate taken from the breakout area

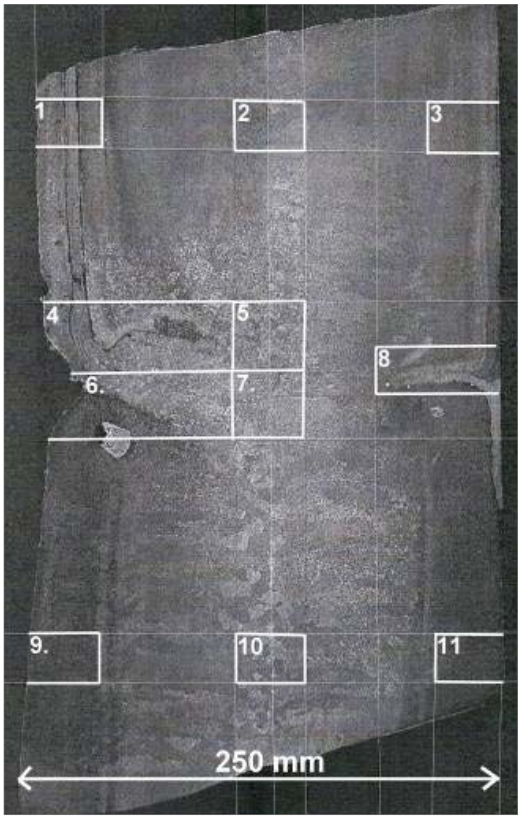

Fig. 8-1b Diagram of positions of the samples 1 to 11

8.1.3 Results of numerical simulation of the slab A and B

The original numerical model of the temperature field of continuously cast steel slab was applied, which was based on the explicit numerical method, which is described in Chapters 5.2., 5.3. [see also L8-4].

Chemical composition of the **steel A** in wt.% (main elements, see also Tab. 8-6 for details):

C = 0.416 Cr = 0.95 Ni = 0.03 Mn = 0.7 Mo = 0.206 Si = 0.28

Chemical composition of the **steel B** in wt.% (main elements, see also Tab. 8-6 for details):

C = 0.174 Cr = 0.07 Ni = 0.02 Mn = 1.46 Mo = 0.005 Si = 0.23

Dependences of the main thermo-physical properties on temperature – heat conductivity, specific heat capacity, enthalpy and density of both steels are shown in **Figs. 8-2 to 8-5** [L8-5].

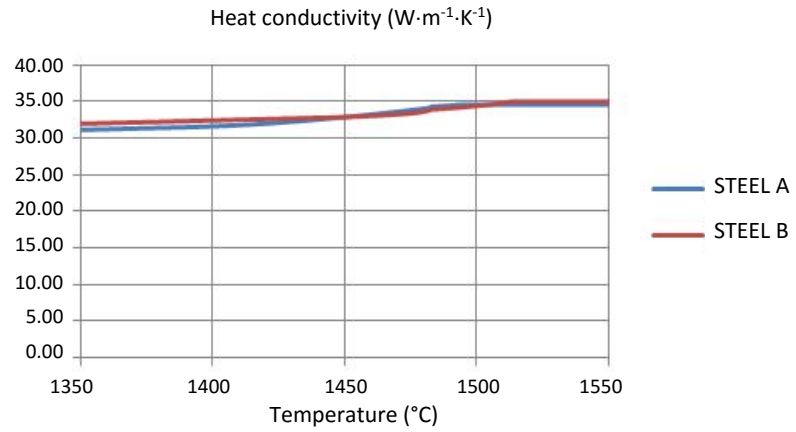

Fig. 8-2 Dependence of heat conductivity of the steels A and B on temperature

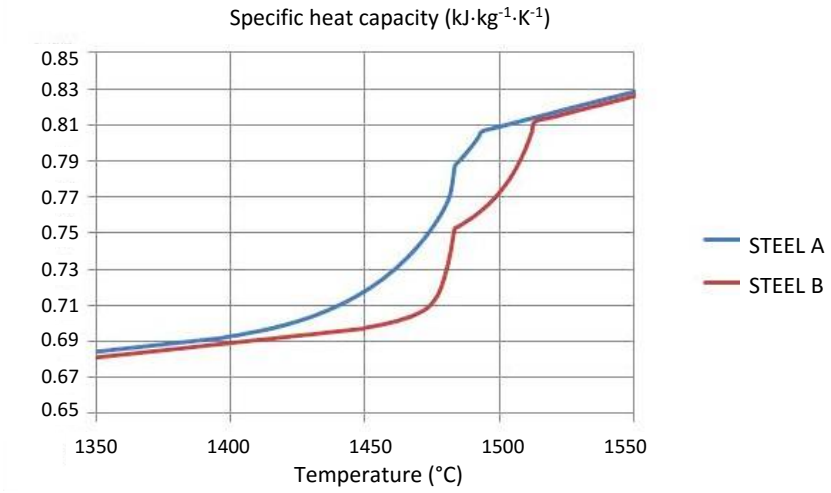

Fig. 8-3 Dependence of specific heat capacity of the steels A and B on temperature

Off-line version of the original temperature model was used now to simulate the temperature field of the steel slab of the grade A, the steel slab of the grade B and the steel slab of the grades A and B (with an average chemical composition). After the computation, it is possible to obtain the temperatures at each node of the network and at any time during the process. **Figure 8-6** shows for example a 3D graph of the temperature field along the longitudinal section of the steel slab of the grade A. Temperature history graphs (**Fig. 8-7a to 8-7c**), which show the temperature at defined points of the cross-section of the slab are very useful. The course of the temperatures can also be displayed in any other user-defined point.

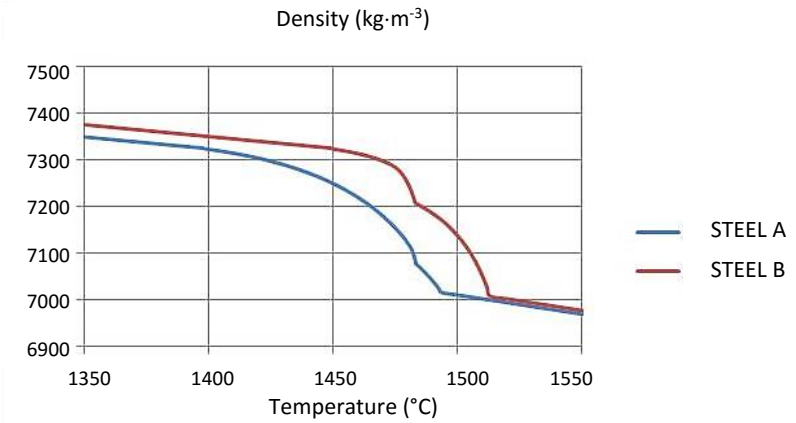

Fig. 8-4 Dependence of density of the steels A and B on temperature

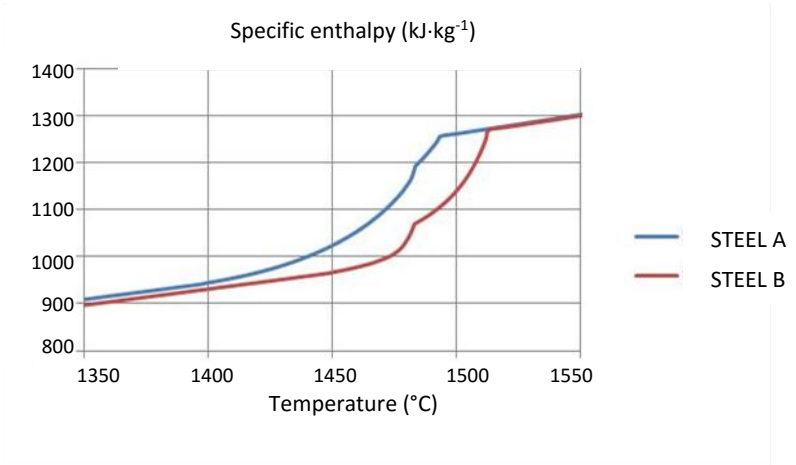

Fig. 8-5 Dependence of enthalpy of the steels A and B on temperature

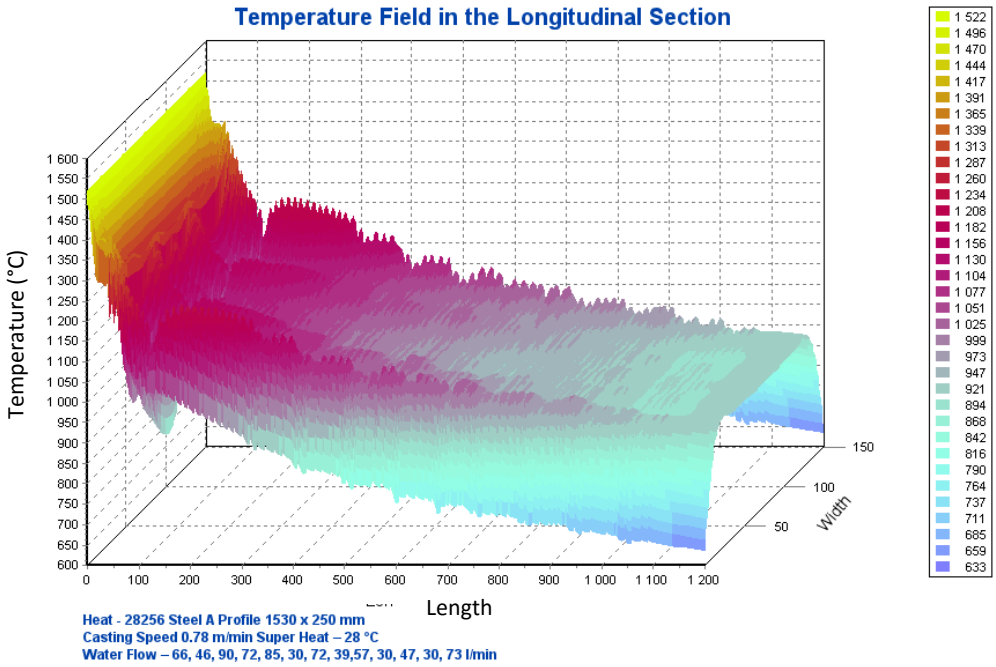

Fig. 8-6 3D graph of the temperature field along the longitudinal section of the steel slab of the grade A

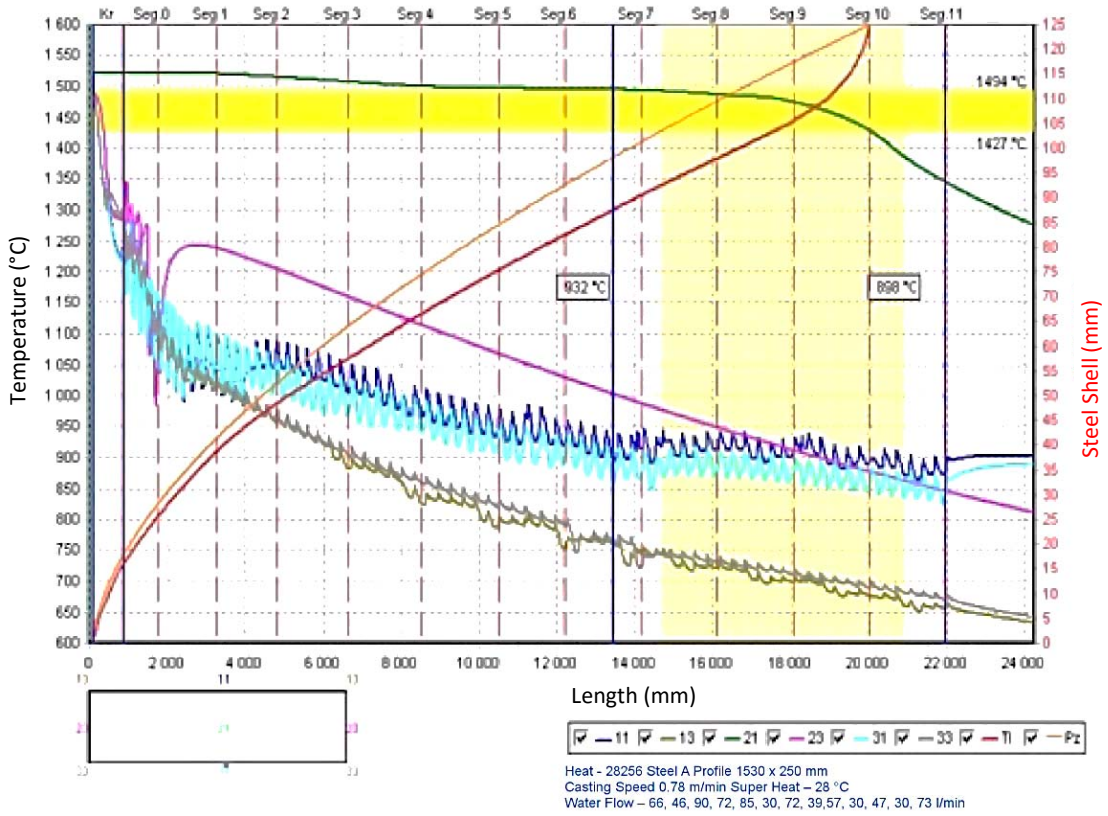

Fig. 8-7a Temperature history of points of the slab cross-section (steel A)

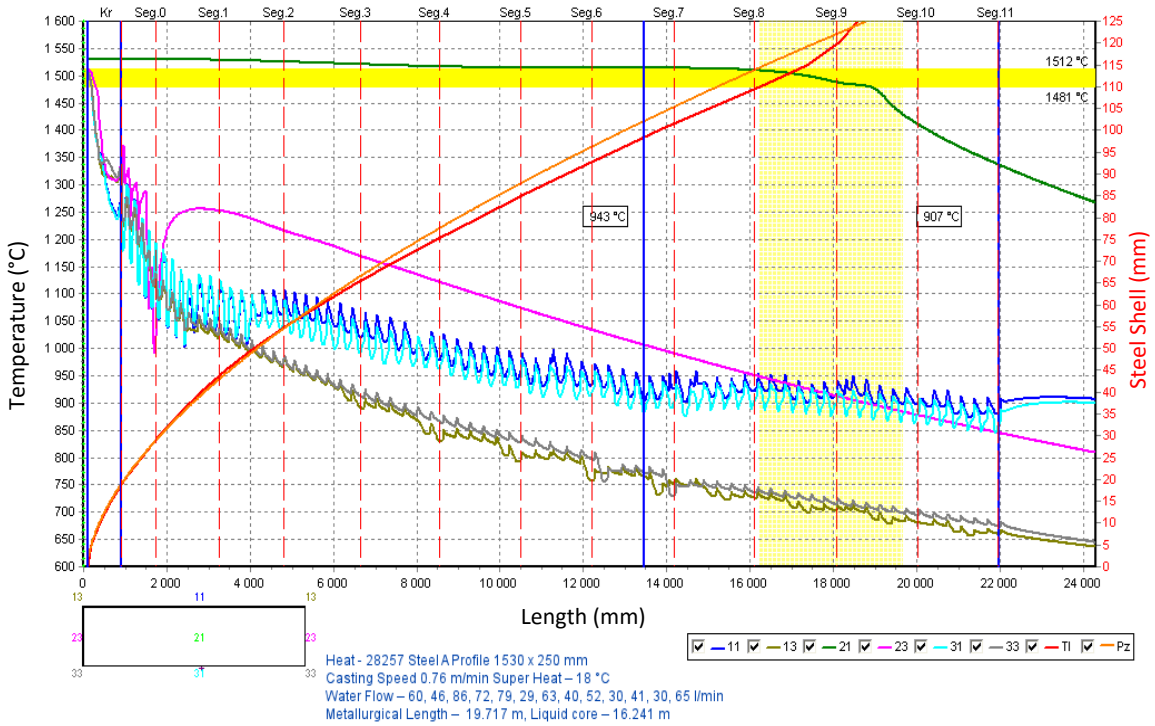

Fig. 8-7b Temperature history of points of the slab cross-section (steel B)

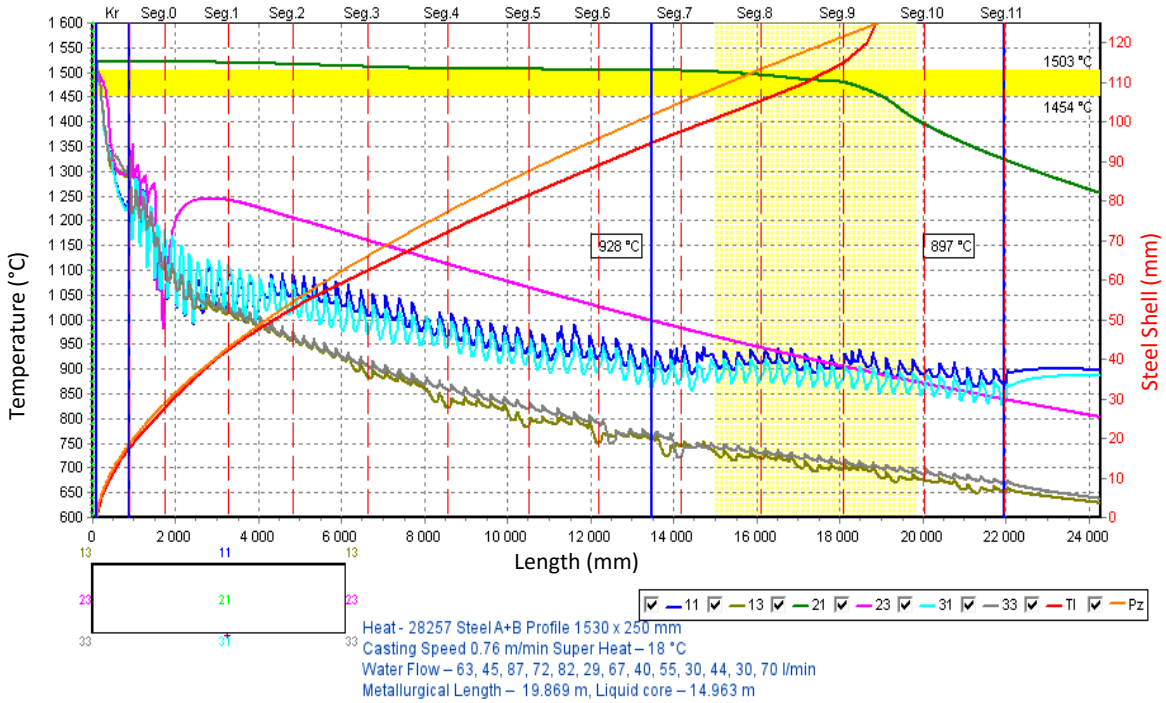

Fig. 8-7c Temperature history of points of the slab cross-section (steel A+B)

The course of the calculated isotherms in the cross section of the breakout, for example for a slab of the grade B at a distance of 14.15 m from the level of the melt in the mould is shown in **Fig. 8-8**.

Calculated iso-liquidus and iso-solidus in both longitudinal axial sections for the steel slab of the grades A, B and A+B are plotted in **Figs. 8-9 and 8-10.**

The model provides also the course of surface temperature and isotherms in any longitudinal section of the slab. The computed surface temperatures of the slab in the large and small radius are shown in **Fig. 8-11** and isotherms in the longitudinal section 20 mm under surface (small radius) in **Fig. 8-12.**

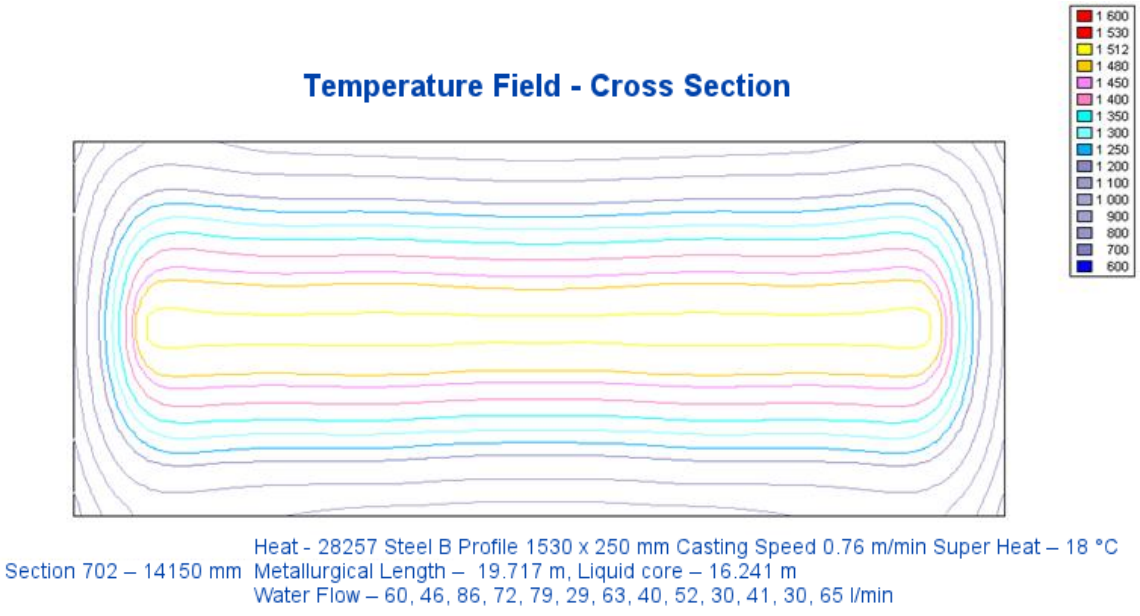

Fig. 8-8 Isotherms in the cross section of the breakout for the steel slab of the grade B

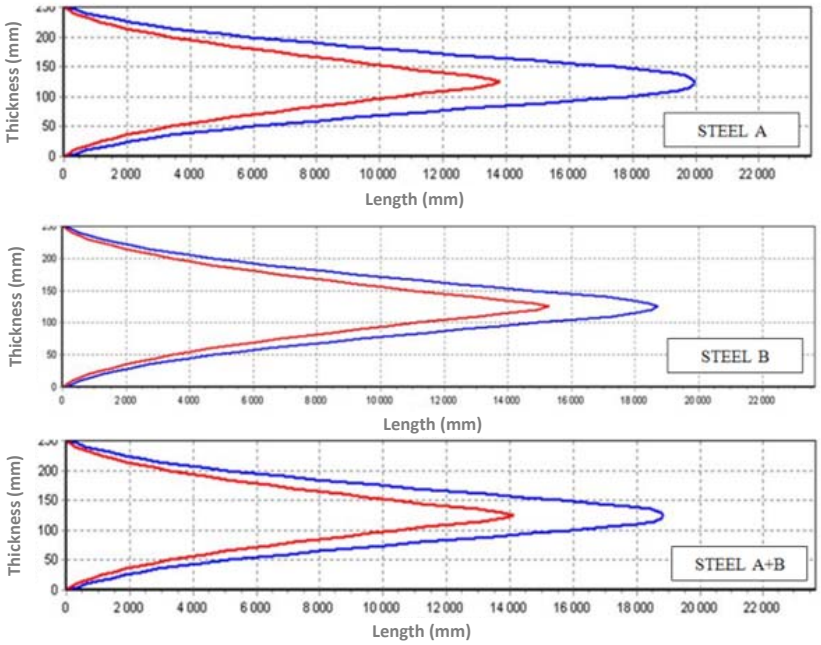

Fig. 8-9 Iso-liquidus and iso-solidus in the vertical longitudinal axial section for the steel slab of the grades A, B and A+B

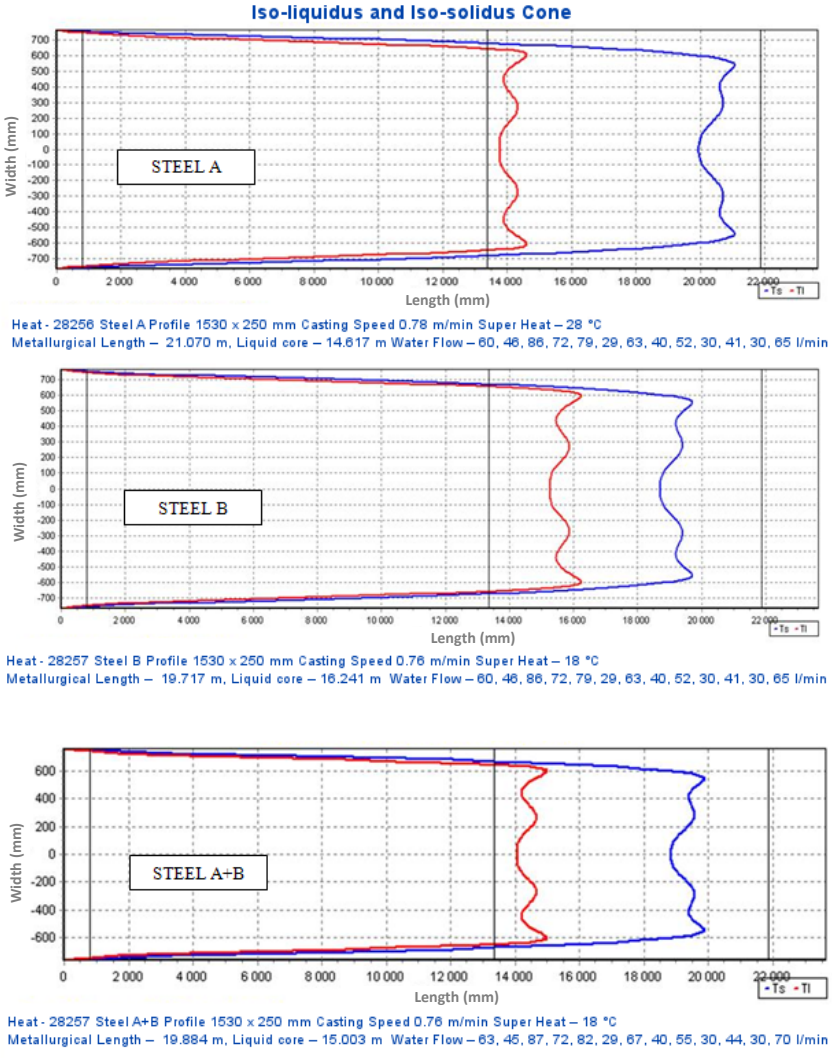

Fig. 8-10 Iso-liquidus and iso-solidus in the horizontal longitudinal axial section for the steel slab of the grades A, B and A+B

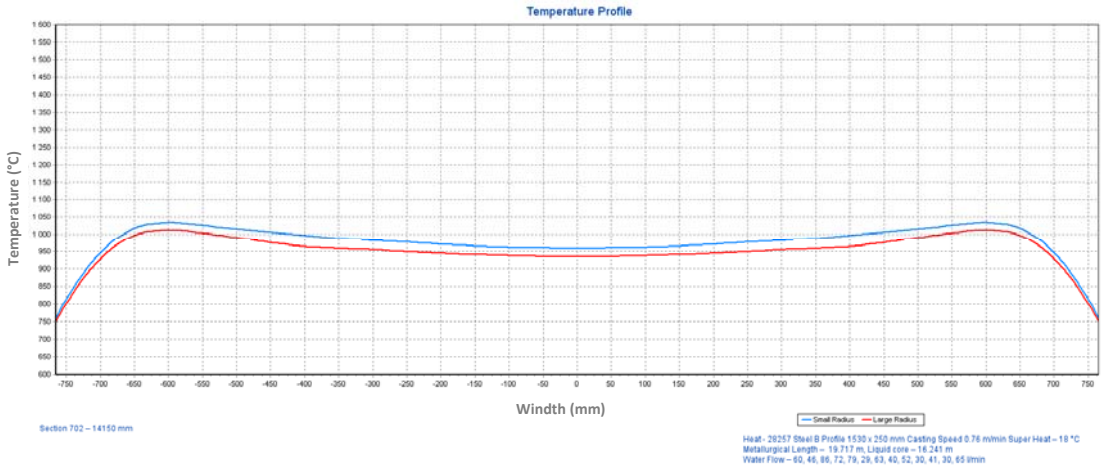

Fig. 8-11 The surface temperature of the slab (steel grade B) in the large (red) and small radius (blue curve)

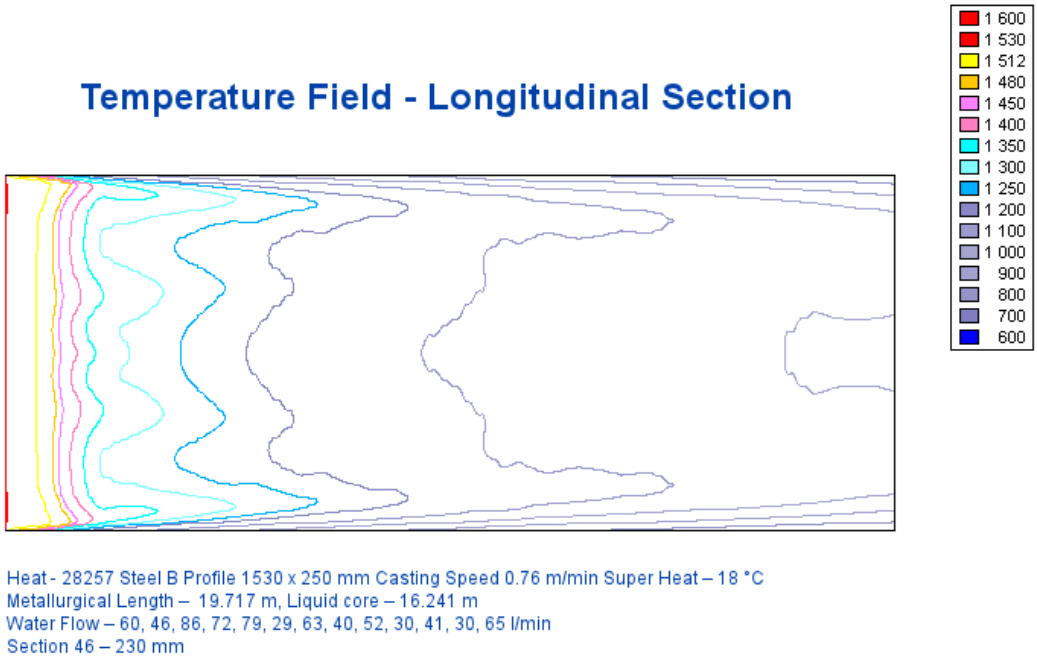

Fig. 8-12 Isotherms in the longitudinal section (steel grade B) 20 mm under surface in the small radius

Figures 8-13 to 8-15 represent computed mushy zones in one half of the breakout cross section for the steel grades A, B and their mixture A+B. These shaded areas bounded by iso-liquidus and iso-solidus will be important geometric parameters for an analysis of the causes of the breakout [L8-6].

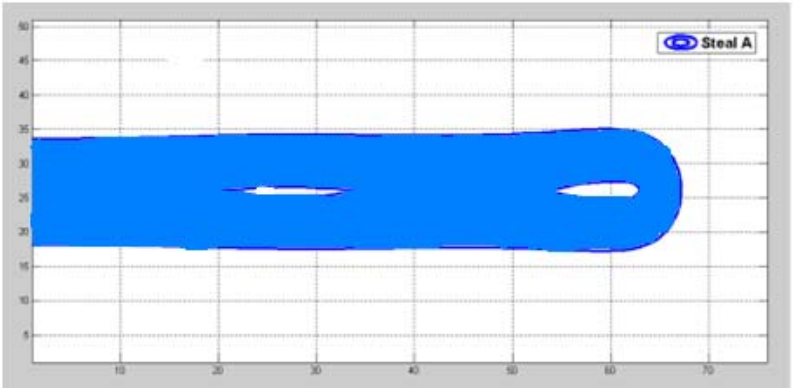

Fig. 8-13 A computed mushy zone in one half of the breakout cross section (steel A)

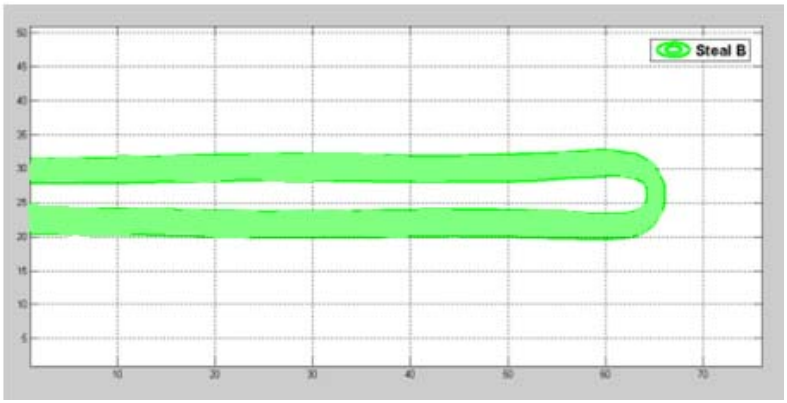

Fig. 8-14 A computed mushy zone in one half of the breakout cross section (steel B)

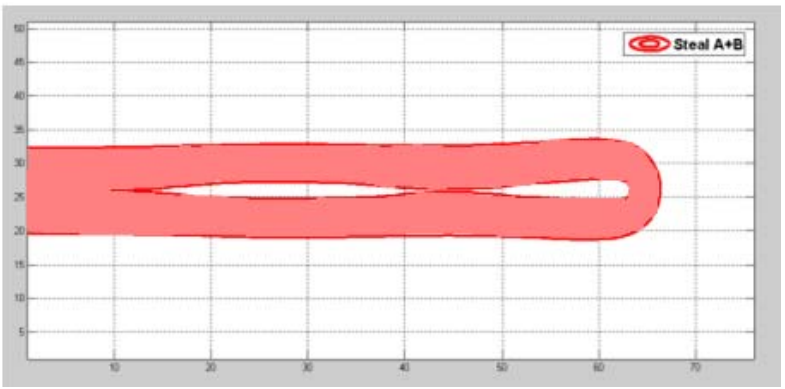

Fig. 8-15 A computed mushy zone in one half of the breakout cross section (steel A+B)

8.1.4 Conclusion

A breakout of the concast slab right under the mould is usually detected and indicated by an anti-breakout system. However, breakouts occur at continuous casting, i.e. failure of strength of solidified shell caused even by a slight change of grade of the cast steel, also on radial caster at the place of straightening of the slab. This irreparable defect is moreover often initiated by surface defects, the origin of which is already in the mould at the beginning of crystallisation. These are oscillation marks and sub-surface pockets - hooks. Both phenomena, i.e. formation of marks and hooks are related to each other. These defects may also lead under certain conditions, such as change of grade of continuously cast steel, to an interruption of casting and to breakout, as it is demonstrated in the photo of macro-structure of defect, taken directly at the place of breakout of continuously cast slab. Moreover the breakout occurred after a quick change of the chemical composition of the continuously cast steel of the grade A and the grade B. The change of the chemical compositions of both steels grades was carried out very quickly by changing the tundish. The pouring continued for another 20 minutes but then, at the point of straightening of the slab a breakout occurred and the caster stopped. Off-line version of the temperature model was used to simulate the temperature field of the slab of steel grades A and B and a mixture of A and B grades. It used thermo-physical parameters of both grades of steel, technological parameters of the caster (casting speed, mould characteristics, etc.) and the data that were obtained by means of off-line temperature model. Mutual dependence of the set of thus determined parameters and quantities will be determined. For this an application based on the theory of physical similarity and the derivation of similarity criteria is assumed.

8.2 Analysis of the causes of the breakout by application of the theory of physical similarity

8.2.1 Introduction

Oscillation marks are transverse grooves forming on the surface of the solidifying shell of continuously cast slab. The course of individual marks is rough, irregularly zigzagged and perpendicular to the direction of the movement of the slab. The formation of the marks is sometimes the result of bending of the solidifying shell during the oscillation of the mould [L8-1]. The hooks are solidified microscopically thin surface layers of steel. Their microstructure is different from that of the base material of the solidifying shell. The shapes of the hooks follow the curvature of the meniscus of the solidifying steel inside the mould and they are covered with oxides and slag from casting powder. Formation of the oscillation marks and of the hooks is related. Formation of the oscillation marks is conditioned by the oscillation movement of the mould, especially by the frequency of its oscillation f (i.e. the oscillation cycle), the amplitude ΔS and the casting speed w, which determines the speed of the movement of the slab. A significant role here is played by the negative strip time [L8-2 and 8-3]. Formation of the hooks is related to the rate of solidification of the melt and to the possibility of its flow – in the area of the meniscus – over the surface of the slab, which is roughened by the oscillation marks [L8-4]. The depth of the oscillation marks and also the shape, size and the microstructure of the hooks vary irregularly. An increasing extent of these changes leads to a defect in the shape of a crack, which reduces the thickness of the solidified shell of the slab at its exit from the mould and causes a dangerous notch. In the zone of secondary cooling, where the slab is beginning to straighten – under especially unfavourable conditions – the breakout of the steel can occur at the points of increased local chemical and temperature heterogeneity of the steel, from the increased tension as a result of the bending of the slab and also due to high local concentration of non-metallic slag inclusions. The changes of the chemical composition of the steel during the actual casting process are particularly dangerous. The consequences of this operational immediate change of the chemical composition of the steel, which are not prevented by an anti-breakout system directly inside the mould, could lead to immediate interruption of the casting process and to a breakout at a greater distance from the mould than usual, thus leading to significant material loss and downtime.

8.2.2 Occurrence of atypical breakout and stopping of the casting machine

Interruption of continuous casting and atypical breakout were described in subchapter 8.1.2 [L8-5]. The plate taken from the breakout area (**Fig. 8-1a**) and the structure of this plate was analysed as well as distribution of sulphur determined by the Bauman print (**Fig. 8-16**).

It detects also the slag inclusion, which interferes with the sample No. 6 in **Fig. 8-1b**. From these figures it is possible to expect in advance that continuously cast steel slab will be affected by massive slag inclusions and that it will have along the cross-section a chemical composition different from the original composition of the grade A (melt 3) and also from the original composition of the steel grade B cast after the flying exchange of the tundish (melt 4). This was confirmed by analysis of chemical composition of the samples 1 to 11, the results of which are summarised in **Tab. 8-1**. The reason is that at the point of breakout a mixed composition of the grades A+B was present [L8-6]. The detected differences of this mixed composition of elements as compared with the original grades A and B are also commented in the work [L8-5].

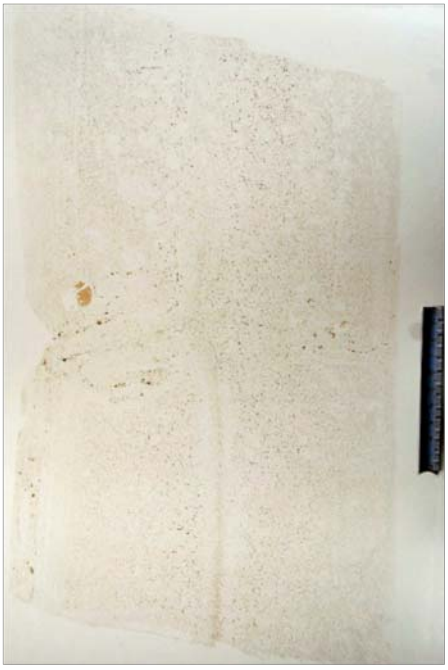

Fig. 8-16 Baumann print

8.2.3 Application of theory of physical similarity

The aim of this study is to clarify, which of the two steels A or B was more significantly involved in the described atypical breakout at the place of slab straightening. The susceptibility of both steels to breakouts can be analysed in two ways:

a) firstly to check, whether it is possible in the first approximation to assess even only semi-quantitatively the nature of mixing of the steels A and B, or extent of such mixing;

b) to assess qualitatively, or at least semi-quantitatively, whether it is possible to obtain with use of dimensionless criteria of physical similarity a basic idea of the relations between dimensional quantities characterising the composition of both A and B steel grades and their susceptibility to breakouts; the condition is to have in accordance with the applicable theorems sufficient necessary, but also reasonably precise, physical-chemical measurements for calculation of the needed similarity criteria.

Tab. 8-1 Analysis of average chemical composition of the samples (wt.%) 1-11 (**Fig. 8-1b**) taken from the place of breakout of the mixed melt A+B

Sample	C	Si	Mn	P	S	Cr	Ni	Mo	Al	Fe
1	0.274	0.252	1.15	0.018	0.0090	0.364	0.037	0.069	0.045	97.700
2	0.197	0.24	1.23	0.014	0.0083	0.199	0.031	0.031	0.050	97.900
3	0.265	0.25	1.15	0.016	0.0087	0.373	0.033	0.069	0.044	97.700
4	0.229	0.248	1.19	0.015	0.0082	0.324	0.032	0.061	0.047	97.800
5	0.228	0.245	1.26	0.015	0.0079	0.278	0.035	0.052	0.052	97.700
6	0.232	0.25	1.35	0.017	0.0082	0.215	0.032	0.039	0.046	97.700
7	0.171	0.24	1.26	0.014	0.0077	0.195	0.033	0.035	0.048	97.900
8	0.326	0.268	0.96	0.015	0.0088	0.640	0.039	0.131	0.042	97.500
9	0.408	0.284	0.73	0.016	0.0091	0.930	0.039	0.190	0.043	97.200
10	0.201	0.241	1.23	0.015	0.0075	0.219	0.031	0.036	0.048	97.900
11	0.382	0.276	0.76	0.016	0.0094	0.870	0.040	0.177	0.042	97.300
C_{av}	0.265	0.254	1.115	0.016	0.0084	0.419	0.035	0.081	0.046	97.664
s_x	0.073	0.014	0.198	0.001	0.0006	0.257	0.003	0.055	0.003	0.227

The first way was semi-quantitatively verified and detailed information about it was published in the works [L8-7 and 8-8]. The verification was made by already mentioned chemical analyses of the samples 1-11 (**Tab. 8-1**). Mass balance analysis showed that during these 20 minutes of casting before stopping the machine the melt contained at the point of breakout approx. 25% of the steel A and 75% of the steel B with the standard deviation of 10%.

It is necessary to make a data table for the way b), containing technological, geometrical, physical and chemical dimensional quantities that characterise both steel grades A and B and process of their continuous casting (**Tab. 8-2**). The data in the lines 11 to 17 were determined by triple calculation of temperature field of one symmetric half of the slab with the chemical composition A, composition B, and mixed composition A + B [L8-6]. Thermo-physical properties of the mixed composition of the steel were determined using the IDS software according to the average chemical composition of the steels A and B [L8-9].

Dimensional variables associated with continuous casting of steel slabs can be expressed in the first approximation in the required number together with their basic dimensions – **Tab. 8-3**. In accordance with the International System of Units (SI) the basic units meter-kilogram-second-Kelvin were used for expression of the dimensional parameters. **Table 8-3** contains twelve dimensional quantities, which on the basis of generally formulated theorems make it possible to express the interdependence of physical and chemical variables and parameters that enter into the technology of continuous casting. It is possible to formulate from the rows of the table, which contains also the basic dimensions m, kg, s and K (and which represents also the basic matrix) the equations for dimensional quantities (exponents), which must be met in each row for progressive determination of dimensionless criteria. These basic theorems include: theorem of dimensional independence in the chosen system of basic

units of measurement; theorem of dimensional homogeneity, which governs all the laws of physics, including the as yet unknown laws, π theorem, which ties the number of dimensional quantities with the number of mutually independent dimensions and with the number of dimensionless criteria.

Tab. 8-2 The parameters characterising continuous casting of steel grades A and B for the of physical similarity

Item	Parameter	Symbol	Units	Steel A	Steel B
1	Casting speed (shift rate)	w	$(m \cdot s^{-1})$	0.0130	0.0126
2	Kinematic viscosity	ν	$(m^2 \cdot s^{-1})$	$8.706 \cdot 10^{-4}$	$7.917 \cdot 10^{-4}$
3	Density	ρ	$(kg \cdot m^{-3})$	7 560.7	7 600.9
4	Specific latent heat of the phase change	L	$(m^2 \cdot s^{-2})$	$246 \cdot 10^3$	$259 \cdot 10^3$
4a	Latent heat of the phase change of one half of the slab with dimensions 0.25 × 0.765 × 14.15 m	L_{slab}	$(m^2 \cdot s^{-2})$	$5.0335 \cdot 10^9$	$5.3274 \cdot 10^9$
5	Specific heat capacity (for a constatnt pressure)	c_p	$(m^2 \cdot s^{-2} \cdot K^{-1})$	632.6	611.0
6	Mould oscillation amplitude	ΔS	(m)	0.006±0.003	0.006±0.003
7	Oscillation frequency	f	(s^{-1})	1.533	1.533
8	Solidus temperature	t_S	(°C)	1 427.0	1 480.6
		T_S	(K)	1 700.15	1 753.75
9	Liquidus temperature	t_L	(°C)	1493.9	1 512.3
		T_L	(K)	1 767.05	1 785.45
10	Difference between the liquidus and solidus temperatures ΔT	$t_L - t_S$	(°C)	66.9	31.7
11	Max. length of the iso-solidus curve from the level (breakout)	$h_S^{\max}$	(m)	21.07	19.72
12	Min. length of the iso-solidus curve from the level	$h_S^{\min}$	(m)	19.92	18.69
13	Max. length of the iso-liquidus curve from the level (breakout)	$h_L^{\max}$	(m)	14.50	16.20
14	Min. length of the iso-liquidus curve from the level (breakout)	$h_L^{\min}$	(m)	13.70	15.20
15	The area of the mushy zone on half of the cross-section of the breakout	F_{mushy}	(m^2)	0.05366	0.04100
16	The overall area on half of the cross-section	F_{slab}	(m^2)	0.19125	0.19125
17	The area of the melt (liquid) zone on half of the cross-section of the breakout	F_{melt}	(m^2)	$1.381 \cdot 10^{-3}$	$13.720 \cdot 10^{-3}$
18	The overheating above liquidus temperature	ΔT_{over}	(°C)	30	27

Note: The mass of one half of the slab with dimensions 0.25 × 0.765 × 14.15 m is $2.04614 \cdot 10^4$ kg (steel A) and $2.0569 \cdot 10^4$ kg (steel B).

In the case of breakout we do not know more detailed information about the internal relationship between dimensional quantities and the essence of the breakout, and we do not have either even partial mathematical and physical description of this phenomenon. That's why it is necessary to use at application of the theory of similarity the dimensional analysis for determination of the dimensionless criteria. In our case for n dimensional quantities (n = 12) and for r mutually independent dimensions (r = 4), as it follows from the rows of the matrix (**Tab. 8-3**), which according to the π theorem makes $n - r$ = 12 – 4 = 8 dimensionless criteria. Methods used for determination of dimensionless criteria based on the assumption of respecting the relevant theorems are described in the work [L8-10], including the list of other recommended literature.

Tab. 8-3 Matrix of physical-chemical dimensions and parameters and quantities of the continuously cast melt (connected with the flying change of tundish, with the so called additional continuous casting and with breakout)

Serial No.	1	2	3	4	5	6	7
Value	Casting speed	Kinematic viscosity	Density	Latent heat of the slab	Specific heat	Amplitude of the mould	Oscillation frequency of the mould
exponent	e1	e2	e3	e4	e5	e6	e7
symbol	w	ν	ρ	L_{slab}	c_P	ΔS	f
m	1	2	-3	2	2	1	0
kg	0	0	1	1	0	0	0
s	-1	-1	0	-2	-2	0	-1
K	0	0	0	0	-1	0	0

Tab. 8-3 continuation

Serial No.	8	9	10	11	12	13	Row
Value	Solidus temperature	Liquidus temperature	Mushy zone	Area of slab cross-section	Area of melt cross-section	Overheating above the liquidus temperature	
exponent	e8	e9	e10	e11	e12	e13	
symbol	T_S	T_L	F_{mushy}	F_{slab}	F_{melt}	ΔT_{over}	
m	0	0	2	2	2	0	1
kg	0	0	0	0	0	0	2
s	0	0	0	0	0	0	3
K	1	1	0	0	0	1	4

One possible way of determination of the necessary dimensionless criteria consists in formulation of mutually independent equations from **Tab. 8-3** for individual rows 1 to 4 of basic independent dimensions (m, kg, s and K). Solution of this system of equations requires always for determination of each similarity criterion progressive selection of 8 variables, and this selection must be repeated altogether eight times. The equations formulated from the rows of the Tab.8-3 used for determination of the eight dimensionless criteria (i.e. eight similarity numbers) are arranged in **Tab. 8-4**.

Tab. 8-4 Equations tying together the exponents of dimensional quantities with the basic dimensions

Row	Equations for exponents	Number of quantities
Row 1 – m	e1 + 2e2 -3e3 + 2e4 + 2e5 + e6 + 2e10 + 2e11 + 2e12 = 0	9
Row 2 – kg	e3 + e4 = 0	2
Row 3 – s	–e1 – e2 –2e4 – 2e5 – e7 = 0	5
Row 4 – K	-e5 + e8 + e9 + e13 = 0	4

Note: We will make sure that the equations formulated from the rows of the matrix represent a mutually independent system of equations of exponents.

8.2.4 Dimensionless similarity criteria and their characteristics

In accordance with the used theorems (Fourier, Buckingham, Langhaare) altogether eight necessary criteria π_1 - π_8 of physical similarity were determined for the steel grades A and B, in which it will be presumed that their increasing numerical values will characterise the susceptibility to breakouts. In the next step we will test the partial susceptibility of the relevant steel A or B to breakouts with use of shares of individual pairs of criteria [L8-11]. Finally, it will be decided how to attribute greater or lesser risk of breakout to one steel on the basis of both the sum and the product of all eight partial criteria determined in this manner. Eight criteria are arranged in the following order:

$$\pi_1 = \frac{L_{slab} \cdot f}{c_p \cdot \rho \cdot \nu \cdot T_L \cdot \Delta S} \quad \text{(eq. 8-1)}$$

The first criterion is complex and it is a function of altogether seven parameters, out of which four are thermo-physical properties of steel (L, c_p, ρ and ν) and three are process parameters (f, T_L, ΔS). Susceptibility to breakouts is proportional to the latent heat and inversely proportional to the product of three thermo-physical properties.

$$\pi_2 = \frac{\Delta S \cdot f}{w} \quad \text{(eq. 8-2)}$$

The second criterion is known as Strouhal's criterion. Tendency to breakouts increases with the increasing amplitude of oscillation and oscillation frequency of the mould.

$$\pi_3 = \frac{\Delta S^2 \cdot f}{v} \quad \text{(eq. 8-3)}$$

This criterion contains in numerator geometrical data of the mould and it is inversely proportional to kinematic viscosity.

$$\pi_4 = \frac{F_{slab}}{F_{solid}} \quad \text{(eq. 8-4)}$$

The fourth criterion is a function of surfaces, namely half of the cross section area of the solidified slab (i.e. $F_{\text{slab}} = 0.25 \times 0.765$ m^2), of the area F_{melt} occupying half of the cross section led through the melt breakout at the temperature higher than the liquidus temperature, and the area F_{mushy} occupying half of the cross section led through the breakout solidifying melt at the temperature lying in the interval of solidification (mushy zone).

Denominator from equation (**eq. 8-4**)

$$F_{solid} = F_{slab} - (F_{\text{melt}} + F_{\text{mushy}}) \quad \text{(eq. 8-5)}$$

thus in fact reflects the current "bearing surface" of the cross section led through the breakout. Tendency to breakout increases with the decreasing denominator, i.e. with reduction of the "bearing surface".

$$\pi_5 = \frac{T_L - T_S}{T_L} \quad \text{(eq. 8-6)}$$

Simplex π_5 is a dimensionless temperature interval of crystallisation. This simplex must be used very carefully in cases where it is not statistically proven by higher number of melts or steels. For example in this particular case it significantly differs for both steels A and B and the steel A has greater susceptibility to breakouts.

$$\pi_6 = \frac{\nu}{f \cdot F_{solid}} \quad \text{(eq. 8-7)}$$

Value of the complex criterion π_6 is directly proportional to the value of the kinematic viscosity v of the melt or of the mushy zone and it is inversely proportional to the oscillation frequency of the mould f and the current "bearing surface" of the section led through the breakout (as in case of the fourth criterion).

$$\pi_7 = \frac{w^2}{c_p \cdot (T_L - T_S)} \quad \text{(eq. 8-8)}$$

The seventh complex criterion is a function of technological parameter contained in the numerator and of thermo-physical properties contained in the denominator. Its value and thus the susceptibility to breakouts increases with the square of the speed of casting and decreases with the value of the product of the specific heat capacity and the crystallisation interval.

$$\pi_8 = \frac{\Delta T_{over}}{T_L} \qquad \text{(eq. 8-9)}$$

The simplex criterion π_8 is a dimensionless temperature of overheating above the liquidus temperature.

8.2.5 Numerical values of criteria and their discussion

Numerical values of individual eight criteria for the steels A and B are summarised in the first two rows of the **Tab. 8-5**.

Tab. 8-5 Assessment of influence of individual dimensionless criteria (similarity numbers)

Criterion π_i	π_1	π_2	π_3	π_4	π_5	π_6	π_7	π_8	Sum
Steel A π_i^A	$1.74784 \cdot 10^5$	0.7070	0.06339	1.4041	0.03786	$4.17 \cdot 10^{-3}$	$3.99 \cdot 10^{-9}$	1.0170	-
Steel B π_i^B	$2.07344 \cdot 10^5$	0.7300	0.06971	1.4008	0.01807	$3.78 \cdot 10^{-3}$	$8.20.10^{-9}$	1.01512	-
Partial share of criteria of the steels B/A: $P_i = \pi_i^B / \pi_i^A$	1.1824	1.0325	1.0997	0.9976	0.4772	0.9064	2.0551	0.99815	8.7780
	P_1	P_2	P_3	P_4	P_5	P_6	P_7	P_8	$\sum_{i=1}^{8}(P_i)$
Progressive product of shares of criteria of the melts B/A $\prod_{i=1}^{i}(P_i)$	1.1863	1.2208	1.3425	1.3393	0.6391	0.5793	1.1905	1.1922	8.6861
	$\prod_{i=1}^{1}(P_i)$	$\prod_{i=1}^{2}(P_i)$	$\prod_{i=1}^{3}(P_i)$	$\prod_{i=1}^{4}(P_i)$	$\prod_{i=1}^{5}(P_i)$	$\prod_{i=1}^{6}(P_i)$	$\prod_{i=1}^{7}(P_i)$	$\prod_{i=1}^{8}(P_i)$	$\sum_{i=1}^{8}(P_1 \ldots P_8$
Partial share of criteria of the steels 3B/A for triple steel B in the mixture at the point of breakout	3.5589	3.0976	3.2991	2.9929	1.4318	2.7194	6.1654	2.9945	26.2588
	P_{1mix}	P_{2mix}	P_{3mix}	P_{4mix}	P_{5mix}	P_{6mix}	P_{6mix}	P_{8mix}	$\sum_{i=1}^{8}(P_{imix})$

The 3rd row of the table contains the calculated partial shares of the pairs of identical criteria for the steels B and A, i.e. $P_i = \pi_i^B / \pi_i^A$. Their sum has a value $\sum_{i=1}^{8}(P_i) = 8.7780.$

Average share of pairs of criteria is equal to one eighth of the sum $P_{i,mean,}$= 8.7780/8 = 1.0972

Product of the shares of all eight dimensionless criteria has the value $\prod_{i=1}^{8} P_i$ = 1.192.2

Their sum has a value $\sum_{i=1}^{8}(P_1 \ldots P_8) = 8.6861$

Its average value is $1.1922^{(1/8)}$ = 1.022. We can see that in both cases the average value of the shares, as well as the average value of the products is greater than 1. It means that the steel grade B has higher susceptibility to breakouts.

It follows from table 5 that partial shares P_2, P_3, P_4 and P_6 in **Tab. 8-5** are alternating for both steels A and B around the number 1. The share P_1 means that criterion π_1 is in the steel B 1.18 times bigger than in the steel A, which manifests bigger susceptibility of the steel B to breakouts. Partial shares P_7 and P_8 show that criteria π_7 and π_8 are in the steel B more than twice higher than in the steel A. This

manifests a distinct tendency of the steel B to initiate breakouts. On the other hand the share P_5 indicates only half tendency of the steel B to breakout in comparison with the steel A.

According to the P_{imean} =1.0972 for the average share of criteria it may be stated that the steel B has at the average the susceptibility to breakouts higher by 9%.

This higher susceptibility of the steel B to breakouts is manifested also by the value of the product of individual shares and by the average value of the product 1.022 ensuing from it. The existing assumption attributed the same initiation effect to formation of breakout to all eight dimensionless similarity criteria provided that notch at the place of the casting mark or crimp or hook (see **Figs. 8-1b** and **8-16**) was not influenced by real mass share of each steel at the point of breakout, but by their thermo-physical and chemical properties.

It followed from the balance analysis [L8-11] that as a result of mixing of melts of both steels the mass share of the steel A was at the place of breakout approx. 25% and that of the steel B was approx. 75%. So, we can express the susceptibility of the given steel to breakouts by the product of the relevant criterion and mass share of the steel. For example for the first criterion the product has the value $\pi_1^A \cdot 0.25 = 4.370 \cdot 10^4$ and for the steel B $\pi_1^B \cdot 0.75 = 1.5335 \cdot 10^5$.

Partial share of the first criteria for the mixture A+B is determined as $P_{1mix} = 1.5551 \cdot 10^5 / 4.370 \cdot 10^4 = 3.5586$. Risk of breakout of the steel B is 3.55 times higher than that of the steel A. It follows from the mass share of the steels A and B in the breakout (i.e. 0.75/0.25 = 3) that $P_{imix} = 3 \cdot P_i$, where P_i are the values from the 3rd row of the Table 5. We will now enter into the last row of the Table 5 partial shares of all criteria P_{imix}. The increased susceptibility of the steel B to breakouts in comparison with the steel A is according to these values of P_{imix} absolutely evident, even for the 5th criterion ($P_{5mix} = 1.4318$), in which value the of simple partial share of criteria indicated even the opposite tendency ($P_5 = 0.4772$). The sum $\sum_{i=1}^{8} (P_{imix})$ is 26.2588 and the average value of the share $P_{imix}^{mean} = 3.2823$ is a triple of the value P_{imean}. However, these values can be considered only as preliminary ones until we know the mass share of both steels in the breakout more precisely. Progressive product of the shares P_{imix} was not calculated anymore.

8.2.6 Conclusion

A typical breakout of the continuously cast slab 250 × 1 530 mm at the place of straightening was analysed with use of the theory of physical similarity. The breakout took place 20 minutes after the flying exchange of tundish, from which the steel grade B was continuously cast right after the previous casting of several heats of the steel grade A and the casting machine was automatically stopped. Atypical nature consisted in the fact that the breakout did not occur right under the mould, which is normally prevented by standard anti-breakout system, but as far as 14.15 m from the level of the melt in the mould and in the depth of 8.605 m below it. With use of dimensional analysis based on the π-theorem altogether 8 similarity criteria were derived. A table was compiled containing 12 technological, geometrical and thermo-physical dimensional quantities that characterise both steel grades A and B and also process of their continuous casting. Several quantities in the table were determined by original calculation of the temperature field of the slabs with the chemical composition A and B, namely the maximum and minimum length of iso-liquidus and iso-solidus curves and surface occupied at the place of breakout by melt at the temperature higher than the temperature of the liquidus, and surface occupied by the solidifying melt at the temperature lying within the interval of solidification. Thermo-physical properties of both steels for the table were determined with use of commercial software IDS. Five out of the 8 criteria were at the same time functions of technological, geometric and thermo-physical parameters, and the first criterion represented a total of 7 variables. The second criterion does not contain any thermo-physical property, the fourth criterion is only a function of the calculated geometric surfaces and the fifth criterion is a simplex. Numerical values of the eight criteria for the steels A and B were determined after entering the values from **Tab. 8-2**. Their number is determined by the π-theorem. Partial shares of all pairs of criteria $P_i = \pi_i^B / \pi_i^A$ were determined, as well as their sum $\sum_{i=1}^{8} (P_{imix})$, average value of the share $P_{i,mean}$, progressive product of these

shares $\prod_{i=1}^{8}(P_i)$ and average value of the product. It was determined by the mass balance analysis that during the already mentioned 20 minutes of casting before stopping of the machine the melt contained at the place of breakout a mixture of approx. 25% of the steel A and 75% of the steel B. It means that the mass share of the steel B was three times bigger. That's why for this mixture triple partial shares of criteria $P_{imix} = 3 \cdot P_i$ were calculated, as well as their sum and also triple average value of the share P_{imix}^{mean} ensuing form it.

An analysis performed with use of the similarity criteria clearly demonstrates objectively significantly increased susceptibility of the steel B to breakouts in comparison with the steel A. In order to prevent repetition of this industrial accident it is necessary to evaluate for both steels, which are to be cast consecutively, the derived criteria of similarity and other operations with them. It assumes also calculation of the temperature field of the slabs to be cast, in order to determine the quantities for **Tab. 8-2**. An increase of the numeric value of criteria of one steel in respect to another steel indicates possible formation of a breakout. If it is impossible to change the technological and geometrical quantities entering into the individual criteria, then it is necessary that remaining 12 quantities of both steels differ as little as possible, particularly thermo-physical properties, which vary with the chemical composition of the steel. From this perspective, the decisive criteria are the first (π_1), seventh (π_7) and eighth (π_8), which are a function of altogether six thermo-physical properties, namely latent heat of phase transformation, specific heat capacity, density, kinematic viscosity, liquidus and solidus temperatures, or their difference. The seventh and eighth criteria are functions of casting speed, which means that their reduction would reduce the risk of breakout. When selecting two steels, which must be cast on the continuous casting machine consecutively one after another, the technologist should therefore follow the value of partial shares of the first, seventh and eighth criteria P_1, P_7 and P_8. He will not have at his disposal more conclusive shares P_{1mix}, P_{7mix} and P_{8mix}, because he will not know the real mass shares of both steels at the place of potential breakout, nor position of the breakout, as was the case of the steels A and B discussed here.

8.3 Experimental research on the causes of the breakout

8.3.1 Introduction

Increasing the production efficiency of the continuous casting process requires casting of longer sequences of ladles without stopping and restarting the caster. As the demand for wider ranges of steel products increases at the same time, the intermixing of dissimilar grades is becoming a problem of growing concern.

Several different procedures exist to handle the casting of dissimilar grades. One of them is the "flying change of tundish", which completely prevents mixing in the tundish. The tundish is changed at the same time when the ladle containing the new grade is opened, so mixing occurs only in the strand. In order to further minimize intermixing, a "grade-separator" plate can be inserted into the mould. This method can completely prevent mixing in the strand. However, physical insertion of the “perfect grade separator” requires significant slowdown or even stoppage of strand, which incurs the risks of excessive bulging and cracks in the strand, breakouts, and even damaging the casting machine [L8-12].

Inhomogeneity (concentration, temperature) in the area of intermixing zone can be the reason for the breakout in the secondary-cooling zone, where a coexistence of solid and liquid phases exists.

The present chapter is the third (and the final) part of a detailed study into an atypical breakout occurred during continuous casting of a slab in the straightening zone. The first part [L8-5] of the study dealt with the simulation of the transient temperature field of continuously cast steel slab of two different chemical compositions with the help of the original numerical model. In the second part [L8-9] the causes of the breakout were analysed on the basis of the theory of physical similarity.

The aim of the present chapter [L8-13] is to study experimentally the causes of the breakout. Several experimental techniques were used for this analysis. The scanning electron microscope and the energy-dispersive analysis were used for measurement of the concentration data sets of elements.

Measurements were conducted on the samples taken from the selected areas of the slab, in the vicinity of the breakout. Then the concentration data sets were processed with the help of the original model of chemical heterogeneity and the concentration distribution of selected elements in micro-volumes and the concentration differences in macro-volumes in the breakout area were calculated. Furthermore a quantitative measurement of inclusions ("micro-cleanness") was performed in the samples using a metallographic microscope. Finally, the differential thermal analysis (DTA) was used for determination of the phase transformation temperatures. Solidus and liquidus temperatures were experimentally determined in the samples taken from the breakout area of the slab.

8.3.2 Experiment

Samples for analyses were taken from longitudinal cut of the solidified steel slab (1 530 × 250 mm), in which a breakout occurred at the change of chemical composition. Taking of samples was performed according to the diagram shown in **Fig. 8-1b**, melt analyses of both steels are given again in **Tab. 8-6** (see also subchapter 8.1.3). The heats differ namely by contents of C, Mn, Cr and Mo. Altogether 11 samples were taken from the mixed zone, both from the area of the breakout itself, and also from its vicinity. Concentration of selected elements (C, Si, Mn, P, S, Cr, Ni, Mo, Al a Fe) was measured in individual samples by spectrometry with use of the instrument SpectroMaxx made by Spectro, software Spark analyser MX. At least 4 analyses were made in each sample in the area beyond the strand shell.

Concentration profiles of the elements Al, Si, P, Cr, Mn, Ni, Mo and Fe were experimentally determined in the samples 1-3 and 9-11 [L8-14]. The samples were prepared by standard metallographic method. Micro-analysis of the element composition was made with use of the scanning electron microscope VEGA II XMU (TESCAN) with X-ray energy dispersive micro- analyser QUANTAX 800 (BRUKER) with detector of SDD type. Measurements were performed in each sample in straight line of 101 points with a step of 10 μm.

Tab. 8-6 Melt analyses of the steels A and B in wt.% (selected elements)

Steel	C	Si	Mn	P	S	Cr	Ni	Mo	Al
A	0.416	0.28	0.70	0.013	0.0064	0.95	0.03	0.206	0.037
B	0.174	0.23	1.46	0.017	0.0058	0.07	0.02	0.005	0.048

Furthermore a quantitative measurement of inclusions (“micro-cleanness”) was performed in the samples 1-3 and 9-11 [L8-15]. Metallographic microscope Neophot 32 and digital camera Olympus C-3030 were used for observation and photo documentation. Micro-purity was evaluated on the image analyser Olympus CUE4 at standard conditions of measurement (i.e. applied magnification 100×, an area of approx. 1 cm^2 was evaluated in each sample).

Method of differential thermal analysis was used for the measurements of temperatures of phase transformations, namely the liquidus and solidus temperatures. Six samples (1-3 and 9-11) from the breakout area were analysed. Determination of temperatures was made with use of experimental laboratory equipment for thermal analysis SETSYS 18_{TM} made by Setaram, and measuring rod TG/DTA of type "S" (S – type rod Pt/PtRh 10%), which enables measurements within the temperature interval from +20 °C up to +1 600 °C. The samples were analysed in corundum (Al_2O_3) crucibles with volume of 100 μl. A permanent inert dynamic atmosphere was maintained during heating/cooling – flow rate of Ar (> 99.9999%) was 2 $l \cdot h^{-1}$. The samples were during experiment control heated at the rate of 10 $K \cdot min^{-1}$.

8.3.3 Results and their discussion

Results of analyses of average chemical composition of the samples 1-3 and 9-11 determined by spectrometer are given in **Tab. 8-1.** From these samples we can see very uneven mixing of both steels, namely in the samples 9-11.

Difference in chemical composition of the samples manifested itself also in different temperatures of solidus and liquidus that were measured experimentally by DTA method (see **Tab. 8-7**). Solidus temperatures vary within the range from 1 422 °C (samples 9 and 11) to 1 486.5 °C (sample 2). Differences in solidus temperatures between the samples 9-10 and 10-11, which lie in one plane (**Fig. 8-1b**) are substantial, they achieve even 46 °C. Such temperature differences can cause considerable tension in solidified material, which may lead to a rupture of that material. The measured liquidus temperatures differ also for individual samples, although the differences are not as big as in the case of solidus temperatures. The differences of solidus and liquidus temperatures in individual samples were confirmed also by calculation performed by the IDS software. This software calculates temperatures of phase transformations on the basis of specified chemical composition and it introduces for the solidification process certain simplifying assumptions [L8-16].

The above mentioned findings are confirmed also by results from micro-analytical measurements. Concentration sets obtained by micro-analysis were subjected to the basic statistical analysis and the following characteristics of the analysed elements for individual samples were determined: average concentration of the element C_{av} and its standard deviation s_x, maximal C_{max} and minimal C_{min} concentration of the element. Out of all the analysed samples for presentation of micro-segregation behaviour and chemical micro-heterogeneity the elements Mn and Cr were chosen, as their concentration differed in melts of the steels A and B. The characteristics mentioned above concern the elements Mn and Cr given in **Tab. 8-7**.

Tab. 8-7 Solidus T_S and liquidus T_L temperatures obtained experimentally and calculated using the SW IDS

Sample	Phase Transformation Temperature			
	DTA (experiment)		IDS (calculation)	
	T_S (°C)	T_L (°C)	T_S (°C)	T_L (°C)
1	1 465.3	1 512.5	1 447.4	1 505.7
2	1 486.5	1 524.7	1 463.6	1 512.4
3	1 459.8	1 507.1	1 449.3	1 506.5
9	1 422.0	1 488.5	1 420.2	1 494.6
10	1 468.0	1 507.9	1 461.2	1 509.6
11	1 422.0	1 489.1	1 425.1	1 496.9

It follows from comparison of the values of average concentrations of Mn and Cr determined by micro-analysis (**Tab. 8-8**, parameter C_{av}) and concentration values of these elements determined by melt analysis (**Tab. 8-6**) and by spectrometer (**Tab. 8-1**), that the values obtained by energy dispersive micro-analysis are distorted by certain error (overestimation). For this reason we will not take into account in future interpretation of the results the absolute values of thus measured concentrations (and of other parameters determined from those concentrations), but only the differences between individual samples. Due to the fact that micro-analytical measurements were performed for all the samples under the same working conditions [L8-14], it is possible to make such differential comparisons.

From statistically processed concentration files indices of micro-heterogeneity I_H were moreover calculated for individual elements, which characterise chemical heterogeneity of the given element in the measured section, i.e. on the abscissa of 1 000 μm. Index of micro-heterogeneity for the given element is determined as a ratio of standard deviation s_x and average concentration C_{av} of the element in the measured section of the sample. The values I_H for Mn and Cr are given in **Tab. 8-8**, which contains for these elements also the so called indices of macro-heterogeneity I_P; $I_P = dc/cm$, where $dc = C_{max} - C_{min}$ and $cm = (C_{max} + C_{min})/2$. Index of macro-heterogeneity characterises chemical heterogeneity of the given element within the whole area of the cross-section, from which the samples were taken for analyses.

Several findings follow from the results given in **Tab. 8-8**. Concentration distribution of Mn and Cr within individual samples is in the measured sections (1 000 μm) comparatively homogenous, as it follows from the values of standard deviations of concentrations s_x. This means that chemical micro-

heterogeneity within the frame of the measured sections, caused by segregation of elements, is not too high. This conclusion has been confirmed also by calculated values of indices of micro-heterogeneity I_H. Values of this parameter do not differ too much for individual samples and they do not differ too much even between both elements. It means that segregation behaviour of elements in micro-volumes is very similar in all the analysed samples.

Courses of micro-segregation of both elements in individual samples were processed also graphically in the form of the so called distribution curves of dendritic segregation (**Figs. 8-17 to 8-20**). These curves represent dependence of the element concentration on the fraction of the solidified phase at crystallisation and solidification of the given material. Details about formation of curves from micro-analytically measured concentration data are given in the work [L6-9].

Tab. 8-8 Basic statistic parameters of micro-analytically measured concentrations of Mn and Cr in the samples and determined indices of micro-heterogeneity I_H and macro-heterogeneity I_P

	Mn						Cr					
Sample	C_{av}	s_x	C_{min}	C_{max}	I_H	I_P	C_{av}	s_x	C_{min}	C_{max}	I_H	I_P
1 (n = 96)	1.619	0.155	1.287	1.998	0.096		0.721	0.072	0.543	0.919	0.100	
2 (n = 98)	1.730	0.162	1.340	2.224	0.094		0.553	0.077	0.368	0.788	0.139	
3 (n = 99)	1.633	0.215	1.213	2.280	0.132		0.718	0.092	0.522	0.930	0.129	
9 (n = 96)	1.224	0.126	0.895	1.559	0.103	0.343	1.230	0.137	0.959	1.549	0.111	0.760
10 (n = 99)	1.633	0.141	1.257	2.040	0.086		0.561	0.076	0.364	0.790	0.135	
11 (n = 99)	1.238	0.140	0.857	1.635	0.113		1.222	0.131	0.938	1.554	0.107	

Note: Concentrations are given in wt.%, n is number of the measured points minus number of the points that were excluded on the basis of the Grubbs' test.

It follows from **Tab. 8-8** that chemical macro-heterogeneity across the slab section is very high. It is manifested by differences of the values of average concentrations of C_{av} calculated for individual samples. Differences are obvious namely in the samples 9-11 and particularly for Cr. High chemical heterogeneity is documented also by the values of indices of macro-heterogeneity I_p, which are higher than indices of micro-heterogeneity, especially for Cr. Chemical macro-heterogeneity was here unequivocally caused by penetration of steel from the next heat into the steel from the previous heat, which was contained in crystallizer during the flying change of tundish.

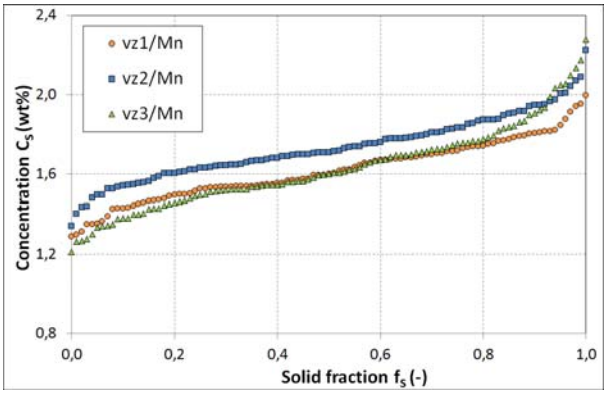

Fig. 8-17 Distribution curves of dendritic segregation of Mn for the samples 1-3

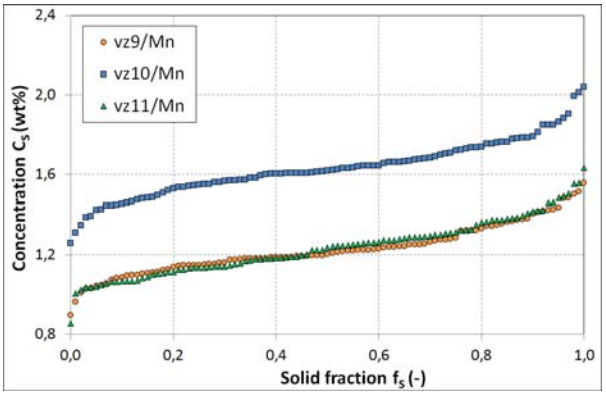

Fig. 8-18 Distribution curves of dendritic segregation of Mn for the samples 9-11

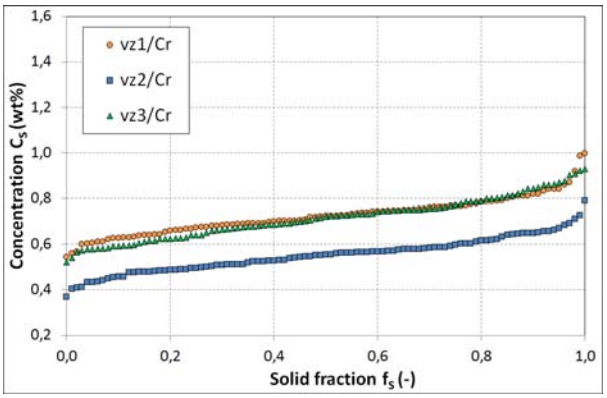

Fig. 8-19 Distribution curves of dendritic segregation of Cr for the samples 1-3

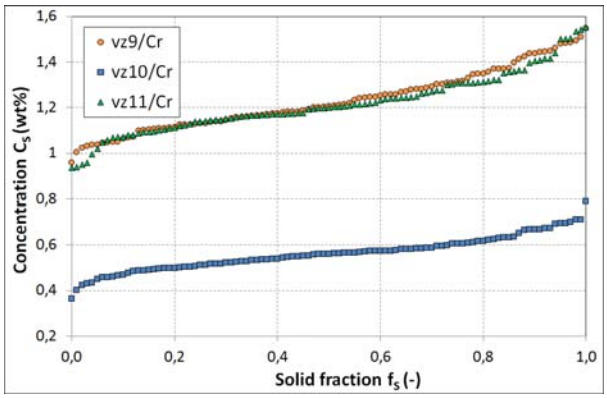

Fig. 8-20 Distribution curves of dendritic segregation of Cr for the samples 9-11

Curves in **Figs. 8-17 to 8-20** also confirm that concentration differences of Mn and Cr are very high between individual samples. The sample 10 particularly distinguishes itself from the whole set of the analysed samples, as it is characterised by high concentration of Mn and low concentrations of C, Cr and Mo in comparison with adjacent samples 9 and 11 (see **Tabs. 8-1 and 8-8 and Figs. 8-17 to 8-20**).

Different behaviour of the area, from which the sample 10 was taken, is confirmed also by analyses of inclusions in individual samples. In all the evaluated samples, regardless of the place of their taking, the same types of inclusions are present – oxi-sulphides of globular shape prevail, and sulphides of rounded and polyhedral shapes are also present, as well as oxides [L8-15]. **Table 8-9** presents selected results – size and number of inclusions in the analysed samples 1-3 and 9-11.

The following order of the samples from the viewpoint of micro-cleanness was established from observations according to the global contamination of the sample by inclusions (**Tab. 8-9** and [L8-15]):

- sample 9 → sample 1 → sample 11 → sample 2 → sample 3 → sample 10;
- at the same time it is possible to divide the samples from the perspective of the level of global contamination approximately into three groups – samples 1, 9 and 11 (up to 0.04%), samples 2 and 3 (0.06%), and the sample 10 (0.11%).

It follows from the above that even from the perspective of contamination by inclusions a big difference exists between individual analysed samples. The smallest contamination was in the sample 9, and the biggest one was in the sample 10. Asymmetric contamination of the continuously cast slab results from asymmetric flow, which could be induced by nozzle clogging, by turbulence and by excessive argon jet injection [L8-17].

It may be stated on the basis of the above facts that the breakout occurred most probably as a consequence of strongly uneven mixing of the melts of the steels A and B in the crystallizer. In the area of mushy zone the differentially enriched melt was already caught in bigger solidified lumps, which prevented its homogenisation. The created temperature and stress gradients together with surface defects of the solidified strand shell evidently caused the breakout. Substantially uneven mixing of the melts of both steels was obviously one of the main causes of occurrence of the breakout, segregation actions in this case might have had a secondary influence.

Tab. 8-9 Size and number of inclusions in the analysed samples

Sample	Average number of inclusions N_{av} with the areas > xxx μm² (inclusions/mm²)								Size of inclusions S (μm²)	
	N_{av} / ± s_x	>5	>10	>15	>20	>25	>50	>100	S_{max}	S_{av} ± s_x
1	24.5±8.0	24.5	17.8	10.8	5.5	3.0	0.5	0.1	366	17±14
2	21.6±9.5	21.6	17.9	14.0	9.6	6.7	1.8	0.4	1 290	26±41
3	26.1±8.7	26.1	19.9	13.1	7.4	4.5	1.1	0.3	4 688	22±90
9	17.7±6.1	17.7	12.6	7.8	4.1	2.2	0.4	0.1	366	18±15
10	39.1±17.8	39.1	32.2	23.1	15.5	10.6	3.7	1.1	1 377	28±51
11	24.4±7.9	24.4	18.1	11.1	5.9	3.6	0.6	0.1	152	18±13

8.3.4 Conclusion

The work investigated the micro-segregation behaviour of selected elements (Cr, Mn) across the longitudinal section of the continuously cast slab, the casting of which had to be stopped due to the breakout. The samples for analyses were taken from the cut of the slab, in vicinity of the breakout. Moreover chemical macro-heterogeneity of selected elements (C, Si, Mn, P, S, Cr, Ni, Mo, Al and Fe) in the area of this cross-section was investigated. On the basis of extensive experimental measurements the following main results were determined:

- chemical composition of individual samples differed considerably, which caused a considerable difference of solidus and liquidus temperatures in individual samples,
- segregation behaviour of the elements Cr and Mn in micro-volumes (i.e. micro-segregation) is very similar in all the analysed samples,
- magnitude of segregation of these elements in the measured sections of 1 000 μm is approximately the same in all the analysed samples,
- chemical macro-heterogeneity is very high across the analysed slab section, elements with different concentration in the melts of the steels A and B are along the longitudinal axis distributed very unevenly,
- from the viewpoint of contamination by inclusions big difference exists between individual analysed samples, which might have been caused by asymmetric flow in the crystallizer,
- very uneven mixing of melts of both steels was probably one of the main causes of formation of the breakout.

The solution has been printed in the peer-reviewed journals and presented at prestigious conferences [L8-18 to 8-21].

8.4 Literature

[L8-1] Schwerdtfeger K. and Hong Sha: Depth of Oscillation Marks Forming in Continuous Casting of Steel, *Metallurgical and Materials Transactions B*, 31 B, (2000) August, 813–826.

[L8-2] Badri A., et al.: *A Mold Simulator for Continuous Casting of Steel. Part II. The Formation of Oscillation Marks during the Continuous Casting of Low Carbon Steel*. *Metallurgical and Materials Transactions B,* 36 B (2005) June, 373–383.

[L8-3] Thomas B.G., Sengupta J. and Ojeda C.: *Mechanism of Hook and Oscillation Mark Formation In Ultra-Low Carbon Steel*. In Second Baosteel Biennial Conference, (May 25-26, 2006, Shanghai, PRC), 1 (2006), 112-117.

[L8-4] Ojeda C., et al.: *Mathematical Modeling of Thermal-Fluid Flow in the Meniscus Region During an Oscillation Cycle*. AISTech 2006 Proceedings - Volume 1, pp. 1017–1028.

[L8-5] Kavička F., Štětina J., Sekanina B., Stránský K., Dobrovská J., Mauder T. and Masarik M.: Analysis of atypical breakout during a radial continuous casting of a slab in the straightening zone. I. Numerical simulation of temperature field of a slab. *Hutnické listy,* 66 (2013) 2, 53–59.

[L8-6] Kavička F., Stránský K., Sekanina B., Štětina J., Mauder T. and Masarik M.: Comparison of the Temperature Field Continuously Cast steel Slabs of Different Chemical Composition. In 21st International Conference on Metallurgy and Materials *METAL 2012*, Brno 2012, Czech Republic, p.142–147.

[L8-7] Stránský K., Kavička F., Dobrovská J., Masarik M., Štětina J. and Sekanina B.: Heterogeneity of the Concast Steel Slab Tightly Before the Breakout. In 21st International Conference on Metallurgy and Materials *METAL 2012*, Brno 2012, Czech Republic, p.148–153.

[L8-8] Dobrovská J., Francová H., Dobrovská V., Kavička F. and Stránský K.: Investigation into Segregation of Selected Elements in the Breakout Area of the Continuously Cast steel slab. In 21st International Conference on Metallurgy and Materials *METAL 2012*, Brno 2012, Czech Republic, p. 115–121.

[L8-9] Louhenkilpi S., Laitinen E. and Nieminen R.: Real-Time Simulation of Heat Transfer in Continuous Casting, *Metallurgical Transactions B,* 24B (1993) 4, 685–693.

[L8-10] Kuneš J., Vavroch O. and Franta V.: *Základy modelování [Basics of modelling]*. SNTL, Praha 1989, 264 pages.

[L8-11] Stránský K., et al.: Analysis of a typical breakout during a radial continuous casting of a slab in the straightening zone. II. An analysis of the causes of the breakout by means of the theory of physical similarity *Hutnické listy,* 66 (2013) 3, 53-59.

[L8-12] Huang X. and Thomas B.G.: Intermixing Model of Continuous Casting during a Grade Transition. *Metallurgical Transactions B*, 27B (1996) 4, 617-632.

[L8-13] Dobrovská J., et al.: Analysis of atypical breakout during a radial continuous casting of a slab in the straightening zone. III. Experimental research on the causes of the breakout. *Hutnické listy,* 66 (2013) 5, 8-13.

[L8-14] Winkler Z., Belko J. and Perničková B.: Analyses of element heterogeneity of the samples 1, 2, 3, 9, 10, 11 from the slab from breakout. *Research report*, VOP-026 ŠTERNBERK, s.p. division VTÚO Brno, October 2011.

[L8-15] Belko J. and Stránský K.: Micro-purity of the samples taken from various places of the slab after the breakout accident. *Research report*, VOP-026 ŠTERNBERK, s.p. division VTÚO Brno, August 2011.

[L8-16] Miettinen J.: Calculation of solidification-related thermophysical properties for steels. *Metall Mater Trans* B, 28 (1997) 2, 281–297.

[L8-17] Zhang L. and Thomas B.G.: Inclusions In Continuous Casting of Steel. In *XXIV National Steelmaking Symposium*, Morelia, Mich, Mexico, 26-28 (Nov. 2003), 138–183.

[L8-18] Stránský K., Kavička F., Sekanina B., Dobrovská J., Štětina J. and Mauder T.: Oscillation Marks and Hooks on the Surface of Concast Slabs and their Relation to Breakout. *Key Engineering Materials.* 2011. 465 (2011) 1, 467–470.

[L8-19] Kavička F., Stránský K., Sekanina B., Štětina J., Masarik M. and Mauder T.: Comparison of the temperature field continuously cast steel slabs with different chemical composition. *Materiali in tehnologije/Materials and technology.* 2013. 47 (2013) 4, 497–501.

[L8-20] Kavička F., Dobrovská J., Stránský K., Sekanina B., Štětina J., Mauder T. and Masarik M.: Breakout of a Slab as the Result of Changes in the Thermo-physical Properties of Continuously Cast Steel. *Fatigue & Fracture of Engineering Materials & Structures.* 2013. 2013 (2). p. 1–10.

[L8-21] Stránský K., Kavička F., Dobrovská J., Dobrovská V., Sekanina B. and Štětina J.: Zone Analysis of Atypical Breakout during Radial Continuous Casting of a Slab in the Straightening Zone II. Analysis of the Causes of the Breakout by Application of the Theory of Physical Similarity. *Hutnické listy,* 66 (2013) 3, 17–25.

9 Electromagnetic stirring (EMS) of the melt of concast billets and its importance

9.1 Introduction

Currently, casters use rotating stators of electromagnetic melt-stirring systems. These stators create a rotating magnetic induction field, which induces eddy currents. Induction and eddy currents create an electromagnetic force, which works on every unit of volume of steel and brings about a stirring motion in the melt. The speeds of the liquid steel caused by the EMS is somewhere from 0.1-to-1.0 $m \cdot s^{-1}$. The stirring parameters are within a broad range of values, depending on the construction and technological application of the stirrer. The power output is mostly between 100 and 800 kW, the electric current between 300 and 1 000 A, the voltage up to 400 V and with billet casting the frequency from 5 to 50 Hz.

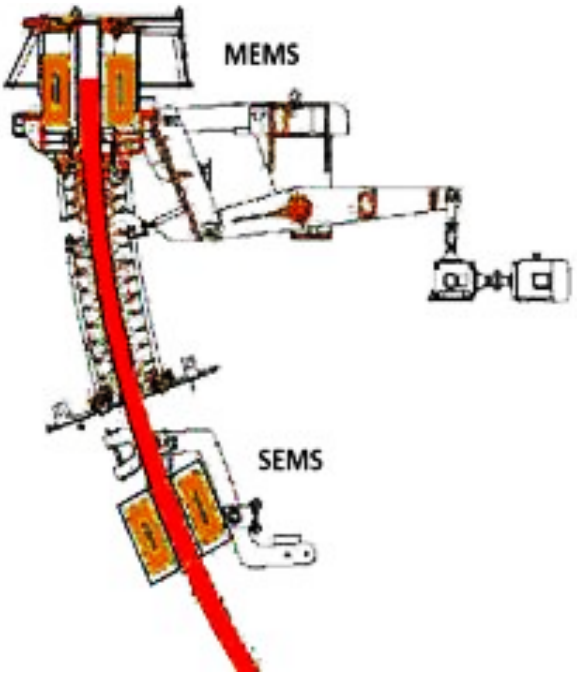

Fig. 9-1 The positions of the MEMS and SEMS stirrers

The EMS applied on the steel caster is basically a magneto-hydraulic process together with crystallisation processes and solidification of billet steel. The complexity of the entire process is enhanced further by the fact that the temperatures are higher than the casting temperatures of concast steel. The temperature of the billet gradually decreases as it passes through the caster down to a temperature lying far below the solidus temperature. From the viewpoint of physics and chemistry, the course of the process is co-determined by a number of relevant material, physical and thermokinetic characteristics of the concast steel and also electrical and magnetic quantities. There is also a wide range of construction and function parameters pertaining to the caster and EMS as well as parameters relating to their mutual arrangement and synchronisation. Numerous works from recent years relate that exact mathematical modelling of EMS on a caster is still unsolvable [L9-1 to 9-3].

The basic EMS experiment was conducted on a concast billet caster where two individual mixers were working as in **Fig. 9-1**. The first stirrer, entitled MEMS (Mould Electromagnetic Stirring), is mounted directly on the mould (crystallizer) and the second stirrer, entitled SEMS (Strand Electromagnetic Stirring), is mounted at the beginning of the flow directly after the first cooling zones but in the secondary-cooling zone. Here the outer structure of the billet is already created by a compact layer of crystallites, however, in the centre of the billet there is still a significant amount of melt that is mixed by the SEMS.

9.2 The conditions of the experiment

The first stirrer (MEMS) stirs the melt still in the mould while the billet is undergoing crystallization and solidification. The second stirrer (SEMS) works at a time when the melt is already enclosed by a shell of crystallites around the perimeter of the billet and inside the billet there is less melt than above in the active zone of the first stirrer.

When both stirrers were switched off, the crystallisation and solidification continued in the normal way, i.e. the solidifying melt did not undergo a forced rotational movement.

Samples were taken throughout the course of the experiment – from parts of the billet cast using the MEMS and SEMS and without and also using either one. The samples were taken in the form of cross-sections (i.e. perpendicular to the billet axis). The samples were fine-ground and etched with the aim of making visible the dendritic structure which is characteristic for individual variants of the solidification of the billet.

The verification of the influence of MEMS and SEMS on the macrostructure of the billet was carried out on two melts of almost the same chemical composition (**Tab. 9-1**).

Tab. 9-1 Chemical composition of experimental melts (wt.%)

Melt	C	Mn	Si	P	S	Cu	Cr	Ni	Al	Ti
A	0.14	0.31	0.22	0.014	0.009	0.03	0.05	0.02	0.02	0.002
B	0.13	0.32	0.22	0.018	0.012	0.09	0.06	0.04	0.02	0.002

The timing of the concasting process of the billets – without the involvement of the stirrers and with the working of the EMS of individual variants of stirrers (MEMS and SEMS) – is given in **Tab. 9-2**. The speed of the concasting (i.e. the movement, the proceeding of the billet through the mould) of the billet was maintained constant during the experimentation at a value of 2.7 $m \cdot min^{-1}$. **Table 9-2** shows that as many as nine concasting variants were verified. The lengths of individual experimental billets – from which samples had been taken – were always a multiple of the metallurgical length. The average superheating of the steel above the liquidus was 32.8±3.1 °C in melt A and 28.0±4.6 °C in melt B, which lies within the standard deviation of the temperature measurements.

Tab. 9-2 The billet concasting modes and sampling

Melt	Concasting mode – sampling	Superheating of steel above liquidus (°C)	MEMS stirring (A)	SEMS stirring (A)	Figure
A	1A	37	210	0	
	2A	31	0	0	**Fig. 9-2**
	3A	33	0	29	
	4A	30	210	57	**Fig. 9-3**
B	1B	35	210	0	
	2B	30	0	0	**Fig. 9-2**
	3B	27	0	57	
	4B	24	210	57	
	5B	24	210	29	**Fig. 9-3**

(Note: Detailed records of the experimental verification of the effects of MEMS and SEMS during concasting on the relevant device pertain to **Tab. 9-2**. The data are appended with a time history of the MEMS and SEMS connection and with information relating to the lengths of individual billets and the points from which the actual samples had been taken (i.e. the cross-sections from which the dendritic structures had been created [L1-36 and L9-4]).

9.3 Evaluating experiments

Evaluation of all nine variants of concasting (**Tab. 9-2**) indicates that the arrangement of dendrites in the cross-section follow the same tendency in the first phase of crystallization. The structure is created by columnar crystals – dendrites – perpendicular to the walls of the billet (**Fig. 9-2**).

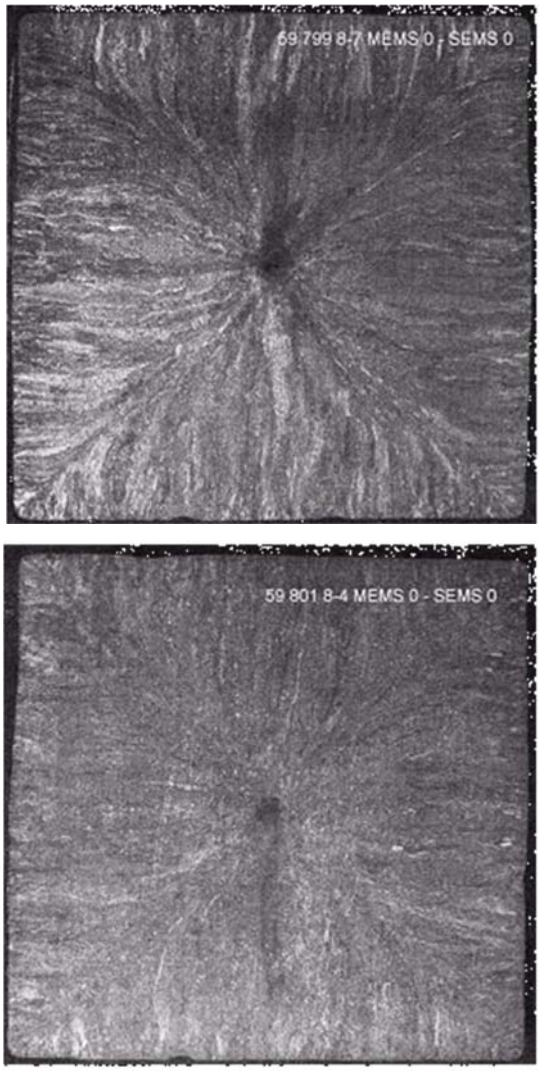

Fig. 9-2 The growth of dendrites without EMS – mode 2A (up) and mode 2B (**Tab. 9-2**)

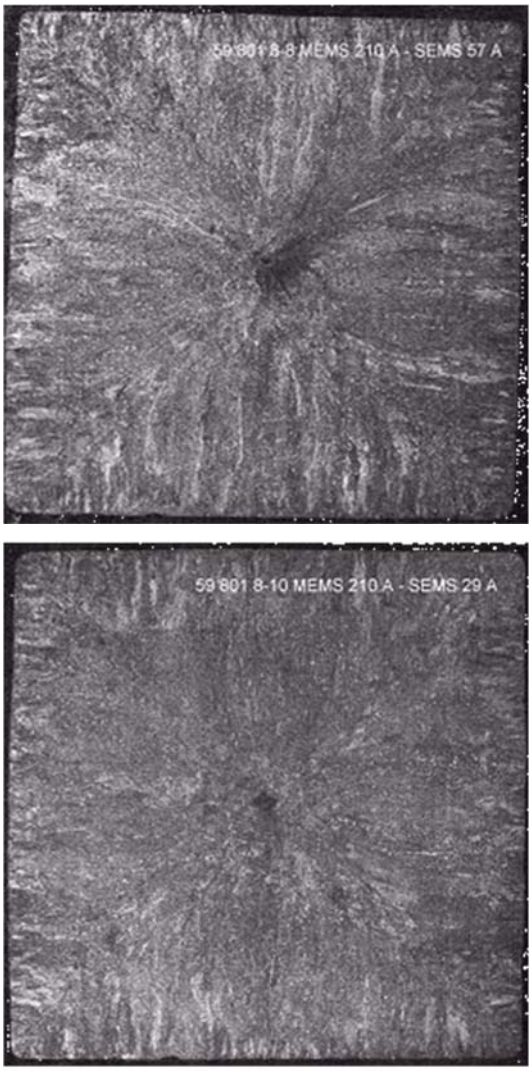

Fig. 9-3 The growth of dendrites using MEMS and FEMS-mode 4A (up) and mode 5B (**Tab. 9-2**)

In the billets that were not stirred the dendrites gradually touch one another on the diagonals of the cross-section. Here their growth either ceases, or the dendrites bend in the directions of the diagonals and their growth continues all the way to the centre of the billet. The columnar dendrites that grow from the middle part of the surface maintain their basic orientation – perpendicular to the surface – almost all the way to the centre of the billet. In the central part of the cross-section there is an obvious hollow on all nine macroscopic images. This is most probably a shrinkage. The above-described mechanism of dendrite growth during concasting without stirring is frequently the object of interest (**Fig. 9-2**).

Inside the billets, when using the MEMS stirrer (or both MEMS and SEMS), the kinetics of solidification and dendrite growth is initially the same as without stirring. This also creates columnar dendrites which touch along the diagonals, however, soon their growth ceases still near the surface. Dendrites, which are called equiaxed dendrites continue to grow – their orientation is more random and only partly directed towards the centre of the billet (**Fig. 9-3**). It appears that this dendrite growth mechanism manifests itself the most when both stirrers are working simultaneously (**Tab. 9-2**: 4A, 4B

and 5B). If MEMS and SEMS are working simultaneously, the stirring effect significantly destroys the formation of columnar crystals. If only MEMS is working and SEMS is switched off (1A and 1B), then the desctruction of columnar crystals is less evident. The working mode of SEMS alone (modes 3A and 3B) cannot be clearly differentiated from the changes in the dendritic structure in relation to the structure formed without stirring (2A and 2B).

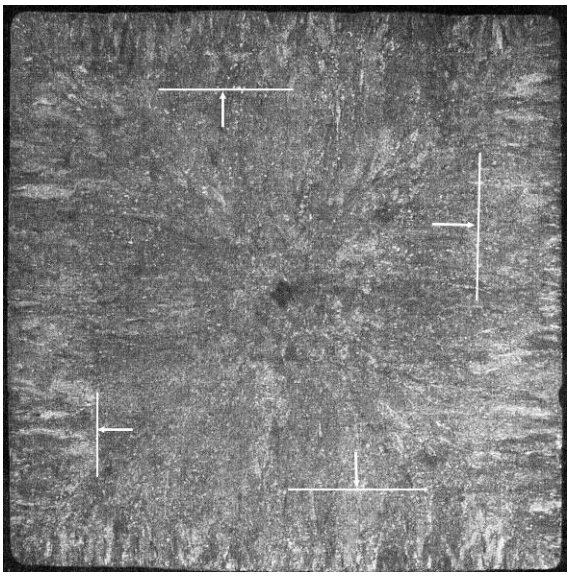

Fig. 9-4 MEMS+SEMS

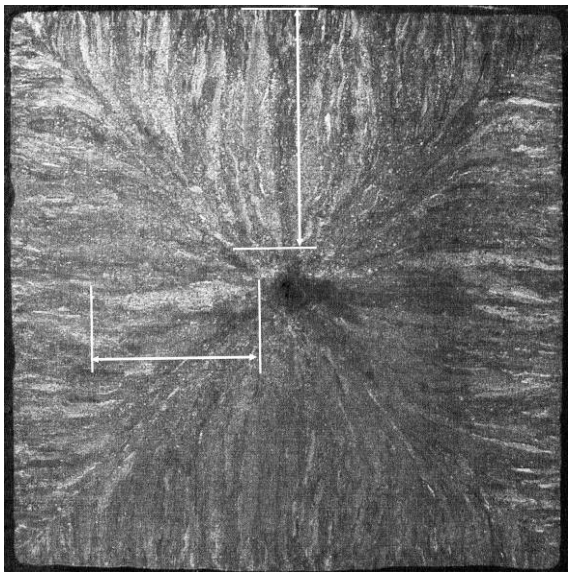

Fig. 9-5 Without stirring

Figure 9-3 (the macro-ground dendritic structure) shows the depth of the columnar band of dendrites in the direction away from the surface of the billet (**Fig. 9-4** – see arrows) and its value, which (with the simultaneous stirring of MEMS and SEMS is 23.4 ± 1.8 mm. The same qualified guess was made for ordinary billet casting (i.e. without stirring). Here, the depth of the dendrites can be guessed almost all the way to the central shrinkage at 70 mm (**Fig. 9-5** – see arrows). It is known that additives and impurities during solidification are often concentrated in points of contact of the growing dendrites, where the maximum of segregated additives and impurities and the greatest probability of technological defects occurs.

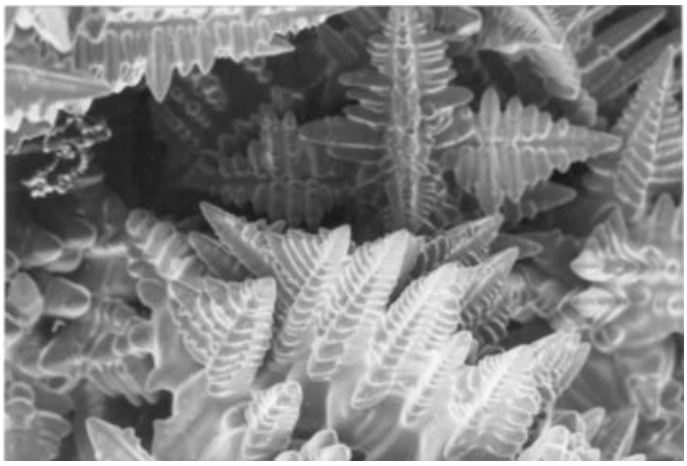

Fig. 9-6 Dendrites in the centre of the billet

In the given case, this undesirable effect can be expected along the diagonals which have a length of up to 100-to-103 mm towards the central shrinkage. This point of contact of the dendrites during the simultaneous working of SEMS and MEMS is only 29.8±1.9 mm, i.e. 3.4× less. The central area of the billet containing a hollow as a result of a shrinkage is then filled with dendrites growing into a vacuum (i.e. under-pressure) (**Fig. 9-6**).

9.4 Discussion

Under the assumption that the maximum of defects (i.e. vacancies, impurities, additives and micro-shrinkages) are formed along the diagonals it is possible to expect that in the areas of the corners – specifically on the edges – the nucleation of cracks will be higher than on the walls of the billet. If the first approximation of the fracture toughness of the relevant billet made from low-carbon steel is

$K_{IC} \sim 75.0$ MPa·m$^{1/2}$, then in the ordinary concasting process it can be assumed that the length of the contact of columnar dendrites along the diagonal will be approximately $\Delta l_{normal} \approx 101.5$ mm (**Fig. 9-5**). On the other hand, if both electromagnetic stirrers (MEMS and SEMS) are engaged simultaneously, the contact length of the columnar dendrites along the diagonal decreases to $\Delta l_{el.magn.} \approx 29.8$ mm (**Fig. 9-4**). Along these lengths (i.e. the areas) it could be expected that during concasting the concentration of the primary defects will increase where according to the mechanical fracture theory the following equations should apply for the preservation of the continuity of the surface: $K_{IC} \geq \sigma_{normal}\sqrt{\pi \Delta l_{normal}}\varphi(\Delta l_{normal}/w)$, $K_{IC} \geq \sigma_{el.magn.}\sqrt{\pi \Delta l_{el.magn.}}\varphi(\Delta l_{el.magn.}/w)$. The first equation applies to normal concasting without EMS and the second to billet casting with both MEMS and SEMS engaged simultaneously. The component $\varphi(\Delta l/w)$ is the shape factor, which in the first approximation could be the same in both equations thus making it possible to estimate the stress and strain at the peaks of the dendrites touching each other along the diagonals [L9-4].

$$\sigma_{normal} \leq \frac{K_{IC}}{\sqrt{\pi\, \Delta l_{normal}}} = \frac{75}{\sqrt{\pi\, 0.0298}} = 245.1\,\text{MPa}, \qquad \text{(eq. 9-1)}$$

which is the limit stress and strain for normal concast billets without EMS, i.e.

$$\sigma_{el.magn.} \leq \frac{K_{IC}}{\sqrt{\pi\, \Delta l_{el.magn.}}} = \frac{75}{\sqrt{\pi\, 0.1015}} = 132.8\ \text{MPa}, \qquad \text{(eq. 9-2)}$$

which is the limit stress and strain in the area of the edges of the billets during concasting if both MEMS and SEMS stirrers are engaged. A comparison of both limit stresses and strains indicates that the billets (otherwise cast under the same conditions) cast without stirring are almost twice as susceptible to cracking along the edges as billets cast using both stirrers.

A similar assumption can be made even in the case of assessing the effect of columnar dendrites in the central part of the surface of the billet where, without stirring, their length grows from the surface of the wall all the way to the central shrinkage (**Fig. 9-5**), while with the stirrers the dendrites are significantly shorter. The boundaries of the dendrites are however much less damaged by technological defects (vacancies, etc.) than the areas of their touching – of the peaks along the diagonals.

Long-term statistical monitoring of the quality of 150×150 mm billets and the chemical composition has proven that the application of EMS has significantly reduced the occurrence of defects (in this case cracks) [L9-4].

9.5 Conclusions

This paper introduces the results of a very demanding experimental verification of the effect of EMS on the dendritic structure of steel during the concasting of billets. As many as nine different variants of concasting were verified on the mould in the following combinations:

a) Ordinary concasting without EMS.

b) Concasting with EMS using MEMS mounted on the mould.

c) Concasting with EMS using SEMS mounted beneath the mould.

d) Concasting using both MEMS and SEMS.

The method of application of these combinations is characterised in detail in **Tab. 9-2** together with the corresponding current.

Macroscopic grinding was conducted on samples taken from cross-sections of individual billets in order to make the dendritic structure visible and evaluate it.

In mode 2A and 2B, columnar dendrites form throughout the entire cross-section and oriented perpendicular to each wall of the billet. The growth of these columnar dendrites ceases upon the touching of the other dendrites along the diagonals of the cross-section. Only those dendrites growing in the centres of the walls reach the centre of the cross-section (**Fig. 9-2**).

The greatest effect of the EMS was experimentally observed during the mixing using both MEMS and SEMS simultaneously. The area of the columnar dendrites oriented perpendicular to the surfaces of the walls has a thickness limited to ¼-to-⅓ of the billet thickness. In the remaining central part of billets stirred in this way the structure which dominates is the equiaxed dendrite structure.

It can be assumed – based on fracture mechanics – that with the application of MEMS and SEMS technologies, and otherwise under the same conditions, the critical stress leading to the initiation cracks is almost double (1.85×) compared to ordinary casting (i.e. without stirring).

Long-term statistical monitoring of the quality of 150 × 150 mm billets and the chemical composition given in **Tab. 9-1** has proven that the application of EMS reduces the occurrence of defects (i.e. cracks).

The solution has been printed in the peer-reviewed journals and presented at prestigious conferences [L9-5 to 9-7].

9.6 Literature

[L9-1] Kunstreich S.: *La Revue de Metallurgie CIT*, 2003, april, s. 395–408.

[L9-2] Chung S.I. and Yoon J.K.: *Ironmaking and Steelmaking,* 23 (1996) 5, 425–432.

[L9-3] Park J., Kim H., Jeong H., Kim G., Cho M.J., Chung J.S., Yoon M., Kim K.R. and Choi J.: Continuous Casting of Steel Billet with High Frequency Electromagnetic Field. *ISIJ*, 43 (2003) 6, 813–819.

[L9-4] Kavička F., Stránský K., Sekanina B., Štětina J. and Dobrovská J.: The effect of electromagnetic stirring on the crystallization of concast billets. *Materiali in tehnologije/ Materials and technology.* 45 (2011) 2, 163–166.

[L9-6] Stránský K., Kavička F., Sekanina B., Štětina J. and Stránský L.: Electromagnetic stirring of the melt for production of the continuously část billets and its importance. *Hutnické listy.* 62 (2009) 3, 26–30.

[L9-7] Kavička F., Stránský K., Dobrovská J., Sekanina B. and Štětina J.: Numerical Models of Crystallization and Its Direction for Metal and Ceramic Materials in Technical Application. In *Crystallization. Science and Technology.* Marcello Andreeta. Rijeka, Croatia, InTech Europe. 2012. p. 65–90.

10 Method for measurement of chemical micro-heterogeneity of carbon in continuously cast billets

10.1 Introduction

The quantitative point X-ray spectral analysis of elements belonging into the second period of the Mendeleyev periodical system and denoted as *light elements*, is still very difficult. The *light elements* comprises the elements from the atomic number 4 (beryllium) to the atomic number 9 (fluorine). The difficulty of analysis is caused by the fact that their X-ray radiation has a wide wavelength, low energy and the X-ray intensity excited by an impact of the electron beam on the analysed surface of the sample is also low, which requires longer exposure times. It is also necessary to use for the wavelength dispersive X-ray analysis of *light elements* special organic crystals with sufficiently wide distance between the planes. Carbon with atomic number 6 is located approximately in the middle of the said *light elements* and contamination of the surface areas of the places of the electron beam incident onto the surface of the analysed sample contributes to considerable disadvantage of the micro-analysis, since fumes containing carbon are formed as a result of interaction of the beam with the residual vacuum. These contaminating fumes increase the measured intensity of carbon, which means duration of measurement of carbon, i.e. dwell of the electron beam at the same spot of the sample surface is time limited. The quantitative X-ray micro-analysis of carbon requires also the use of suitable standard or standards. The standard of the cementite Fe_3C, or samples of steels with graded carbon contents proved successful at determination of the calibration curve of carbon in steels.

The actual measurement of the carbon content in the samples of steel requires extremely careful preparation of metallographic specimens, preferably finish polished with use of diamond pastes. At the X-ray analysis it is necessary to observe strictly the orientation of the analysed surface in the direction perpendicular to the incident electron beam. Detailed information is contained for example in the works [L10-1 to 10-3].

10.2 Conditions of samples preparation and procedure of measurement

The samples were taken from continuously cast billet (with dimensions 300 × 350 mm) marked as A with the following chemical composition in wt.%: 0.806 C, 0.64 Mn, 0.20 Si, 0.011 P, 0.009 S, 0.06 Cu, 0.05 Cr and 0.04 Ni. The samples with basic dimensions of approx. 17 × 17 × 22 mm were taken from the cross-section of the billet and individual samples were marked according to the diagram in **Fig. 10-1**. The samples marked as 11, 13, 31 and 33 were located in the corners of the billet, the samples marked 12, 21, 32 and 23 were taken from the surface of the billet in the middle of the relevant length, and the sample marked as 22 was taken directly from the central area of the billet cross-section. Metallographic polished sections were prepared on the surfaces perpendicular to the direction of the billet movement. Metallographic sections were prepared by wet grinding with use of metallographic papers and by finish polishing with use of the diamond paste with grain size ≤ 1 μm. Thus prepared metallographic section was finely etched with use of a 2% nital in order to make visible the microstructure, and approximately in the centre of the sample an area suitable for analysis was selected and marked with a circle. Then the direction of micro-analysis was in this area marked on the light microscope NEOPHOT II by micro-indents made with use of the micro-hardometer. The samples were then re-polished again by a diamond paste in order to remove the layers etched by nital and they were immediately inserted into the chamber of the micro-analyser.

- smaller radius of the billet

11	21	31
12	22	32
13	23	33

- larger radius of the billet

Fig. 10-1 Diagram of taking of the samples from the billet

10.2.1 Measurement of concentration of elements

The actual measurement used the micro-analytical complex JEOL JXA-8600/KEVEX/Delta V-Sesame, which had four wavelength spectrometers, the analytical crystals of which were used for the measurement of carbon (crystal of *lead stearate*), manganese (crystal of *LiF*), silicon and phosphorus (crystals of *PET*). The working conditions at the wave dispersive X-ray analyses were identical for all the samples and they were as follows: accelerating voltage of the primary electron beam $U = 15$ kV, current of the primary electron beam $I = 10$ nA, duration of one measurement (exposure) $t = 50$ s. Special user program was applied for a segmental micro-analyser Brno Linescan made by the company SAM_X, developed some time ago for the VTÚO Brno as customised device according to the defined specification.

The concentration measurement was performed on each of the set of nine samples always on 100 points lying on the line segment with a length of 990 μm with the gradation of the measured points after 10 μm. Each measured data set thus contains one hundred of the measured point concentrations of carbon, manganese, silicon and phosphorus. The first measured point of the concentration set was always oriented towards the side adjacent to the central axis of the billet, and the last hundredth point of the concentration set point was on the side distant from the centre-line of the billet.

The manner of evaluation of concentrations of manganese, silicon and phosphorus was quantitative with use of the standards of pure elements for manganese and silicon, and with application of the standard Cu_3P for phosphorus. The background (i.e. the intensity of spectral line of pure element) was measured for Mn, Si and P on the standard of spectrally pure iron. For correction of the measured intensities of these three elements the ZAF correction factors were applied, which were calculated with use of the program Magic of the company Kevex for determination of chemical composition of the billet. The quantitative evaluation of micro-analysis of carbon was carried out with use of two methods. At use of the first method (**eq. 10-1**), the carbon content was calculated by method of differential (suspended) concentration developed at the VTÚO in Brno, it means with use of the standard of graphite, correction coefficient $k = 2.4963$ obtained from the measurements on the standard Fe_3C and from the combined measurements of carbon graphite/standard Fe_3C followed by a suspension to the value measured on the standard of the ÚFM AV Brno containing 0.88 wt.% C. At use of the second method (**eq. 10-2**), the carbon content was calculated with use of the calibration curve obtained from the measurements on the standards of ÚFM AV Brno containing 0.06 and 0.88 wt.% C. Evaluation of the measured X-ray radiation intensities Kα of carbon by the first and the second method corresponded with the average deviation of 0.064 wt.% C.

10.2.2 Detectability limit and measurement errors

Limit of detectability of an element is usually defined as element concentration, which is measured with the relative standard error of approx. 50% [L10-1 to 10-3]. The limit of detectability of carbon in pure iron is calculated from the measured intensities of X-ray radiation using the following relation

$$C^{C}_{Fe(\min)} = \frac{2\sqrt{I_{BC}}}{(I_{P-ST} - I_{B-ST}).\sqrt{\tau}} C_C \ , \qquad \text{(eq. 10-1)}$$

where $C^{C}_{Fe(\min)}$ is the smallest detectable concentration of carbon determined with a relative standard error of approx. 50%, I_{BC} is intensity of noise of the spectral line of carbon measured on pure iron at the time τ, $(I_{P-ST} - I_{B-ST})$ is pure intensity of spectral line of carbon measured on the standard used for carbon at the time τ, and C_C is concentration of carbon on the standard. With use of control determination of the limit of detectability of carbon the value $C^{C}_{Fe(\min)} = 0.0581$ wt.% C [L10-2] was measured for pure iron under the given conditions of micro-analysis for the exposure of 50 s. This minimal value of carbon concentration (detectability limit) is in the envisaged point measured with the relative standard error of approx. 50% of the determined concentration, which corresponds in the absolute value to the content of 0.0291 wt.% C [L10-2]. With the increasing concentration of carbon in steel the relative standard error decreases approximately according to a hyperbole and it approaches

the relative standard error of measurement of carbon concentration on the standard Fe_3C, which is for normal measurements approx. ≈7.6%.

It is possible to estimate in a qualified manner the relative standard error of the measured carbon concentration C_{meas} in wt.% using the relation

$$\delta_{rel} \approx \sqrt{\left(\frac{C^{C}_{Fe(\min)}}{2C_{meas}}\right)^2 + \delta^{Fe_3C}_{rel}} \qquad \text{(eq. 10-2)}$$

It follows from this equation that measurement of the average concentration of carbon in the billet containing 0.806 wt.% C is accompanied by a relative standard error of ≈ 0.084%, i.e. by the absolute error of 0.068 wt.% C. Assuming variations in the content of carbon in the measured concast billet the range of approx. 0.5 to 1.5 wt.% (see for example **Fig. 10-2**), the relative standard error of measurement δ_{rel} is in the interval of approximately 0.096 to 0.078%. The relevant mean absolute errors of measurement are then approximately 0.048 wt.% C to 0.118 wt.% C for the measured contents of 0.5 and 1.5 wt.% C.

10.3 Results of measurements

Detailed measurements of chemical micro-heterogeneity of carbon, manganese, silicon and phosphorus are presented in the research reports [L10-4 and 10-5]. In this work we give only a brief summary related to the billet with the chemical composition determined by melt analysis in wt.% of the measured elements 0.806 C, 0.64 Mn, 0.20 Si and 0.011 P. Example of basic measurement of concentration distribution of the four elements C, Mn, Si and P in the sample marked as 12 in the continuously cast billet A is shown in **Fig. 10-2**.

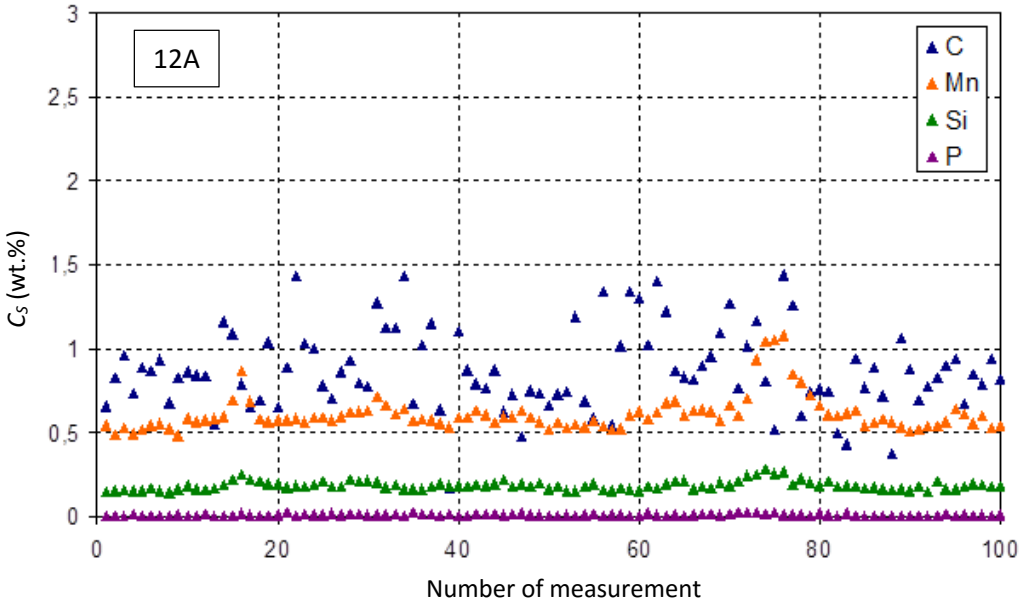

Fig. 10-2 Measured values of concentrations of selected elements in the sample 12 taken from the billet A. Length of the measured section - 990 μm, distance between the points - 10 μm. Concentration of elements increases in the order P, Si, Mn and C.

It follows from the results of measurements shown in **Fig. 10-2** that the distribution of carbon in the continuously cast billet has comparatively high micro-heterogeneity what concerns the distribution of Mn, Si and P. Similar distribution of elements was measured also in the remaining eight samples distributed over the cross-section of the billet according to the diagram on **Fig. 10-1**. The basic measured distribution of the concentrations of elements in a set of nine samples was further processed according to the original model [L6-34] in such a manner, that the measured concentrations were first subjected to a mathematical-statistical processing to characterise the arithmetic means of the measured concentrations of elements in the selected section C_{av}, their standard deviation σ_C, and also the minimum and maximum concentrations of the measured elements - $C_{\min}$ and $C_{\max}$, heterogeneity

indexes defined by the relationship $I_H = s_x/C_{av}$ and segregation indexes defined by the $I_S = C_{max}/C_{av}$. After that the measured concentrations of elements were sorted in an ascending order according to the Gungor's method [L6-7] and they were used for determination of the effective partition coefficients k_{ef} of all four measured elements. The used model together with its application for the determination of partition coefficients is described in detail in the work [L6-34].

Example of distribution curves of the measured concentrations of carbon, manganese, silicon and phosphorus in the billet A in the samples 12 and 13 ordered by the Gungor's method is shown in **Fig. 10-3**. It follows from the graphic representation that the distribution of element concentrations in dependence on the solid fraction f_S (each value of which corresponds to one measured point in the structure) shows the distribution of the relevant measured element in the dendrite. Positions of concentrations of the measured elements for $f_S \rightarrow 0$ correspond to the axes of dendrites, while positions for $f_S \rightarrow 1$ correspond to concentrations between dendrites during the last stage of solidification.

Example of evolution of the calculated effective partition coefficients of carbon, manganese, silicon and phosphorus from the distribution curves (in **Fig. 10-3** from the work [L6-34]) is shown in **Fig. 10-4**.

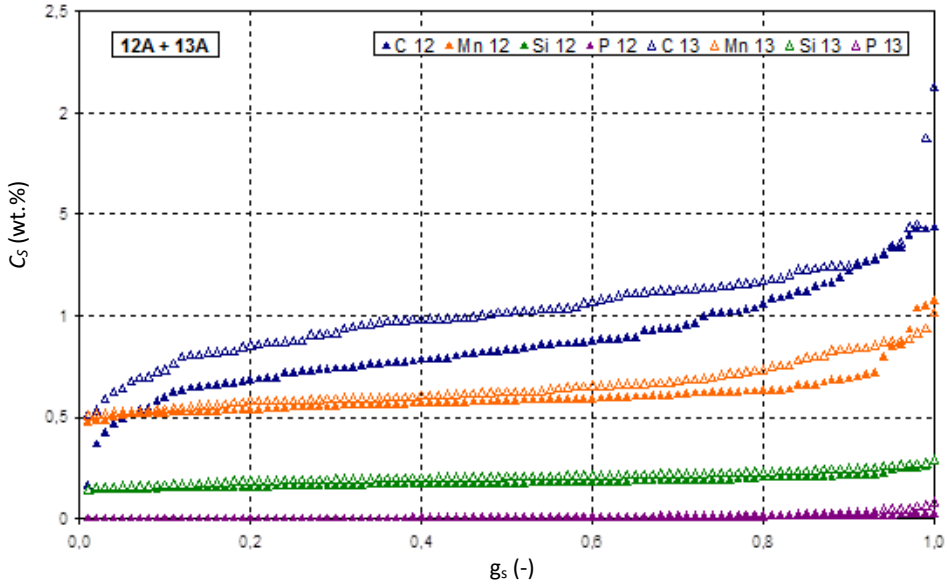

Fig. 10-3 Distribution curves of dendritic segregation for the samples 12A and 13A plotted from the experimentally measured concentration sets of the relevant samples. Mean values of the ordered concentration of elements increase (for $f_S \approx 0.5$) in the order P, Si, Mn and C.

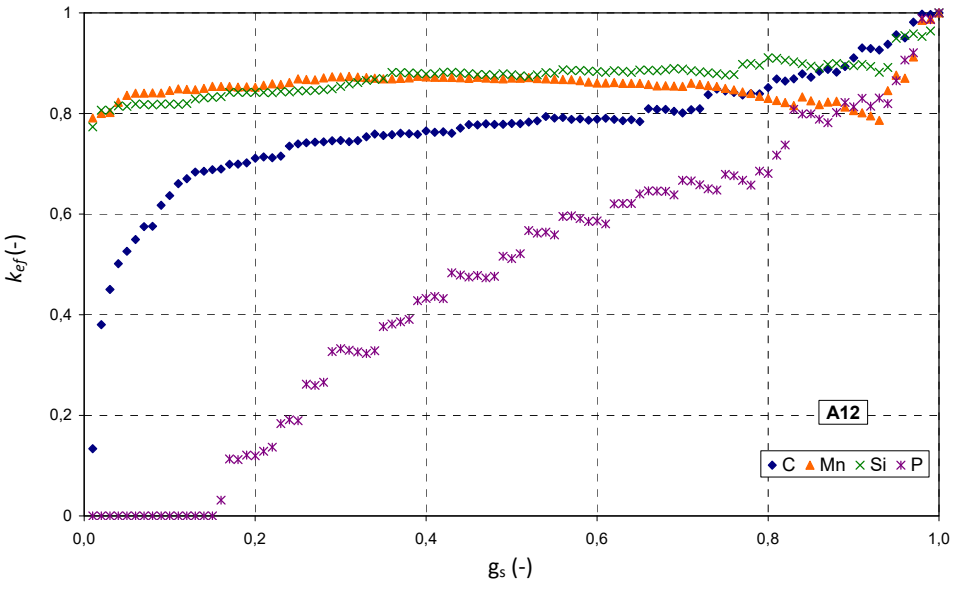

Fig. 10-4 Evolution of effective partition coefficients of phosphorus, carbon, manganese and silicon in the sample 12 in the billet A calculated from the measured concentration sets

Tab. 10-1 Basic statistical parameters of the measured concentrations of elements in the samples taken from the billet A for n = 100 measured points

Sample	Parameter	Element (wt.%)				
		C	Mn	Si	P	Fe
11	C_{av}	0.9508	0.6122	0.1887	0.0101	98.2382
	s_x	0.3091	0.0625	0.0208	0.0071	0.3203
	$C_{\min}$	0.2847	0.4926	0.1397	0.0000	97.1792
	$C_{\max}$	2.0543	0.7688	0.2521	0.0289	98.9657
12	C_{av}	0.8704	0.6098	0.1839	0.0082	98.3278
	s_x	0.2610	0.1084	0.0271	0.0069	0.3100
	$C_{\min}$	0.1162	0.4824	0.1423	0.0000	97.1733
	$C_{\max}$	1.4800	1.0764	0.2836	0.0268	99.1551
13	C_{av}	1.0370	0.6603	0.2103	0.0126	98.0798
	s_x	0.2453	0.1089	0.0293	0.0159	0.2929
	$C_{\min}$	0.5042	0.5113	0.1432	0.0000	97.0210
	$C_{\max}$	2.1704	1.0169	0.2944	0.0853	98.7417
21	C_{av}	0.8944	0.6514	0.2020	0.0133	98.2389
	s_x	0.2378	0.0801	0.0269	0.0087	0.2798
	$C_{\min}$	0.0544	0.5161	0.1390	0.0000	97.5568
	$C_{\max}$	1.3782	0.8891	0.3021	0.0425	99.1923
22	C_{av}	0.9228	0.6635	0.2236	0.0080	98.1821
	s_x	0.2351	0.1079	0.0298	0.0078	0.2948
	$C_{\min}$	0.3888	0.5084	0.1673	0.0000	97.3527
	$C_{\max}$	1.5869	1.0138	0.2936	0.0347	98.8959
23	C_{av}	0.9339	0.6526	0.2027	0.0148	98.1960
	s_x	0.2024	0.0949	0.0263	0.0086	0.2619
	$C_{\min}$	0.1633	0.4791	0.1543	0.0000	97.2631
	$C_{\max}$	1.4471	1.0169	0.2575	0.0380	99.1296
31	C_{av}	0.9014	0.6280	0.2248	0.0121	98.2336
	s_x	0.2310	0.0884	0.0322	0.0109	0.2803
	$C_{\min}$	0.1003	0.4985	0.1473	0.0000	97.5061
	$C_{\max}$	1.4787	0.9231	0.3022	0.0643	99.0411
32	C_{av}	0.8085	0.6293	0.1992	0.0083	98.3547
	s_x	0.2501	0.0685	0.0226	0.0069	0.2859
	$C_{\min}$	0.1322	0.4365	0.1534	0.0000	97.2602
	$C_{\max}$	1.8110	0.8239	0.2592	0.0296	99.1574
33	C_{av}	0.8587	0.6518	0.2133	0.0125	98.2638
	s_x	0.2334	0.1012	0.0302	0.0128	0.2692
	$C_{\min}$	0.2321	0.4802	0.1463	0.0000	97.6122
	$C_{\max}$	1.3893	0.9532	0.2911	0.0861	99.0166
$x_\Sigma = \sum_{i=11}^{i=33} \frac{x_i}{9}$	$C_{av\Sigma}$	0.909	0.640	0.205	0.0111	–
	s_x	±0.064	±0.020	±0.014	±0.0025	
Melt analysis		0.806	0.64	0.20	0.011	–

Note: The mean values of Fe concentrations given in the last column were obtained by completing the sum to 100% (the value comprises also admixtures); carbon content is an average of $C = (C_{(1)} + C_{(2)})/2$ – see section 10.2.1.

It is evident from the graphic representation of effective partition coefficients in **Fig. 10-4**, that for carbon and particularly for phosphorus it is possible to expect substantial differences in determination of the values k_{ef}^{C} and k_{ef}^{P}. It may be expected that the axes of dendrites, solidifying as the first ones, will have a very low concentration of carbon and practically zero concentration of phosphorus. What concerns manganese and silicon, the differences in the determined values of the partition coefficients k_{ef}^{Mn} and k_{ef}^{Si} are small. It can be, however, expected that the highest concentrations of all elements will be located between dendrites during the final stage of solidification of an inter-dendritic melt.

Table 10-1 presents an example of basic statistical evaluation of the set of all nine samples taken from the billet A. It is evident from the results in the table that the average carbon content determined in the set of nine samples by wavelength dispersive X-ray spectral micro-analysis corresponds very well (satisfactorily) with the value of its content determined by the melt analysis of the billet A. The difference makes 0.909 to 0.806 = 0.103 wt.% C. The standard deviation of the average values from the nine samples with the value of $s_x = \pm 0.064$ wt.% C (**Tab. 10-1**) also agrees satisfactorily with the mean absolute error of the measured concentrations of carbon - 0.068 wt.% C. This was determined from a qualified estimate of the relative mean error, which corresponds to the concentration of 0.806 wt.% C according to the sample of the melt (see subchapter 10.2.2). Analogous conclusion can be made also for the measured results of the analysis of the remaining elements - Mn, Si and P, for which the results determined by an micro-analysis on the set of nine samples is also consistent with the results of the melt analysis (**Tab. 10-1**).

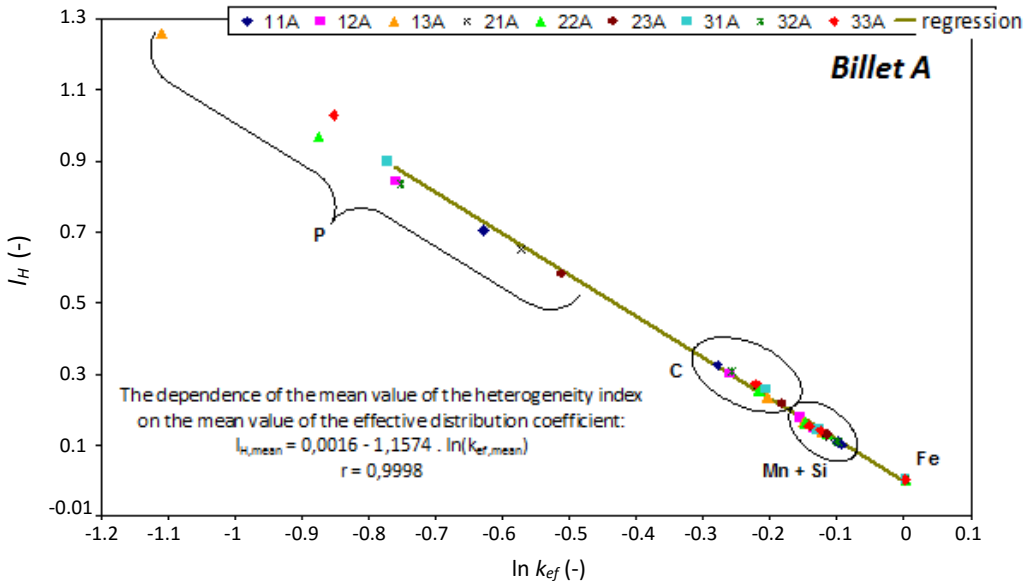

Fig. 10-5 Dependence of the heterogeneity index on the effective partition coefficient in the samples taken from the billet A

The basic mathematical-statistical evaluation of the measured concentration data, which indicate the concentration of all four measured elements and iron at each measured point, can be also examined by pair correlations of relations between these elements. It was found by data processing [L10-5 and 10-6] that in respect to iron the correlation coefficient of the elements C, Mn, Si and P is negative, which suggests that these elements segregate to the melt. The coefficient of correlation between the carbon and iron $k_{(Fe\text{-}C)} = -(0.916 \pm 0.033)$, as well as that between the silicon and manganese $k_{(Mn\text{-}Si)} = (0.650 \pm 0.092)$ and between the phosphorus and manganese $k_{(Mn\text{-}P)} = (0.303 \pm 0.144)$, and between the silicon and phosphorus $k_{(Si\text{-}P)} = (0.218 \pm 0.139)$ is strongly statistically significant, and the positive correlation between the manganese and carbon is also important.

The relationship between the effective partition coefficient of the measured elements and their chemical micro-heterogeneity index is shown in the graphical representation in **Fig. 10-5**. We can see that in the semi-logarithmic representation the measured points lie on a straight line $I_H = 0.0016 - 1.1574 \cdot \ln(k_{ef,mean})$, which corresponds with the high value of the correlation coefficient $r = 0.9998$. It follows from the relation that the chemical micro-heterogeneity of elements increases in the order of the elements Si, Mn, C, and P. Phosphorus has in the billet A the highest chemical micro-heterogeneity. Closer analysis revealed that the highest heterogeneity of phosphorus is in the central part, i.e. in the axis of the concast billet.

10.4 Conclusions

The previous text demonstrates the conditions and possibilities of use of method of wave dispersive X-ray micro-analysis of carbon in continuously cast block with dimensions 300 × 350 mm. It is shown that this method of analysis, which is experimentally comparatively highly demanding, makes it possible to obtain very valuable comprehensive information on the distribution of carbon and other elements, in this case of manganese, silicon and phosphorus in the structure of continuously cast steel.

The average and maximal values of all four measured elements - carbon, manganese, silicon and phosphorus are arranged in **Tab. 10-1**. It follows from **Tab. 10-1**, that for example the content of carbon on the larger radius of the billet reaches even 2.17 wt.% (sample A13) and on the smaller radius of the concast billet the highest measured carbon content was 1.48 wt.% (sample A12).

The contents of manganese and silicon are in the billets distributed more evenly. The average chemical heterogeneity of manganese is in wt.% 0.4530 with the standard deviation of 0.0917. The average silicon heterogeneity in wt.% is 0.1346 with the standard deviation of 0.0221. Phosphorus is distributed in the blocks very unevenly, its average concentration in nine samples is in wt.% 0.0485 with the standard deviation of 0.0225.

10.5 Literature

[L10-1] Rek A.: X-*ray spectral micro-analysis and possibilities of its application in marginal areas of physical metallurgy*, Dissertation thesis, Technical University in Brno, Brno 1980.

[L10-2] Stránský K. and Rek A.: Detectability of the method of elemental X-ray spectral analysis in alloys based on silicon, iron, silver and gold. *Jemná mechanika a optika,* (1994) 3-4, 92–96.

[L10-3] Rek A. and Stránský K.: The Contribution to the Analysis Carbon and Nitrogen in Steel Joint Weldments by Means of WD X-Ray Microanalysis. Invited Lecture. In *Proceedings EMAS 2000, 4th EMAS Regional Workshop on Electron Probe Microanalysis Today, Practical Aspects*, 17–20 May 2000, Třešť, Czech Republic, p. 157–163.

[L10-4] Rek A. and Stránský K.: *Micro-analysis of carbon, manganese, silicon and phosphorus for determination of their heterogeneity in a steel billet*, Military Technical Institute of Protection, Brno 2002, 40 pages.

[L10-5] Dobrovská J., Dobrovská V., Rek A. and Stránský K.: Chemical heterogeneity of carbon, manganese, silicon and phosphorus in continuously cast billets, *Research Report*. VŠB – TUO, FMMI, Ostrava 2003.

[L10-6] Stránský K., Rek A., Dobrovská J., Dobrovská V., Kavička F. and Sekanina B.: Method for measurement of chemical micro-heterogeneity of carbon in continuously cast blocks. *Hutnické listy*, 66 (2013) 5, 66–73.

11 Symbols

A	(J)	work to rupture
A_x; A_y; A_z	(m^{-2})	the area perpendicular to the direction *x,y,z*
A_5	(%)	ductility
c, c_p	($J \cdot kg^{-1} \cdot K^{-1}$)	specific heat capacity
C_{av}	(wt.%)	average concentration of the element
C_{eq}	(wt.%)	equivalent carbon content
C_0	(wt.%)	initial liquid concentration
C_L, C_S	(wt.%)	concentration of an element in the corresponding phase (liquid, solid)
C_{max}, C_{min}	(wt.%)	maximal and minimal concentration of the element
D_S	($m^2 \cdot s^{-1}$)	diffusion coefficient in solid phase
F	(N)	tensile force
F_{mushy}	(m^2)	area of the mushy zone on half of the cross-section of the breakout (Tab. 8-2)
F_{slab}	(m^2)	overal area on half of the cross-section of the breakout (Tab. 8-2)
F_{melt}	(m^2)	area of the melt zone on half of the cross-section of the breakout (Tab. 8-2)
f	(s^{-1})	oscillation of the crystallizer frequency
f_S	(-)	solid fraction of the solidified phase
h_S, h_L	(m)	length of the iso-solidus (iso-liquidus) curve from the level (Tab. 8-2)
htc	($W \cdot m^{-2} \cdot K^{-1}$)	heat transfer coefficient
H_v	($J \cdot m^{-3}$)	specific volume enthalpy
I_H	(-)	index of dendritic heterogeneity
I_P	(-)	index of macro-heterogeneity
I_S	(-)	index of segregation
k	($W \cdot m^{-1} \cdot K^{-1}$)	heat conductivity
k_{ef}	(-)	effective partition coefficient
K_{IC}	($MPa \cdot m^{1/2}$)	fracture toughness
L	(m)	secondary dendrite arm spacing, i.e. distances beetwen secondary dendrite arms (in steels)
L	(m)	distances between individual cells (in ceramics)
L_g	(m)	distance between the edges of graphite particles
L	($m^2 \cdot s^{-2}$)	specific latent heat of the phase change (Tab. 8-2)
m_i	(-)	the slope of the liquidus line of i^{th} element in the pseudobinary Fe-*i* phase diagram (eq. 6-9)
n	(-)	number of the measured points
n	(m)	normal line
q	($W \cdot m^{-2}$)	specific heat flow
$\dot{Q}_{source}$	($W \cdot m^{-3}$)	latent heat of the phase or structural change
$\dot{Q}X$, $\dot{Q}Y$, $\dot{Q}Z$	(W)	heat flow in the direction of *x, z, y* (Fig. 5-2 and eq. 5-4)
R_c	(m)	radius of the graphite cells
R_g	(m)	radius of the spheroids of graphite
s_x	(wt.%)	standard deviation of concentration (Tab. 6-2 and 7-2)
s_I		standard deviation of heterogeneity index (Tab. 6-2)
s_k		standard deviation of effective distribution coefficient (Tab. 6-2)
ΔS	(m)	mould oscillation amplitude

T	(K)	temperature
$T_{ambient}$	(K)	ambient temperature
T_{cast}	(K)	casting (melt) temperature
T_L	(K)	liquidus temperature
$T_{surface}$	(K)	surface temperature
T_S	(K)	solidus temperature
ΔT	(K)	interval of the solidification
ΔT_{over}	(K)	overheating above liquidus temperature
VX, VY, VZ	($W \cdot K^{-1}$)	heat conductivity in the direction of x, z, y (Fig. 5-2 and eq. 5-3)
w	($m \cdot s^{-1}$)	casting speed
$w_x; w_y; w_z$		components of casting speed in cartesian coordinates
w_{cool}	($K \cdot s^{-1}$)	average cooling rate of the mushy zone
x, y, z	(m)	Cartesian coordinates or dimensions
$\Delta x; \Delta y; \Delta z$	(m)	dimensions of the elementary volume (Fig. 5-2)
Z	(%)	contraction
α	(-)	dimensionless Fourier's number of the 2nd kind for mass transfer
β	(-)	back diffusion parameter
δ_{rel}	(-)	relative standard error of measurement (eq. 10-2)
ν	($m^2 \cdot s^{-1}$)	kinematic viscosity
θ	(s)	local solidification time
ρ	($kg \cdot m^{-3}$)	density
π_1 to π_8	(-)	dimensionless similarity criteria (subchapter 8.2.4.)
τ	(s)	time
$\Delta\tau$	(s)	time step
σ	($W \cdot m^{-2} \cdot K^{-4}$)	Stefan-Bolzmann constant (eq. 5-12d)
ε	(-)	emissivity (eq. 5-12d)
$\sigma_{c(i)}$	(wt.%)	standard deviation of element concentration *(*subchapters 8.3.3. and 10.3.)
σ_B, σ_C	(MPa)	the strains on the structure defects' tips (of the sample B, C)

indexes

L	melt, liquid phase
S	solid phase

abbreviation

eq.	Equation
Fig.	Figure
Tab.	Table
GAČR	Czech Scientific Foundation
MŠMT	Ministry of Education, Youth and Sports
MPO	Ministry of Industry and Trade
VTÚO	Military Technical Institute of Protection

NUMERICAL MODELS OF SOLIDIFICATION AND THEIR APPLICATION IN METAL AND CERAMIC TECHNOLOGY

Autors:
prof. Ing. František Kavička, CSc.; prof. Ing. Jana Dobrovská, CSc.
prof. Ing. Josef Štětina, Ph.D.; prof. Ing. Karel Stránský, DrSc.
doc. Ing. Jaroslav Katolický, Ph.D.; Ing. Bohumil Sekanina, CSc.
doc. Ing. Jaromír Heger, CSc., Ing. Hana Francová, Ph.D.

Published by: Brno University of Technology, Antonínská 548/1, 601 90 Brno, Czech Republic
Faculty of Mechanical Engineering
New Technologies for Mechanical Engineering Centre

VŠB - Technical University of Ostrava, 17. listopadu 15/2172,
708 33 Ostrava-Poruba, Czech Republic
Faculty of Metallurgy and Materials Engineering
Regional Materials Science and Technology Centre

Print: Ing. Vladimír Pokorný - Litera Brno, polygrafická výroba, Tábor 43a, 612 00 Brno, Czech Republic

Typographical design: Ing. Dana Horáková

Issue 1st
Number of pages 161
Number of copies 140

ISBN 978-80-214-5377-7
ISBN 978-80-248-3966-0